

# **Dynamics of continuously stratified and two-layer incompressible Euler fluids and internal waves**

Shengqian Chen

A dissertation submitted to the faculty of the University of North Carolina at Chapel Hill in partial fulfillment of the requirements for the degree of Doctor of Philosophy in the Department of Mathematics.

Chapel Hill  
2013

Approved by:

David Adalsteinsson

Roberto Camassa

Jingfang Huang

Richard M. McLaughlin

Laura Miller

## Abstract

**SHENGQIAN CHEN: Dynamics of continuously stratified and two-layer incompressible Euler fluids and internal waves.  
(Under the direction of Roberto Camassa.)**

The first part reveals a phenomenon in fluid mechanics that can be viewed as paradoxical: horizontal momentum conservation is violated in the dynamics of a stratified ideal fluid filling an infinite horizontal channel between rigid bottom and lid boundaries, starting from localized initial conditions, even though external forces only act on the vertical direction. The paradox is shown to be a consequence of the rigid lid constraint coupling through incompressibility with the infinite inertia of the far ends of the channel, assumed to be at rest in hydrostatic equilibrium. By the perturbation theory based on small density variance, an analytical study quantifies the momentum development at the initial time. These results are compared with direct numerical simulations for variable density Euler fluids.

The second part is a numerical study of strongly nonlinear models for internal waves. We emulate numerically the generation of solitary wave motivated by a laboratory experiment. The dam-break problem for internal waves can be solved by direct numerical simulations (DNS). By smoothing out the dam and symmetric extension of the wave tank, the strongly nonlinear model is ready for implementation. The Kelvin-Helmholtz instability associated with the model is treated by a time-dependent low-pass filter. The regularized strongly nonlinear model with less-restrictive stability criterion is also considered. The snapshots of the models and DNS show excellent agreements between models and DNS. The effect of numerical filters are considered to behave as reducing dissipation.

The third part consists of the comparisons among weakly nonlinear models for

internal waves by providing predictions for the two-layer dam-break problem. We regularized a completely integrable but ill-posed system, the two-layer Kaup equations. The new equations are numerically solvable and provide better agreement with the inverse scattering transform prediction for the Kaup equations than the Boussinesq equations, another weakly nonlinear model for bi-directional waves. A higher order uni-directional model is also considered to cope with moderate amplitude waves. These models are compared for their traveling wave solutions, phase speed and amplitude relations, and dispersion relations. The time evolutions for the two-layer dam-break problem from weakly nonlinear models are compared with DNS.

## Acknowledgments

First and foremost I want to thank my advisor, Dr. Roberto Camassa, for his encouragement, patience, and rigorous yet pleasant training during these years, which have directly contributed to my general understanding of fluid mechanics and mathematical modeling. His childlike enthusiasm and curiosity of science have greatly influenced my way of thinking about and performing research. I feel really fortunate to have the opportunity to work under his supervision so that the process of solving problems is composed of joyful intellectual stimulations.

I also wanted to thank the members of my committee for all the suggestions they gave me in writing this thesis. I am greatly indebted to the entire applied math faculty. I want to thank Dr. Jingfang Huang for years of friendship and encouragement when I felt puzzled, confused about directions of my future career.

I am very grateful to Dr. Ann Almgren for her invaluable help with the numerical work and to Dr. Wooyoung Choi and Dr. Tae-Chang Joe for illuminating discussions. I want to thank Dr. Avadh Saxena, who kindly hosted me during a summer internship at LANL. During my stay at LANL, I had many useful discussions with Dr. J. Mac Hyman, for which I thank him. I also want to thank Dr. Gregorio Falqui, who invited me for a visit at University of Milano - Bicocca. And thanks to Dr. Giovanni Ortenzi and Dr. Marco Pedroni, with whom I initiated one of my thesis topics. For data analysis, I have used extensively DataTank. I thank its creator, Dr. David Adalsteinsson for all his help.

I thank my colleagues Dr. Roxana Tiron and Dr. Claudio Viotti for helpful sug-

gestions. Also I want to thank my dear officemate, Claudia Falcon, for the positive energy she always brings to me. I am also indebted to so many friends who helped me accommodate in a foreign country.

Last but not least, I thank my parents for the understanding and support for my decision to come to the States for the journey of truth-seeking and the pursuit of freedom. I have always been a naughty girl kicking social norms. Thanks for your tolerance.

## Table of Contents

<b>List of Figures</b>	ix
<b>List of Tables</b>	xiv
<b>1 General introduction</b>	1
<b>2 Effects of inertia and stratification in incompressible ideal fluids: pressure imbalances by rigid confinement</b>	6
2.1 Introduction	6
2.2 The physical system and its governing equations	11
2.2.1 Pressure imbalances and horizontal momentum	12
2.2.2 Small $\rho_\Delta$ limit and the scaling relation between $P_\Delta$ and $\rho_\Delta$	16
2.2.3 Interfacial pressure imbalance and total vorticity	19
2.3 Long-wave models	21
2.3.1 Equations of motion	23
2.3.2 Effects of dispersion	24
2.4 Full Euler system: pressure jump at $t = \mathbf{0}$ in the small $\rho_\Delta$ asymptotic limit	27
2.4.1 The small $\rho_\Delta$ expansion	27
2.4.2 Comparison with the long wave model	33
2.4.3 Special initial conditions: piecewise-constant interfaces	33
2.4.4 Special initial conditions: linear interfaces	38
2.5 Dam-breaking class	41
2.6 Time evolution: numerical results	45
2.6.1 The effect of infinite inertia	48
2.6.2 Step function simulations	51

2.7	Time derivative of $\langle \mathbf{p} \rangle_{\Delta}$ at $\mathbf{t} = \mathbf{0}$	55
2.8	Conclusions	57
3	<b>An extended application for the strongly nonlinear internal wave models</b>	60
3.1	Introduction	60
3.2	Motivations	63
3.3	Mathematical models	64
3.3.1	Governing equations	64
3.3.2	Strongly nonlinear internal wave model	65
3.3.3	Regularized nonlinear long wave model	66
3.4	Numerical algorithms	67
3.4.1	Direct numerical simulations for Euler equations	67
3.4.2	Strongly nonlinear model	68
3.4.3	Regularized model	70
3.4.4	Artificial filter for long wave models	71
3.5	Results	72
3.5.1	Parameter set-up	72
3.5.2	The effect of gate smoothing	75
3.5.3	Small amplitude waves	76
3.5.4	Moderate amplitude waves	78
3.5.5	Large amplitude waves	78
3.5.6	Choice of the optimal filter	82
3.5.7	Primary wave forming solitary waves	83
3.5.8	Horizontal shear velocity reconstruction	85
3.6	Discussion	88
4	<b>Weakly nonlinear models for internal waves</b>	90
4.1	Introduction	90
4.2	Governing equations	92

4.3	The strongly nonlinear model . . . . .	93
4.4	The Kortwegg-de Vries equation . . . . .	94
4.5	Weakly nonlinear models for bi-directional waves . . . . .	98
4.5.1	The two-layer Kaup model . . . . .	98
4.5.2	Regularized Kaup equations . . . . .	102
4.5.3	The two-layer Boussinesq equations . . . . .	106
4.5.4	The derivation of KdV equation from the Kaup equation . . . .	111
4.6	Higher-order uni-directional models . . . . .	115
4.6.1	Choice of $\mu$ for conserved quantity . . . . .	116
4.7	The solitary waves produced by an arbitrary initial disturbance . . . .	118
4.7.1	Solutions for the two-layer KdV equation . . . . .	120
4.7.2	Solutions for the two-layer weakly nonlinear models for bi-directional waves . . . . .	122
4.7.3	Higher order uni-directional model . . . . .	128
4.8	Discussion . . . . .	129
A	<b>Translational invariance and symmetries</b> . . . . .	131
B	<b>Boundary effects in air water systems</b> . . . . .	137
C	<b>Independent direct numerical simulations</b> . . . . .	139
C.1	Solitary wave collisions . . . . .	139
C.2	Dam-break problem . . . . .	140
D	<b>Codes for models</b> . . . . .	142
D.1	The strongly nonlinear model . . . . .	142
D.2	The regularized Kaup equations . . . . .	165
D.3	The Boussinesq equations . . . . .	173
D.4	The KdV equation . . . . .	185
D.5	Higher order uni-directional model . . . . .	195
	<b>Bibliography</b> . . . . .	205



## List of Figures

2.1	A two-layer configuration with different asymptotic heights. . . . .	12
2.2	The contours for Stokes theorem in the case of a two-layer fluid. . . . .	20
2.3	Sketch of a typical interface configuration for a two-fluid density distribution for which boundary contributions are relevant. . . . .	22
2.4	A two-bump configuration. Only when $S$ is comparable with the typical width of the bumps $P_\Delta$ is nonzero. . . . .	26
2.5	Initial hook-like configuration for a two-fluid density distribution in an $x$ -infinite channel between two rigid plates located at $z = 0, 1$ . . . . .	35
2.6	(a) Full hook case, with $A_2 - A_1 = A_3 - A_2 = 1.5$ , $z_3 = z_0$ , $z_1 = 0$ , $z_2 = 1$ , $\rho_\Delta = 0.01$ (crosses), $\rho_\Delta = 0.1$ (diamonds), from numerics (§ 2.6), theoretical value (solid line) from asymptotics $\rho_\Delta \rightarrow 0$ . (b) Kink-like case, with $A_2 - A_1 = A_3 - A_2 = 1.5$ , $z_1 = 0.3$ , $z_2 = 0.8$ , $z_3 = 0.5$ , $\rho_\Delta = 0.01$ (crosses), $\rho_\Delta = 0.1$ (diamonds), from numerics (§ 2.6), theoretical value (solid line) from asymptotics $\rho_\Delta \rightarrow 0$ (equation (2.71)).	36
2.7	Pressure imbalance $P_\Delta$ vs. density difference $\rho_\Delta$ . Theory (solid line) from equation (2.71) and VARDEN simulation (dots). The interface is a hook (figure 2.5) with parameters given by $z_0 = z_3 = 0.5$ , $z_1 = 1$ , $z_2 = 0$ , and $A_2 - A_1 = A_3 - A_2 = 1.5$ as in figure 2.6(a). The 2:1 slope is maintained up to density differences as large as $\rho_\Delta \simeq 0.2$ (in units of $\rho_2$ ).	37
2.8	The special configuration of a staircase hook for a two-fluid density distribution in an $x$ -infinite channel between two rigid plates located at $z = 0, 1$ . . . . .	38
2.9	The “incline hook” configuration for a two-fluid density distribution in an $x$ -infinite channel between two rigid plates located at $z = 0, 1$ . . . . .	39
2.10	The piecewise constant vs. linear configurations for a two-fluid density distribution in an $x$ -infinite channel between two rigid plates located at $z = 0, 1$ . . . . .	40
2.11	Dam-break configuration for a two-fluid density distribution. The pressure is everywhere continuous (and so, $\partial_z p_1 = \partial_z p_2$ at the interface $x = 0$ ) with the jump condition for its normal derivative at the interface $\partial_x p_1 = (\rho_1/\rho_2)\partial_x p_2$ . . . . .	42
2.12	The geometric limit from the hook to dam configuration. . . . .	45

2.13	Sketch of the fluid test domain and its symmetrical padding by wings of increasing length, doubling and quadrupling the period as shown. . . .	47
2.14	Density field from the numerical simulation of the evolution from the initial data in the 1232 cm long tank with the center 308 cm test section marked by the vertical lines. . . . .	47
2.15	(a) Horizontal momentum time evolutions for the test section embedded in progressively larger periodic domains, starting from the same initial condition. The solid line correspond to the rigid wall boundaries. (b) Time series of fluxes $Q(t)$ with respect to increasing period $L$ , for the same cases as (a). The flux decreases as $1/L$ in response to the larger inertia of the channel “padding” wings. . . . .	49
2.16	(a) Pressure jump and (b) total vorticity time history for the dam-break initial condition sketched in figure 2.11, in the time interval $0s < t < 2.8s$ with 512 (solid line) and 256 (dotted line) vertical points resolutions. The initial velocities of the fluids are zero, the fluid densities are $\rho_1 = .9$ and $\rho_2 = 1$ and the height of the channel is fixed to 1. . . . .	52
2.17	(a) Same as figure 2.16 but for the “hook with sliver” initial condition (figure 2.5) with $z_0 = z_3 = 0.5$ , $z_1 = 0.1$ and $z_2 = 0.9$ . . . . .	53
2.18	(a) Same as figure 2.16 but for “complete hook” initial condition (figure 2.5) with $z_0 = z_3 = 0.5$ , $z_1 = 0$ and $z_2 = 1$ . . . . .	53
2.19	Snapshots of density $\rho$ and velocities $(u, w)$ (for horizontal and vertical component, respectively) for the time evolution of motion with the dam-breaking initial condition sketched in figure 2.11. Resolution is 512 vertical points, with physical parameters for this computation listed in the caption of figure 2.16. The initial density configuration is depicted in the top panel, which also illustrates the actual computational domain and its aspect ratio. . . . .	54
2.20	Same as figure 2.19 but for the “hook with sliver” initial condition case (figure 2.5). Physical parameters listed in caption of figure 2.17. . . . .	54
2.21	Same as figure 2.19 but for the “complete-hook” initial condition case (figure 2.5). Physical parameters listed in caption of figure 2.18. . . . .	54

2.22	Convergence of numerical algorithm for the “hook with sliver” initial data. Plotted here is the density difference at $t = 2.8$ , generated by subtracting off the density from computations with 512 and 256 (vertical) nodes. Only the central portion (1/3 of the total length) of the channel is shown. For initial conditions that do not smooth the density jump, the resolution error becomes noticeable along the interface, where slight differences in its position in addition to numerical diffusion lead to nonzero density differences between the two computations. . . . .	55
3.1	Dam-break experiment setup . . . . .	72
3.2	Initial condition for long wave models by a symmetric extension of the wave tank and smoothed gate. . . . .	73
3.3	Snapshots of VarDen simulations. Top: H10LD1; bottom: H50LD1 . .	74
3.4	Snapshots at $T = 80$ s from VarDen simulations with different $\lambda$ , corresponding to different smoothing effect for runs H10’s (a) and H50’s (b). Solid black: $\lambda = 0.1 \text{ cm}^{-1}$ ; solid gray: $\lambda = 0.2 \text{ cm}^{-1}$ ; dash-dot black: $\lambda = \infty$ (no smoothing). . . . .	75
3.5	Snapshot of H10LD1 at $T = 80$ s. Solid: mean density isopycnocline from VarDen simulation; dashed: strongly nonlinear model; dotted: regularized model. The three vertical lines are at locations $x = 1420, 1510$ and $1610 \text{ cm}$ . . . . .	77
3.6	Time series of relative energy loss from VarDen simulations (a1, a2, and a3), the strongly nonlinear model (b1, b2, b3), and the regularized model (c1, c2, c3), with number 1, 2 and 3 denoting runs H10LD1, H20LD1 and H50LD1, respectively. . . . .	79
3.7	Snapshot of H20LD1 at $T = 80$ s. Solid: isopycnocline of the mean density from VarDen simulation; dashed: strongly nonlinear model; dotted: regularized model. The three vertical lines are at locations $x = 1525, 1610$ and $1700 \text{ cm}$ . . . . .	80
3.8	Snapshot of H50LD1 at $T = 80$ s. Solid: isopycnocline of the mean density from VarDen simulation; dashed: strongly nonlinear model; dotted: regularized model. The three vertical lines are at locations $x = 1550 \text{ cm}, 1610 \text{ cm}$ and $1800 \text{ cm}$ . . . . .	80
3.9	Convergence study for run H50LD1 in VarDen simulations with different resolutions. Black: $nz = 512$ ; gray: $nz = 1024$ , with the grid points at the vertical direction. . . . .	81

3.10	Solutions from the strongly nonlinear model for run H50LD1 with fixed $C = 1.3$ and different $K_{\text{upp}}$ at $T = 80$ s. Solid: mean density isopycnocline from VarDen simulation; dashed black: $K_{\text{upp}} = 0$ ; dashed blue: $K_{\text{upp}} = 500$ ; dashed red: $K_{\text{upp}} = 900$ . . . . .	82
3.11	Time series of relative energy loss for the strongly nonlinear model with fixed $C = 1.3$ and different $K_{\text{upp}}$ . Solid black: $K_{\text{upp}} = 0$ ; solid blue: $K_{\text{upp}} = 500$ ; solid red: $K_{\text{upp}} = 900$ ; dashed purple: $K_{\text{upp}} = 100$ ; dashed green: $K_{\text{upp}} = 300$ ; dashed orange: $K_{\text{upp}} = 700$ . . . . .	83
3.12	The front half of the primary waves from models at time $T = 60$ s (black short-dashed), $T = 80$ s (black long-dashed) and $T = 100$ s (black solid), VarDen simulations at $T = 100$ s (red solid) traveling wave solutions from the strongly nonlinear model with matching amplitude at $T = 100$ s (green solid). (a1), (a2) and (a3) are from the strongly nonlinear model for runs H10LD1, H20LD1 and H50LD1; (b1), (b2) and (b3) are from the regularized model for the same runs. . . . .	84
3.13	Amplitudes (left) and phase locations (right) of the wave peak for H10LD1 (a), H20LD1 (b) and H50LD1 (c). Square: the strongly nonlinear model; cross: VarDen simulation . . . . .	86
3.14	Horizontal shear velocities reconstructions for runs H10LD1 (a), H20LD1 (b) and H50LD1 (c) at locations noted in figures 3.5, 3.7 and 3.8. . . .	87
4.1	The solitary wave solution from the Kaup equations with the physical parameters $\rho_1 = 0$ , $\rho_2 = 1 \text{ g}\cdot\text{cm}^{-3}$ , $h_1 = 1.95 \text{ cm}$ , $h_2 = 2 \text{ cm}$ , $g = 1 \text{ cm}\cdot\text{s}^{-2}$ corresponding to the critical wavenumber $k_{\text{critical}} = 0.86$ . The Fourier modes below this instability threshold are not sufficient for recovering the solution. Solid: solitary wave solution; dashed: solitary wave solution with truncated Fourier coefficients satisfying the stability criterion. . . . .	102
4.2	Sketch of $f(U)$ in equation (4.82) with all possibilities for different values of $d_1$ . Note that the gray curves do not lead to solitary wave solutions. . . . .	112
4.3	The relationship between traveling wave speed and amplitude with parameters in the laboratory experiments introduced in Chapter 3. Solid: strongly nonlinear; long dashed: Boussinesq; dotted: regularized Kaup; short dashed: Kaup model . . . . .	113
4.4	Traveling wave solutions from the strongly nonlinear model (solid green), the Kaup equations (solid), the regularized Kaup equations (dashed) and the Boussinesq equations (dotted) matching amplitude $a$ with physical parameters introduced in § 4.7. (a): $a = -1 \text{ cm}$ , (b): $a = -5 \text{ cm}$ and (c): $a = -10 \text{ cm}$ . . . . .	114

4.5	Traveling wave solutions from the strongly nonlinear model (solid), the higher-order unidirectional model with $\mu = \tilde{\mu}$ (dashed) and the KdV equation (dotted) matching amplitude $a$ with physical parameters introduced in § 4.7. (a): $a = -1$ cm, (b): $a = -5$ cm and (c): $a = -10$ cm. . . . .	119
4.6	Snapshot of time evolution at $T = 500$ s from the KdV equation. . . . .	119
4.7	Snapshot of the time evolution from the regularized Kaup equations (dashed), the Boussinesq equations (dotted), the strongly nonlinear model (solid green) and the Euler simulation (solid) with the initial condition $h_{\text{gate}} = 10$ cm and $L_{\text{gate}} = 100$ cm, at $T = 500$ s. . . . .	124
4.8	Snapshot of the time evolution from the regularized Kaup equations (dashed), the Boussinesq equations (dotted), the strongly nonlinear model (solid green) and the Euler simulation (solid) with the initial condition $h_{\text{gate}} = 10$ cm and $L_{\text{gate}} = 200$ cm, at $T = 500$ s. . . . .	125
4.9	Snapshot of the time evolution from the regularized Kaup equations (dashed), the Boussinesq equations (dotted), the strongly nonlinear model (solid green) and the Euler simulation (solid) with the initial condition $h_{\text{gate}} = 1$ cm and $L_{\text{gate}} = 100$ cm, at $T = 500$ s. . . . .	126
4.10	Initial conditions of $\zeta$ with the set-up from the dam-break experiment (solid) and a long wave in the expression of equation (4.119) with the same amplitude ( $h_{\text{gate}} = 1$ cm) (dotted dash) . . . . .	127
4.11	Snapshot of the time evolution from the regularized Kaup equations (dashed), the Boussinesq equations (dotted), the strongly nonlinear model (solid green) and the Euler simulation (solid) with the initial condition $h_{\text{gate}} = 1$ cm, at $T = 500$ s. . . . .	128
4.12	Snapshots for higher-order uni-directional model with $\mu = \tilde{\mu}$ at $T = 80$ s with domain $L = 2464$ cm. Thick gray: Euler; solid: the strongly nonlinear model; dashed: higher-order uni-directional model with $\mu = \tilde{\mu}$ ; dotted: the KdV equation . . . . .	129
C.1	Snapshots of collisions of two solitary waves generated from dam-break at two ends. (a): symmetric case; (b) asymmetric case with different gate height at two ends . . . . .	140
C.2	Time series of $P_{\Delta}$ for solitary wave collisions with symmetric dam set-up (dashed) and asymmetric dam set-up (solid) . . . . .	141
C.3	Snapshots of the dam-break problem with a gate in the dimension of $L_{\text{gate}} = 900$ cm and $h_{\text{gate}} = 9$ cm in a 2688 cm long tank. . . . .	141

## List of Tables

2.1	Comparison of pressure imbalances $P_{\Delta}/\rho_{\Delta}^2$ as predicted by long-wave model and full Euler results for interface (2.47) with asymptotic height $z_0 = 1/2$ . . . . .	32
3.1	Labels for numerical runs with different parameters . . . . .	74
3.2	Numerical values for amplitudes $a$ and phases $X$ of the primary wave from VarDen simulation, the strongly nonlinear model and the regularized model for runs H10LD1, H20LD1 and H50LD1 at $T = 80$ s. . . . .	80
4.1	Tracking front wave amplitude $a^{\text{KdV}}$ and phase $X^{\text{KdV}}$ from two-layer KdV model for the two-layer dam-break problem with $L_{\text{gate}} = 100$ cm and $h_{\text{gate}} = 10$ cm at different snapshots. . . . .	122
4.2	Tracking front wave amplitudes $a$ and phases $X$ from the two-layer regularized Kaup equations and the Boussinesq equations for the two-layer dam-break problem with $L_{\text{gate}} = 100$ cm and $h_{\text{gate}} = 10$ cm at different snapshots. . . . .	124
4.3	Values of amplitudes from inverse scattering predictions from Kaup equations and time evolutions from regularized Kaup equations, the Boussinesq equations and the Euler simulations at $T = 500$ s for $L_{\text{gate}} = 200$ cm and $h_{\text{gate}} = 10$ cm. . . . .	126
4.4	Amplitudes and phases of front waves from models and the Euler simulations when the initial interface displacement is $\zeta = \text{sech}^2(\frac{x}{200})$ at $T = 500$ s.128	

## Chapter 1

### GENERAL INTRODUCTION

Ideal fluids are theoretical simplifications of real fluids obtained by ignoring viscosity and thermal conductivity. Such idealization is useful in many cases, such as flows considered in oceanography, where the Reynolds numbers are high. The mathematical description for ideal fluids are the Euler equations, representing conservation of mass, momentum and energy, which can be viewed as the Navier-Stokes equations in the limit of zero viscosity and heat conductivity. This thesis is concerned with incompressible ideal fluids with variable densities. Such setup allows for internal waves, which in their simplest occurrence can be seen as propagating at the interface between two fluids of different densities. Such ultimate simplification may in fact still be useful in oceanographic settings, and can be closely approximated in laboratory conditions.

Internal waves are gravity waves that oscillate within, rather than at the surface of, a fluid medium. In the ocean, where the density variations are much smaller than the density of the fluid itself, internal waves have much higher amplitudes than surface gravity waves because gravity, the restoring force for fluid parcels at the surface of a body of fluid, is much weaker on fluids parcels within the body, due to the buoyancy exerted by the surrounding fluid. Internal waves are especially common over the coastal regions where density variations, usually mostly due to temperature contrast from the top to the bottom of the water column, are also aided by salinity contrast due to fresh water influx from large rivers. Typical scales from field observations of internal waves

show that they are usually long with respect to the average fluid depth, e.g., wavelengths be of the order of 10 kilometers with the layer depths less than 1000 meters (Apel *et al.* [2], Helfrich & Melville [24]). Hence, in order to gain insight into wave dynamics of the Euler equations, whose solution for the most part are amenable to numerical methods only, it is useful to study asymptotic models built on the long wave assumption. These models can be derived with further simplifying assumptions such as idealized domains horizontal directions extending to infinity or confined in periodic lattices.

This thesis studies three problems concerning the derivation and properties of long internal-wave models from incompressible ideal fluids with variable densities. Each of these problems is essentially self contained:

1. The mathematical idealization of extending the container of the fluid to infinite lengths simplifies the physical problem. On the other hand, this setup seemingly brings in some paradoxical property, which are analyzed the first part of this work in some detail.
2. The model asymptotic derivation assumes initial conditions that satisfy the long wave assumption. When this is violated, how robust are the models with respect to the long time evolution with respect to the parent Euler system? This question is taken up for a class of initial and boundary conditions of relevance in laboratory experiments in the second part of this thesis.
3. The previous study shows that solitary waves are a dominant feature of the dynamics of a certain class of initial data. Can the presence and features of these waves be analytically predicted from models? This is the subject of the third part of this work.

Throughout this work, we restrict the upper surface by a “rigid lid,”, arguing that the surface signature of the internal waves is typically  $10^3$  smaller than typical internal



pycnocline displacements, i.e., the scales associated with internal wave motion greatly exceed the scales of the surface (barotropic) waves (Vlasenko *et al.* [36]).

This dissertation is organized as following. Chapter 2 focuses on an effect that could also be viewed as paradoxical: horizontal momentum conservation is violated in the dynamics of a stratified ideal fluid filling an infinite horizontal channel between rigid bottom and lid boundaries, starting from localized initial conditions, even though the only external forces acting on the system are vertical (gravity and constraint forces from the horizontal boundary), and the fluid is free to move laterally. Of course, even for an inviscid fluid, lateral boundaries could lead to horizontal forces by action-reaction mechanisms due to the constrained motion, and so horizontal momentum conservation cannot in general be expected to hold for a stratified Euler fluid filling a finite domain enclosed by a rigid boundary. However, we see that for a domain extending horizontally to infinity, the infinite inertia possessed by the far fluid at rest acts as an effective lateral wall, giving rise to the violation of horizontal momentum conservation. While stratification is necessary for creating the relative inertia of the lateral fluid at rest, a subtlety of this effect is that incompressibility is also required to transmit forces arising from finite-range motion instantaneously all the way to infinity. Accordingly, the “light-cone” provided by the maximum speed of propagation of internal baroclinic modes gives a rough estimate of the boundary of the exterior region that can be considered as contributing to an effective-wall lateral confinement. In particular, we adopt a perturbative point of view (in the limit of density difference goes to zero) to solve the elliptic equation which determines the pressure at initial time with the setting of zero-velocity configurations. Our analysis will be carried out directly on the Euler equations of motion in two dimensions; however, as a benchmark for testing ideas, we also consider long-wave one-dimensional reductions of our two-dimensional set-up, such as the strongly nonlinear model introduced in Choi & Camassa [15], for the description

of strongly nonlinear internal waves in two-fluid systems.

Appendix A reviews the Lagrangian and Hamiltonian formalism of the Euler equations, in particular adapting it to the two-fluid configuration, which allows the framework of conservation laws to be established from a more general standpoint.

Appendix B briefly examines the limiting case of “air-water” systems, in which one of the densities goes to zero. Non-trivial boundary effects on the pressure imbalance which are masked by the opposite near-density limit emerge in this case, due to the interface profile touching the channel plates along some intervals.

In Chapter 3, we conduct numerical experiments with direct Euler simulations and two long internal wave models for large amplitude waves: the strongly nonlinear model (Choi & Camassa [15]) and the regularized model (Choi *et al.* [14]). Studies of these models have mostly been limited to traveling wave solutions only. Our numerical experiments are motivated by laboratory experiments (Grue *et al.* [23]), with stratification achieved by pouring a layer of fresh water above a layer of brine in a long rectangular tank. By adding a volume of fresh water behind a gate which is lowered at one end of tank, a corresponding mass of the brine then slowly moves to the other side of the gate such that hydrostatic balance is maintained. By removing the gate, the initial pycnocline depression develops into a leading solitary wave propagating ahead of a transient dispersive wave train. The mathematical formulation of this dam-break internal wave problem is that of a step function representing the initial interface displacement, which clearly does not satisfy the long wave assumption for initial data of the models. In fact, it turns out that the models are sufficient to numerically predict front waves with low computational cost and remarkable accuracy when comparing to the full Euler simulations.

In Chapter 4, we compare several weakly nonlinear models in an attempt to provide analytical solutions for the internal dam-break problem described in Chapter 3. For the

most popular two-layer models such as Kortweg-de Vries equation (Choi & Camassa [15]) the initial value problem can be solved exactly by the inverse scattering transform method on the infinite domain. However, as a uni-directional model, the initial conditions for the KdV equation which properly reflect those in the experiments can only be defined approximately. Therefore the accuracy from the KdV equation prediction is not expected to excel. This motivates us to explore the completely integrable two-layer Kaup equations (Craig *et al.* [17]), a bi-directional model, which also can be solved via the inverse scattering transform (Kaup [27], Kaup [28]). The Kaup equations, however, suffer from the ill-posedness at high wave numbers, thus we propose a regularization of Kaup equations which are asymptotically equivalent to the original model. We compare the results from the new model to another well-posed weakly nonlinear model for bi-directional waves, the known Boussinesq equations (Choi & Camassa [15]). In turn, these three models are compared to direct numerical simulations with solitary wave solutions in the time evolution for the dam-break problem. We finally consider a higher-order uni-directional model (Choi & Camassa [15]) with similar form as the KdV equation, which is able to deal with moderate amplitude waves.

## Chapter 2

### EFFECTS OF INERTIA AND STRATIFICATION IN INCOMPRESSIBLE IDEAL FLUIDS: PRESSURE IMBALANCES BY RIGID CONFINEMENT

*This Chapter is collaborative work with Gregorio Falqui, Giovanni Ortenzi and Marco Pedroni. The content of this Chapter is from our published articles [8] and [9] in Journal of Fluid Mechanics.*

#### 2.1 Introduction

Among the many areas of classical mechanics, fluid dynamics arguably holds a special distinction for being a rich source of the sort of paradoxes that often arise from simplifying limit assumptions. Thus, for instance, the limit of zero viscosity gives rise to D'Alembert's paradox on the drag experienced by rigid bodies moving in ideal fluids, while the opposite limit of dominating viscous stresses leads to the Stokes or Whitehead paradoxes of unphysical divergences for the same problem.

This chapter focuses on an effect that could also be viewed as paradoxical: horizontal momentum conservation is violated in the dynamics of a stratified ideal fluid filling an infinite horizontal channel between rigid bottom and lid boundaries, starting from localized initial conditions, even though the only external forces acting on the system are vertical (gravity and constraint forces from the horizontal boundaries) and the fluid is free to move laterally. Of course, even for an inviscid fluid, lateral boundaries could

lead to horizontal forces by action-reaction mechanisms due to the constrained motion, and so horizontal momentum conservation cannot in general be expected to hold for a stratified Euler fluid filling a finite domain enclosed by a rigid boundary. However, we shall see below that for a domain extending horizontally to infinity the infinite inertia possessed by the far fluid at rest acts as an effective lateral boundary, giving rise to violation of horizontal momentum conservation. While stratification is necessary for creating the relative inertia of the lateral fluid at rest, a subtlety of this effect is that incompressibility is also required to transmit forces arising from finite-range motion instantaneously all the way to infinity. Accordingly, the “light-cone” provided by the maximum speed of propagation of internal baroclinic modes gives a rough estimate of the boundary of the exterior region that can be considered as contributing to an effective-wall lateral confinement.

This violation can be viewed as surprising, as the only acting body-force field is the vertical gravity and the fluid is free to move laterally. Possibly the first mention of this peculiar feature of stratified fluid dynamics can be traced back to Benjamin [5], in his investigation of the Hamiltonian formalism for inviscid incompressible fluids. Despite the relatively long time elapsed, it appears that Benjamin’s observation about (in his own words) “this curious fact” have been largely ignored since.

In the horizontal slab set-up, whenever hydrostatic conditions apply at infinity, this violation of momentum conservation is proportional (up to terms that arise from possibly different configurations at  $x = \pm\infty$ ) to the difference of the layer-averaged pressure at the far ends of the channel. As we will see, this pressure imbalance enters another physically interesting quantity, namely the (total) vorticity of the system. Admittedly, the effects herewith considered can be viewed as small, because the violation of momentum conservation must necessarily be a vanishing function of the difference  $\rho_\Delta$  of the density range of the fluid as this goes to zero (momentum conservation recovers

in the limit of a homogeneous fluid). Small density variations are common to many applications such as geophysics, however the large scales often involved in such applications justify considering the idealized set-up of laterally infinite fluids and might lead to non-negligible cumulative effects, even when these are small over local scales. Of course, the implications arising from considering rigid lids upper constraints in these applications remain to be seen; however, this limiting case may be relevant for establishing a comprehensive framework in which the dynamics of the incompressible limit for density-stratified fluids can be properly interpreted.

We shall mainly deal with incompressible, inviscid two-layer (Euler) fluids of constant different densities  $\rho_2 > \rho_1$ , separated by an interface located at  $z = \eta(x, t)$  (not necessarily smooth), where  $(x, z)$  are horizontal and vertical Cartesian coordinates in the plane. This choice is convenient for analytical purposes, and while numerically challenging, it can nonetheless be implemented in direct simulations of stratified Euler flows. While restrictive, the two-layer assumption can be representative of the dynamics of Euler fluids with smooth density variations as well (see, e.g., Camassa *et al.* [10], Camassa & Tiron [12]). In particular, for two-layer fluids in which the interface height is the same at  $\pm\infty$ , the pressure imbalance  $P_\Delta \equiv \lim_{x \rightarrow +\infty} p(x, \eta(x, t)) - \lim_{x \rightarrow -\infty} p(x, \eta(x, t))$  is equal to the difference of the pressures  $p(\pm\infty, z_0)$  for any reference height  $z_0$ , as it could be obtained from Benjamin [4] for smooth stratifications.

Our main focus will be on initial conditions with *null* velocity and small  $\rho_\Delta \equiv \rho_2 - \rho_1$ . This choice, as shown below, restricts the effects on the pressure imbalance of stratification at initial times to order  $\rho_\Delta^2$ , as opposed to order  $\rho_\Delta$ , as it might be expected at first. However, besides being simpler to implement numerically, this choice has the advantage of leading to closed form formulae, and identifies from a theoretical viewpoint a significant class of interface profile configurations giving rise to pressure imbalance. In turn, these correspond to horizontal momentum non-preserving time evolutions. In

particular, the setting of zero-velocity configurations will be instrumental in Section 2.4, where we shall adopt a perturbative point of view (in the limit  $\rho_\Delta \rightarrow 0$ ) to solve the elliptic equations which determine the pressure at  $t = 0$ . Some compact expressions for the pressure imbalances can then be obtained. Our analysis will be carried out directly on the Euler equations of motion in two dimensions; however, as a kind of benchmark for testing ideas, we shall also consider long-wave one-dimensional reductions of our two-dimensional set-up, such as the strongly nonlinear model introduced in Choi & Camassa [15] for the description of strongly nonlinear internal waves in two-fluid systems. We will also briefly review the Lagrangian and Hamiltonian formalism of the Euler equations, in particular adapting it to the two-fluid configuration, which allows the framework of conservation laws to be established from a more general standpoint.

More specifically, the layout of this chapter is as follows. In § 2.2 we introduce the set-up of our physical system within the Euler formalism, and, in particular, focus on the relation between non-conservation of horizontal momentum and the pressure imbalance  $P_\Delta$ . § 2.2.2 describes the asymptotic behavior of  $P_\Delta$  with respect to the small  $\rho_\Delta$  expansion. In particular, we establish that this behavior is linear for generic initial configurations with nonzero initial velocities, while it becomes *quadratic* when static initial conditions are considered. The relation between the time derivative of the total vorticity and the pressure imbalance is derived in § 2.2.3, both in the smooth and the two-layer stratification. In § 2.3 we use strongly nonlinear models to derive predictions about the pressure imbalances. The analytical and numerical fidelity of the models to the parent Euler system is tested on special configurations for zero-velocity initial data. It is worthwhile to remark that, in the zero-velocity case, the dispersionless limit of the long-wave model fails to provide the correct predictions for the pressure imbalance  $P_\Delta$ . Accuracy can be restored by including the first order dispersive correction of the model as introduced in Choi & Camassa [15].

Next, in § 2.4 we discuss pressure imbalances with zero-velocity initial data for two-layer fluids. The exact problem of solving the Laplace equation for the initial pressure can be viewed as a form of Neumann-to-Dirichlet problem for a (two-layer) strip. We adopt a simple perturbative approach in the limit of small density difference  $\rho_\Delta$ , turning this problem into an iterative family of Poisson equations which allow for a closed-form integral expression for the second order term  $P_\Delta^{(2)}$  of the pressure imbalance associated with any interface profile  $z = \eta(x)$ . In some cases (e.g., piecewise linear profiles) this expression easily yields explicit formulae for  $P_\Delta^{(2)}$  (which in suitable limits are expressed by Bernoulli-like polynomials). A sample of these formulae and their interpretation is contained in § 2.4.3 and § 2.4.4. In particular, within a certain class of initial data, we determine the configuration that maximizes the pressure imbalance. In § 2.5 the dam-break configuration is studied. At  $t = 0$  an exact explicit value for  $\langle p \rangle_\Delta$  can be obtained. The comparison of the theoretical results with full-Euler numerical experiments, in § 2.6, further illustrates the (short-time) dynamics arising from these pressure imbalances of these configurations and its effects on the horizontal momentum. Computations are performed with the VARDEN algorithm (Almgren *et al.* [1]) which solves the inhomogeneous Euler equations. The two-layer (sharp interface) set-up can be viewed as a severe test for the code, which gets validated by the overall good agreement with the analytical results. In § 2.8 we discuss our findings and point to future work.

We have also provided additional information in appendices. Specifically, Appendix A is devoted to reconcile the apparent paradox of lack of momentum conservation with the self-evident translational symmetry of the systems we study.



## 2.2 The physical system and its governing equations

We study the Euler equations for an ideal incompressible and inhomogeneous fluid subject to gravity,

$$\mathbf{v}_t + \mathbf{v} \cdot \nabla \mathbf{v} = -\frac{\nabla p}{\rho} - g\mathbf{k}, \quad \nabla \cdot \mathbf{v} = 0, \quad \rho_t + \mathbf{v} \cdot \nabla \rho = 0. \quad (2.1)$$

Here  $\mathbf{v} = (u, v, w)$  is the velocity field with respect to Cartesian coordinates  $(x, y, z)$  oriented by unit vectors  $(\mathbf{i}, \mathbf{j}, \mathbf{k})$ , with  $\mathbf{k}$  directed vertically upwards,  $\rho$  and  $p$  are the density and pressure fields, respectively, and  $g$  is the constant gravity acceleration; all physical variables depend on spatial coordinates and time  $t$ . Besides their well known theoretical interest, this set of equations can be viewed as governing the motion of real fluids with sufficient accuracy whenever viscosity, compressibility and diffusivity effects can be considered small during the time evolution. In particular, the fluid domains we shall consider here are slabs in the  $(x, z)$  plane rigidly confined by horizontal plates of infinite extent located at  $z = z_{\text{bottom}} \equiv 0$  and  $z = z_{\text{top}} \equiv h$ . Our study will mainly focus on two dimensional  $y$ -independent dynamics, though it can be generalized to fully three dimensional cases. The Euler equations (2.1) are supplemented by the boundary conditions:

$$\mathbf{v}(x, \cdot) \rightarrow 0 \text{ for } |x| \rightarrow \infty, \quad w(x, 0) = w(x, h) = 0, \quad (2.2)$$

with the fluid at the far ends of the channel in hydrostatic equilibrium,

$$\frac{\partial p}{\partial z} = -g\rho, \quad |x| \rightarrow \infty. \quad (2.3)$$

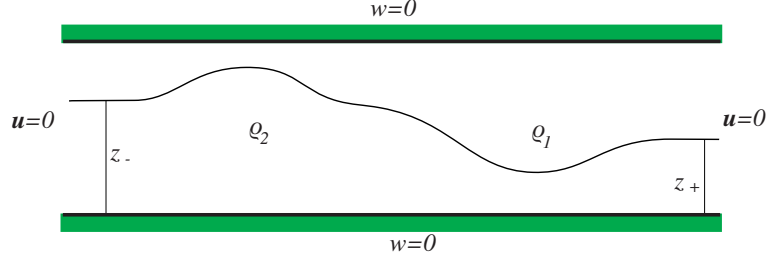


Figure 2.1: A two-layer configuration with different asymptotic heights.

### 2.2.1 Pressure imbalances and horizontal momentum

Consider the Euler equations for the horizontal component of the fluid's momentum

$$(\rho u)_t = -u(\rho u)_x - w(\rho u)_z - p_x. \quad (2.4)$$

Assuming a smooth stratification and integrating this equation on the strip  $\mathcal{S} = \mathbb{R} \times [0, h]$  yields the time variation of the horizontal component  $\Pi_1$  of the total momentum

$$\begin{aligned} \frac{d}{dt} \Pi_1 &= \int_{\mathcal{S}} (\rho u)_t \, dA = - \int_{\mathcal{S}} ((\rho u^2)_x + (\rho u w)_z - \rho u(u_x + w_z) + p_x) \, dA \\ &= - \int_0^h \left( \int_{\mathbb{R}} (\rho u^2 + p)_x \, dx \right) \, dz = -h(\langle p(+\infty) \rangle - \langle p(-\infty) \rangle), \end{aligned} \quad (2.5)$$

where we used incompressibility and the asymptotic hydrostatic conditions (see also Benjamin [5]). Hereafter the symbol  $\langle f \rangle$  stands for the (total) vertical channel average,

$$\langle f(\cdot) \rangle \equiv \frac{1}{h} \int_0^h f(\cdot, z) \, dz.$$

#### The two-layer case

The dynamics of an inviscid and incompressible fluid stratified in layers of uniform density  $\rho_j$  is governed by the Euler equations for the velocity components  $(u_j, w_j)$  and

the pressure  $p_j$ , for each of the layers; in two dimensional Cartesian coordinates  $(x, z)$ :

$$u_{jx} + w_{jz} = 0 \quad (2.6)$$

$$u_{jt} + u_j u_{jx} + w_j u_{jz} = -p_{jx}/\rho_j \quad (2.7)$$

$$w_{jt} + u_j w_{jx} + w_j w_{jz} = -p_{jz}/\rho_j - g. \quad (2.8)$$

For a two-layer fluid,  $j = 1$  ( $j = 2$ ) will stand for the upper (lower) fluid, respectively, and  $\rho_1 \leq \rho_2$  must be assumed for stable stratification (see figure 2.1 for a sketch of this set-up). The boundary conditions at the interface  $z = \eta(x, t)$  are the continuity of normal velocity and pressure

$$\eta_t + u_1 \eta_x = w_1, \quad \eta_t + u_2 \eta_x = w_2, \quad p_1 = p_2 \equiv P \quad \text{at} \quad z = \eta(x, t), \quad (2.9)$$

where  $P(x, t)$  denotes the interfacial pressure. Let us rewrite the Euler system (2.8) in terms of layer-averages (see, e.g., Wu [38] and Camassa & Levermore [11]). (For a smoothly stratified fluid, this is equivalent to singling out an intermediate level set of constant density  $z = \eta(x, t)$  and carrying similar manipulations since such a set will always be a material surface.) Layer-mean quantities  $\bar{f}$  are defined by

$$\bar{f}_j(x, t) \equiv \frac{1}{\eta_j} \int_{[\eta_j]} f(x, z, t) dz, \quad (2.10)$$

where  $\eta_j$  are the layer-thicknesses (i.e.,  $\eta_1 = h - \eta$  and  $\eta_2 = \eta$ ) and the intervals of integration  $[\eta_j]$  are  $z \in (\eta, h)$  for the upper- and  $z \in (0, \eta)$  for the lower-layer, respectively. With this notation, integration (2.6)–(2.7) across the layers with the boundary conditions (2.2) and (2.9) yields the layer-mean equations for the upper

(lower) fluid

$$\eta_{jt} + (\eta_j \bar{u}_j)_x = 0 \quad (2.11)$$

$$\rho_j(\eta_j \bar{u}_j)_t + \rho_j(\eta_j \overline{u_j u_j})_x = -(\eta_j \bar{p}_j)_x + (-1)^j \eta_x P, \quad j = 1, 2. \quad (2.12)$$

Layer averages are just a local version of the integral form of the horizontal momentum balance for each layer, which can be expressed for a section of the channel by integrating equations (2.12) over some  $x$ -interval  $L_- \leq x \leq L_+$ . The horizontal momentum balances of the upper ( $j = 1$ ) and lower ( $j = 2$ ) layer for this section are, respectively,

$$\frac{d\Pi_{1j}^\ell}{dt} \equiv \frac{d}{dt} \int_{L_-}^{L_+} \rho_j \eta_j \bar{u}_j dx + \rho_j \eta_j \overline{u_j u_j} \Big|_{L_-}^{L_+} = -\eta_j \bar{p}_j \Big|_{L_-}^{L_+} + (-1)^j \int_{L_-}^{L_+} \eta_x P dx, \quad (2.13)$$

since neither the pressure at the rigid horizontal surfaces nor the external gravity field contribute horizontal components of forces. Taking into account that

$$\sum_{j=1}^2 \eta_j \bar{p}_j \Big|_{L_-}^{L_+} = h(\langle p(L_+) \rangle - \langle p(L_-) \rangle),$$

and that the total horizontal momentum of the two-fluid's system is the sum of the contributions of the individual layers, in the limit  $L_\pm \rightarrow \pm\infty$  (e.g.,  $L_\pm = \pm L$ ) and  $\Pi_1^\ell \rightarrow \Pi_1$ , system (2.13) yields the two-layer analogue of Equation (2.5), i.e.,

$$\frac{d\Pi_1}{dt} = \frac{d\Pi_{11}}{dt} + \frac{d\Pi_{12}}{dt} = -h\langle p \rangle_\Delta, \quad (2.14)$$

where  $\langle p \rangle_\Delta \equiv \langle p(+\infty) \rangle - \langle p(-\infty) \rangle$ . In hydrostatic equilibrium the layer-mean pressures are

$$\bar{p}_j = (-1)^j g \rho_j \frac{\eta_j}{2} + P, \quad j = 1, 2. \quad (2.15)$$

Taking this into account at  $\pm\infty$ , we get

$$\frac{d\Pi_1}{dt} = \frac{d\Pi_{11}}{dt} + \frac{d\Pi_{12}}{dt} = -hP_\Delta - \frac{1}{2}\rho_\Delta g(z_+^2 - z_-^2) - \rho_1 g h(z_+ - z_-), \quad (2.16)$$

where  $P_\Delta \equiv \lim_{x \rightarrow +\infty} p(x, \eta(x, t)) - \lim_{x \rightarrow -\infty} p(x, \eta(x, t))$ ,

$$z_- \equiv \lim_{x \rightarrow -\infty} \eta(x, t), \quad z_+ \equiv \lim_{x \rightarrow +\infty} \eta(x, t), \quad \text{for all } t, \quad (2.17)$$

and  $\rho_\Delta = \rho_2 - \rho_1$ . In particular, by comparing (2.14) and (2.16), we have

$$\langle p \rangle_\Delta = P_\Delta + \frac{\rho_\Delta g}{2h}(z_+^2 - z_-^2) + \rho_1 g(z_+ - z_-),$$

so that if the asymptotic interfacial heights are the same at both far ends of the channel, equality between asymptotic imbalances of the interfacial pressure and of the mean pressure follows,

$$\langle p \rangle_\Delta = P_\Delta. \quad (2.18)$$

It is interesting to view the pressure imbalance from the perspective of a center of mass for the stratified fluid. For a laterally unbounded channel, the total mass of the fluid is clearly infinite, and care should be taken to avoid divergent integrals. The local center of mass horizontal coordinate for a section of the channel between  $x = L_-$  and  $x = L_+$  can be defined as

$$X_c^\ell(t) \equiv \frac{1}{M^\ell} \int_{L_-}^{L_+} x(\rho_1 \eta_1(x, t) + \rho_2 \eta_2(x, t)) dx, \quad (2.19)$$

where

$$M^\ell \equiv \int_{L_-}^{L_+} (\rho_1 \eta_1(x, t) + \rho_2 \eta_2(x, t)) dx \quad (2.20)$$

is the total mass of the fluid in the section. Differentiating with respect to time, and taking into account (2.11), yields

$$M^\ell \frac{dX_c^\ell}{dt} = \int_{L_-}^{L_+} (\rho_1 \eta_1 \bar{u}_1 + \rho_2 \eta_2 \bar{u}_2) dx + \left[ (X_c^\ell - x)(\rho_1 \eta_1 \bar{u}_1 + \rho_2 \eta_2 \bar{u}_2) \right] \Big|_{L_-}^{L_+}. \quad (2.21)$$

For velocities that decay sufficiently fast at infinity the end-point terms in this expression vanish and the right-hand-side is well defined in the limit  $L_\pm \rightarrow \pm\infty$ , being equal to the total horizontal momentum  $\Pi_1$  of the fluid. Thus, the position of the center of mass for a sufficiently long section of the channel moves in the direction defined by the total horizontal momentum, as can be expected.

### 2.2.2 Small $\rho_\Delta$ limit and the scaling relation between $P_\Delta$ and $\rho_\Delta$

Some of the results of the previous subsection can be used to unravel a particular scaling of the momentum evolution with respect to stratification. In particular, we shall focus on the class of zero-velocity initial data. As we will see later, these initial conditions also allow to derive closed-form expressions for the initial pressure imbalance.

From the equations of motion and, in particular, from the constraint  $\eta_1 + \eta_2 = h$  we have

$$\partial_x \left( \eta_1 \overline{u_1 u_1} + \eta_2 \overline{u_2 u_2} + \frac{1}{\rho_1} \eta_1 \bar{p}_1 + \frac{1}{\rho_2} \eta_2 \bar{p}_2 \right) = \left( \frac{1}{\rho_2} - \frac{1}{\rho_1} \right) \eta_x P. \quad (2.22)$$

If hydrostatic equilibrium at infinity is enforced, the layer-mean pressures are given by (2.15), so that in the case of equal asymptotic heights, that is,  $z_- = z_+ = z_0$ , the interfacial pressure difference  $P_\Delta$  between the ends of the channel is

$$P_\Delta(\rho_\Delta) = P|_{-\infty}^{+\infty} = \frac{\rho_\Delta}{h_1 \rho_2 + h_2 \rho_1} \int_{-\infty}^{+\infty} \eta_x P dx \equiv \frac{\rho_\Delta}{h_1 \rho_2 + h_2 \rho_1} I_P(\rho_\Delta), \quad (2.23)$$

where  $h_1 = h - z_0$  and  $h_2 = z_0$ . A couple of relevant consequences follow from this relation: First, pressure imbalances and their associated physical phenomena, such as

the nonconservation of total momentum and vorticity, cannot arise in uniform density fluids. Next, and perhaps more remarkably, these phenomena cannot be detected in the Boussinesq approximation of neglecting density stratification in the inertial terms.

Relation (2.23) further shows that  $P_\Delta$  scales at least linearly with  $\rho_\Delta$ . Of course, the integral term  $I_P$  also depends on  $\rho_\Delta$ , so that it cannot be concluded that this linear scaling has general validity. In fact, in the limit  $\rho_\Delta \rightarrow 0$  with  $\rho_2$  fixed, the scaling can be different than linear. Assume that the interfacial pressure  $P$  admits the expansion

$$\begin{aligned} & P_\Delta(0) + P'_\Delta(0)\rho_\Delta + \frac{1}{2}P''_\Delta(0)\rho_\Delta^2 + \dots \\ &= \frac{1}{h_1\rho_2 + h_2\rho_1}I_P(0)\rho_\Delta + \frac{1}{h_1\rho_2 + h_2\rho_1}I'_P(0)\rho_\Delta^2 + \dots \\ &= \frac{1}{h\rho_1}I_P(0)\rho_\Delta + \left[ \frac{1}{h\rho_1}I'_P(0) - \frac{h_1}{h^2\rho_1^2}I_P(0) \right] \rho_\Delta^2 + o(\rho_\Delta^2), \end{aligned} \quad (2.24)$$

where  $o(\rho_\Delta^2)$  denotes, as usual, terms going to zero faster than  $\rho_\Delta^2$ . This implies that  $I_P(\rho_\Delta) \rightarrow 0$  as  $\rho_\Delta \rightarrow 0$  for localized displacements of the interface. Equating term by term yields  $P_\Delta(0) = 0$ , as already manifest from (2.23). Now, for a homogeneous fluid, equation (2.16) shows that horizontal momentum is conserved if  $P_\Delta(0) = 0$ . On the other hand, recalling that the time variation of each layer's total horizontal momentum is

$$\frac{d\Pi_{1j}}{dt} \equiv \frac{d}{dt} \int_{-\infty}^{+\infty} \rho_j \eta_j \bar{u}_j dx + \rho_j \eta_j \bar{u}_j \bar{u}_j|_{-\infty}^{+\infty} = -\eta_j \bar{p}_j|_{-\infty}^{+\infty} + (-1)^j I_P, \quad j = 1, 2, \quad (2.25)$$

we can see that if the upper and lower layer momentum are separately conserved, then not only  $P_\Delta = 0$ , but also  $I_P = 0$ . Indeed, the lateral equilibrium boundary conditions imply that for each infinite upper and lower layer the horizontal momenta are conserved if and only if

$$-h_1 P_\Delta - I_P = 0, \quad -h_2 P_\Delta + I_P = 0, \quad (2.26)$$

at all times, that is, if and only if

$$I_P = 0 \quad \text{and} \quad P_\Delta = 0. \quad (2.27)$$

Now, given that  $\rho_\Delta = 0$  implies horizontal momentum conservation, and for zero initial velocities the initial value of each layer's total horizontal momentum is clearly zero, the conserved value of the horizontal momentum in each layer is null for all times (and hence so is the total fluid's horizontal momentum). Therefore (2.27) shows that the linear term in expansion (2.24) vanishes. Thus, for zero velocities,  $P_\Delta(\rho_\Delta)$  is at least quadratic in  $\rho_\Delta$ , since from (2.24) we obtain

$$P_\Delta = \frac{1}{h_1\rho_2 + h_2\rho_1} I'_P(0) \rho_\Delta^2 + o(\rho_\Delta^2). \quad (2.28)$$

Notice that this result is general for zero-velocity initial conditions. If the velocity of the system is different from zero, the difference of pressure between the ends of the channel can be expected, in general, to scale linearly with the density difference  $\rho_\Delta$ , at least initially in time.

We remark that, if different asymptotic heights are enforced on the fluid's configuration, formula (2.23) has to be modified as

$$\frac{\rho_\Delta}{\rho_1\rho_2} I_P(\rho_\Delta) = \left( \frac{h - z_+}{\rho_1} + \frac{z_+}{\rho_2} \right) P(+\infty) - \left( \frac{h - z_-}{\rho_1} + \frac{z_-}{\rho_2} \right) P(-\infty) + gh(z_+ - z_-). \quad (2.29)$$

We will henceforth refer to this case as the “kink-like” configuration. Its limiting case, by which one or both of the two different asymptotic heights reach the channel's boundaries, will be referred to as “dam-like.”



### 2.2.3 Interfacial pressure imbalance and total vorticity

Next, we briefly examine how the asymptotic interface pressure differential  $P_\Delta$  is related with variation of the total vorticity. This link can be obtained from the Helmholtz-type equation for the vorticity,

$$\boldsymbol{\omega}_t + \nabla \times (\boldsymbol{\omega} \times \mathbf{v}) = -\nabla \left( \frac{1}{\rho} \right) \times \nabla p. \quad (2.30)$$

For a system in the strip  $\mathcal{S} = \mathbb{R} \times [0, h]$ , the total vorticity is

$$\mathbf{\Gamma} = \int_{\mathbb{R} \times [0, h]} \boldsymbol{\omega} \, dA. \quad (2.31)$$

Its time variation follows directly by integrating (2.30), and by using the Green-Stokes' formula. Taking into account the boundary conditions on the velocity field yields

$$\frac{d\mathbf{\Gamma}}{dt} = \int_{\mathbb{R} \times [0, h]} \nabla p \times \nabla \left( \frac{1}{\rho} \right) \, dA. \quad (2.32)$$

Notice that any barotropic component of the pressure  $p_b = p_b(\rho)$  will not contribute to this formula, which ultimately rephrases the content of the Bjerknes theorem (see, e.g., Yih [40]) applied to the whole fluid domain.

We now consider the two-layer case. In this case,  $\rho = \rho_2 - H(z - \eta(x, t))\rho_\Delta$  (by denoting the Heaviside function as  $H$ ), and hence the gradient of  $1/\rho$  is

$$\nabla \left( \frac{1}{\rho} \right) = \begin{pmatrix} -\eta_x \\ 1 \end{pmatrix} \frac{\rho_\Delta}{\rho_1 \rho_2} \delta(z - \eta(x, t)), \quad (2.33)$$

which is normal to the interface  $\eta(x, t)$ . The integrand in the total vorticity derivative (2.32) will then involve products of  $\nabla p$ -components with a delta-function. Such products are well defined, in general, only if the functions multiplying the Dirac- $\delta$  are

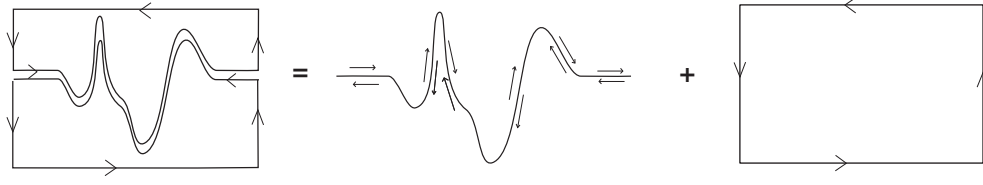


Figure 2.2: The contours for Stokes theorem in the case of a two-layer fluid.

continuous. In our case, while the component of the pressure gradient normal to the interface suffers a jump, the tangential component is continuous, and hence so is the  $\delta$  multiplier. We have

$$\nabla p \times \nabla \left( \frac{1}{\rho} \right) = -(p_x + p_z \eta_x) \frac{\rho_\Delta}{\rho_1 \rho_2} \delta(z - \eta(x, t)) \mathbf{j}, \quad (2.34)$$

where  $\mathbf{j}$  is the unit vector normal to the fluid plane. Similar care is needed to apply the Green-Stokes formula in the two-layer case, because the integrand is again singular at the interface, in general. The contour of integration has to be modified by separating the different domains where the density is constant, thereby breaking the contour path used in the smooth density case into two paths enclosing the domain of each fluid. This decomposition, depicted in figure 2.2, reduces the problem to evaluating the contour integration at the interface, because the contributions of the channel boundaries vanish for the same reason as for the smooth density case. In this chapter we will be concerned mainly with the case of zero-velocity initial conditions, so that the fluid vorticity  $\boldsymbol{\omega}$  is concentrated on the interface  $\gamma$  in a vortex sheet (see also Yih [40], p. 14). Therefore the kinetic contribution to  $d\Gamma/dt$  is

$$\int_{\gamma} (\boldsymbol{\omega} \times \mathbf{v}_1) \cdot d\mathbf{r} - \int_{\gamma} (\boldsymbol{\omega} \times \mathbf{v}_2) \cdot d\mathbf{r} = \int_{\gamma} \boldsymbol{\omega} \times (\mathbf{v}_2 - \mathbf{v}_1) \cdot d\mathbf{r}. \quad (2.35)$$

Since the shear velocity  $\mathbf{v}_2 - \mathbf{v}_1$  is tangent to the interface, these line integrals also vanish and, with zero-velocity initial conditions, formula (2.32) still holds. Thus, by

using (2.34) we can express the time variation of the total vorticity in terms of the (interface) pressure imbalance as

$$\begin{aligned}
\frac{d\Gamma}{dt} &= \int_{-\infty}^{\infty} \left( \int_0^h (p_x + p_z \eta_x) \frac{\rho_{\Delta}}{\rho_1 \rho_2} \delta(z - \eta(x, t)) dz \right) dx \\
&= \frac{\rho_{\Delta}}{\rho_1 \rho_2} \int_{-\infty}^{\infty} (p_x + p_z \eta_x)|_{z=\eta(x, t)} dx = \frac{\rho_{\Delta}}{\rho_1 \rho_2} \int_{-\infty}^{\infty} \frac{dP}{dx} dx \\
&= \frac{\rho_{\Delta}}{\rho_1 \rho_2} (P(+\infty) - P(-\infty)) = \frac{\rho_{\Delta} P_{\Delta}}{\rho_1 \rho_2},
\end{aligned} \tag{2.36}$$

where we have used the definition  $P(x) = p(x, \eta(x))$ .

Formula (2.36), connecting the time variation of the total vorticity with the asymptotic pressure imbalance, has to be corrected if the interface touches the boundary of the channel. Indeed, let  $\mathcal{C}$  be the set in which the interface coincides with one of the boundaries (see figure 2.3). For  $x \in \mathcal{C}$  and every  $z \in [0, h]$  the gradient of the density is zero, so that the set  $\mathcal{C} \times [0, h]$  does not contribute to the total vorticity time-variation. Therefore

$$\frac{d\Gamma}{dt} = \frac{\rho_{\Delta}}{\rho_1 \rho_2} \int_{\mathbb{R}/\mathcal{C}} \frac{dP}{dx} dx = \frac{\rho_{\Delta}}{\rho_1 \rho_2} \left( P_{\Delta} - \sum_{i=1}^n [p(x_i^R, \eta(x_i^R)) - p(x_i^L, \eta(x_i^L))] \right). \tag{2.37}$$

We remark that the correction terms might be, in some cases, dominant. Indeed, for vanishing velocity initial configurations,  $P_{\Delta}$  behaves as  $\rho_{\Delta}^2$ , while the point contributions can produce linear terms in  $\rho_{\Delta}$ .

### 2.3 Long-wave models

We now briefly describe strongly nonlinear long-wave models for two-layer fluids (see, e.g., Choi & Camassa [15]). Variants of these models have been extensively studied in the literature, especially for the classical dispersionless limit, see for instance the monograph in Baines [3], and, more recently, Milewski *et al.* [33] and Boonkasame &

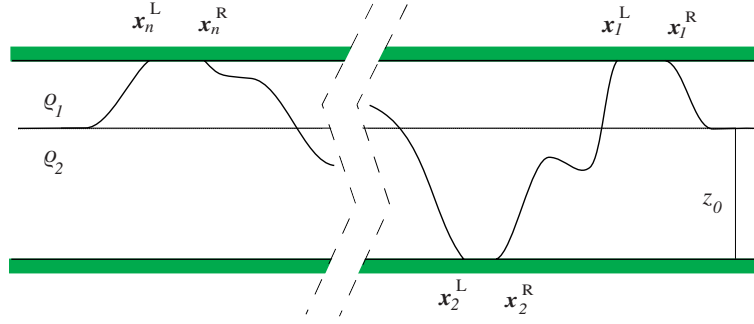


Figure 2.3: Sketch of a typical interface configuration for a two-fluid density distribution for which boundary contributions are relevant.

Milewski [6] for a study of the stability properties of the motion governed by these models. While derived under the long-wave approximation, the dispersive case has been studied in the context of an internal “dam-breaking” problem (which leads to high wavenumber initial conditions) by Esler & Pearce [18] in the Boussinesq regime; we will return to this class of initial conditions for the parent Euler system in § 2.5. By using these models, one can derive in a relatively straightforward manner fairly general results, whose fidelity with respect to the parent Euler equations can be tested on explicit solutions for special configurations (typically for zero-velocity initial data). Thus, in this section we anticipate some of the results that will be computed explicitly later on for the special configurations of vanishing initial velocity within the *full* Euler equation study. We remark that models may differ substantially in their effectiveness to predict the “true” physical behaviour of the systems under consideration. For instance, as mentioned in § 2.2, the Boussinesq limit (of both models) does not capture any pressure imbalance; in turn, the dispersionless limit notably yields a vanishing pressure imbalance for the vanishing velocity case. The non-vanishing pressure imbalance in the static case can be obtained by taking into account dispersive terms in the strongly nonlinear models.

### 2.3.1 Equations of motion

For a two-layer incompressible Euler fluid in a channel of height  $h$ , the equations of motion (2.11)–(2.12) can be written as

$$\overline{u}_{it} + \overline{u}_i \overline{u}_{ix} + (-1)^i g \eta_{ix} = -\frac{P_x}{\rho_i} + D_i(u_i, v_i, \eta_i), \quad \eta_{it} + (\eta_i \overline{u}_i)_x = 0, \quad i = 1, 2, \quad (2.38)$$

where  $\eta_1 + \eta_2 = h$ , and the terms denoted by  $D_i$  lump all the contributions from pressure, vertical velocity components and from switching layer-averages with products. Shallow water long-wave models can be derived from this in the case when the layer thicknesses are small with respect to a typical wavelength  $L$ , by retaining only the leading order terms in  $D_i$ , and provide effective approximations of (two-layer) incompressible Euler fluid (see. e.g., Choi & Camassa [15]). Denoting the small parameter of the model by  $\delta \equiv h/L$ , at the first order in  $\delta$  the hydrostatic equilibrium is valid everywhere and the relations (2.15) hold not only asymptotically but along the whole channel. Also, at this order  $D_i = 0$ , i.e., system (2.38) is turned into its dispersionless limit

$$\overline{u}_{it} + \overline{u}_i \overline{u}_{ix} + (-1)^i g \eta_{ix} = -\frac{P_x}{\rho_i}, \quad \eta_{it} + (\eta_i \overline{u}_i)_x = 0, \quad i = 1, 2. \quad (2.39)$$

In case of zero asymptotic velocities the total flux  $Q(t) \equiv \eta_1 \overline{u}_1 + \eta_2 \overline{u}_2$  is zero. Solving for  $P_x$  the dispersionless equations (2.39) and using the constraint  $\eta_1 + \eta_2 = h$ , yields for the interface pressure asymptotic difference the (dispersionless) formula

$$P_\Delta = h \int_{-\infty}^{\infty} \frac{(\overline{u}_1 \overline{u}_2)_x}{\eta_1/\rho_1 + \eta_2/\rho_2} dx. \quad (2.40)$$

We remark that in the Boussinesq approximation the integral becomes a total derivative, and hence this difference is zero (see, e.g., Milewski *et al.* [33]). This fact should not be regarded as a surprise, since pressure imbalances are phenomena due to the rela-

tive inertia of the stratified fluid, and not to the relative buoyancy. Still, formula (2.40) shows that  $P_\Delta = 0$  when the interface is flat (with any averaged velocities). On general grounds, this can also be seen from (2.23), since  $\eta_x = 0$  for a flat interface. However, the dispersionless formula (2.40) predicts  $P_\Delta = 0$  for zero velocities as well, which is not true in general. Next, we show how such a pressure imbalance can be qualitatively understood by restoring the dispersive terms in the strongly nonlinear model.

### 2.3.2 Effects of dispersion

The fact that for zero-velocities formula (2.40) fails to yield a nonzero value for  $P_\Delta$  suggests that for small velocities (or interface profile) the dispersive terms  $D_i$  of Equation (2.38) could play a significant corrective role. In fact, if such terms are nonzero, then relation (2.40) turns into

$$P_\Delta = \int_{-\infty}^{+\infty} \left( \frac{\eta_1}{\rho_1} + \frac{\eta_2}{\rho_2} \right)^{-1} [h(\bar{u}_1 \bar{u}_2)_x + (\eta_1 D_1 + \eta_2 D_2)] dx. \quad (2.41)$$

The first nontrivial dispersion contribution is given asymptotically as  $\delta \rightarrow 0$  by (see Choi & Camassa [15])

$$D_i \sim \frac{1}{3\eta_i} \left( \eta_i^3 (\bar{u}_{ixt} + \bar{u}_i \bar{u}_{ixx} - (\bar{u}_{ix})^2) \right)_x, \quad i = 1, 2. \quad (2.42)$$

If  $\bar{u}_i = 0$ , this implies

$$P_\Delta \sim \frac{1}{3} \int_{-\infty}^{\infty} \left( \frac{\eta_1}{\rho_1} + \frac{\eta_2}{\rho_2} \right)^{-1} (\eta_1^3 \bar{u}_{1tx} + \eta_2^3 \bar{u}_{2tx})_x dx. \quad (2.43)$$

which, by bringing into the integrand the time-derivatives of the velocities shows that the pressure jump can be non-zero even if the velocities are initially zero. In particular, antisymmetric initial displacements of the interface can lead to non-zero  $P_\Delta$ , whereas

this pressure jump always vanishes for symmetric initial data.

A consistent approximation of this formula can be given by inserting the expressions for the  $\overline{u}_{it}$ 's obtained in the zero-dispersion limit. The dispersionless equation of motions (2.39), when the velocities are near zero, yield

$$\overline{u}_{1t} \sim \rho_{\Delta} g \frac{\eta_2 \eta_{2x}}{\rho_1 \eta_2 + \rho_2 \eta_1}, \quad \overline{u}_{2t} \sim -\frac{\eta_1}{\eta_2} \overline{u}_{1t} = \rho_{\Delta} g \frac{\eta_1 \eta_{1x}}{\rho_1 \eta_2 + \rho_2 \eta_1} \quad (2.44)$$

asymptotically as  $\delta \rightarrow 0$ . Therefore

$$P_{\Delta} \sim \frac{\rho_{\Delta} g}{3} \int_{-\infty}^{\infty} \left( \frac{\eta_1}{\rho_1} + \frac{\eta_2}{\rho_2} \right)^{-1} \left( \eta_1^3 \left( \frac{\eta_2 \eta_{2x}}{\rho_1 \eta_2 + \rho_2 \eta_1} \right)_x + \eta_2^3 \left( \frac{\eta_1 \eta_{1x}}{\rho_1 \eta_2 + \rho_2 \eta_1} \right)_x \right) dx. \quad (2.45)$$

When  $\rho_{\Delta}$  is small, asymptotic relation (2.45) can be simplified to

$$P_{\Delta} \sim \frac{\rho_{\Delta} g}{3h} \int_{-\infty}^{\infty} \left( \frac{1}{h} + \frac{\eta_2}{h^2} \frac{\rho_{\Delta}}{\rho_1} \right) (\eta_1^3 (\eta_2 \eta_{2x})_x + \eta_2^3 (\eta_1 \eta_{1x})_x) dx + o(\rho_{\Delta}^2).$$

The linear term in  $\rho_{\Delta}$  is a total derivative in  $x$  and therefore, confirming the general results of the previous section, does not contribute to  $P_{\Delta}$ . As expected, the first nonzero term for  $P_{\Delta}$  is proportional to  $\rho_{\Delta}^2$ ,

$$P_{\Delta} \sim \frac{\rho_{\Delta}^2 g}{6\rho_1 h^3} \int_{-\infty}^{\infty} \eta_2 (\eta_1^3 (\eta_2^2)_{xx} + \eta_2^3 (\eta_1^2)_{xx})_x dx + o(\rho_{\Delta}^2). \quad (2.46)$$

This formula allows explicit analytic computations for special cases. For instance, when the interface profile (see figure 2.4) is

$$\eta(x) = z_0 + A \exp(-(x+S)^2/\sigma^2) - B \exp(-(x-S)^2/\sigma^2), \quad (2.47)$$

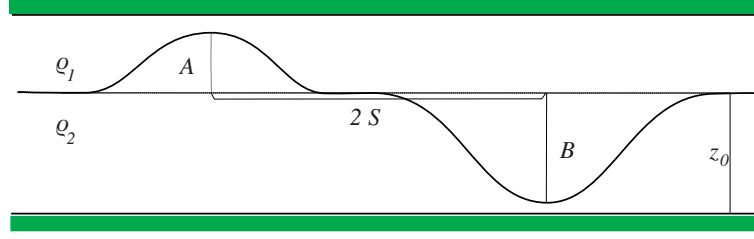


Figure 2.4: A two-bump configuration. Only when  $S$  is comparable with the typical width of the bumps  $P_\Delta$  is nonzero.

the asymptotic difference of pressure is given by

$$P_\Delta \sim \frac{64\sqrt{3\pi}g}{81\rho_1} \frac{S^3 e^{-\frac{8S^2}{3\sigma^2}}}{\sigma^5} AB(A+B)\rho_\Delta^2 + o(\rho_\Delta^2). \quad (2.48)$$

Here, for long-wave asymptotic consistency,  $\sigma$  should be taken sufficiently large, and  $A$  and  $B$  need to be such that the extrema of function (2.47) do not touch the channel boundary.

Some interesting conclusions can be extracted from (2.48). First, if  $A = -B$  the interface of the system becomes symmetric and, as always in these configurations,  $P_\Delta = 0$ . Second, explicit dependence on the asymptotic height  $z_0$  does not appear in formula (2.48). However, notice that the ranges of  $A$  and  $B$  are constrained by the choice of  $z_0$  if the interface has to stay away from the channel boundaries. Thus, by choosing, e.g.,  $A + B = k$  and  $B = z_0 - s$  (for given parameters  $k$  and  $s$ ) we fix the maximum and the minimum of the interface leaving only  $z_0$  as a free variable. In this case  $P_\Delta$  is a quadratic function of the interface height  $z_0$  and the vertex of the parabola is at  $A = B$ . Third, the most interesting behaviour is related to the dependence on the separation parameter  $S$ . If the two bumps are well separated ( $S \gg \sigma$ ), then  $P_\Delta$  is exponentially small. However, when the supports of the two bumps have an intersection ( $S \simeq \sigma$ ), then  $P_\Delta$  is nonzero to leading order  $O(\rho_\Delta^2)$ .



## 2.4 Full Euler system: pressure jump at $t = 0$ in the small $\rho_\Delta$ asymptotic limit

We consider again the full Euler system for a two-layer fluid with zero initial velocity. As seen in Section 2.2.2, in this case the expansion in  $\rho_\Delta$  of the pressure imbalance starts with the quadratic term. We now compute this term explicitly. Throughout this section, unless otherwise stated, we will reference density to that of the lower fluid, so that  $\rho_2 = 1$ .

### 2.4.1 The small $\rho_\Delta$ expansion

Consider an initial condition for the two-fluid stratification such as the one depicted in figure 2.1. Let the initial velocity be identically zero, with the fluid in hydrostatic equilibrium as  $|x| \rightarrow \infty$ . In this case, the Euler equations (2.1) determine the pressure  $p(x, z)$  at time  $t = 0$  through the solution of the elliptic equation

$$\nabla \cdot \left( \frac{1}{\rho} \nabla p \right) = 0 \quad (2.49)$$

subject to the Neumann boundary conditions

$$\frac{\partial p}{\partial x} \rightarrow 0 \quad \text{as} \quad |x| \rightarrow \infty, \quad \frac{\partial p}{\partial z} = -g\rho \quad \text{at} \quad z = 0, h. \quad (2.50)$$

Of course, non-differentiability of the density distribution for the case of figure 2.1 requires an appropriate interpretation of equation (2.49). We will enforce (2.49) separately in each of the  $\rho_1$  and  $\rho_2$  domains,  $\Omega_1$  and  $\Omega_2$  say,

$$\nabla^2 p = 0, \quad (x, z) \in \Omega_i, \quad i = 1, 2,$$

so that  $p$  is harmonic in each subdomain, and assign boundary conditions at the discontinuities of  $\rho$ . These consist of continuity of  $p$  everywhere, while its normal derivatives jump according to the “flux-continuity” condition

$$\left. \frac{1}{\rho_1} \frac{\partial p}{\partial n} \right|_1 = \left. \frac{1}{\rho_2} \frac{\partial p}{\partial n} \right|_2, \quad (2.51)$$

with obvious meaning of the notation.

Let the variable density be defined as a perturbation away from a uniform density fluid

$$\rho = \rho_2 - \epsilon r(x, z), \quad 0 < \epsilon \ll 1, \quad (2.52)$$

where  $r$  positive, so that  $\rho_2$  is the maximum density of fluid. For notational convenience, we further choose units in such a way that  $h = 1$ , and  $g = 1$ . We seek a solution for the pressure equation as an asymptotic expansion

$$p = p^{(0)} + \epsilon p^{(1)} + \epsilon^2 p^{(2)} + o(\epsilon^2) \quad (2.53)$$

whence, equating like-powers of  $\epsilon$ ,

$$\nabla^2 p^{(0)} = 0, \quad \nabla^2 p^{(1)} + \nabla \cdot (r \nabla p^{(0)}) = 0, \quad \nabla^2 p^{(2)} + \nabla \cdot (r \nabla p^{(1)}) + \nabla \cdot (r^2 \nabla p^{(0)}) = 0, \dots \quad (2.54)$$

with boundary conditions, respectively,

$$\begin{aligned} \left. \frac{\partial p^{(0)}}{\partial z} \right|_{z=0,1} &= -1, & \left. \frac{\partial p^{(1)}}{\partial z} \right|_{z=0,1} &= r|_{z=0,1}, & \left. \frac{\partial p^{(2)}}{\partial z} \right|_{z=0,1} &= 0, \\ \frac{\partial p^{(k)}}{\partial x} &\rightarrow 0 \quad \text{as } |x| \rightarrow \infty \text{ for } k \geq 0. \end{aligned} \quad (2.55)$$

The  $O(\epsilon^0)$ -equation is simply solved by  $p^{(0)} = -z + \text{const.}$ , which yields the equation

for  $p^{(1)}$  in the form

$$\nabla^2 p^{(1)} = r_z.$$

Since the system is two-layer, still denoting the usual Heaviside function as  $H$ , we have

$$r(x, z) = H(z - \eta(x)),$$

where the interface location  $z = \eta(x)$  behaves as

$$\eta(x) \rightarrow z_{\pm} \quad \text{as} \quad x \rightarrow \pm\infty, \quad 0 < \eta(x) < 1.$$

This means that the heavy fluid density is  $\rho_2 = 1$  and the light fluid density is  $\rho_1 = 1 - \epsilon$ , so that, in the chosen units,  $\rho_{\Delta} = \epsilon$ . Let

$$p^{(1)} = p_h^{(1)} + (z - z_0)H(z - z_0), \quad (2.56)$$

where  $z_0$  is any reference height. The summand  $(z - z_0)H(z - z_0)$  takes care of the top and bottom boundary conditions, leaving a homogeneous Neumann problem for  $p_h^{(1)}(x, z)$  in the infinite strip. The equation for  $p_h^{(1)}(x, z)$  is then

$$\nabla^2 p_h^{(1)} = \delta(z - \eta(x)) - \delta(z - z_0). \quad (2.57)$$

To solve this we can make use of the identity

$$\sum_{n=1}^{\infty} \cos(n\pi\theta) = -\frac{1}{2} + \delta_p(\theta) \equiv -\frac{1}{2} + \sum_{k=-\infty}^{+\infty} \delta(\theta + 2k),$$

from the theory of distributions (Gelfand & Shilov, 1964). Indeed, we have

$$\begin{aligned} 2 \sum_{n=1}^{\infty} \cos(n\pi z) \cos(n\pi \eta) &= \sum_{n=1}^{\infty} \left( \cos(n\pi(z - \eta)) + \cos(n\pi(z + \eta)) \right) \\ &= -1 + \delta_p(z - \eta) + \delta_p(z + \eta) = -1 + \delta(z - \eta) \end{aligned}$$

since  $0 < z < 1$  and  $0 < \eta < 1$ , so that the support of the second Dirac- $\delta$  always falls outside the channel. For the same reason the periodic shifts can be ignored for the first  $\delta$ . Hence, we are lead to the following expression of the right-hand side of (2.57):

$$\delta(z - \eta(x)) - \delta(z - z_0) = 2 \sum_{n=1}^{\infty} \cos(n\pi z) (\cos(n\pi \eta(x)) - \cos(n\pi z_0)), \quad (2.58)$$

from which, taking the homogeneous Neumann boundary conditions into account, the coefficient of the Fourier series expression of  $p_h^{(1)}(x, z)$  can be read off. Indeed,

$$p_h^{(1)}(x, z) = \sum_{n=0}^{\infty} a_n(x) \cos(n\pi z) \quad (2.59)$$

yields

$$a_n'' - n^2 \pi^2 a_n = 2(\cos(n\pi \eta(x)) - \cos(n\pi z_0)) \text{ for } n \geq 0.$$

For  $n = 0$ ,  $a_0'' = 0 \Leftrightarrow a_0 = \text{constant}$ , say  $a_0 = 0$ . For  $n > 0$ , the equation for  $a_n$  can be solved by use of the Green function for the operator  $\partial_x^2 - n^2 \pi^2$  on the real line,

$$G_n(x, \xi) = -\frac{1}{2n\pi} e^{-n\pi|x-\xi|},$$

to finally obtain

$$p_h^{(1)}(x, z) = \int_{-\infty}^{+\infty} \sum_{n=1}^{\infty} \frac{e^{-n\pi|x-\xi|}}{n\pi} \cos(n\pi z) \left( \cos(n\pi z_0) - \cos(n\pi \eta(\xi)) \right) d\xi. \quad (2.60)$$

This expression shows that the layer-average of  $p_h^{(1)}$  is always zero at any fixed  $x$ -location, as integration of  $\cos(n\pi z)$  vanishes for all  $n$ . Since the average of  $p^{(0)}$  and the component  $(z - z_0)H(z - z_0)$  of (2.56) is the same for any fixed  $x$ , we can conclude that no contribution to the average pressure differential  $\langle p(+\infty) \rangle - \langle p(-\infty) \rangle$  can arise at order  $\epsilon$ , as expected from the results of § 2.2.2, and the fact that, for equal asymptotic interfacial heights, the average and interface pressure imbalances are equal.

Next, we work on the second order pressure contribution  $p^{(2)}$ . We concentrate only on the layer-average of the boundary term  $\partial_x p^{(2)}$  instead of the exact  $z$ -dependence. Multiplying the  $p^{(2)}$  equation by  $x$ , integrating over the fluid volume and taking into account the boundary conditions yields

$$\lim_{L \rightarrow \infty} \int_0^1 (p^{(2)}(L, z) - p^{(2)}(-L, z)) dz = - \lim_{L \rightarrow \infty} \int_{[-L, +L] \times [0, 1]} r \partial_x p^{(1)} dx dz.$$

The top and bottom boundary contributions cancel out exactly from the  $p_h^{(1)}$  and  $p^{(2)}$  terms. Passing to the limit we retrieve a close relative of the general formula for the pressure differential in an infinite strip,

$$\langle p^{(2)} \rangle_\Delta \equiv \int_0^1 (p^{(2)}(\infty, z) - p^{(2)}(-\infty, z)) dz = - \int_{\mathbb{R} \times [0, 1]} r \partial_x p^{(1)} dx dz. \quad (2.61)$$

Substituting expression (2.60) for  $p_h^{(1)}$  yields

$$\begin{aligned} \langle p^{(2)} \rangle_\Delta = & - \int_{-\infty}^{+\infty} \left( \int_{-\infty}^{+\infty} \text{sgn}(x - \xi) \sum_{n=1}^{\infty} e^{-n\pi|x-\xi|} (\cos(n\pi\eta(\xi)) - \cos(n\pi z_0)) d\xi \right. \\ & \left. \times \int_0^1 \cos(n\pi z) H(z - \eta(x)) dz \right) dx. \end{aligned} \quad (2.62)$$

The last integral is

$$\int_{\eta(x)}^1 \cos(n\pi z) dz = -\frac{1}{n\pi} \sin(n\pi\eta(x))$$

Table 2.1: Comparison of pressure imbalances  $P_\Delta/\rho_\Delta^2$  as predicted by long-wave model and full Euler results for interface (2.47) with asymptotic height  $z_0 = 1/2$ .

$A$	$B$	$\sigma$	S	Model (eq. (2.48))	Euler (eq. (2.63))	Model/Euler
1/3	1/3	$\sqrt{8/3}$	1	$5.69 \times 10^{-3}$	$4.01 \times 10^{-3}$	1.42
2/5	1/5	$\sqrt{8/3}$	1	$3.69 \times 10^{-3}$	$2.62 \times 10^{-3}$	1.40
3/5	1/3	$2\sqrt{8/3}$	1	$9.49 \times 10^{-4}$	$8.25 \times 10^{-4}$	1.15
3/5	1/3	$3\sqrt{8/3}$	1	$1.44 \times 10^{-4}$	$1.32 \times 10^{-4}$	1.09
4/5	1	$4\sqrt{8/3}$	1	$2.76 \times 10^{-4}$	$2.57 \times 10^{-4}$	1.07
3/5	2/3	$4\sqrt{8/3}$	3	$1.59 \times 10^{-3}$	$1.49 \times 10^{-3}$	1.06
1/3	1/3	$4\sqrt{8/3}$	20	$1.68 \times 10^{-12}$	$1.70 \times 10^{-12}$	0.99

and hence

$$\begin{aligned}
\langle p^{(2)} \rangle_\Delta &= \sum_{n=1}^{\infty} \int_{-\infty}^{+\infty} \sin(n\pi\eta(x)) \\
&\times \left( \int_{-\infty}^{+\infty} \operatorname{sgn}(x - \xi) \frac{e^{-n\pi|x-\xi|}}{n\pi} (\cos(n\pi\eta(\xi)) - \cos(n\pi z_0)) d\xi \right) dx.
\end{aligned} \tag{2.63}$$

We remark that all the theoretical arguments for the determination of the pressure jump  $\langle p^{(2)} \rangle_\Delta$  have assumed that the interface does not touch the channel boundaries. Thus, there are always slivers of light and heavy fluid near the top and bottom lid, respectively. However, it is not difficult to realize that, since all integrals are bounded, and the integrands decay exponentially, we can pass to the limit of zero sliver-width in the above formulae. Furthermore, since  $p^{(2)}$  is no longer affected by the density difference at the top and bottom interfaces, this limit coincides with the “physical” instance of zero sliver-width. Indeed, the density difference is taken care by  $p^{(1)}$ , while  $p^{(2)}$  satisfies a Neumann problem with vanishing boundary conditions at  $z = 0$  and  $z = 1$ . It is however suitable to anticipate here that, in general, care should be taken in performing such limits for general density values. In particular, in Appendix B we shall show that the behaviour of  $p(x, z)$  in “air-water” systems, obtained by considering the limit  $\rho_1 \rightarrow 0$ , might not follow from the *naïve* limit of vanishing sliver width.

### 2.4.2 Comparison with the long wave model

Expression (2.63) can be used to test the long-wave model result (2.46) with, e.g.,  $\eta(x)$  given by (2.47). While we are unable to compute the integrals in (2.63) explicitly, their numerical evaluation for up to 25 terms in the series yields agreement over a broad range of parameters. Table 2.1 reports a few examples. For these, the long wave model pressure imbalance (2.46) is always of the same order of its Euler counterpart (2.63), with the discrepancy decreasing as the main long wave parameter  $\sigma$  increases. Remarkably, the agreement is acceptable already for  $\sigma = 3\sqrt{8/3} \simeq 4.9$ , which for a channel of height  $h = 1$  would correspond to a value of the long-wave small parameter  $\delta \simeq 0.2$ . The trend exemplified by table 2.1 persists in general for all the parameter combinations we have checked.

We note that the convergence of the series in (2.63) is slow for the class of smooth profiles from (2.47) we have explored, which partially adds to the discrepancy in table 2.1. A general convergence proof and an estimate of the convergence rate shows that the series coefficients are bounded by  $1/n^2$ , for any interface function  $\eta$  of bounded variation class. Next, we focus instead on special profiles where the series summation can be performed explicitly.

### 2.4.3 Special initial conditions: piecewise-constant interfaces

Let us consider the integral formula (2.63) for a profile  $\eta$  that is smooth on the whole line, except possibly at a finite number of points  $A_1, A_2, \dots, A_N$ , where the jumps  $\eta(A_\alpha^+) - \eta(A_\alpha^-)$  are finite. We also require, as usual, that  $\lim_{x \rightarrow \pm\infty} \eta(x) = z_\pm$  for some asymptotic values  $z_\pm$ . Taking into account the distributional identity

$$\operatorname{sgn}(x - \xi) e^{-n\pi|x-\xi|} = \frac{1}{n\pi} \frac{d}{d\xi} e^{-n\pi|x-\xi|},$$

integrating by parts, and considering the distributional derivative of  $\cos(n\pi\eta(\xi))$ , leads to an expression equivalent to (2.63),

$$\begin{aligned} \langle p^{(2)} \rangle_{\Delta} &= \sum_{n=1}^{\infty} \frac{1}{n\pi} \int_{-\infty}^{+\infty} \sin(n\pi\eta(x)) \left( \int_{-\infty}^{+\infty} e^{-n\pi|x-\xi|} \eta'(\xi) \sin(n\pi\eta(\xi)) d\xi \right) dx \\ &\quad - \sum_{n=1}^{\infty} \frac{1}{n^2\pi^2} \sum_{\alpha=1}^N \int_{-\infty}^{+\infty} dx \sin(n\pi\eta(x)) e^{-n\pi|x-A_{\alpha}|} \left( \cos(n\pi\eta(A_{\alpha}^{-})) - \cos(n\pi\eta(A_{\alpha}^{+})) \right) dx. \end{aligned} \quad (2.64)$$

Now, for piecewise-constant interface profiles

$$\begin{aligned} \eta(\xi) &= z_i \quad \text{for } A_i < \xi < A_{i+1}, \quad i = 1, \dots, N-1, \\ \eta(\xi) &= z_- \equiv z_0 \text{ for } \xi < A_1 \text{ and } \eta(\xi) = z_+ \equiv z_N \text{ for } \xi > A_N, \end{aligned} \quad (2.65)$$

only the second line of equation (2.64) provides a contribution, and we have  $\eta(A_{\alpha}^{-}) = z_{\alpha-1}$ ,  $\eta(A_{\alpha}^{+}) = z_{\alpha}$ .

Because of the shape achieved by each fluid's domain in the limiting three step case with  $z_1 = 0$  and  $z_2 = 1$ , i.e., disconnected domains with no connecting slivers at the top and bottom plates, in what follows we will often refer to this class of initial conditions as “hooks,” see figure 2.5. We remark that these are possibly the simplest configurations yielding explicit expressions for non-vanishing pressure imbalances. Moreover, hooks can in principle be implemented experimentally by use of gates separating the fluids, just as in the limiting configuration of the dam-break case (corresponding to  $z_0 = 0$ ,  $z_3 = 1$ ,  $z_1 = z_2 = 0$ , all  $A$ 's zero) with a single gate spanning the whole width of the channel. Performing the integrations in (2.64) we get that the pressure jump at the second order in the  $\rho_{\Delta}$  expansion is given by

$$\langle p^{(2)} \rangle_{\Delta} = \sum_{k=1}^{\infty} \frac{1}{\pi^3 k^3} \left( \Delta_0^{(k)} + \sum_{1 \leq \alpha < \beta \leq N} \Delta_{[\alpha, \beta]}^{(k)} e^{k\pi(A_{\alpha} - A_{\beta})} \right), \quad (2.66)$$



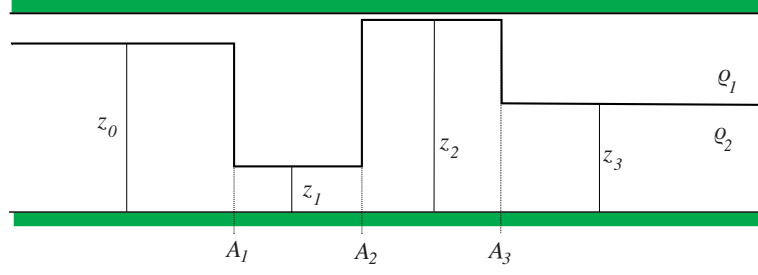


Figure 2.5: Initial hook-like configuration for a two-fluid density distribution in an  $x$ -infinite channel between two rigid plates located at  $z = 0, 1$ .

where

$$\Delta_0^{(k)} = \sum_{\alpha=1}^N \sin(k\pi(z_\alpha - z_{\alpha-1})) + \frac{1}{2} (\sin(2k\pi z_0) - \sin(2k\pi z_N)), \quad (2.67)$$

and

$$\begin{aligned} \Delta_{[\alpha,\beta]}^{(k)} = & (\cos(k\pi z_\beta) - \cos(k\pi z_{\beta-1}))(\sin(k\pi z_\alpha) - \sin(k\pi z_{\alpha-1})) + \\ & - (\cos(k\pi z_\alpha) - \cos(k\pi z_{\alpha-1}))(\sin(k\pi z_\beta) - \sin(k\pi z_{\beta-1})), \end{aligned} \quad (2.68)$$

or, equivalently,

$$\begin{aligned} \Delta_{[\alpha,\beta]}^{(k)} = & \sin(k\pi(z_\alpha - z_\beta)) - \sin(k\pi(z_{\alpha-1} - z_\beta)) + \\ & - \sin(k\pi(z_\alpha - z_{\beta-1})) + \sin(k\pi(z_{\alpha-1} - z_{\beta-1})). \end{aligned} \quad (2.69)$$

In particular, for the ‘three-jump’ case, with discontinuities located at  $A_1 \leq A_2 \leq A_3$  and arbitrary heights  $0 \leq z_0, z_1, z_2 \leq 1$ ,  $z_0 = z_3$ , we have

$$\begin{aligned} \langle p^{(2)} \rangle_\Delta = & \sum_{k=1}^{\infty} \frac{1}{\pi^3 k^3} \left[ (\sin(k\pi(z_1 - z_0)) + \sin(k\pi(z_2 - z_1)) + \sin(k\pi(z_0 - z_2))) \right. \\ & \times (1 - e^{k\pi(A_1 - A_2)}) (1 - e^{k\pi(A_2 - A_3)}) \left. \right]. \end{aligned} \quad (2.70)$$

Setting for simplicity  $A_3 = -A_1 = A$ ,  $A_2 = 0$ , and  $z_1 = 0$ ,  $z_2 = 1$ , yields the compact

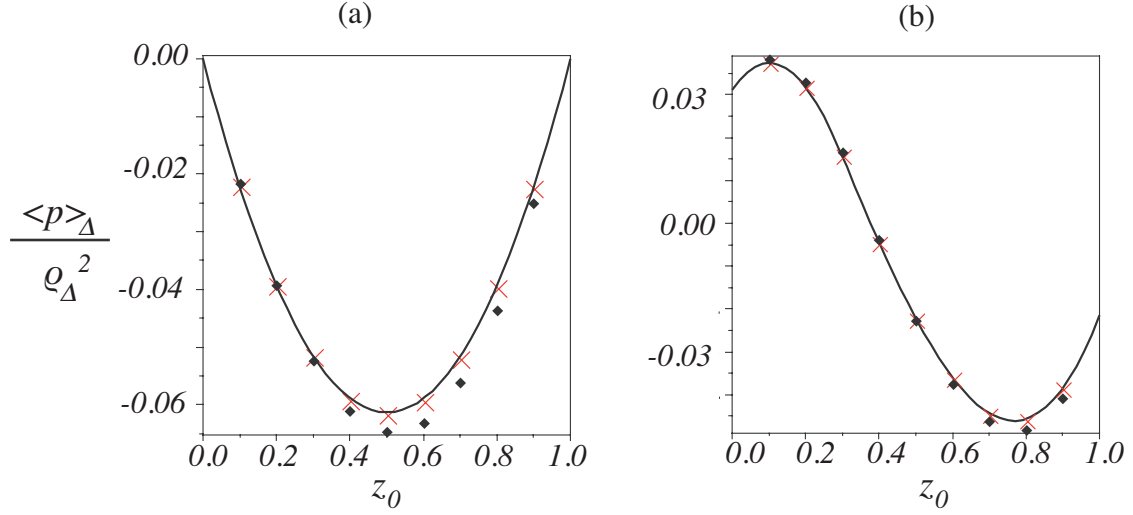


Figure 2.6: (a) Full hook case, with  $A_2 - A_1 = A_3 - A_2 = 1.5$ ,  $z_3 = z_0$ ,  $z_1 = 0$ ,  $z_2 = 1$ ,  $\rho_\Delta = 0.01$  (crosses),  $\rho_\Delta = 0.1$  (diamonds), from numerics (§ 2.6), theoretical value (solid line) from asymptotics  $\rho_\Delta \rightarrow 0$ . (b) Kink-like case, with  $A_2 - A_1 = A_3 - A_2 = 1.5$ ,  $z_1 = 0.3$ ,  $z_2 = 0.8$ ,  $z_3 = 0.5$ ,  $\rho_\Delta = 0.01$  (crosses),  $\rho_\Delta = 0.1$  (diamonds), from numerics (§ 2.6), theoretical value (solid line) from asymptotics  $\rho_\Delta \rightarrow 0$  (equation (2.71)).

expression

$$\langle p^{(2)} \rangle_\Delta = -2 \sum_{n=0}^{\infty} \frac{\sin((2n+1)\pi z_0)}{((2n+1)\pi)^3} \left(1 - e^{-(2n+1)\pi A}\right)^2. \quad (2.71)$$

If  $A$  is sufficiently large the exponentials can be neglected and we get the simple quadratic expression

$$\langle p^{(2)} \rangle_\Delta = -\frac{2}{\pi^3} \sum_{n=0}^{\infty} \frac{\sin((2n+1)\pi z_0)}{(2n+1)^3} = -\frac{1}{4} z_0 (1 - z_0).$$

As shown in figures 2.6(a) and 2.6(b), the comparison between the results predicted by these formulae and those obtained numerically with an Euler solver (more on this in section 2.6 below) are very reasonable. Another comparison with the numerics is offered by figure 2.7. Here, for the hook configuration, the quadratic asymptotic scaling of  $\langle p \rangle_\Delta \propto \rho_\Delta^2$  can be seen explicitly, with the theory providing an excellent fit for small values of  $\rho_\Delta$ . The agreement persists up to fairly large values of  $\rho_\Delta$ . A relative error of 10% is not reached until  $\rho_\Delta \simeq 0.2$ .

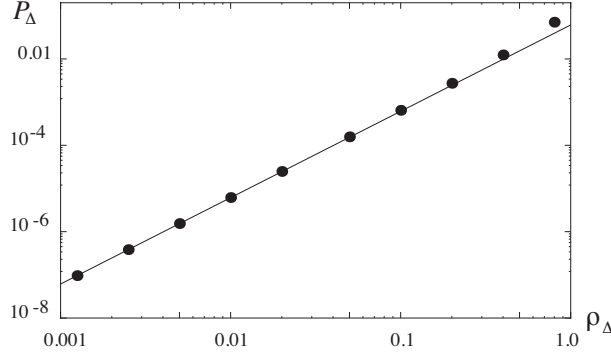


Figure 2.7: Pressure imbalance  $P_\Delta$  vs. density difference  $\rho_\Delta$ . Theory (solid line) from equation (2.71) and VARDEN simulation (dots). The interface is a hook (figure 2.5) with parameters given by  $z_0 = z_3 = 0.5$ ,  $z_1 = 1$ ,  $z_2 = 0$ , and  $A_2 - A_1 = A_3 - A_2 = 1.5$  as in figure 2.6(a). The 2:1 slope is maintained up to density differences as large as  $\rho_\Delta \simeq 0.2$  (in units of  $\rho_2$ ).

In general, in the limit  $(A_{i+1} - A_i)$  large (as compared with the height of the channel), the Fourier series of (2.66) can be easily summed. Indeed, in this case the expression of the pressure jump reduces to

$$\langle p^{(2)} \rangle_\Delta = \left( \sum_{\alpha=1}^N \sum_{k=1}^{\infty} \frac{1}{\pi^3 k^3} (\sin(k\pi(z_\alpha - z_{\alpha-1}))) + \frac{1}{2} \sum_{k=1}^{\infty} \frac{1}{\pi^3 k^3} (\sin(2k\pi z_0) - \sin(2k\pi z_N)) \right),$$

which yields

$$\langle p^{(2)} \rangle_\Delta = \left( \sum_{\alpha=1}^N \text{sgn}(z_\alpha - z_{\alpha-1}) \mathcal{Q}_1(|z_\alpha - z_{\alpha-1}|) + \mathcal{Q}_2(z_0) - \mathcal{Q}_2(z_N) \right), \quad (2.72)$$

where  $\mathcal{Q}_1$  and  $\mathcal{Q}_2$  are the polynomials (see, e.g., Gradshteyn *et al.* [21])

$$\begin{aligned} \mathcal{Q}_1(x) &= \frac{1}{12}x^3 - \frac{1}{4}x^2 + \frac{1}{6}x = \frac{1}{12}x(x-1)(x-2) \\ \mathcal{Q}_2(x) &= \frac{1}{3}x^3 - \frac{1}{2}x^2 + \frac{1}{6}x = \frac{1}{3}x(x-1)\left(x - \frac{1}{2}\right). \end{aligned} \quad (2.73)$$

It is interesting to note that even for a piecewise constant interfacial profile a qualitative agreement with the long-wave model result (2.48) can be detected. For the

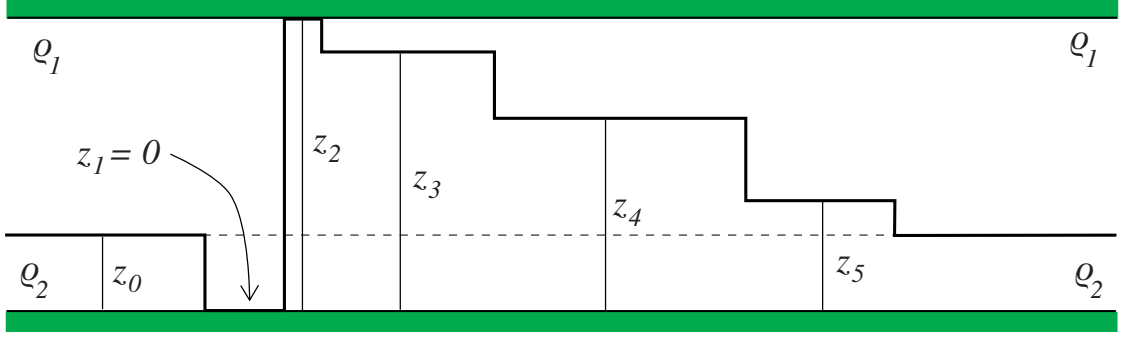


Figure 2.8: The special configuration of a staircase hook for a two-fluid density distribution in an  $x$ -infinite channel between two rigid plates located at  $z = 0, 1$ .

configuration depicted in figure 2.4, with an upward tooth of height  $A$  followed by a downward tooth of height  $B$ , equation (2.70) shows exponential decay of the pressure imbalance with increasing separation of the teeth. Further, the leading order behavior is cubic in the heights  $A$  and  $B$ , and both expressions (2.48) and (2.70) are independent of rigid  $z$ -translations of the profile, for as long as the profile does not hit the channel's boundaries.

#### 2.4.4 Special initial conditions: linear interfaces

We next consider the problem of the maximal  $\langle p \rangle_\Delta$  with respect to special configurations. An interesting example is the “crooked hook” configuration depicted in figure 2.8: with the asymptotic heights at  $z = z_0$ , the first jump is to  $z_1 = 0$ , the second is to  $z_2 = 1$ , followed by a sequence of “steps” of heights

$$z_3 \geq z_4 \geq \cdots z_N = z_0.$$

We assume  $\min(A_{i+1} - A_i) \gg 1$ , so that we can safely use formula (2.72) to determine the pressure jump as a function of the decreasing heights  $z_3, z_4, \dots, z_0$ . The outcome is that the configuration maximizing  $|\langle p^{(2)} \rangle_\Delta|$  is that of the left-hand side of the “crooked hook” being a well-crafted staircase, with steps of equal heights (e.g., in the figure, for

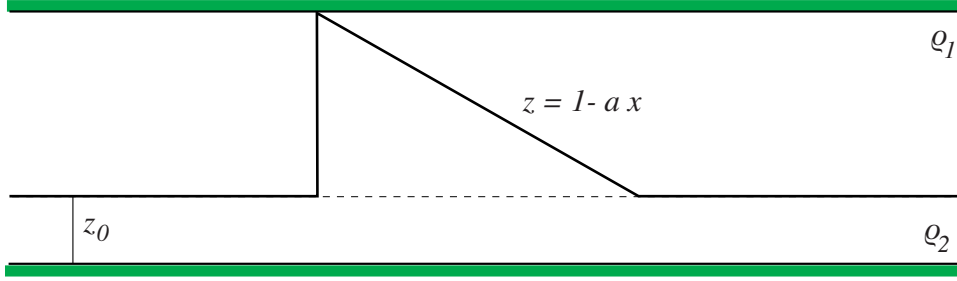


Figure 2.9: The “incline hook” configuration for a two-fluid density distribution in an  $x$ -infinite channel between two rigid plates located at  $z = 0, 1$ .

$N = 5$  we have  $z_0 = 1/5, z_3 = 4/5, z_4 = 3/5, z_5 = 2/5$ ). The sequence of the values of  $\langle p^{(2)} \rangle_\Delta$  as  $N$  varies can be shown to admit  $\langle p^{(2)} \rangle_\Delta = -\frac{1}{6}$  as the asymptotic value (as  $N \rightarrow \infty$ ).

Other cases where the computations can be easily performed are those of piecewise linear profiles. For instance, let us consider the case of the “incline hook” as in figure 2.9, that is, a configuration of a jump located at  $x = 0$ , followed by a constant (negative) slope connecting the top of the step to the asymptotic height  $z = z_0$ . From formula (2.64), the quantity  $\langle p^{(2)} \rangle_\Delta$  is the sum of two terms, one given by the jump at  $x = 0$ , and the other given by the slope of the incline. Performing the integration, we get

$$\langle p^{(2)} \rangle_\Delta = \sum_{k=1}^{\infty} \left( \frac{\Phi_3 a^3 + \Phi_2 a^2 + \Phi_1 a + \Phi_0}{k^3 \pi^3 (1 + a^2)^2} \right), \quad (2.74)$$

with

$$\begin{aligned} \Phi_3 &= \left( 1 + (-1)^k \cos(k\pi z_0) \right) \left( e^{k\pi(z_0-1)/a} - 1 \right) \\ \Phi_2 &= k\pi(z_0 - 1) - (-1)^k \sin(k\pi z_0) \left( 1 + 2e^{k\pi(z_0-1)/a} \right) \\ \Phi_1 &= - \left( 1 - (-1)^k \cos(k\pi z_0) \right) \left( 1 + e^{k\pi(z_0-1)/a} \right) \\ \Phi_0 &= k\pi(z_0 - 1) - (-1)^k \sin(k\pi z_0). \end{aligned} \quad (2.75)$$

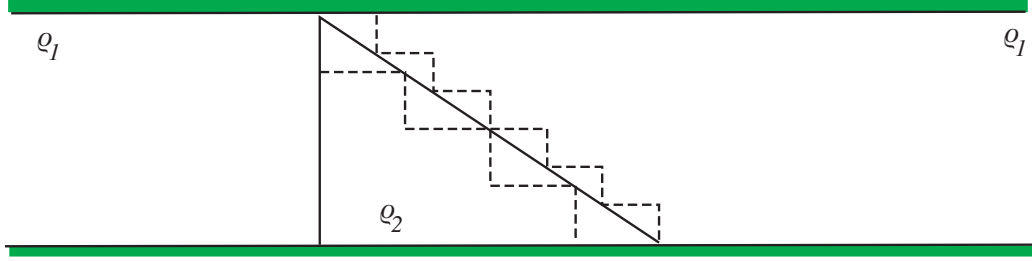


Figure 2.10: The piecewise constant vs. linear configurations for a two-fluid density distribution in an  $x$ -infinite channel between two rigid plates located at  $z = 0, 1$ .

In the limit  $a \rightarrow 0, z_0 \rightarrow 0$ , the series (2.74) reduces to

$$-\sum_{k=1}^{\infty} \frac{1}{\pi^2 k^2} = -\frac{1}{6}.$$

This result matches the limiting value of the staircase of figure 2.8. Its interest lies in part on the fact that, although geometrically one would expect the limit of zero slope of the incline to yield a dam-break configuration, in which half of the channel is filled with “light” fluid and the remaining half is filled with “heavy” fluid, we see that the pressure differential is not given by the naïve geometrical limit. As computed exactly (for any density variation) in section 2.5 below, the dam-break configuration leads to zero pressure imbalance.

As a final example, we examine the pressure imbalances associated with sequences of staircase configurations with a fixed total width (see figure 2.10), with an increasing number of smaller and smaller steps. By using symbolic manipulators (Maple or Mathematica), it can be shown that the configuration that maximizes the pressure imbalance is that of the incline (solid line in figure 2.10), and that the limits from below and from above of the pressure imbalances of the piecewise constant staircases coincide with the pressure imbalance of their limiting linear profile. In this case the pressure imbalance agrees with the geometrical limit.

The above examples illustrate in a simple way how pressure imbalances can arise from localized variations of stratification, and how limiting processes can be affected by subtleties that require some care in order to be handled correctly. Next, we take a closer look at this issue in the context of an exact result, valid for all density differences, for the stratified Euler system.

## 2.5 Dam-breaking class

A nontrivial exact solution of equation (2.49), with the usual boundary conditions, can be obtained in the dam-break configuration depicted in figure 2.11: the heavier fluid (density  $\rho_2$ ) fills the right side of the channel (assumed of height  $h = 1$ ) and the rest of the channel (density  $\rho_1$ ) is filled with the lighter fluid. The interface is therefore vertical, say at  $x = 0$ . In this case the asymptotic values of the interface are obviously different. By variable separation and solving by Fourier series, one finds closed-form expressions for pressure,

$$\begin{aligned} p_1 &= -\rho_1 g z - \rho_1 g \frac{\rho_\Delta}{\rho_1 + \rho_2} \left( \frac{1}{2} - 4 \sum_{n \text{ odd}} \frac{1}{n^2 \pi^2} \cos(n\pi z) e^{n\pi x} \right) & \text{if } x \leq 0 \\ p_2 &= -\rho_2 g z + \rho_2 g \frac{\rho_\Delta}{\rho_1 + \rho_2} \left( \frac{1}{2} - 4 \sum_{n \text{ odd}} \frac{1}{n^2 \pi^2} \cos(n\pi z) e^{-n\pi x} \right) & \text{if } x \geq 0 \end{aligned} \quad (2.76)$$

where  $p_1$  ( $p_2$ ) is the pressure in the domain filled with the fluid with density  $\rho_1$  ( $\rho_2$ ). The pressure given in (2.76) is continuous in the whole channel, with a discontinuous  $x$ -derivative at  $x = 0$ . Moreover, this gradient has a (logarithmic) divergence at the points where the interface touches the boundaries. Indeed, it can be shown that

$$\left. \frac{\partial p_1}{\partial x} \right|_{x=0^-} = \frac{\rho_1 \rho_\Delta g}{\pi(\rho_1 + \rho_2)} \log \left( \frac{1 + \cos(\pi z)}{1 - \cos(\pi z)} \right).$$

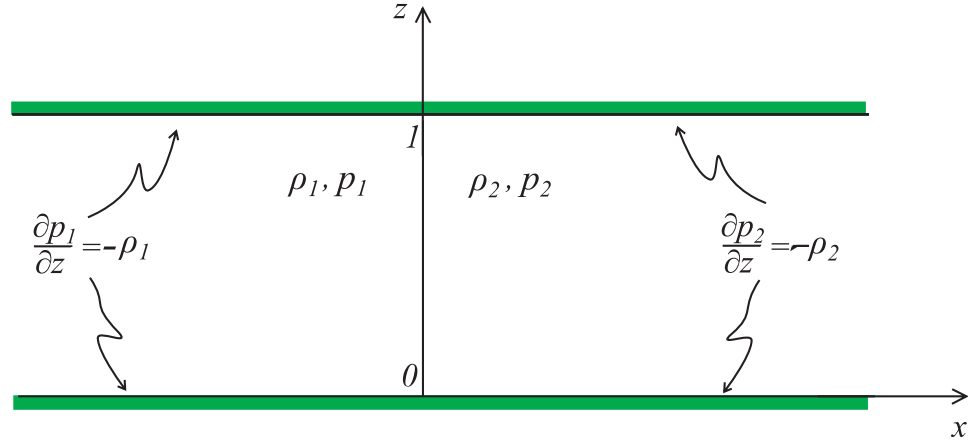


Figure 2.11: Dam-break configuration for a two-fluid density distribution. The pressure is everywhere continuous (and so,  $\partial_z p_1 = \partial_z p_2$  at the interface  $x = 0$ ) with the jump condition for its normal derivative at the interface  $\partial_x p_1 = (\rho_1/\rho_2)\partial_x p_2$ .

One could expect that this configuration, due to the overall mass imbalance of the fluid, would consequently generate an overall pressure imbalance. However, this is not the case since for all  $x \in \mathbb{R}$

$$\int_0^1 p_1(x, z, 0) dz = \int_0^1 p_2(x, z, 0) dz = -g \frac{\rho_1 \rho_2}{\rho_1 + \rho_2}. \quad (2.77)$$

Hence we have that  $\langle p \rangle_\Delta = 0$  at  $t = 0$ . (Notice however that the numerical simulations presented in figure 2.16 show that a pressure imbalance will develop at times  $t > 0$ , so that the horizontal momentum is not conserved in the course of evolution.)

This example confirms that the nonconservation of the total horizontal momentum does not simply rely on the asymptotic difference of the purely hydrostatic pressure. In particular, we can interpret this result as an occurrence of another non trivial instance of boundary effects. In fact, let us consider a partial dam-break configuration, with the heavier fluid in the region  $[0, +\infty) \times [0, z_1]$ . One could expect it to generate a pressure difference which increases with the partial-dam height  $z_1 \in [0, 1]$ . However, as equation (2.77) shows, this is once again not the case, since the pressure differential



for the dam-break limit ( $z_1 = 1$ ) is null. This discontinuity might be regarded as a boundary effect, as suggested by the perturbative results of Section 2.4.3. Indeed, the expression for  $\langle p^{(2)} \rangle_\Delta$  in this partial dam-break case, obtained by appropriate use of the polynomial formulae (2.72), yields  $\langle p^{(2)} \rangle_\Delta(z_1) = (z_1^2 - z_1^3)/4$ , whose minimum is at  $z_1 = 2/3$ .

Next, we remark that total horizontal momentum is always equal to that of the subsection of the channel spanned by the (maximal) horizontal support of the interface between the two fluids. In fact, volume conservation by incompressibility implies that at all times the volume flux

$$\int_0^1 u(x, z, t) dz = 0$$

as this is satisfied as  $|x| \rightarrow \infty$  (or at the lateral vertical walls for a finite channel). Since for homogeneous fluid the mass flux is simply proportional to the volume flux, the horizontal momentum for any channel's section of homogeneous fluid, i.e., sections that the “gravity currents” developing from the dam-break have not had time to reach, is zero. Further, the horizontal momentum of the fluid from a dam-break is directed towards the lighter fluid, since for computing horizontal momentum one needs to weigh the zero-volume-flux currents resulting from the dam-break with their different densities. The sign of pressure imbalance as it grows past the initial time can then be predicted to be opposite that of the momentum (i.e., positive when the denser fluid is to the right of the dam). This can also be seen intuitively from the center of mass time evolution (2.21). The two-fluid system admits a configuration of minimum potential energy corresponding to a flat interface, and it can be expected that the fluid's initial motion would be in the direction to achieve such configuration. Thus, the center of mass for a section between end points fully lying in regions of homogeneous fluids (where mass flux is zero), would move towards the lighter fluid, giving rise to a corresponding total horizontal momentum according to (2.21).

Let us now consider total vorticity evolution for the dam-break class. A general feature of the motion can be gleaned from (2.32). Taking into account that the interface is the segment  $\{(0, z) \mid z \in [0, 1]\}$  and the density is given by  $\rho = \rho_1 H(x) + \rho_2 H(-x)$  yields  $\nabla p \times \nabla(1/\rho) = -\delta(x) p_z(0, z) \rho_\Delta / (\rho_1 \rho_2)$ . Thus, from (2.32),

$$\begin{aligned} \Gamma_t^{\text{dam}} &= \int_{\mathbb{R} \times [0, 1]} \nabla p \times \nabla \left( \frac{1}{\rho} \right) dA \\ &= - \int_{\mathbb{R} \times [0, 1]} \frac{p_z(x, z) \rho_\Delta}{\rho_1 \rho_2} \delta(x) dA = \frac{\rho_\Delta}{\rho_1 \rho_2} (p(0, 0) - p(0, 1)). \end{aligned} \quad (2.78)$$

The explicit solution (2.76) for the dam configuration implies

$$\Gamma_t^{\text{dam}} = - \frac{2\rho_\Delta}{\rho_1 + \rho_2}. \quad (2.79)$$

We remark that this behavior can be described as a boundary effect, by considering a limit in which the interface between the two fluids is made to coincide with one the boundaries of the channel (the lower for  $x > 0$  and the upper for  $x < 0$ ). Formula (2.37) can be used as depicted in figure 2.12, understanding the dam configuration as the limit of the full hook case when  $A \rightarrow +\infty$ , with  $A$  the length of the hook “teeth.” In this limit the interface at  $-\infty$  goes to 1 while at  $+\infty$  it goes to 0. From (2.37) the time derivative of the total vorticity for the hook configuration is

$$\Gamma_t^{\text{hook}} = \frac{\rho_\Delta}{\rho_1 \rho_2} [P_\Delta - (p(A, 0) - p(0, 0)) - (p(0, 1) - p(-A, 1))]. \quad (2.80)$$

In the dam-break limit  $A \rightarrow \infty$ ,  $z_- \rightarrow 1$ , and  $z_+ \rightarrow 0$ , where  $P_\Delta = p(+\infty, 0) - p(-\infty, 1)$ ,

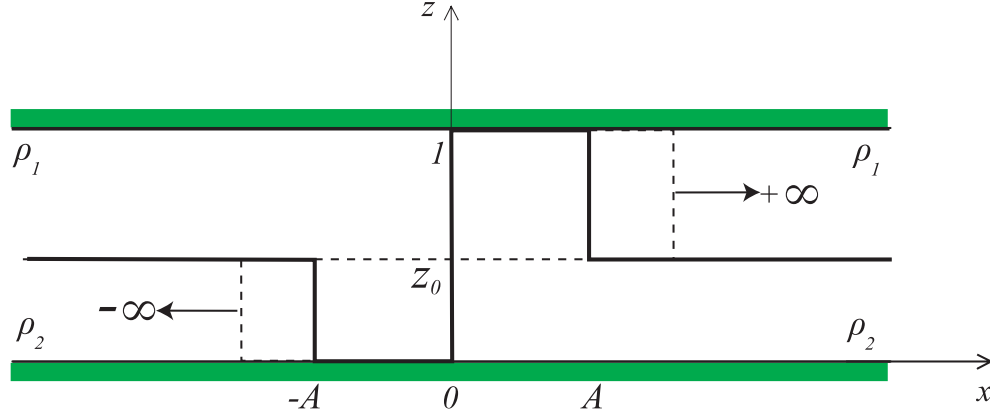


Figure 2.12: The geometric limit from the hook to dam configuration.

we have

$$\begin{aligned}
 \Gamma_t^{\text{dam}} &= \lim_{A \rightarrow +\infty} \Gamma_t^{\text{hook}} \\
 &= \frac{\rho_\Delta}{\rho_1 \rho_2} [(p(+\infty, 0) - p(-\infty, 1)) - (p(+\infty, 0) - p(0, 0)) - (p(0, 1) - p(-\infty, 1))] \\
 &= - \left( \frac{1}{\rho_1} - \frac{1}{\rho_2} \right) [p(0, 1) - p(0, 0)],
 \end{aligned} \tag{2.81}$$

which agrees with (2.78).

## 2.6 Time evolution: numerical results

The above discussion was conducted with laterally unbounded domains in mind. Of course, such an idealization cannot be used either in reality or in numerical studies. However, in this section we provide numerical evidence that the effective-wall lateral confinement, and hence non-conservation of horizontal momentum, can occur in *finite* domains, due to the relative inertia of a stratified, incompressible Euler fluid. First, we remark that, for domains bounded by rigid lateral walls, the finite-domain version of equation (2.23) (obtained by writing  $\pm L/2$  in place of  $\pm\infty$ ) continues to hold; in the limit of the walls moving to infinity we simply recover the hydrostatic balance

as expressed by (2.23). Next, consider the case of periodic boundary conditions in the periodic box  $[-L/2, L/2]$ . This requires  $P|_{-L/2}^{+L/2} = 0$  and hence the horizontal momentum for the whole periodic domain is conserved. We focus on a subset of the fluid domain, henceforth referred to as the “test section,” obtained by taking a (much) smaller interval embedded in the period (cf. figure 2.13). Within this test section, we apply localized initial conditions for velocity and pycnocline displacement, e.g., by requiring that the data have compact support on a small subset of the test section’s region. The analogue of equation (2.23) for a periodic domain becomes an equation for the flux  $Q$ ,

$$L\dot{Q} = \left(\frac{1}{\rho_2} - \frac{1}{\rho_1}\right) \int_{-L/2}^{L/2} \zeta_x P \, dx. \quad (2.82)$$

Consider the limit  $L \rightarrow \infty$  of this equation. For definiteness, let  $\zeta$  be a function with compact support and suppose that all the velocities are zero at  $t = 0$ . The integral on the right-hand side will be bounded as  $L \rightarrow \infty$  (assuming that  $P$  remains bounded on finite domains), so that  $\dot{Q} \sim L^{-1}$ . Suppose the test section extends from  $-A/2$  to  $A/2$  and  $\text{supp}(\zeta) \subset [-A/2, A/2]$ . At  $t = 0$ , after integrating (2.22) in the test section and eliminating  $\dot{Q}$ , we obtain

$$\left(\frac{1}{\rho_2} - \frac{1}{\rho_1}\right) \left(1 - \frac{A}{L}\right) \int_{\text{supp}(\zeta)} \zeta_x P \, dx = \left(\frac{h_2}{\rho_2} + \frac{h_1}{\rho_1}\right) P \Big|_{-A/2}^{+A/2}. \quad (2.83)$$

If we extend the test section to infinity with the double scaling limit  $A, L \rightarrow \infty$  and  $A/L \rightarrow 0$ , the previous formula becomes (2.23). Though valid only at time  $t = 0$ , this argument shows how the limit of infinite period for localized initial data can agree with the pressure differential of the infinite channel in hydrostatic balance at infinity.

We now explore numerically the time evolution of localized initial data under both periodic and rigid (impermeable) wall boundary conditions. In particular, we first compute the evolution of the flux  $Q(t)$  and horizontal momentum  $\Pi_1(t)$  for the test section

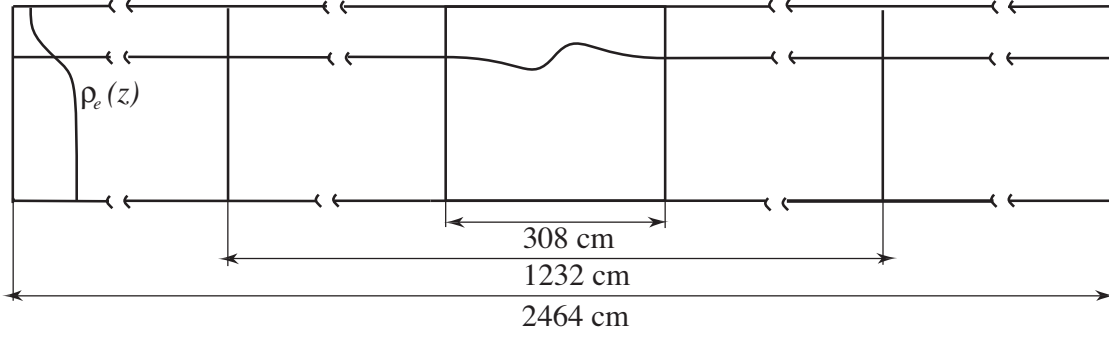


Figure 2.13: Sketch of the fluid test domain and its symmetrical padding by wings of increasing length, doubling and quadrupling the period as shown.

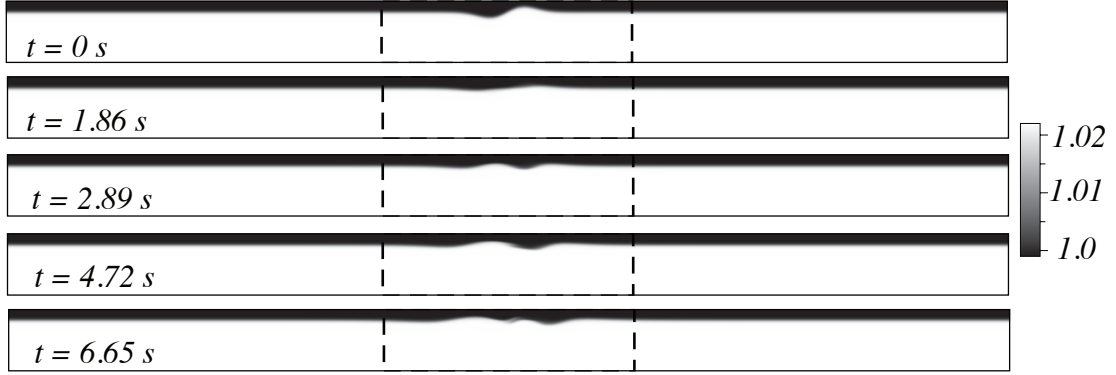


Figure 2.14: Density field from the numerical simulation of the evolution from the initial data in the 1232 cm long tank with the center 308 cm test section marked by the vertical lines.

alone. We then compare the resulting time series with those from simulations from the same initial conditions in progressively longer channels *under periodic boundary conditions*, see figure 2.13. Thus, while the total horizontal momentum for these longer periodic channels is conserved, that computed only in the embedded test-section will in general exhibit time dependence. Owing to the added inertia of the “padding” wings bracketing the test section in the longer channels, we expect this time dependence to show some similarity with that of the walled-in test section. That is, the added inertia acts as virtual walls, which could then approximate actual walls in the limit of an infinite periodic channel.

### 2.6.1 The effect of infinite inertia

We first perform long wave simulations using dimensional quantities, and translating the origin of the coordinates to the bottom. The interface displacement is chosen to be antisymmetric through  $\zeta_0(x) = h_2 + x/2 \exp(-x^2/\sigma^2)$  together with zero initial velocities. This function displaces the smooth equilibrium density function  $\rho_e(z)$  to give the initial condition  $\rho_0$  (with obvious meaning of notation)

$$\rho_0(x, z) = \rho_1 + \frac{\rho_2 - \rho_1}{2} (1 + \tanh [\gamma(\zeta_0(x) - z)]) , \quad z \in [0, H] . \quad (2.84)$$

Here,  $\sigma = 30$  cm,  $\rho_1 = 0.999$  g·cm<sup>-3</sup>,  $\rho_2 = 1.022$  g·cm<sup>-3</sup>,  $H = 77$  cm,  $h_2 = 62$  cm, and the thickness of the pycnocline (defined as the distance between density isolines corresponding to 10% and 90% of the total density jump) is set by the parameter  $\gamma = 0.5$  to correspond to about 4.5 cm (all of these parameters are suggested by those typical for experiments with salt-stratified water). Notice that this choice of parameters gives effectively an initial condition of compact support, with the initial departure from hydrostatic equilibrium for  $|\rho - \rho_e|/\rho_e$  of order  $10^{-10}$  at the boundary of the test section  $x = \pm 154$  cm; this departure remains below  $10^{-7}$  in all our runs. The simulations (see figure 2.14) are performed using the numerical code VARDEN which solves the stratified incompressible Euler equations (for details see Almgren *et al.* [1].) We typically use a square grid with 512 points along the vertical, although we have run cases with doubled and half this resolution to assess convergence. Figure 2.15a shows the time series of the horizontal momentum of the test section for the walled-in configuration, and compares it to that computed with periodic boundary conditions with quadrupled and octupled periodic extensions. As can be seen, there is indeed a tendency for the longer channel to yield a momentum evolution closer to that of the walled section, for the initial (short) time displayed. As expected, later time evolution shows larger discrepancies but still

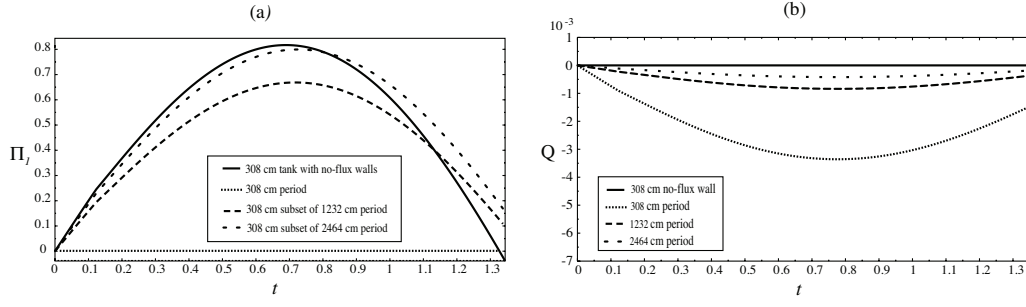


Figure 2.15: (a) Horizontal momentum time evolutions for the test section embedded in progressively larger periodic domains, starting from the same initial condition. The solid line correspond to the rigid wall boundaries. (b) Time series of fluxes  $Q(t)$  with respect to increasing period  $L$ , for the same cases as (a). The flux decreases as  $1/L$  in response to the larger inertia of the channel “padding” wings.

with similar overall behavior and magnitudes. This is in rough agreement with the estimate from the fastest baroclinic wave speeds, which for this parameter choice are of order 16 cm/s, and with the horizontal scale of the initial condition with respect to that of the test section. For reference, we remark that the code maintains the total horizontal momentum for the periodic channels close to zero (the initial value) with an error of order  $10^{-3}$ . Figure 2.15b presents the time series of the flux  $Q(t)$  for the same runs. The flux is computed at different  $x$ -locations, yielding the same value to within a relative error of  $10^{-10}$  (thus further validating the convergence of the code). As can be seen by the different curves, the flux appears to scale as the inverse of the channel length  $L$ , in agreement with expression (2.82) for its initial time derivative. This can be taken as further evidence of the inertia provided by the padding wings (growing as  $L$ ) which acts to oppose the fluid flux (recall that in the limit of an unbounded domain  $Q \equiv 0$  due to the equilibrium at infinity). The inverse scaling with  $L$  can be given further analytic interpretation. In fact, the analogue of (2.40) for the leading-order hydrostatic (and hence dispersionless) long-wave approximation is

$$\dot{Q} \int_{-L/2}^{+L/2} \frac{1}{\eta_1/\rho_1 + \eta_2/\rho_2} dx + \int_{-L/2}^{+L/2} \frac{(\eta_1 \bar{u}_1^2 + \eta_2 \bar{u}_2^2)_x}{\eta_1/\rho_1 + \eta_2/\rho_2} dx = 0. \quad (2.85)$$

For zero-velocity initial conditions, this expression yields  $\dot{Q}(0) = 0$ , in contrast to the time series depicted in figure 2.15b. This discrepancy brings forth a limitation of the hydrostatic (and hence dispersionless) long-wave model. It is generally accepted that the dispersionless approximation works well at intermediate times, while at long times the system could display a gradient catastrophe, which can be avoided by restoring dispersive effects (Esler & Pearce [18]). Remarkably, equation (2.85) shows that dispersive effects can also be qualitatively relevant at short times, even in the absence of large  $x$ -derivatives. Specifically, at  $t = 0$  with zero initial velocities the dispersive terms turn (2.85) into

$$\int_{-L/2}^{+L/2} \frac{-\dot{Q}(0) + \frac{1}{3}(\eta_1^3 \bar{u}_{1xt} + \eta_2^3 \bar{u}_{2xt})_x}{\eta_1/\rho_1 + \eta_2/\rho_2} dx = 0. \quad (2.86)$$

By computing the leading-order long-wave asymptotic expressions for the time derivatives (Choi & Camassa [15]) in equation (2.86), the initial slope of the flux turns out to be

$$\dot{Q}(0) = \left( \int_{-L/2}^{+L/2} \frac{B_x}{\eta_1/\rho_1 + \eta_2/\rho_2} dx \right) \left( \int_{-L/2}^{+L/2} \frac{1 - A_x}{\eta_1/\rho_1 + \eta_2/\rho_2} dx \right)^{-1}, \text{ where}$$

$$A = \frac{\eta_1^3}{3} \left( \frac{\rho_2}{\eta_2 \rho_1 + \eta_1 \rho_2} \right)_x + (1 \leftrightarrow 2), \quad B = \frac{g(\rho_2 - \rho_1)\eta_1^3}{3} \left( \frac{\eta_2 \eta_{2x}}{\eta_2 \rho_1 + \eta_1 \rho_2} \right)_x - (1 \leftrightarrow 2).$$

Even within this leading-order approximation, there is rough agreement (in particular by capturing the correct sign) with the numerical data in figure 2.15b. This can also be seen as an a posteriori check on the robustness of the two-layer model. For instance, the theoretical prediction (adjusting for smooth stratification, as in Camassa & Tiron [12]) is  $\dot{Q}(0) \simeq -8.1 \times 10^{-3} \text{ cm}^2/\text{s}^2$  for the case in figure 2.15b with  $L = 1232 \text{ cm}$ , whereas the numerical result is  $\dot{Q}(0) \simeq -1.9 \times 10^{-3} \text{ cm}^2/\text{s}^2$ . Finally, we remark that the inertia effects can be further magnified by taking larger density variations. We have carried out tests with various density ratios, e.g., for  $\rho_2 = 2\rho_1$  and  $\rho_2 = 1.022$



$\text{g/cm}^3$  the model predicts  $\dot{Q}(0) \simeq -9.62 \text{ cm}^2/\text{s}^2$ , while the measured numerical value is  $\dot{Q}(0) \simeq -2.04 \text{ cm}^2/\text{s}^2$ .

### 2.6.2 Step function simulations

We now focus on providing examples of the time evolution ensuing from the class of initial data we have analyzed. So far as we can see, this can only be done numerically. Of course, our analysis of inertia and incompressibility effects of the previous sections has been carried out with laterally unbounded domains in mind. For numerical investigations these infinite domains have to be truncated, for instance by erecting vertical no-flux walls. In the context of the theoretical examples studied in the previous sections, these inertia effects can be illustrated with direct numerical simulations of the time evolution of Euler equations in two dimensions. The initial conditions in all our simulations (all performed using nondimensional quantities) are chosen among the specific cases discussed in Section 2.4 with zero initial velocities. The computation domain is  $[-8, 8] \times [0, 1]$ , and gravity is unity. We typically use a square grid of 512 points along the vertical, although we have run cases with doubled and half the resolution to assess convergence. For  $t = 0$  results, two to three significant digits are kept as they are the same for all three resolutions. As fluid motion ensues, different resolutions show some discrepancies. However, the general density and velocity profiles as well as the important features in pressure jumps and total vorticity remain similar across resolutions.

#### Exact solutions: the dam problem

We begin our numerical simulations with the dam case, which is solved exactly in Section 2.5, and hence provides possibly the best test for numerical validation. We choose density parameters of the top and lower layers to be  $\rho_1 = 0.9$  and  $\rho_2 = 1.0$ .

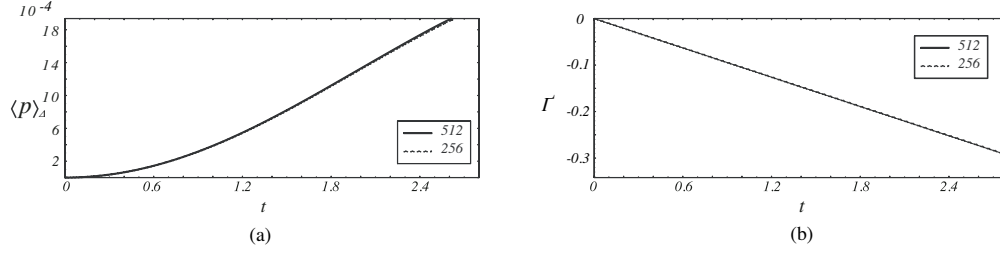


Figure 2.16: (a) Pressure jump and (b) total vorticity time history for the dam-break initial condition sketched in figure 2.11, in the time interval  $0s < t < 2.8s$  with 512 (solid line) and 256 (dotted line) vertical points resolutions. The initial velocities of the fluids are zero, the fluid densities are  $\rho_1 = .9$  and  $\rho_2 = 1$  and the height of the channel is fixed to 1.

Figure 2.16(a) shows the time evolution of  $\langle p \rangle_\Delta$ , from which we can see that  $\langle p \rangle_\Delta = 0$  and  $\partial_t \langle p \rangle_\Delta = 0$  at  $t = 0$ , validating our theoretical results. Here, as well as in figures 2.17 and 2.18, we perform numerical simulations with 256 and 512 vertical grid points, confirming that the time evolution is largely independent of resolutions. Figure 2.16(b) shows the total vorticity, exhibiting a linear behaviour of  $\Gamma$  near to  $t = 0$ , despite the fact that the pressure imbalance evolves from zero with zero slope. With the density parameters we have chosen in this section the value of the total vorticity obtained from this formula is  $\Gamma_t^{\text{dam}} = -1.05 \times 10^{-1}$ . The value obtained from the numerical simulation related to figure 2.16(b) is  $\Gamma_t^{\text{dam}} = -1.05 \times 10^{-1}$  which agrees rather well with the theory. Snapshots of fluid time evolutions are shown in figure 2.19.

### Asymptotic solutions: the hook case(s)

The first example is the case of figure 2.5, in which  $z_0 = z_3 = 0.5$ ,  $z_1 = 0.1$ ,  $z_2 = 0.9$ , and  $A_2 - A_1 = A_3 - A_2 = 1.5$ . We choose density parameters of the top and lower layers to be  $\rho_1 = 0.9$  and  $\rho_2 = 1.0$  so that the case qualifies small  $\rho_\Delta$  analysis discussed in Section 4.1. Figure 2.20 are snapshots of density profile up to time  $t = 2.8$ . Figures 2.17(a) and 2.17(b) show the pressure jump  $\langle p \rangle_\Delta$  and the total vorticity  $\Gamma$  for  $t = 0 \sim 2.8$ . The pressure jump is  $-4.95 \times 10^{-4}$  at  $t = 0$ , in reasonable quantitative

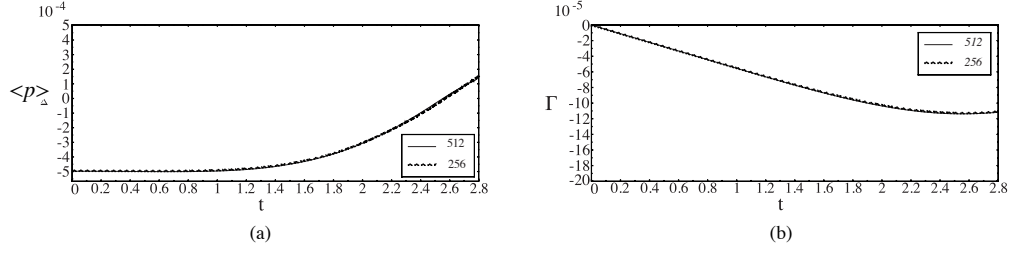


Figure 2.17: (a) Same as figure 2.16 but for the “hook with sliver” initial condition (figure 2.5) with  $z_0 = z_3 = 0.5$ ,  $z_1 = 0.1$  and  $z_2 = 0.9$ .

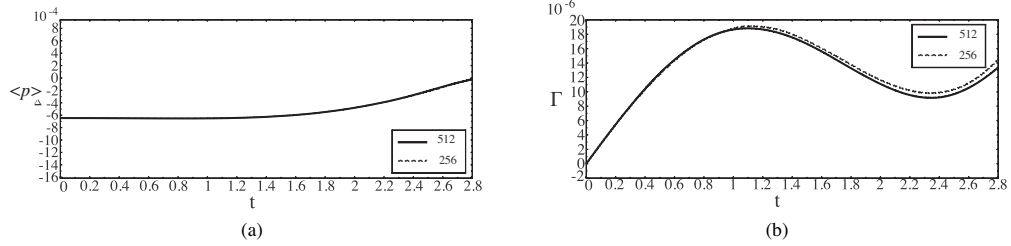


Figure 2.18: (a) Same as figure 2.16 but for “complete hook” initial condition (figure 2.5) with  $z_0 = z_3 = 0.5$ ,  $z_1 = 0$  and  $z_2 = 1$ .

agreement with equation (2.70), which predicts  $\langle p \rangle_\Delta \sim \rho_\Delta^2 \langle p^{(2)} \rangle_\Delta = -4.72 \times 10^{-4}$ . The total vorticity time derivative  $\Gamma_t = -5.49 \times 10^{-5}$  also shows a good agreement with equation (2.37), by which  $\Gamma_t \sim -5.25 \times 10^{-5}$ . Since in this case the interface does not reach either the top or the bottom of the channel, the pressure difference between the interacting points  $x_i^L$  and  $x_i^R$  is neglected. When  $t < 0.5$ , the pressure jump is almost constant and the total vorticity behaves linearly, which can be explained by  $\langle p \rangle_{\Delta t} = 0$  for  $t = 0$  in case of zero initial velocities. Next we let  $z_1 = 0$  and  $z_2 = 1$ , so that the interface touches the channel’s boundary. Figure 2.21 shows the snapshots of density profile for time between 0 and 2.8. At  $t = 0$ , the pressure jump (figure 2.18(a)) is  $-6.46 \times 10^{-4}$  and the total vorticity time derivative (figure 2.18(b)) is  $2.80 \times 10^{-5}$ . Equations (2.70) and (2.37) provide  $\langle p \rangle_\Delta \sim -6.13 \times 10^{-4}$  and  $\Gamma_t \sim 2.82 \times 10^{-5}$ . The error is consistent with a second order- $\rho_\Delta^2$  estimate when  $\rho_\Delta = 0.1$ . From the figures it is apparent that, in both the full hook and in the hook with slivers, the pressure imbalance  $\langle p \rangle_\Delta$  has initial zero time-derivative (this point is further taken on in § 2.7).

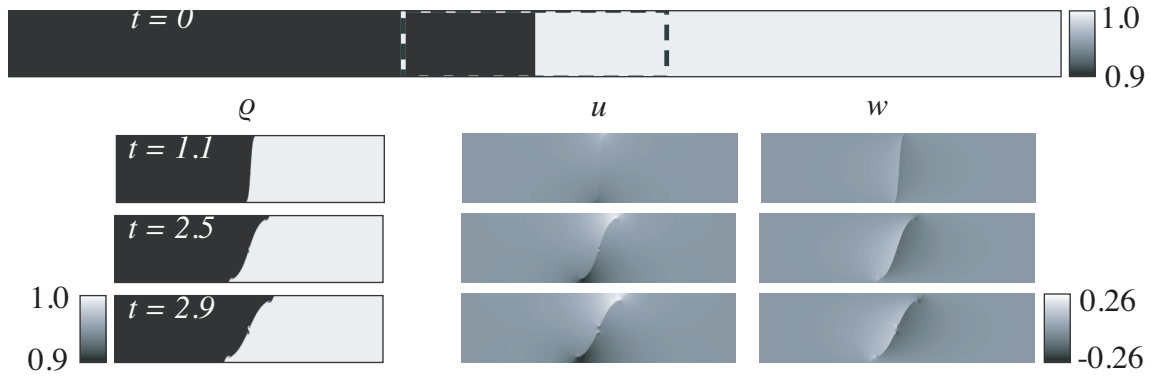


Figure 2.19: Snapshots of density  $\rho$  and velocities  $(u, w)$  (for horizontal and vertical component, respectively) for the time evolution of motion with the dam-breaking initial condition sketched in figure 2.11. Resolution is 512 vertical points, with physical parameters for this computation listed in the caption of figure 2.16. The initial density configuration is depicted in the top panel, which also illustrates the actual computational domain and its aspect ratio.

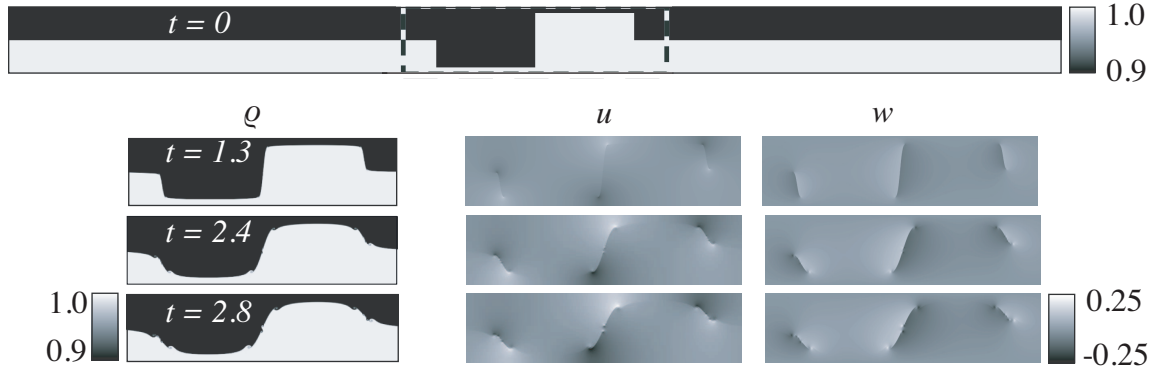


Figure 2.20: Same as figure 2.19 but for the “hook with sliver” initial condition case (figure 2.5). Physical parameters listed in caption of figure 2.17.

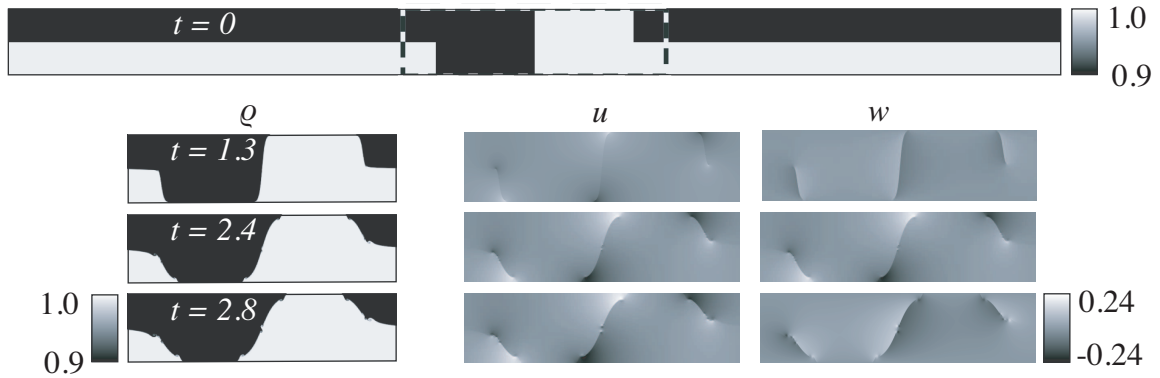


Figure 2.21: Same as figure 2.19 but for the “complete-hook” initial condition case (figure 2.5). Physical parameters listed in caption of figure 2.18.



Figure 2.22: Convergence of numerical algorithm for the “hook with sliver” initial data. Plotted here is the density difference at  $t = 2.8$ , generated by subtracting off the density from computations with 512 and 256 (vertical) nodes. Only the central portion (1/3 of the total length) of the channel is shown. For initial conditions that do not smooth the density jump, the resolution error becomes noticeable along the interface, where slight differences in its position in addition to numerical diffusion lead to nonzero density differences between the two computations.

We remark that we limited the time of evolution in all our numerical simulations to relatively short times, in order to maintain reasonable accuracy. An example of convergence for our numerical simulations is depicted in figure 2.22. As can be seen, the difference of two resolutions, 256 and 512 in the vertical directions, in the density field is maximal within a thin layer around the interface of the two fluids, not unexpectedly due to slight differences in the interface position and the effects of numerical diffusivity.

## 2.7 Time derivative of $\langle \mathbf{p} \rangle_{\Delta}$ at $t = 0$

The results of § 2.4 in general hold only when the velocity  $\mathbf{v}$  vanishes (the initial condition for all our numerical simulations). Here we consider the time derivative of  $\langle p \rangle_{\Delta}$  and show how the behaviour of our numerical simulations for small (but nonzero) time can be framed within our theoretical set-up.

The continuity equation implies that if  $\mathbf{v} = 0$  then  $\rho_t = 0$ . Differentiating the momentum equations with respect to time when  $\mathbf{v} = 0$  yields

$$\mathbf{v}_{tt} + \frac{1}{\rho} \nabla p_t = 0. \quad (2.87)$$

From incompressibility of the fluid we have that

$$\nabla \cdot \left( \frac{1}{\rho} \nabla p_t \right) = 0. \quad (2.88)$$

Therefore  $p_t$  satisfies the same equation as  $p$  but with *homogeneous* boundary conditions. Indeed,

$$\frac{\partial p_t}{\partial x} \rightarrow 0 \quad \text{as} \quad |x| \rightarrow \infty, \quad \frac{\partial p_t}{\partial z} = 0 \quad \text{at} \quad z = 0, h, \quad t = 0, \quad (2.89)$$

where we used again the fact that  $\rho_t = 0$  when  $\mathbf{v} = 0$ . If  $\rho$  is smooth, we can use Gauss theorem to obtain

$$\begin{aligned} 0 &= \int_{\mathbb{R} \times [0, h]} p_t \nabla \cdot \left( \frac{1}{\rho} \nabla p_t \right) dx dz \\ &= \int_{\mathbb{R} \times [0, h]} \left( \nabla \cdot \left( \frac{p_t}{\rho} \nabla p_t \right) - \frac{1}{\rho} |\nabla p_t|^2 \right) dx dz \\ &= \int_0^h \left( \frac{p_t}{\rho} p_{xt} \Big|_{x=+\infty} - \frac{p_t}{\rho} p_{xt} \Big|_{x=-\infty} \right) dz + \int_{-\infty}^{+\infty} \left( \frac{p_t}{\rho} p_{zt} \Big|_{z=0} - \frac{p_t}{\rho} p_{zt} \Big|_{z=h} \right) dx \\ &\quad - \int_{\mathbb{R} \times [0, h]} \frac{1}{\rho} |\nabla p_t|^2 dx dz. \end{aligned} \quad (2.90)$$

By using the vanishing Neumann boundary conditions, the first two integrals are zero and we obtain

$$\int_{\mathbb{R} \times [0, h]} \frac{1}{\rho} |\nabla p_t|^2 dx dz = 0. \quad (2.91)$$

Therefore  $\nabla p_t = 0$  and in particular its first component  $p_{xt}$  vanishes. Hence

$$\partial_t \langle p \rangle_{\Delta} = \int_0^h p_t \Big|_{x=+\infty} dz - \int_0^h p_t \Big|_{x=-\infty} dz = \int_0^h \left( \int_{-\infty}^{+\infty} p_{xt} dx \right) dz = 0. \quad (2.92)$$

Therefore, if at  $t = 0$ , the velocity data are  $\mathbf{v} = 0$ , then the time derivative of the pressure imbalance vanishes as well.

The presence of an interface implies a discontinuity in the density which requires some attention in applying Gauss theorem. For this, in analogy with what we have done in computing the time derivative of the total vorticity in § 2.2, we have to break the integration domain according to figure 2.2. The only new term in the integral (2.90) is given by the net flux through the interface between the two fluids

$$\int_{\gamma} \frac{1}{\rho_1} \frac{\partial p_t}{\partial n_1} d\sigma + \int_{\gamma} \frac{1}{\rho_2} \frac{\partial p_t}{\partial n_2} d\sigma \quad (2.93)$$

where  $n_1$  ( $n_2$ ) is the normal to the interface exterior to the domain of fluid with density  $\rho_1$  ( $\rho_2$ ), and integration is taken along the interface  $\gamma = \{(x, \eta(x)) \mid x \in \mathbb{R}\}$ . The boundary conditions on the interface given in (2.51) imply

$$\frac{1}{\rho_1} \frac{d}{dt} \frac{\partial p}{\partial n_1} = - \frac{1}{\rho_2} \frac{d}{dt} \frac{\partial p}{\partial n_2} \quad (2.94)$$

because  $n_2 = -n_1 \equiv n$ . Notice that the normal to the interface between the two fluids depends on time. However, when the velocity of the fluid is everywhere zero, the kinematic boundary condition reduces to  $\eta_t = 0$ , so that  $n_t = 0$ . Finally,

$$\frac{1}{\rho_1} \frac{\partial p_t}{\partial n_1} = - \frac{1}{\rho_2} \frac{\partial p_t}{\partial n_2} \quad (2.95)$$

and therefore the new interface contribution (2.93) is identically zero. Thus, for the special case of vanishing velocity initial condition,  $\partial_t \langle p \rangle_{\Delta} = 0$  at  $t = 0$ .

## 2.8 Conclusions

Total momentum conservation in the time-evolution of a stratified, incompressible ideal fluid is subject to a subtle interplay among boundary forces, incompressibility and inertia linked to the spatial extent of the fluid's domain. The case of an inhomogeneous,

laterally infinite fluid confined between two-horizontal rigid plates offers perhaps the simplest set-up to illustrate this interplay and remarked by Benjamin [5] in his study of Hamiltonian invariants. General formulae established by either approach suggest that horizontal momentum can fail to be conserved, even though only forces along the vertical direction act on such systems. These formulae connect momentum conservation to the pressure imbalance in the far field dynamics of the fluid, with the dynamics evolving from localized initial data and hydrostatic equilibrium enforced at infinity. While general plausibility arguments, together with long-wave model calculations and direct numerical simulations, certainly make a convincing case for the validity of the conclusions in the above studies, an explicit computation of such pressure imbalances has so far been lacking. In the present study we fill this gap by providing explicit examples.

Specifically, we have presented a systematic study of classes of initial data which allow closed-form expressions for pressure imbalances to be derived. In particular, we have examined in detail the case of zero initial velocities and two-fluid systems, showing that in this case the nonlocal pressure component arising from localized density displacements is the result of a Neumann-to-Dirichlet boundary map. In the limit of small density differences such map can be computed asymptotically, revealing non-intuitive properties of limiting configurations with simple piecewise constant initial conditions. (A similar analysis can be performed in the opposite limit  $\rho_1 \rightarrow 0$ , akin to an “air-water” system whenever air can be viewed as approximately incompressible, with some preliminary results in Appendix B). In particular, an exact expression shows that an internal “dam-breaking” problem, which leads to evolution of internal gravity currents, initially evolves maintaining constant horizontal momentum, as the total pressure imbalance is zero for such configuration.

Throughout our study, the long-wave models, and in particular the strongly non-



linear dispersive terms, have provided intuition, while correctly predicted scalings and parametric dependences for pressure imbalances for all the cases we have examined. Remarkably, qualitative and partially quantitative agreement continued to hold even when non-smooth data violated the asymptotic assumption that lay at these models' foundation. To this end, we have treated the technical point arising in connection with distributional derivatives due to density and velocity jumps. We have further shown how global-vorticity balance-laws for the class of initial data we have studied relate to pressure imbalances.

Lastly, in Appendix A we briefly discuss how our set-up can be framed within known variational principles. This allows a compact formulation of conservation laws through invariance under symmetry and Noether's theorem.

It is worth stressing again that in this study we have focussed on providing explicit expressions for the initial conditions we have examined. More general results along these lines of investigation properly pertain to mathematical analysis of general elliptic problems, and in particular to their Neumann-to-Dirichlet operators. These go beyond a fluid mechanical perspective, though nonetheless worth pursuing in future studies.

## Chapter 3

### AN EXTENDED APPLICATION FOR THE STRONGLY NONLINEAR INTERNAL WAVE MODELS

*This Chapter is collaborative work with*

*Wooyoung Choi, Tae-Chang Jo and Roxana Tiron.*

*(Article in preparation)*

#### 3.1 Introduction

*Synopsis:* Strongly nonlinear models of internal wave propagation for incompressible stratified Euler fluids are investigated numerically and analytically to determine the evolution of a class of initial conditions of interest in laboratory experiments. This class of step-like initial data severely tests the robustness of the models beyond their strict long-wave asymptotic validity, and model fidelity is assessed by direct numerical simulations (DNS) of the parent Euler system. It is found that the primary dynamics of near-solitary wave formation is remarkably well predicted by the models for both wave and fluid properties, at a fraction of the computational costs of the DNS code.

Large-amplitude internal waves are a common occurrence in many areas of the world oceans, and have been successfully observed and measured in both field and laboratory experiments. They occur in a stratified body of water under gravity whenever isolines of constant density are displaced from their equilibrium location. In fact, perhaps the simplest case for observing internal waves is perhaps when they occur at the a sharp

interface between two fluids of different densities. Scientific interests in internal waves are motivated by a myriad of applications, such as the need to quantify induced loads on submerged engineering constructions, as well as by the mathematical perspective of the need to understand the interplay between nonlinearity and dispersion which gives rise to a variety of nonlinear dispersive evolution equations in the discipline of hydrodynamics. Field observations report amplitudes of internal waves greater than 100 meters in fluid bodies of depth less than 1000 meters with wavelength of 1 to 10 kilometers (e.g., Apel *et al.* [2], Helfrich & Melville [24]). This is a highly nonlinear regime of wave motion, characterized by large amplitudes that are nevertheless of small slope.

While the main features of internal wave dynamics can be assumed to be governed by the stratified, incompressible Euler equations, such system is hardly amenable to analytical studies, and predictions based on it have to be extracted by numerical solutions. These are often costly, especially in fully three dimensional setting and when multidimensional parametric studies are needed to determine dynamical ranges, to the point of becoming prohibitive. An alternative approach is offered by strongly nonlinear long-wave asymptotic models which aim at retaining as much as possible of the dynamics from the parent Euler system, especially for large amplitude wave-propagation, while maintaining a relative simplicity which allows for some analytical results, such as traveling wave solutions, to be derived and studied.

A strongly nonlinear internal wave model have been derived (Miyata [34] [35], Choi & Camassa [15]) for large amplitude motion using long-wave asymptotics. This model consists of a set of coupled nonlinear equations evolving the layer-mean velocities, the interface displacement and the interfacial pressure. In finite domains, the strongly nonlinear model is unstable for large wave numbers because of the Kelvin-Helmholtz instability (Choi *et al.* [14]), an effect that needs to be addressed when implementing

numerical computations. One direct strategy is to apply a numerical low-pass filter to the system, an approach that allows the conserved quantities such as mass and energy to be well preserved for traveling wave solutions (Jo & Choi [26]). Another method is to regularize the model by introducing related variables for the horizontal velocities. It turns out that by choosing to work with the velocities at the top and bottom boundaries in place of their layer-mean counterparts has a beneficial effect on the high-wave number instability (Choi *et al.* [14]). Thus, the regularized model expands the stability regime of the strongly nonlinear model, and is able to sustain the solitary wave solutions from the strongly nonlinear model for quite long time due to their asymptotic equivalence.

Unlike KdV-type models as single equations, for which abundant mathematical results are known and been thoroughly carried out, studies of the strongly nonlinear internal wave model have been mostly limited to traveling wave solutions and it has not been broadly explored in dynamical time-dependent situations. The present work aims at filling this gap. In particular, we want to investigate motion emanating from initial conditions that do not necessarily respect the long-wave asymptotic of the model's derivation, in order to test the robustness and broad applicability of the model for practical applications.

Motivated by the laboratory work of Grue *et al.* [23], we concentrate on internal waves' generation from an internal dam-break problem, where the initial displacement of the interface is a step function. The details of the experiment are described in § 3.2. We then review the strongly nonlinear regularized models in § 3.3, along with their stability criteria. § 3.4 lays out numerical methods for the strongly nonlinear model, the regularized model as well as the direct Euler simulations. With the zero-flux constraint, the strongly nonlinear model can be reduced to a set of two nonlinear equations from a set of four. A filter is described to cure the instability in the strongly nonlinear model. The results from simulations are discussed in § 3.5. We study three cases

generating solitary waves with small, moderate and large amplitudes. Comparisons between models and Euler simulations are presented both in wave and fluid quantities. For large amplitude waves, the effect of the filter is important. In fact, our direct Euler simulations show that these are the regimes when Kelvin-Helmholtz instability also appears in the course of the evolution. We propose a possible method to choose the optimal filter for the long-wave models, and of course expect that the details of the Kelvin-Helmholtz dynamics, which occurs in the wake of the primary waves, can not be described by the model (captured at best in some form of spatial averages)

### 3.2 Motivations

The physical problem we are looking at is motivated by laboratory experiments (Grue *et al.* [23]) calibrated with a layer of fresh water above a layer of brine in a long rectangular tank. By adding a volume of fresh water behind a gate which is lowered at one end of the tank, a corresponding mass of the brine then slowly moves to the other side of the gate maintaining hydrostatic balance. By quickly removing the gate, an initial depression develops into a leading solitary wave propagating ahead of a transient dispersive wave train. Here we focus on the generations of solitary waves by applying long wave models. The experiments are based on a free-surface set-up. However, observations show that the free surface does not move substantially during the experiment, and enforcing a slip rigid wall boundary conditions at the upper layer simplified the numerical computation while keeping the general features of internal waves intact.

Long wave models are based on the long-wave shallow-water assumption, for which the typical wave length is much larger than the depth of each layer, and the slopes are assumed to be compatible with this small number. In this experiment, the initial condition certainly does not comply with this assumption at the step location. The no-

penetration boundary condition at the tank ends also need to be enforced. Because the model computation is essentially one dimensional in space, it is relatively inexpensive to use large computational domains, so that it is convenient to simply symmetrically extend the wave tank to double its length and enforce periodic boundary conditions. This exactly describes the reflection at the ends of the tank. To help the model in its first few time steps, the vertical interface displacement can be smoothed out with a suitable choice of smoothing functions, such as hyperbolic tangents.

With these assumptions for the model setup, we next explore how the strongly nonlinear wave model behaves in comparison with direct Euler simulations for the corresponding identical physical setup.

### 3.3 Mathematical models

#### 3.3.1 Governing equations

For an inviscid and incompressible fluid of density  $\rho$ , the velocity components in Cartesian coordinates  $(u, w)$  and the pressure  $p$  satisfy the continuity equation, the Euler governing equations are

$$u_x + w_z = 0, \quad (3.1)$$

$$u_t + uu_x + ww_z = -\frac{p_x}{\rho}, \quad (3.2)$$

$$w_t + uw_x + ww_z = -\frac{p_z}{\rho} - g, \quad (3.3)$$

$$\rho_t + u\rho_x + w\rho_z = 0, \quad (3.4)$$

where  $g$  is the gravitational acceleration. A two-layer fluid system with uniform densities in each layer can be assumed for smooth stratifications that satisfy a near two-layer configuration. This allows a substantial simplification, although it leads in general to a velocity discontinuity at the interface. In this case, the dynamic of waves is governed

by the Euler equations for the velocity components  $(u_i, w_i)$  and the pressure  $p_i$ , where  $i = 1(2)$  stands for the upper (lower) fluid and densities  $\rho_1 < \rho_2$  is assumed for a stable stratification. The boundary conditions at the interface are the continuity of normal velocity and pressure,

$$\zeta_t + u_1 \zeta_x = w_1, \quad \zeta_t + u_2 \zeta_x = w_2, \quad p_1 = p_2 = P \text{ at } z = \zeta(x, t), \quad (3.5)$$

where  $\zeta$  is the interface displacement. At the upper and lower rigid surfaces, the kinematic boundary conditions are given by

$$w_1(x, h_1, t) = 0, \quad w_2(x, h_2, t) = 0, \quad (3.6)$$

where  $h_1(h_2)$  is the undisturbed thickness of the upper (lower) fluid layer.

### 3.3.2 Strongly nonlinear internal wave model

The strongly nonlinear internal wave model for describing the interface displacement of a two-layer fluid system follows asymptotically from the long-wave assumption (Miyata [34], [35] and Choi & Camassa [15] ),

$$\eta_{i_t} + (\eta_i \bar{u}_i)_x = 0, \quad (3.7)$$

$$\bar{u}_{i_t} + \bar{u}_i \bar{u}_{i_x} + g \zeta_x = -\frac{P_x}{\rho_i} + \frac{1}{\eta_i} \left( \frac{1}{3} \eta_i^3 G_i \right)_x, \quad i = 1, 2 \quad (3.8)$$

where

$$\eta_1(x, t) = h_1 - \zeta(x, t), \quad \bar{u}_1(x, t) = \frac{1}{\eta_1} \int_{\zeta}^{h_1} u_1(x, z, t) dz, \quad (3.9)$$

$$\eta_2(x, t) = h_2 + \zeta(x, t), \quad \bar{u}_2(x, t) = \frac{1}{\eta_2} \int_{-h_2}^{\zeta} u_2(x, z, t) dz, \quad (3.10)$$

and  $G_i$  denotes the nonlinear dispersive effect:

$$G_i(x, t) = \bar{u}_{ixt} + \bar{u}_i \bar{u}_{ixx} - (\bar{u}_{ix})^2. \quad (3.11)$$

The model approximates the Euler equations with an error of  $O(\epsilon^4)$ , where  $\epsilon$  is the long-wave parameter defined by  $\epsilon = h_1/l$  and  $l$  is the typical wave length;  $h_2 = O(h_1)$  is assumed. This strongly nonlinear model is, however, accompanied by an undesirable tangential velocity discontinuity across the interface, which in turn introduces a jump in the horizontal velocity, implying that the time-dependent model initialized with a deformed interface could suffer from the Kelvin-Helmholtz instability when it is solved numerically. One can perform a local stability analysis to find the following criterion for stability (Liska, Margolin & Wendroff [32], Jo & Choi [26]):

$$U_0^2 \leq \frac{g(\rho_2 - \rho_1)(\rho_1 \alpha_1 \eta_2 + \rho_2 \alpha_2 \eta_1)}{\rho_1 \rho_2 \alpha_1 \alpha_2} \quad (3.12)$$

for each  $x$ , where

$$U_0 = |\bar{u}_1 - \bar{u}_2|$$

and  $\alpha_i = 1 + \frac{1}{3}k^2\eta_i^2$ . We note that there always exists an unstable mode  $k$  for all nonzero  $U_0$  since the righthand side of (3.12) vanishes as  $k \rightarrow \infty$ .

### 3.3.3 Regularized nonlinear long wave model

By taking velocities at the top and bottom boundaries,  $\hat{u}_1$  and  $\hat{u}_2$ , respectively (Choi *et al.* [14]), the strongly nonlinear model (3.7)-(3.8) can be regularized as

$$\eta_{i,t} + \left[ \eta_i \left( \hat{u}_i - \frac{1}{6}\eta_i^2 \hat{u}_{i,xx} \right) \right]_x = 0 \quad (3.13)$$



$$\hat{u}_{i,t} + \left( \frac{1}{2} \hat{u}_i^2 + g\zeta + \frac{P}{\rho_i} \right)_x = \left[ \frac{1}{2} \eta_i^2 (\hat{u}_{i,xt} + \hat{u}_i \hat{u}_{i,xx} - \hat{u}_{i,x}^2) \right]_x \quad (3.14)$$

With the same asymptotic behavior, the regularized model acquires a wider stable range with the following stability criterion:

$$U_0^2 \leq \frac{3g(\rho_2 - \rho_1)[\rho_1\eta_2(3 + \eta_1^2k^2) + \rho_2\eta_1(3 + \eta_2^2k^2)]}{\rho_1\rho_2(3 + \eta_1^2k^2)(3 + \eta_2^2k^2)}. \quad (3.15)$$

for each  $x$ , where now

$$U_0 = \hat{u}_2 - \hat{u}_1.$$

The regularized model is linearly stable for all wave number  $k$  when its shear velocity  $U_0$  satisfies

$$U_0^2 \leq \frac{g(\rho_2 - \rho_1)(\rho_2\eta_1 + \rho_1\eta_2)}{3\rho_1\rho_2} \quad (3.16)$$

when we consider the dynamics of long waves.

### 3.4 Numerical algorithms

We compare the strongly nonlinear internal wave models described above with full Euler simulations by adopting them to emulate the laboratory experiment described in § 3.2. A numerical filter is applied for the strongly nonlinear model and the regularized model whenever necessary in the time stepping of the algorithm.

#### 3.4.1 Direct numerical simulations for Euler equations

Solutions of the fully nonlinear Euler system for continuously stratified fluids are obtained using the numerical algorithm VarDen for variable density, constant viscosity, incompressible flow based on a second-order projection method (Almgren *et al.* [1]). By setting viscosity to zero and the allowing for only the external force of gravity, VarDen solves the incompressible Euler equations with variable density (3.1)-(3.4). The method

is based on a projection formulation, in which advection-diffusion equations are first solved to predict intermediate velocities, and then project these velocities onto a space of approximately divergence-free vector fields. The treatment of the first step uses a specialized second-order upwind method for differencing the nonlinear convection terms, which provides a robust treatment of these terms suitable for inviscid or high Reynolds number flow.

### 3.4.2 Strongly nonlinear model

As mentioned above, the symmetric extension of the wave tank is of great convenience for the numerical solution of the problem by reducing a four variable system to a coupled two-equation problem under the zero-flux horizontally assumption:

$$Q = \eta_1 \bar{u}_1 + \eta_2 \bar{u}_2 = 0 \quad (3.17)$$

for  $x \in [-L, L]$  and  $t \in [0, \infty)$ . While in general  $dQ/dt \neq 0$  (see Chapter 2), for symmetric initial data we know that the constraint flux-cons is maintained in time. With (3.17), and eliminating interface pressure  $P$  from (3.7)-(3.8), we get the reduced system in  $\zeta$  and  $\bar{u}_1$ :

$$\zeta_t - [(h_1 - \zeta)\bar{u}_1]_x = 0 \quad (3.18)$$

$$\mathcal{L}\bar{u}_{1t} = RHS \quad (3.19)$$

where  $\mathcal{L}$  is defined as

$$\mathcal{L} = f_1(x, t) + g_1(x, t) \frac{\partial}{\partial x} + h_1(x, t) \left( \frac{\partial}{\partial x} \right)^2, \quad (3.20)$$

with

$$f_1(x, t) = \rho_1 - \rho_2 + \rho_2 \frac{H}{\eta_2} + \frac{1}{3} \rho_2 H \left( \zeta_{xx} + \frac{\zeta_x^2}{\eta_2} \right), \quad (3.21)$$

$$g_1(x, t) = \rho_1 \eta_1 \zeta_x + \frac{1}{3} \rho_2 (3\eta_2 - H) \zeta_x, \quad (3.22)$$

$$h_1(x, t) = -\frac{1}{3} [\rho_1 \eta_1^2 + \rho_2 \eta_1 \eta_2], \quad (3.23)$$

and RHS is

$$\text{RHS}(x, t) = \text{RHS}_1(x, t) + f_2(x, t) \zeta_t + g_2(x, t) \zeta_{xt} + h_2(x, t) \zeta_{xxt} \quad (3.24)$$

with

$$\begin{aligned} \text{RHS}_1(x, t) &= (\rho_2 \bar{u}_2 \bar{u}_{2xx} - \rho_1 \bar{u}_1 \bar{u}_{1x}) + g(\rho_2 - \rho_1) \zeta_x \\ &\quad + \rho_2 \eta_2 \zeta_x (\bar{u}_2 \bar{u}_{2xx} - \bar{u}_{2x}^2) + \rho_1 \eta_1 \zeta_x (\bar{u}_1 \bar{u}_{1xx} - \bar{u}_{1x}^2) \\ &\quad + \frac{\rho_2 \eta_2^2}{3} (\bar{u}_2 \bar{u}_{2xx} - \bar{u}_{2x}^2)_x - \frac{\rho_1 \eta_1^2}{3} (\bar{u}_1 \bar{u}_{1xx} - \bar{u}_{1x}^2)_x \end{aligned} \quad (3.25)$$

and

$$f_2(x, t) = \frac{\rho_2 H \bar{u}_1}{\eta_2^2} + \frac{H \rho_2}{3} \left( \frac{2\bar{u}_1 \zeta_{xx}}{\eta_2} + \frac{\bar{u}_{1x} \zeta_x}{\eta_2} - \bar{u}_{1xx} \right), \quad (3.26)$$

$$g_2(x, t) = \frac{H \rho_2}{3} \left( \frac{\bar{u}_1 \zeta_x}{\eta_2} - 2\bar{u}_{1x} \right), \quad (3.27)$$

$$h_2(x, t) = -\frac{1}{3} \rho_2 H \bar{u}_1. \quad (3.28)$$

As described in § 3.2, the rigid wall boundary condition on the wave tank can be viewed as periodic boundary condition for the symmetric extended domain. A pseudo-spectral algorithm is implemented with fourth order Runge-Kutta time evolution and the nonlinear operator  $\mathcal{L}$  is solved through iteration by introducing the linear operator

$\bar{\mathcal{L}}$ :

$$\bar{\mathcal{L}} = \bar{f}_1 + \bar{g}_1 \frac{\partial}{\partial x} + \bar{h}_1 \left( \frac{\partial}{\partial x} \right)^2 \quad (3.29)$$

where  $\bar{f}_1$ ,  $\bar{g}_1$  and  $\bar{h}_1$  are the average values of  $f_1$ ,  $g_1$  and  $h_1$  over the computation domain  $[-L, L]$ , *e.g.*  $\bar{f}_1 = \frac{1}{2L} \int_{-L}^L f_1(x, t) dx$ . A standard iteration method is used for computing  $\bar{u}_{1t}$ .

### 3.4.3 Regularized model

The numerical algorithm for the regularized model has a layout similar to that of the strongly nonlinear model. We use

$$\zeta_t = \left[ \eta_1 \left( \hat{u}_1 - \frac{1}{6} \eta_1^2 \hat{u}_{1,xx} \right) \right]_x \quad (3.30)$$

for updating  $\zeta$  in time and use

$$\eta_1 \left( \hat{u}_1 - \frac{1}{6} \eta_1^2 \hat{u}_{1,xx} \right) + \eta_2 \left( \hat{u}_2 - \frac{1}{6} \eta_2^2 \hat{u}_{2,xx} \right) = 0 \quad (3.31)$$

and

$$\begin{aligned} & \rho_1 \left[ \hat{u}_{1,t} + \left( \frac{1}{2} \hat{u}_i^2 + g\zeta \right)_x \right] - \rho_2 \left[ \hat{u}_{1,t} + \left( \frac{1}{2} \hat{u}_i^2 + g\zeta \right)_x \right] \\ &= \rho_1 \left[ \frac{1}{2} \eta_1^2 \left( \hat{u}_{i,xt} + \hat{u}_i \hat{u}_{i,xx} - \hat{u}_{i,x}^2 \right) \right]_x + \rho_2 \left[ \frac{1}{2} \eta_2^2 \left( \hat{u}_{i,xt} + \hat{u}_i \hat{u}_{i,xx} - \hat{u}_{i,x}^2 \right) \right]_x \end{aligned} \quad (3.32)$$

for updating velocities. Taking time derivative in equation (3.31), we have

$$\eta_1 \left( \hat{u}_{1,t} - \frac{1}{6} \eta_1^2 \hat{u}_{1,txx} \right) + \eta_2 \left( \hat{u}_{2,t} - \frac{1}{6} \eta_2^2 \hat{u}_{2,txx} \right) = R_1 \quad (3.33)$$

where

$$R_1 = \zeta_t \left[ \left( \hat{u}_1 - \frac{1}{2} \eta_1^2 \hat{u}_{1,xx} \right) - \left( \hat{u}_2 - \frac{1}{2} \eta_2^2 \hat{u}_{2,xx} \right) \right]. \quad (3.34)$$

We solve equations (3.32)-(3.33) by using the iteration method described in Choi *et al.* [16].

#### 3.4.4 Artificial filter for long wave models

Keeping in mind that the mathematical wave model for the shallow configuration captures correctly the long wave behavior, it is justifiable to adopt a numerical filter to suppress the short-wave instability without affecting the long-wavelength behavior. This is equivalent to assuming that significant viscous dissipation occurs only in the high wave-number regime, and to this end we adopt the following smooth low-pass filter to keep unstable short-wavelength disturbances from growing:

$$f_k = \begin{cases} 1 & \text{for } k < k_{f_1} \\ \cos^2 \left[ \frac{\pi(k-k_{f_1})}{2(k_{f_2}-k_{f_1})} \right] & \text{for } k_{f_1} \leq k \leq k_{f_2} \\ 0 & \text{for } k_{f_2} \leq k \end{cases} \quad (3.35)$$

where  $k_{f_1} = 0.9k_{\text{critical}}$ , and  $k_{f_2} = \max\{C \cdot k_{\text{critical}}, k_{\text{upp}}\}$  with  $C$  and  $k_{\text{upp}}$  to be determined. These wave numbers are counted on the domain of length  $2\pi$ . In numerical computations with domain size of  $2L$ , waves numbers are converted by the condition  $K = \frac{L}{\pi}k$ . This filter is effective for ill-posed problems, in particular, propagation of traveling wave solutions for strongly nonlinear model as shown in (Jo & Choi [26]). In our problem, where short waves form rapidly at the beginning of the motion, the critical wave number  $k_{\text{critical}}$  depends on time. The choices of coefficients for  $k_{f_1}$  and  $k_{f_2}$  are rather arbitrary and are not based on an a-priori mathematical criterion. Experience shows that a minimal number of parameters molding the filters seems to suffice, and judge their effectiveness by monitoring diagnostically the most significant conserved quantities, such as the (physical) energy.

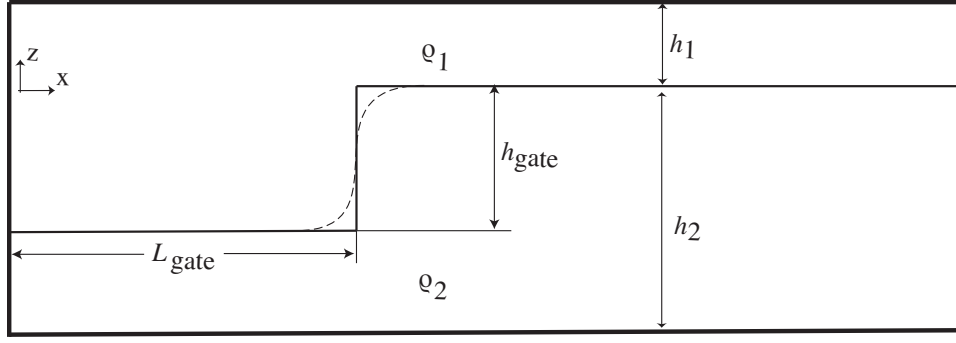


Figure 3.1: Dam-break experiment setup

### 3.5 Results

#### 3.5.1 Parameter set-up

We choose the physical parameters based on the laboratory experiment, for which  $\rho_1 = 0.999 \text{ g} \cdot \text{cm}^{-3}$ ,  $\rho_2 = 1.022 \text{ g} \cdot \text{cm}^{-3}$ ,  $h_1 = 15 \text{ cm}$ ,  $h_2 = 62 \text{ cm}$ ,  $g = 981 \text{ cm} \cdot \text{s}^{-2}$ , and the length of the wave tank is  $L = 2464 \text{ cm}$ . The initial condition is chosen to be a symmetric extension of the experimental setup (figure 3.1). Further, to eliminate the stiffness of the step function, the jump of interface  $\zeta$  is smoothed out by a hyperbolic tangent function (figure 3.2). The initial condition for the model is

$$\zeta(x, 0) = \frac{h_{\text{gate}}}{2} \tanh[\lambda(x - L_{\text{gate}})] + \frac{h_{\text{gate}}}{2} \tanh[\lambda(x + L_{\text{gate}})], \quad (3.36)$$

where  $x \in [-L, L]$ . When  $\lambda = 0.1$ , the transition length  $l$  is 29 cm to achieve 10% and 90% of  $h_{\text{gate}}$ . When  $\lambda = 0.2 \text{ cm}^{-1}$ , the according transition length is 15 cm. We typically choose the length of the gate to be  $L_{\text{gate}} = 100 \text{ cm}$  and the height of the gate  $h_{\text{gate}}$  varies among 10, 20 and 50 cm representing small, moderate and large amplitude waves. For VarDen simulations, we only need the right half of the domain and the initial condition needs the prescription of density,

$$\rho(x, z, 0) = \rho_2 - \frac{\rho_2 - \rho_1}{2} [\sigma(z - \zeta(x, 0))], \quad (3.37)$$

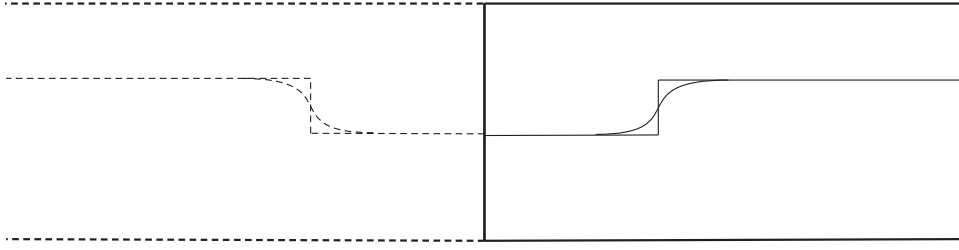


Figure 3.2: Initial condition for long wave models by a symmetric extension of the wave tank and smoothed gate.

where

$$\zeta(x, 0) = \frac{h_{\text{gate}}}{2} \tanh [\lambda(x - L_{\text{gate}})]. \quad (3.38)$$

Here  $\sigma = 0.5 \text{ cm}^{-1}$  so that the thickness of the transition layer is about 4 cm comparing to a tank of total height of 77 cm. We label our simulations in table 3.1 for different choices of  $h_{\text{gate}}$ . The full Euler simulations are done with VarDen on a cluster with parallel processors.

Figure 3.3 (a) and (b) are snapshots for runs H10LD1 and H50LD1, respectively. In H10LD1, there is no apparent instability. A solitary wave begins to emerge from  $T = 69 \text{ s}$ . In H50LD1, Kelvin-Helmholtz roll-ups appear quite early. The front wave travels fast, forming a solitary wave with large amplitude and leaving the roll-ups behind.

To link the two-layer system with its continuously stratified counterpart, we reparameterize the three physical parameters (top and bottom densities and quiescent-state interface position) of the two layer system to values informed by the continuous stratification. This is done by matching the linearized phase speed and optimizing the potential energies and masses of upper and lower layers. The strongly nonlinear model with the set of optimized parameters greatly improves the agreement for the traveling wave solutions between the strongly nonlinear model's and the Euler system's solutions.

Table 3.1: Labels for numerical runs with different parameters

$h_{\text{gate}}$ (cm)	$\lambda = 0.1 \text{ cm}^{-1}$	$\lambda = 0.2 \text{ cm}^{-1}$	$\lambda = \infty$
10	H10LD1	H10LD2	H10LD9
20	H20LD1	H20LD2	H20LD9
50	H50LD1	H50LD2	H50LD9



Figure 3.3: Snapshots of VarDen simulations. Top: H10LD1; bottom: H50LD1



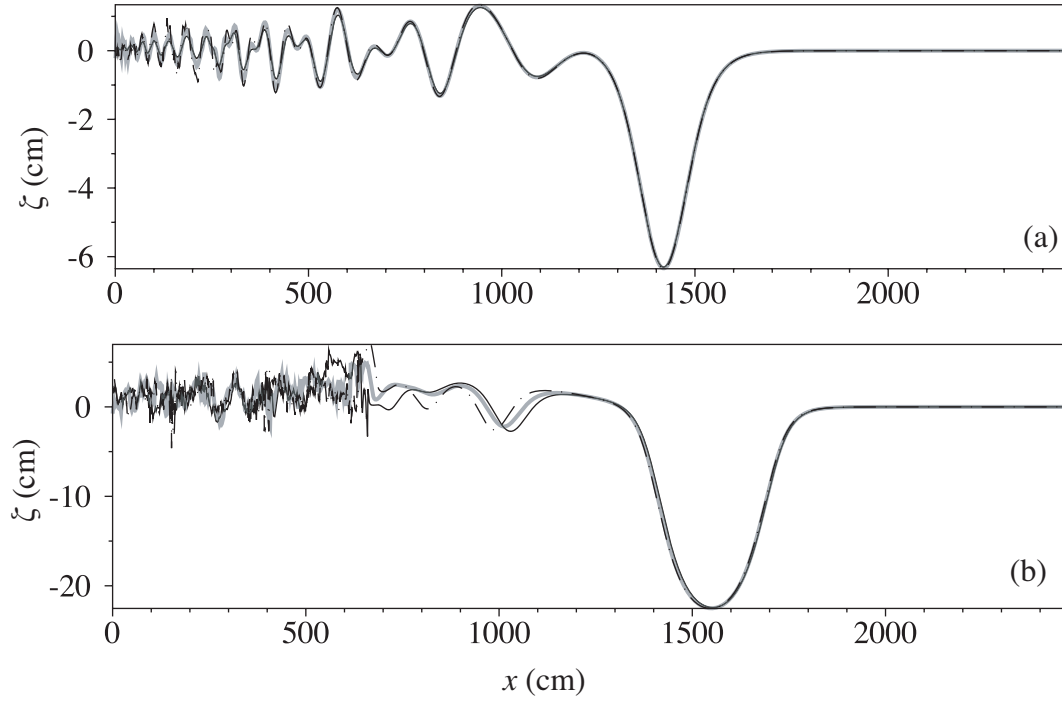


Figure 3.4: Snapshots at  $T = 80$  s from VarDen simulations with different  $\lambda$ , corresponding to different smoothing effect for runs H10's (a) and H50's (b). Solid black:  $\lambda = 0.1 \text{ cm}^{-1}$ ; solid gray:  $\lambda = 0.2 \text{ cm}^{-1}$ ; dash-dot black:  $\lambda = \infty$  (no smoothing).

### 3.5.2 The effect of gate smoothing

The laboratory experiments are performed with the gate forming a jump displacement of the interface, while the model needs to handle smooth initial conditions. For small and moderate amplitude waves, the VarDen simulation appears to be identical for the mean density isopycnocline in runs H10s and H20s with different choices of  $\lambda$  (figure 3.4). For the large amplitude waves, however, different smoothing choices do have an effect on the secondary wave. Nonetheless, this differences are far less than that from long wave models to VarDen simulations as we will see in § 3.5.5. Therefore, we conclude that it is sufficient to use the smoothed gate with  $\lambda = 0.1$  for the long wave model initial conditions.

### 3.5.3 Small amplitude waves

Figure 3.5 is the snapshot of runs H10LD1 at  $T = 80$  s. For the Euler simulation, we interpolate to get the isopycnocline of the mean density  $\rho_{\text{mid}} = \frac{1}{2}(\rho_1 + \rho_2)$  as the interface displacement. VarDen simulations are run on a square grids with 512 points on the vertical direction. By doubling and halving the grid points, we conclude that the mean density isopycnocline is accurate with relative error  $1e - 2$  measured in the sup-norm. For the strongly nonlinear and the regularized models, we typically choose the number of grid points  $N = 8192$  over the extended domain and  $\Delta t = 0.01$  s. For the strongly nonlinear model, the filter is applied every 0.01 second while the regularized model can run without instabilities without applying the filter. We test the convergence by half and double grid points, and half and double time-step. The relative accuracy is within  $8e - 5$  for the strongly nonlinear model and  $2.5e - 2$  for the regularized model in the sup-norm. The strongly nonlinear model achieves better accuracy because the higher modes are filtered away.

In runs H10LD1, both models show good agreement with the VarDen simulation by capturing the amplitude and phase of the front wave, with the strongly nonlinear wave model being a better match, even agreeing for a large portion of the dispersive tail (figure 3.5) where we expect to see discrepancies owing to the presence of short waves and possible influence of dissipation from the filter. The primary waves from both strongly nonlinear and regularized models are in good agreement with those from the VarDen simulation. The amplitude of the primary wave from the strongly nonlinear model is slightly smaller than that from the VarDen simulation, while the opposite is true for the regularized model. The differences in amplitudes of primary waves between VarDen simulation and models are within 5% and 8% for the strongly nonlinear model and the regularized model, respectively. The phases of primary waves for VarDen simulation and the strongly nonlinear model has an excellent agreement with less than

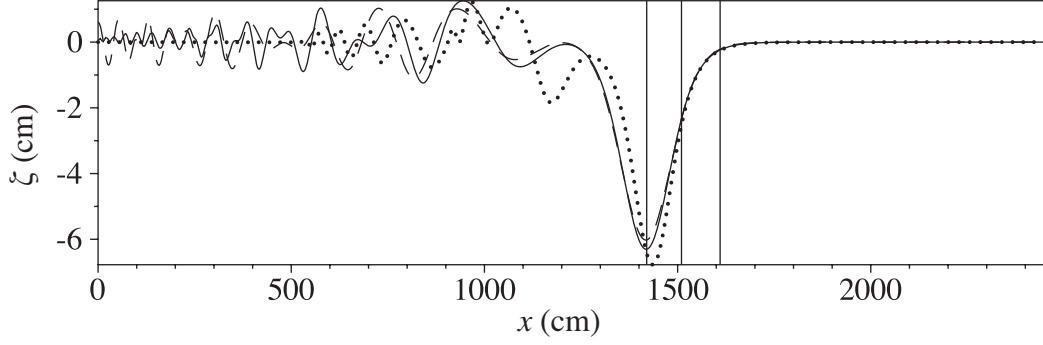


Figure 3.5: Snapshot of H10LD1 at  $T = 80$  s. Solid: mean density isopycnocline from VarDen simulation; dashed: strongly nonlinear model; dotted: regularized model. The three vertical lines are at locations  $x = 1420, 1510$  and  $1610$  cm

0.1% difference. The phase difference between VarDen simulation and regularized model is also small as shown in table 3.2. The primary wave speed agrees well with both two-layer models.

High wave modes act as dissipation in long wave models when the stability criteria are not satisfied. The filter, by cutting off unstable modes, reduces dissipation so as to prevent excessive energy loss. We record the total energy along with time evolutions. The strongly nonlinear model (with no filter) has an exact energy expression,

$$E = \frac{1}{2} \int \left[ g(\rho_2 - \rho_1) \zeta^2 + \sum_{i=1,2} \rho_i \left( \eta_i \bar{u}_i^2 + \frac{1}{3} \eta_i^3 \bar{u}_{i,x}^2 \right) \right] dx, \quad (3.39)$$

which is conserved. The regularized model, on the other hand, does not seem to have an explicit conserved energy quantity, however it is expected to conserve the physical energy to within asymptotic accuracy. Thus, this pseudo-energy for the regularized model,

$$E_{\text{pseudo}} = \frac{1}{2} \int \left[ g(\rho_2 - \rho_1) \zeta^2 + \sum_{i=1,2} \rho_i \eta_i \left( \hat{u}_i^2 + \frac{1}{3} \eta_i^2 (\hat{u}_{i,x}^2 - \hat{u}_i \hat{u}_{i,xx}) \right) \right] dx, \quad (3.40)$$

is a time-dependent quantity. Denoting  $E_0$  as the total energy at  $T = 0$  s for each

simulations, and  $E(t)$  as the energy at time  $t$ , after  $T = 80$  s the normalized energy loss  $\delta E/E_0 = (E(t) - E_0)/E_0$  appears to be much smaller for the strongly nonlinear model with  $6.4e - 7$  than for the regularized model with  $1.5e - 2$ , whereas the VarDen simulation only introduces  $9e - 10$  of normalized energy loss (figure 3.6).

A remark is in order on the robustness of the filtering effect. For the strongly nonlinear model, different filters are attempted. The upper limits of  $K_{\text{upp}}$  are chosen to vary from 0 to 3000 (corresponding to  $k_{\text{upp}} = 3.8$  wave numbers in the normalized form). The frequencies of applying the filters varies between every 0.01 and 0.1 second. The relative difference among different filters are  $7e - 3$  for the interface displacement  $\zeta$  measured in sup-norm.

#### 3.5.4 Moderate amplitude waves

For the H20LD1 case, the snapshots at  $T = 80$  s are shown in figure 3.7. Similar to runs H10LD1, the primary wave from the VarDen simulation is well captured by the strongly nonlinear model with relative amplitude difference of 5% and relative phase difference of 0.28%. The regularized model has a slightly larger amplitude, with relative difference of 4.1%, and travels a bit faster with a 0.83% relative phase difference. Once again, in this run the filter is only applied for the strongly nonlinear model. From figure 3.6, we notice that the energy loss for the VarDen simulation gets  $6e-8$  at  $T = 80$  s. The energy loss from models also has an increment compared with runs in H10LD1, but the scaling remains similar.

#### 3.5.5 Large amplitude waves

The run H50LD1 is a case when the real Kelvin-Helmholtz instability occurs, as displayed by figure 3.3 (b). The instability is numerically challenging for the VarDen simulation in order to achieve the desired accuracy. By halving the grids, with 512 and

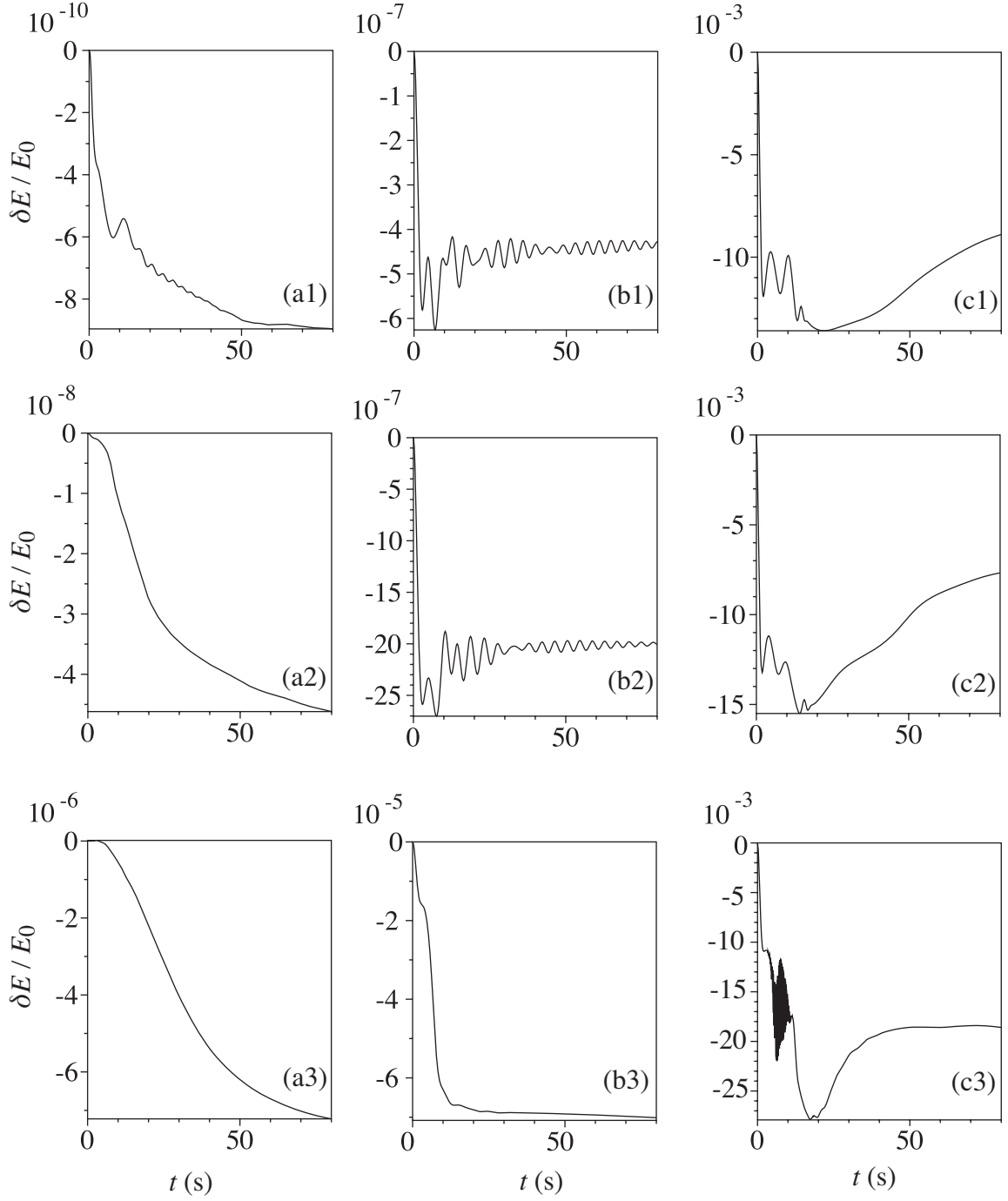


Figure 3.6: Time series of relative energy loss from VarDen simulations (a1, a2, and a3), the strongly nonlinear model (b1, b2, b3), and the regularized model (c1, c2, c3), with number 1, 2 and 3 denoting runs H10LD1, H20LD1 and H50LD1, respectively.

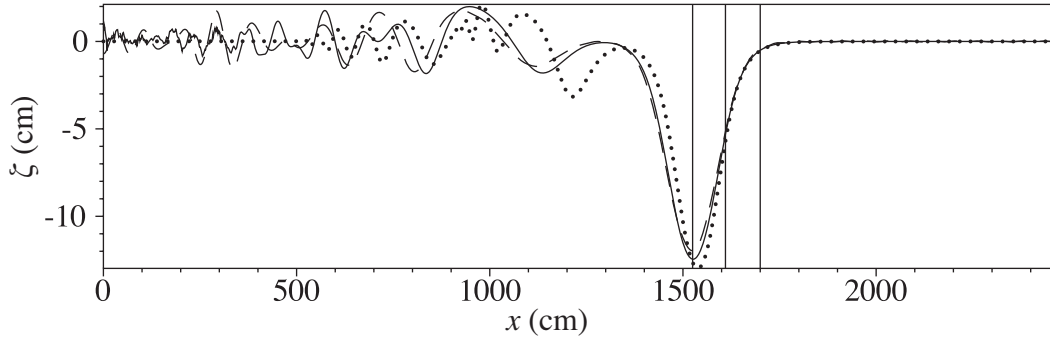


Figure 3.7: Snapshot of H20LD1 at  $T = 80$  s. Solid: isopycnocline of the mean density from VarDen simulation; dashed: strongly nonlinear model; dotted: regularized model. The three vertical lines are at locations  $x = 1525$ ,  $1610$  and  $1700$  cm.

Table 3.2: Numerical values for amplitudes  $a$  and phases  $X$  of the primary wave from VarDen simulation, the strongly nonlinear model and the regularized model for runs H10LD1, H20LD1 and H50LD1 at  $T = 80$  s.

	H10LD1		H20LD1		H50LD1	
	$a$ (cm)	$X$ (cm)	$a$ (cm)	$X$ (cm)	$a$ (cm)	$X$ (cm)
VarDen	-6.306	1418.8	-12.456	1526.2	-22.440	1552.9
Strongly	-6.024	1417.9	-11.837	1522.0	-21.556	1556.2
Regularized	-6.775	1435.3	-12.979	1538.8	-22.330	1546.6

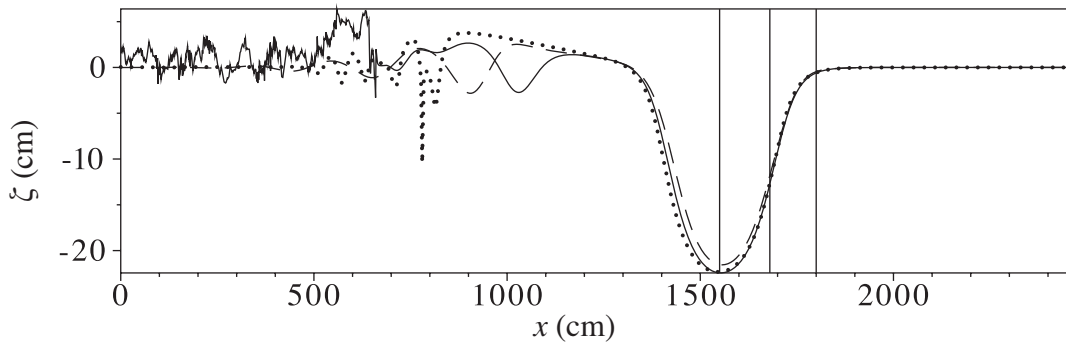


Figure 3.8: Snapshot of H50LD1 at  $T = 80$  s. Solid: isopycnocline of the mean density from VarDen simulation; dashed: strongly nonlinear model; dotted: regularized model. The three vertical lines are at locations  $x = 1550$  cm,  $1610$  cm and  $1800$  cm

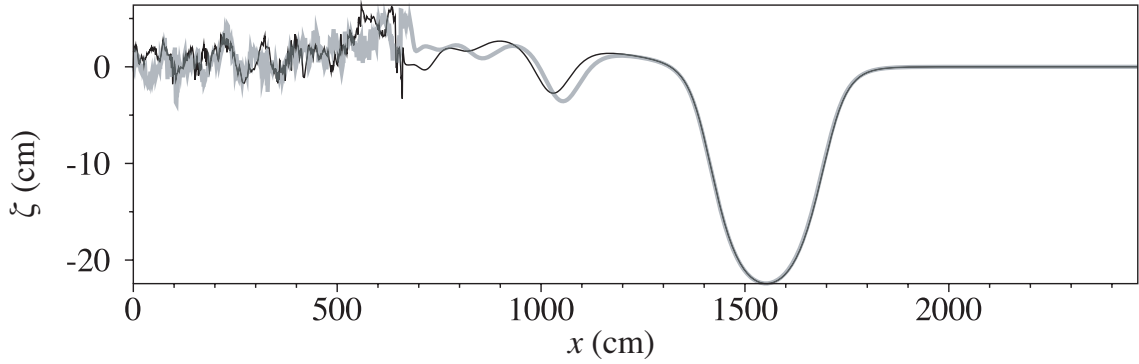


Figure 3.9: Convergence study for run H50LD1 in VarDen simulations with different resolutions. Black:  $nz = 512$ ; gray:  $nz = 1024$ , with the grid points at the vertical direction.

1024 grid points on the vertical directions, the discrepancy in the secondary wave is visible (figure 3.9). To resolve the issue of convergence of the simulation for this secondary wave, it would be necessary to run the code on a significantly higher resolutions which becomes too expensive. However, if we still place our emphasis on the primary wave it is clear that 1024 grid points on the vertical direction is sufficient to provide a reliable reference.

For run H50LD1, numerical filters are required for both the strongly nonlinear and the regularized models. For the latter, the solution is robust with respect to different choices of the filter, while for the strongly nonlinear model the solution is somewhat sensitive to the choices. In § 3.5.6, we describe how the choice of  $K_{\text{upp}} = 500$  and  $C = 1.3$  is optimal in this case. With the optimal filter, the strongly nonlinear model captures the amplitude by a relative difference with 2.1%. The regularized model is about twice this difference at 4.9%. The phase differences are 0.2% and 0.4% for the strongly nonlinear model and the regularized model, respectively.

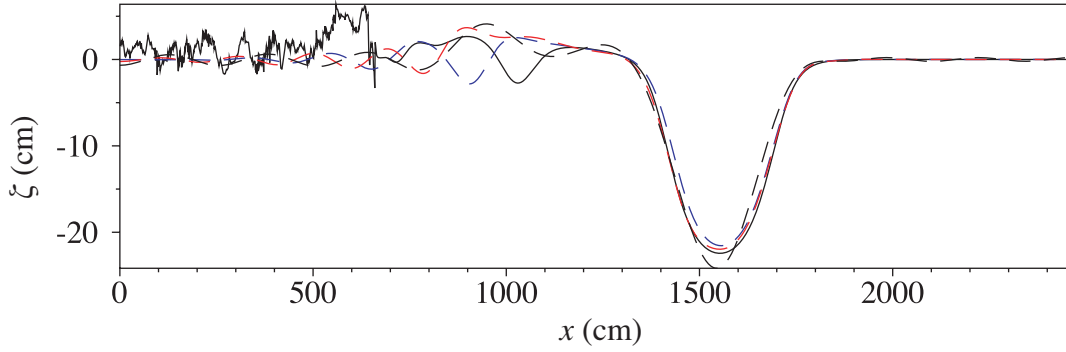


Figure 3.10: Solutions from the strongly nonlinear model for run H50LD1 with fixed  $C = 1.3$  and different  $K_{\text{upp}}$  at  $T = 80$  s. Solid: mean density isopycnocline from VarDen simulation; dashed black:  $K_{\text{upp}} = 0$ ; dashed blue:  $K_{\text{upp}} = 500$ ; dashed red:  $K_{\text{upp}} = 900$ .

### 3.5.6 Choice of the optimal filter

The numerical filter is applied to the strongly nonlinear model for all three runs and to the regularized model for the high amplitude run H50LD1. We tested the different parameters in the filter ( $k_{\text{upp}}$  and  $C$ ), and found that the solution is robust for small and moderate amplitude waves. When the amplitude gets bigger, choices of  $k_{\text{upp}}$  can become more critical for obtaining consistency of amplitude, phase, and shape for the front waves.

Figure 3.10 is the solution from the strongly nonlinear model for runs H50LD1, with different choices of  $K_{\text{upp}}$  values. For  $K_{\text{upp}} = 500$ , the front wave shows good agreements with the VarDen simulation. For the solution with  $K_{\text{upp}} = 0$ , the front wave is larger but narrower, while for  $K_{\text{upp}} = 900$ , the amplitude of the front wave is smaller than the VarDen simulation. The choices of  $K_{\text{upp}}$  also affect the relative energy loss (figure 3.11). We notice that for  $K_{\text{upp}} = 0, 100, 300$  and  $500$ , the energy loss is within a similar range, while for  $K_{\text{upp}} = 700$  and  $900$ , the energy loss is increasing with the increment of  $K_{\text{upp}}$ . Based on this,  $K_{\text{upp}} = 500$  seems to be an optimal choice for the upper bound for the filter. Fixing  $K_{\text{upp}} = 500$ , we alter the value of  $C$  among 1.1, 1.3 and 1.5. The solution appears to be identical and so does the energy loss, and we conclude that the



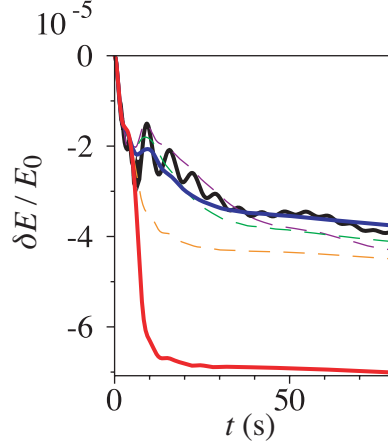


Figure 3.11: Time series of relative energy loss for the strongly nonlinear model with fixed  $C = 1.3$  and different  $K_{\text{upp}}$ . Solid black:  $K_{\text{upp}} = 0$ ; solid blue:  $K_{\text{upp}} = 500$ ; solid red:  $K_{\text{upp}} = 900$ ; dashed purple:  $K_{\text{upp}} = 100$ ; dashed green:  $K_{\text{upp}} = 300$ ; dashed orange:  $K_{\text{upp}} = 700$ .

solution is insensitive to these parameters.

### 3.5.7 Primary wave forming solitary waves

The primary waves emerging from the time evolution appears to travel steadily without significant deformations. We extract data from the right sides of the primary waves at different times ( $T = 60, 80$  and  $100$  s), and compare them with the closed-form traveling wave solution from the strongly nonlinear model, by matching the amplitudes at  $T = 100$  s (figure 3.12). Note that the left parts of the primary waves are still evolving, separating solitary waves from dispersive tails.

The front waves emerging from the strongly nonlinear model simulations have already settled to the traveling wave solution for runs H10LD1 and H20LD1. On the other hand, more time may be necessary for run H50LD1 in order for the primary wave to settle close to a solitary traveling wave. We tested this tendency by comparing the difference between snapshots at  $100$  s and at  $80$  s, which looks smaller than that between snapshots at  $80$  s and  $60$  s. The primary waves from the regularized model is also compared with the traveling wave solution from the strongly nonlinear model

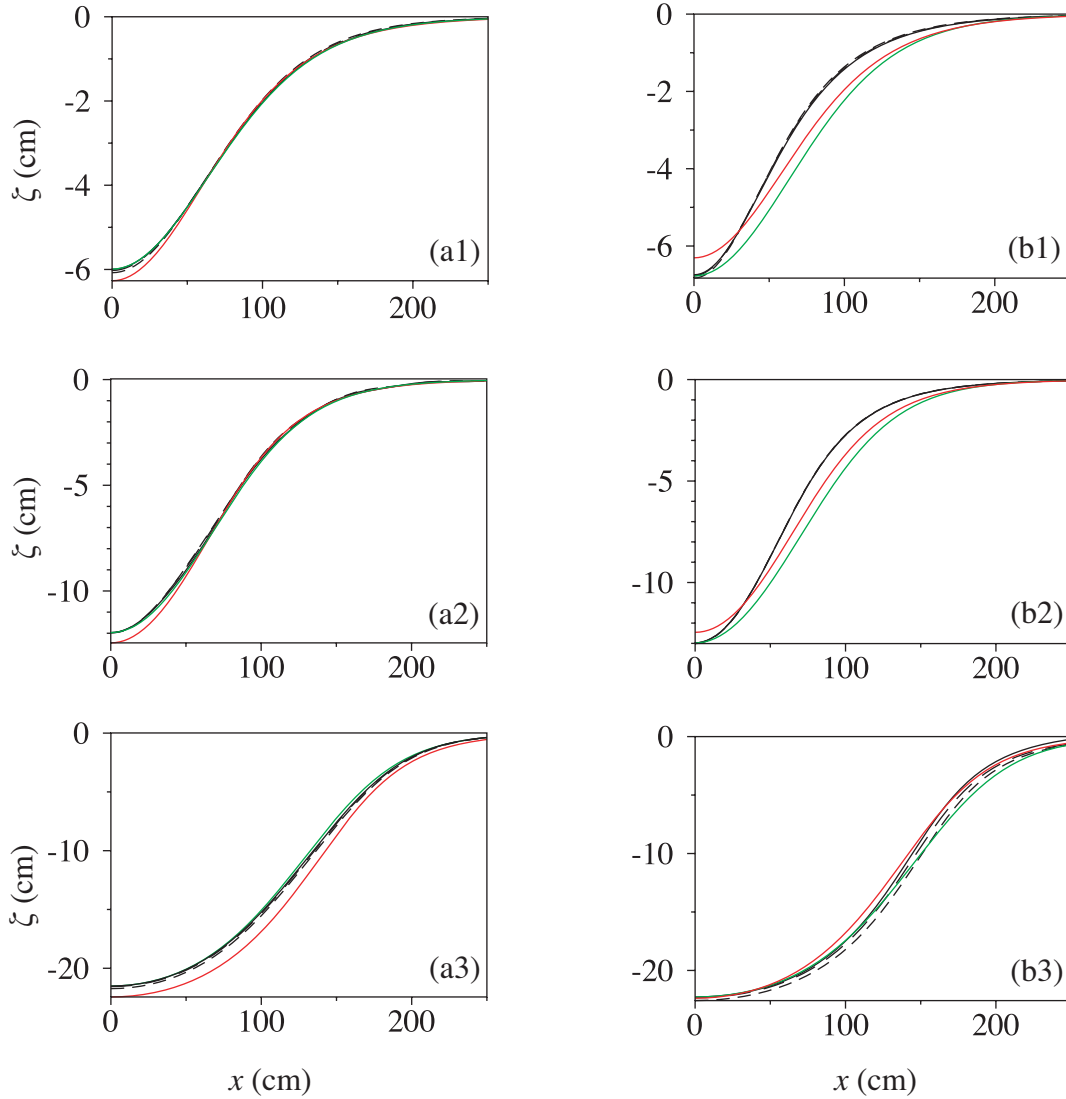


Figure 3.12: The front half of the primary waves from models at time  $T = 60$  s (black short-dashed),  $T = 80$  s (black long-dashed) and  $T = 100$  s (black solid), VarDen simulations at  $T = 100$  s (red solid) traveling wave solutions from the strongly nonlinear model with matching amplitude at  $T = 100$  s (green solid). (a1), (a2) and (a3) are from the strongly nonlinear model for runs H10LD1, H20LD1 and H50LD1; (b1), (b2) and (b3) are from the regularized model for the same runs.

by matching amplitudes. In all three runs, the primary waves are settling down by comparing snapshots at different times. Front waves from the VarDen simulations at  $T = 100$  s are also recorded. The shapes of the strongly nonlinear model appear to better match the Euler solutions for small and moderate amplitude waves, whereas this advantage is somewhat lost for runs H50LD1. In all three cases, the regularized model provides deeper and narrower front waves.

We also track the time history of the peak of the primary waves. Figure 3.13 are plots of the amplitudes and phase locations of the wave peaks from the strongly nonlinear model and the Euler solutions. We notice that the amplitudes of the wave peaks decrease during the evolutions and show a trend of settling to a fixed value, which should be the amplitude of the solitary wave. The strongly nonlinear model always have a smaller amplitude than the Euler simulations. The phase locations of the two are very close.

### 3.5.8 Horizontal shear velocity reconstruction

Besides wave profiles, the models also provide fluid velocity information which can be reconstructed from the long wave assumption. The horizontal velocity  $z$ -dependence can be reconstructed to order  $O(\epsilon^4)$  at fixed  $x$  location by using  $\bar{u}_i$  in the strongly nonlinear model (Camassa *et al.* [10])

$$u_i(x, z, t) = \bar{u}_i(x, t) + \left( \frac{(\eta_i(x, t))^2}{6} - \frac{(h_i \mp z)^2}{2} \right) \partial_x^2 \bar{u}_i(x, t), \quad (3.41)$$

and by  $\hat{u}_i$  in the regularized model,

$$u_i(x, z, t) = \hat{u}_i(x, t) + \left( \frac{(\eta_i(x, t))^2}{2} - \frac{(h_i \mp z)^2}{2} \right) \partial_x^2 \hat{u}_i(x, t), \quad (3.42)$$

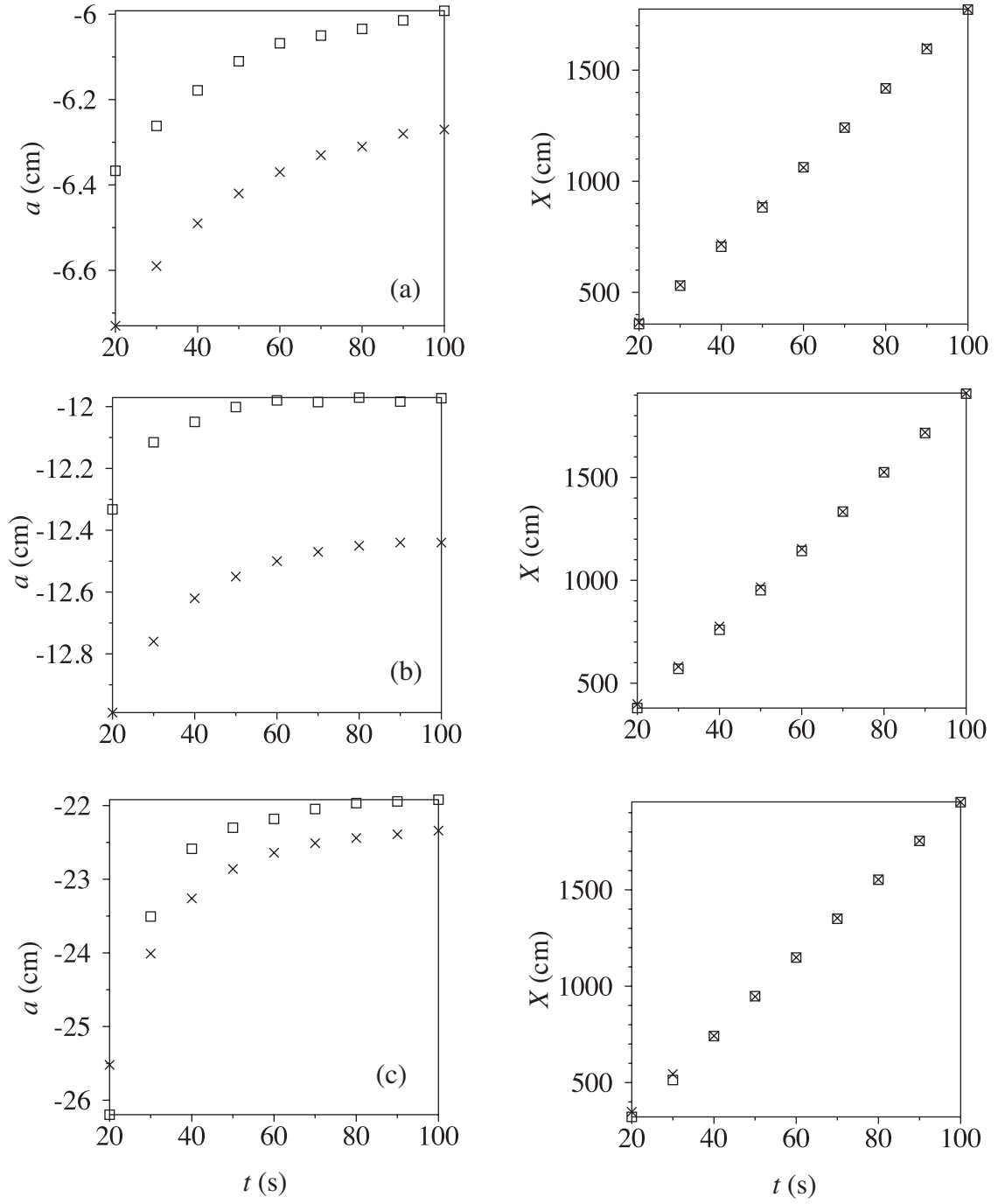


Figure 3.13: Amplitudes (left) and phase locations (right) of the wave peak for H10LD1 (a), H20LD1 (b) and H50LD1 (c). Square: the strongly nonlinear model; cross: VarDen simulation

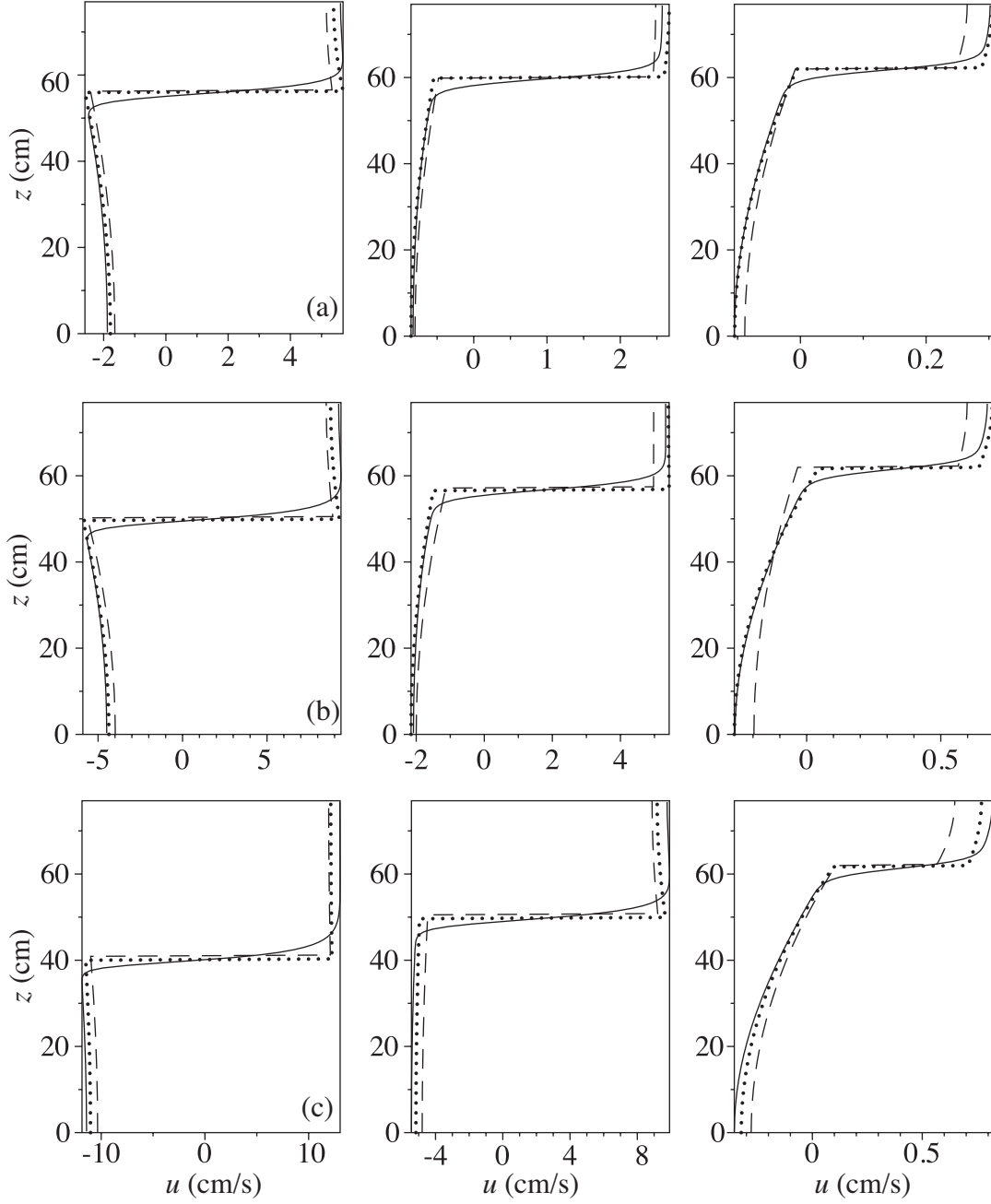


Figure 3.14: Horizontal shear velocities reconstructions for runs H10LD1 (a), H20LD1 (b) and H50LD1 (c) at locations noted in figures 3.5, 3.7 and 3.8.

Shear velocities are reconstructed through (3.41) and (3.42) from both the strongly nonlinear model and the regularized model. We choose three locations for each runs: at the crest, the inflection point and the very front of the primary waves. The regularized model seems to match better with the VarDen simulations for all three runs. Though the origin of this increased accuracy is not clear, this might be due to the vigorous filter applied to the strongly nonlinear model which results in an additional slowing down of the flow.

### 3.6 Discussion

The application of the strongly nonlinear model and its regularized companion are extended to simulate a laboratory experiment that can be described as a dam-break problem for internal waves. This initial state does not satisfy the long wave assumption and hence constitutes a severe test for models' predictive capability and robustness. The rigid wall boundary condition for the wave tank is transferred to the long wave models by symmetrically extending the wave tank, which allows the use of periodic boundary conditions. The gate-introduced step-function of the interface displacement is smoothed out to carry out numerical computations of long wave models, and its analog is used for the full Euler (DNS) simulations. We compare solutions from long wave models with DNS simulations using the algorithm VarDen to validate the model.

The ill-posedness of the strongly nonlinear model induced by the shear instability is treated with a numerical filter adjustable along with the time evolution. The regularized model partially cures the instability by writing the model in terms of horizontal velocity at the top and bottom boundary instead of the mean velocities of each layer.

We compare the models with the Euler simulations by taking snapshots of the interface displacements and by recording the time series of energy loss. The strongly nonlinear model presents excellent agreements for the small and moderate amplitude

waves by well capturing the shape, amplitude and phase of the primary wave, while the regularized model, albeit also showing good agreement, generates waves traveling slightly faster and manifesting deeper but narrower fronts. The case with large amplitude waves, however, is challenging for the strongly nonlinear model because the solution becomes somewhat sensitive to the choice of the filter, and an optimal choice becomes necessary. In this case, the regularized model seems preferable over the strongly nonlinear model even when the optimal filter is used. Both models show the tendency of the primary waves beginning to settle to a solitary wave, as seen by comparing their fronts at a series of time snapshots to the closed-form traveling wave solutions of the strongly nonlinear model. Besides wave profile, we also reconstruct the shear velocity of the front waves, a quantity that can be important in applications. The regularized model presents better agreement with the VarDen simulations than the regularized model for this variable, possibly due to the more vigorous application of the numerical filter necessary for large waves.

With good agreements at hand, we still cannot downplay the remaining questions for extending the applications of the long wave models. Just like the two-layer parent Euler system, the ill-posedness of the strongly nonlinear model presents a problem for the optimal choice of filters. We have presented a possible way to monitor a choice effectiveness by looking at the time series of energy loss, and a more systematic study using this diagnostic tool may be possible to explore different filtering algorithms. This might have to be tailored to information provided by the initial conditions. A better understanding of these questions will further enhance the applicability of long wave models, which are computationally inexpensive comparing to the full Euler simulations, especially over long computational times out of reach for even massive parallel machines.

## Chapter 4

### WEAKLY NONLINEAR MODELS FOR INTERNAL WAVES

*(Article in preparation)*

#### 4.1 Introduction

In Chapter 3, the strongly nonlinear model and the regularized model have been studied numerically by emulating the dam-break problem for internal waves. These two models show good agreement with the Euler simulations for the primary waves spanning a fairly wide range from small to large amplitudes. However, any prediction on the outcome of the internal dam-break has to still rely on numerical simulations, and it would highly desirable to have an analytical way to predict the outcome of the strongly nonlinear models without recourse to numerics. Of course, it is not reasonable to expect that an analytic result can account for complex dynamics that ensues from such initial conditions, such as Kelvin-Helmholtz instability. Nonetheless, however approximate might an “back of the envelope” prediction be, it would be preferable to not having any information at all before running a code. Therefore, in this chapter, we focus on weakly nonlinear models, because it is in this class that some systems solvable by the Inverse Scattering Transform (IST) can be found. In particular, the primary wave ought to be the main point of interest, as it is the one with the fastest speed and most of the energy, and as it separates from its dispersive tail, it is natural



to seek a result which is asymptotic in time for the limit of an infinite channel. For solvable evolution equations, solitary waves are linked by IST to the real eigenvalues of an associated isospectral problem (Whitham [37], Kaup [27]). However, while solvable, some of these models have the drawback of being ill-posed, and even when that is not the case, highly oscillatory wavetrains may develop in the solution (such as for the Korteweg de Vries equation), thereby preventing standard numerical approaches from achieving the desired accuracy. Thus, alternative models which are asymptotically equivalent are sometimes preferable and should be considered.

We review the governing equations and strongly nonlinear internal wave models in § 4.2 and § 4.3. The two-layer Kortweg-de Vries equation (see, e.g., Choi & Camassa [15]) with its associated inverse scattering transform method is reviewed in § 4.4. The possible Talbot fractal effect (Chen & Olver [13]) determined by the dispersion relation of the KdV equation is also discussed. In § 4.5, we propose a regularized version of the ill-posed two-layer Kaup (Craig *et al.* [17]), and the solitary wave solution for the new model is provided. The general solution of initial value problem for the new regularized Kaup equations does not appear to be available in closed form, unlike that of the original Kaup system, which is in principle analytically solvable (Kaup [28]) through IST. However, apart from special cases, this technique is in fact hardly of practical use for following the time evolution of general initial data, and one has to resort to numerical solutions. Here, the particular nature of the ill-posedness of Kaup's system proves to be rather challenging for designing numerical solution algorithms, a situation that is completely by-passed by the new regularized Kaup system. We provide numerical evidence showing that our regularization has little influence on the prediction offered by IST: the soliton content of initial data based on Kaup's system is left basically intact by its regularized counterpart, as tested by the numerical simulations of the new model.

Another well-posed weakly nonlinear model for bi-directional waves, the Boussinesq equations (see, e.g., Choi & Camassa [15]) is also asymptotically equivalent to the two-layer Kaup equations with a zero-flux constraint. This system has not been studied extensively for the internal wave setup. We fill this gap here, beginning with a comparison among the weakly nonlinear models based on their solitary wave solutions, and then moving on to full time dependent simulations.

Finally, in § 4.6, a higher-order uni-directional model is derived from the strongly nonlinear model for moderate amplitude waves. In § 4.7, well-posed models are numerically computed for the two-layer dam break problem. These numerical solutions are then compared with the full Euler simulations, and the analytical predictions of IST of the emerging solitons are tested for this class of initial data.

## 4.2 Governing equations

For an inviscid and incompressible fluid of density  $\rho_i$ , the velocity components in Cartesian coordinates  $(u_i, w_i)$  and the pressure  $p_i$  satisfy the continuity equation and the Euler equations,

$$u_{i_x} + w_{i_z} = 0, \quad (4.1)$$

$$u_{i_t} + u_i u_{i_x} + w_i u_{i_z} = -p_{i_x} / \rho_i, \quad (4.2)$$

$$w_{i_t} + u_i w_{i_x} + w_i w_{i_z} = -p_{i_z} / \rho_i - g, \quad (4.3)$$

where  $g$  is the gravitational acceleration and subscripts with respect to space and time represent partial differentiation. In a two-fluid system,  $i = 1 (i = 2)$  stands for the upper (lower) fluid and  $\rho_1 < \rho_2$  is assumed for a stable stratification.

The boundary conditions at the interface are the continuity of normal velocity and

pressure:

$$\zeta_t + u_1 \zeta_x = w_1, \quad \zeta_t + u_2 \zeta_x = w_2, \quad b_1 = b_2 = P \text{ at } z = \zeta(x, t), \quad (4.4)$$

where  $\zeta$  is a displacement of the interface. At the upper and lower rigid surfaces, the kinematic boundary conditions are given by

$$w_1(x, h_1, t) = 0, \quad w_2(x, h_2, t) = 0, \quad (4.5)$$

where  $h_1(h_2)$  is the undisturbed thickness of the upper (lower) fluid layer.

From the linearized problem of (4.1)-(4.5), the dispersion relation between wave speed  $c$  and wave number  $k$  (Lamb [29]) is

$$c^2 = \frac{(g/k)(\rho_2 - \rho_1)}{\rho_1 \coth(kh_1) + \rho_2 \coth(kh_2)}. \quad (4.6)$$

Under the shallow water assumption ( $kh_i \rightarrow 0$ ), the asymptotic behavior of the linear dispersion becomes

$$c = c_0 \left[ 1 - \frac{k^2}{6} \frac{\rho_1 h_1^2 h_2 + \rho_2 h_1 h_2^2}{\rho_1 h_2 + \rho_2 h_1 + O(k^4 h_i^4)} \right], \quad c_0^2 = \frac{gh_1 h_2 (\rho_2 - \rho_1)}{\rho_1 h_2 + \rho_2 h_1} \quad (4.7)$$

This linear dispersion relation results in linear dispersive terms in the weakly nonlinear models as described in the following sections.

### 4.3 The strongly nonlinear model

The strongly nonlinear model is introduced in § 3.3.2 with the shallow water assumption

$$O(l/h_i) = O(\epsilon), \quad (4.8)$$

where  $l$  is the typical wave length. The speed  $c$  of the solitary wave is related to its amplitude  $a$  by

$$\frac{c^2}{c_0^2} = \frac{(h_1 - a)(h_2 + a)}{h_1 h_2 - (c_0^2/g) a}. \quad (4.9)$$

The maximum wave amplitude and speed are given by

$$a_m = \frac{h_1 - h_2 \sqrt{\rho_1/\rho_2}}{1 + \sqrt{\rho_1/\rho_2}}, \quad (4.10)$$

$$c_m^2 = g(h_1 + h_2) \frac{1 - \sqrt{\rho_1/\rho_2}}{1 + \sqrt{\rho_1/\rho_2}}. \quad (4.11)$$

#### 4.4 The Kortwegg-de Vries equation

The two-layer Kortwegg-de Vries (KdV) equation (see, e.g., Choi & Camassa [15]) is a uni-directional model for small amplitude waves where the amplitude of the wave  $a$  is small with respect to the depth of each layer,

$$O(a/h_i) = O(\alpha), \quad (4.12)$$

in addition to the shallow water assumption (4.8), and the small parameters  $\epsilon$  and  $\alpha$  satisfy the order relation  $\alpha = \epsilon^2$ . In terms of the interfacial displacement  $\zeta$ , the KdV equation is written as

$$\zeta_t + c_0 \zeta_x + c_1 \zeta \zeta_x + c_2 \zeta_{xxx} = 0, \quad (4.13)$$

where

$$c_0 = \left( \frac{g(\rho_2 - \rho_1)h_1 h_2}{\rho_1 h_2 + \rho_2 h_1} \right)^{\frac{1}{2}}, \quad c_1 = -\frac{3c_0}{2} \frac{\rho_1 h_2^2 - \rho_2 h_1^2}{\rho_1 h_1 h_2^2 + \rho_2 h_1^2 h_2}, \quad \text{and} \quad c_2 = \frac{c_0}{6} \frac{\rho_1 h_1^2 h_2 + \rho_2 h_1 h_2^2}{\rho_1 h_2 + \rho_2 h_1}. \quad (4.14)$$

The KdV equation is a completely integrable system, whose initial value problem can be solved analytically through the inverse scattering transform technique (Whitham

[37]). Rescaling the variables in (4.13):

$$x' = c_2^{-\frac{1}{3}}(x - c_0 t), \quad \zeta' = \frac{c_1}{6c_2^{\frac{1}{3}}}\zeta, \quad (4.15)$$

we get

$$\zeta'_t - 6\zeta'\zeta'_{x'} + \zeta'_{x'x'} = 0 \quad (4.16)$$

The corresponding Schrödinger eigenvalue problem is

$$\psi_{x'x'} + (\zeta' - \gamma)\psi = 0, \quad (4.17)$$

where  $\psi$  is an unknown function of  $t$  and  $x'$ , and  $\zeta'$  is the solution of the Korteweg-de Vries equation to be determined from its initial condition at  $t = 0$ . From the Schrödinger equation we obtain

$$\zeta' = \frac{1}{\psi} \frac{\partial^2 \psi}{\partial x'^2} - \gamma. \quad (4.18)$$

The complete integrability of the KdV equation allows to find  $\zeta'$  depending on time while the set of eigenvalues  $\gamma$  remain constant. After eigenvalues are found, the time evolution of eigenfunctions associated to each eigenvalue  $\gamma$ , the norming constants, and the reflection coefficients – comprising the so-called scattering data – is given by a system of linear ordinary differential equations which can be solved analytically. Finally, performing the inverse scattering procedure by solving the Gelfand-Levitan-Marchenko integral equation (Gel'fand [19], Marchenko [31]), a *linear* integral equation, the final solution of the original nonlinear partial differential equation is recovered. For the Schrödinger equation, the discrete spectrum eigenvalues essentially correspond to solitary wave solutions emerging asymptotically in time from the evolution governed by the KdV equation, while the continuous spectrum gives rise to dispersive tails. The

solitary wave corresponding to  $\gamma = \sigma^2$  are given by

$$\zeta' = -2\sigma^2 \text{sech}^2(\sigma x' - 4\sigma^3 t) \quad (4.19)$$

In the physical domain, the corresponding traveling wave solution is

$$\zeta = \frac{12c_2^{\frac{1}{3}}\sigma^2}{c_1} \text{sech}^2(\sigma c_2^{-\frac{1}{3}}(x - c_0 t) - 4\sigma^3 t). \quad (4.20)$$

The speed  $c$  of the solitary wave and the amplitude are related by

$$a = \frac{3(c - c_0)}{c_1}, \quad (4.21)$$

and there is no maximum amplitude or wave-speed for these solutions of the KdV equation, clearly an unphysical feature of the equation, and one that conflicts with its derivation under small amplitude assumptions.

The KdV equation is a favorite model for studies of wave propagation, when applicable, for its simplicity and its complete integrability. However, in applications, we note there are two deficiencies. First, the equation is a model for uni-directional propagating waves, whereas bi-directional waves propagation is the generic outcome of most physical process where the models apply. For traveling wave solutions, Wu [39] linked the KdV equation with the bi-directional weakly nonlinear model to the order of  $O(\epsilon^4)$ . However, this approach is hard to extend to general initial conditions. The best we can do with a zero initial velocity is to simply divide the physical initial condition into two uncoupled components traveling in opposite directions.

Another pitfall of the KdV equation is that the solution is accompanied by a dispersive tail which may travel at speeds that are not faithfully representing those of the parent Euler equations. In infinite domain, where short waves quickly travel away from

the region of interest, this may not be a problem. Nonetheless, in a practical sense, and specifically with periodic boundary conditions, the dispersive tail can pollute the solution that one is trying to follow numerically. In the two-layer KdV equation, the problem becomes more apparent by looking at the linear dispersion relation at  $\zeta = 0$ :

$$\omega(k) = c_0 k - c_2 k^3. \quad (4.22)$$

As  $k \rightarrow \infty$ , the linear dispersion relation  $\omega(k) \sim -c_2 k^3$  with  $c_2 \leq 0$  often large in the two-layer physical set-ups, implying a fast propagating of high modes (Chen & Olver [13]). This feature also brings difficulties in numerical computations. Writing

$$\zeta(x, t) = \sum_0^{k=K} A(t) \exp(ikx) \quad (4.23)$$

for the linearized two-layer equation, we get

$$A'(t) = i(c_2 k^3 - c_0 k) A(t) = -i\omega(k)t. \quad (4.24)$$

The solution is  $A(t) = \exp(-i\omega(k)t)$ , which is highly oscillatory in time for large wave numbers. This indicates that in order to achieve a desired accuracy, the time-step for the numerical computations has to be small enough to capture the highly oscillatory behavior. In § 4.5, we introduce weakly nonlinear models for bi-directional waves which offers some remedy for this situation.

## 4.5 Weakly nonlinear models for bi-directional waves

### 4.5.1 The two-layer Kaup model

By using an Hamiltonian perturbation approach (Craig *et al.* [17]), a two-layer Kaup system can be derived

$$\zeta_t + b_1 v_x + b_3 (\zeta v)_x + b_4 v_{xxx} = 0, \quad (4.25)$$

$$v_t + b_2 \zeta_x + b_3 v v_x = 0, \quad (4.26)$$

where  $\zeta$  is the interface displacement, and

$$v = \rho_2 \check{u}_2 - \rho_1 \check{u}_1 \quad (4.27)$$

with  $\check{u}_i$  ( $i = 1, 2$ ) horizontal velocities near the interface for upper and lower fluids.

The coefficients  $b_j$  are

$$b_1 = \frac{h_1 h_2}{\rho_1 h_2 + \rho_2 h_1}, \quad b_2 = g(\rho_2 - \rho_1), \quad b_3 = \frac{\rho_2 h_1^2 - \rho_1 h_2^2}{(\rho_1 h_2 + \rho_2 h_1)^2}, \quad b_4 = \frac{(h_1 h_2)^2 (\rho_1 h_1 + \rho_2 h_2)}{3(\rho_1 h_2 + \rho_2 h_1)^2}. \quad (4.28)$$

This is an integrable system and can be solved by inverse scattering theory (Kaup [27], [28]). The system (4.25)-(4.26), under the scaling

$$x' = \sqrt{\frac{b_1}{b_4}} x, \quad t' = \sqrt{\frac{b_1^2 b_2}{b_4}} t, \quad \zeta' = -\frac{b_3}{b_1} \zeta, \quad v' = \frac{b_3}{\sqrt{b_1 b_2}} v \quad (4.29)$$

becomes the completely integrable Kaup equations

$$\zeta'_{t'} - v'_{x'} - (\zeta' v')_{x'} - v'_{x'x'} = 0 \quad (4.30)$$

$$v'_{t'} - \zeta'_{x'} - v' v'_{x'} = 0. \quad (4.31)$$



The eigenvalue problem for (4.30)-(4.31) is

$$\psi_{x'x'} + (\gamma^2 + \frac{1}{4} + i\gamma q + r)\psi = 0 \quad (4.32)$$

where

$$q = \frac{1}{2}v', \text{ and } r = -\frac{1}{4}(\zeta' + \frac{1}{4}v'^2).$$

The inverse scattering transform for (4.32) is different from (4.17) by its “transformation kernel” (Kaup [28]). The eigenvalue is written as  $\gamma^2 = -(\sigma_1^2 - \frac{1}{4})$ , with real values of  $\sigma_1$  yielding solitary wave solutions by the following steps

$$\sigma_1 = \frac{1}{4}(\xi - \frac{1}{\xi}), \quad \sigma_2 = \frac{1}{8}(\xi^2 - \frac{1}{\xi^2}), \quad (4.33)$$

$$\chi' = \frac{\mp 8\sigma_1}{\cosh(2\sigma_1 x' + 2\sigma_2 t') \pm \frac{1}{2}(\xi + \frac{1}{\xi})}, \quad (4.34)$$

$$\zeta' = \sigma_2 \chi' + \frac{\sigma_1^2}{2} \chi'^2, \quad (4.35)$$

$$v' = \sigma_1 \chi'. \quad (4.36)$$

Back to physical variables, we have

$$\chi = \frac{\mp 8\sigma_1}{\cosh(2\sigma_1 \sqrt{\frac{3b_1}{b_4}}x + 2\sigma_2 \sqrt{\frac{3b_1^2 b_2}{b_4}}t) \pm \frac{1}{2}(\xi + \frac{1}{\xi})}, \quad (4.37)$$

$$\zeta = -\frac{b_1}{b_3} \left( \sigma_2 \chi + \frac{\sigma_1^2}{2} \chi^2 \right), \quad (4.38)$$

$$v = \frac{\sqrt{b_1 b_2}}{b_3} \sigma_1 \chi. \quad (4.39)$$

When  $1 < \xi < \infty$ , this correspond to a soliton moving to the left, while for  $-1 < \xi < 0$ , the soliton is moving to the right; the sign is chosen so that the denominator of

(4.37) does not vanish. It is easy to show through (4.37)-(4.39) that the amplitude  $a$  and the traveling wave speed  $c$  are related linearly for the Kaup system solitons,

$$a = \frac{2b_1(c - c_0)}{b_3c_0}. \quad (4.40)$$

This relation is in fact the same as that from the KdV equation in (4.21). The Kaup equations have the merit to be analytically solvable in the infinite domain. However, by looking into its linear dispersion relation at  $(v = 0, \zeta = 0)$ , a serious mathematical drawback immediately comes to the fore. By writing  $v = v_0 e^{i(kx - \omega t)}$  and  $\zeta = \zeta_0 e^{i(kx - \omega t)}$ , the dispersion relation for the linearized system is

$$\omega^2 = b_2 k^2 (b_1 - b_4 k^2), \quad (4.41)$$

where  $b_1$ ,  $b_2$  and  $b_4$  are all positive, indicating that the system is ill-posed for wave numbers  $k$  larger than the critical value

$$k_{\text{critical}} = \sqrt{\frac{b_1}{b_4}} = \sqrt{\frac{3(\rho_1 h_2 + \rho_2 h_1)}{h_1 h_2 (\rho_1 h_1 + \rho_2 h_2)}} \quad (4.42)$$

This critical value exists for *any* choice of the “hardware” physical parameters  $\rho$ ’s and  $h$ ’s, and more importantly it is independent of fluid velocity shears. This property is quite different from the ill-posedness for the Euler equations or its strongly-nonlinear models, where it is always generated by the presence of a jump in velocity across fluid interfaces, and as such it is physically, as well as mathematically, undesirable. In particular, an algorithm to filter wavenumbers past  $k_{\text{critical}}$  may suppress a range of  $k$  that is necessary for an accurate solution reconstruction by Fourier Transform.

For instance the instability in the strongly nonlinear model is triggered by the shear velocity, i.e., the weaker the shear, the larger the local  $k_{\text{critical}}$  becomes. With zero

shear, the linear dispersion relation from the strongly nonlinear model becomes stable. As shown by (4.42), this is not the case for the Kaup equations. When applying linear stability analysis around  $(v, \zeta) = (V, H)$ , we have the dispersion relation

$$\omega(k) = b_3 V k \pm k \sqrt{b_2 b_3 H + b_2 (b_1 - b_4 k^2)}, \quad (4.43)$$

so that

$$k_{\text{critical}} = \sqrt{\frac{1}{b_4} (b_3 H + b_1)} \quad (4.44)$$

For solitary wave solutions, from (4.37)-(4.38), we can show that  $b_3 H > 0$  always holds, indicating that for larger amplitude waves, the stability criterion actually improves by allowing for larger wavenumbers, in contrast to the physics supported by the parent Euler equations. Thus, the most unstable locations for solutions of the Kaup equations are actually the ones where no wave motion occurs as in (4.42).

It is natural to implement a low-pass filter for the Kaup equations in a similar fashion as for the strongly nonlinear model. However, the value of  $k_{\text{critical}}$  in (4.42) can be very small by the choice of physical parameters  $\rho_i$ s and  $h_i$ s. Specifically, write

$$\frac{b_1}{b_4} = \frac{3(\rho_1 h_2 + \rho_2 h_1)}{h_1 h_2 (\rho_1 h_1 + \rho_2 h_2)} = \frac{\rho h_2 + h_1}{h_1 h_2 (\rho h_1 + h_2)} = R(\rho), \quad (4.45)$$

where  $\rho = \frac{\rho_1}{\rho_2}$ . We have

$$R'(\rho) = \frac{h_2^2 - h_1^2}{(\rho h_1 + h_2)^2}, \quad (4.46)$$

When  $h_2 > h_1$ ,  $R(\rho)$  achieves its minimum at  $\rho = 0$ , the situation where the two-layer case turns into a single layer and

$$R(0) = \frac{3}{h_2^2} \quad (4.47)$$

On the other hand, when  $h_2 < h_1$ ,  $R(\rho)$  achieves its maximum at  $\rho = 0$ . For instance, with the physical parameters chosen as in Grue's experiment, this critical wave

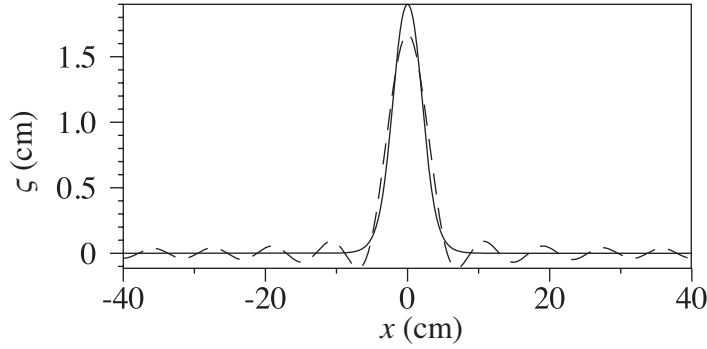


Figure 4.1: The solitary wave solution from the Kaup equations with the physical parameters  $\rho_1 = 0$ ,  $\rho_2 = 1 \text{ g}\cdot\text{cm}^{-3}$ ,  $h_1 = 1.95 \text{ cm}$ ,  $h_2 = 2 \text{ cm}$ ,  $g = 1 \text{ cm}\cdot\text{s}^{-2}$  corresponding to the critical wavenumber  $k_{\text{critical}} = 0.86$ . The Fourier modes below this instability threshold are not sufficient for recovering the solution. Solid: solitary wave solution; dashed: solitary wave solution with truncated Fourier coefficients satisfying the stability criterion.

frequency is  $k_{\text{critical}} = 0.057$ .

Just like KdV, the Kaup equations support solitary waves with no maximum amplitude requirement. Unlike KdV, the stability criterion prevents these solutions from being used in numerical simulations. For instance, we choose the parameters in the Kaup equations as  $\rho_1 = 0$ ,  $\rho_2 = 1 \text{ g}\cdot\text{cm}^{-3}$ ,  $h_1 = 1.95 \text{ cm}$ ,  $h_2 = 2 \text{ cm}$ ,  $g = 1 \text{ cm}\cdot\text{s}^{-2}$ , and the amplitude  $a = 1.9 \text{ cm}$ . The critical wave frequency is  $k_{\text{critical}} = 0.86$ . The domain is  $[-40, 40] \text{ cm}$  so that the value of  $\zeta$  is less than  $1e-15$  at boundaries, corresponding to 11 wave numbers in the domain within the stability criterion. These 11 wave numbers cannot recover a good approximation to the solitary wave solution as demonstrated in figure 4.1.

#### 4.5.2 Regularized Kaup equations

It is possible however to make use of the leading-order terms in these equations to recombine the asymptotic expansion so as to obtain well-posed models. From the

leading order of (4.25)-(4.26), we have

$$\zeta_{xxt} + b_1 v_{xxx} = O(\epsilon^2 \alpha^2), \quad (4.48)$$

$$v_{xxt} + b_2 \zeta_{xxx} = O(\epsilon^2 \alpha^2), \quad (4.49)$$

By multiplying (4.48)-(4.49) by arbitrary constants  $\mu$  and  $\nu$ , and adding them to (4.25)-(4.26), different models asymptotically equivalent to (4.25)-(4.26) can be constructed:

$$\zeta_t + b_1 v_x + b_3 (\zeta v)_x + b_4 v_{xxx} = \mu (\zeta_{xxt} + b_1 v_{xxx}) \quad (4.50)$$

$$v_t + b_2 \zeta_x + b_3 v v_x = \nu (v_{xxt} + b_2 \zeta_{xxx}) \quad (4.51)$$

The dispersion relation

$$\omega^2(k) = \frac{b_2 k^2 [b_1 + (\mu b_1 - b_4) k^2]}{1 + \mu k^2} \quad (4.52)$$

is independent of  $\nu$ . In order to cure the instability completely, it is required that  $\omega(k)^2 \geq 0$  for all  $k$  therefore we choose  $\mu = \frac{b_4}{b_1}$  and  $\nu = 0$ . The “regularized Kaup equations” then become

$$\zeta_t - \frac{b_4}{b_1} \zeta_{xxt} + b_1 v_x + b_3 (\zeta v)_x = 0 \quad (4.53)$$

$$v_t + b_2 \zeta_x + b_3 v v_x = 0 \quad (4.54)$$

We can obtain exact solutions for the regularized Kaup model. Writing  $v(x, t) = V(X)$

and  $\zeta(x, t) = H(X)$ , where  $X = x - ct$  with the traveling wave speed  $c$ , we have from

$$H'^2 = \frac{2b_1}{b_4c} \left[ \left( \frac{c^3}{2b_2^2} - \frac{b_1c}{2b_2} \right) V^2 + \left( \frac{b_1b_3}{3b_2} - \frac{5b_3c^2}{6b_2^2} \right) V^3 \right] + \frac{2b_1}{b_4c} \left[ + \frac{b_3^2c}{2b_2^2} V^4 - \frac{b_3^3}{10b_2^2} V^5 \right], \quad (4.55)$$

$$H = \frac{1}{b_2} (cV - \frac{b_3}{2} V^2). \quad (4.56)$$

This system becomes a differential equation of  $V$  only:

$$V' = \pm \frac{b_2 \sqrt{f(V)}}{c - b_3 V}, \quad (4.57)$$

where

$$\begin{aligned} f(V) &= \frac{2b_1}{b_4c} \left[ \left( \frac{c^3}{2b_2^2} - \frac{b_1c}{2b_2} \right) V^2 + \left( \frac{b_1b_3}{3b_2} - \frac{5b_3c^2}{6b_2^2} \right) V^3 + \frac{b_3^2c}{2b_2^2} V^4 - \frac{b_3^3}{10b_2^2} V^5 \right], \\ &= -\frac{b_1b_3^3}{5b_2^2b_4c} V^2 \left[ V^3 - \frac{5c}{b_3} V^2 - \frac{5(2c_0^2 - 5c^2)}{3b_3^2} V - \frac{5c(c^2 - c_0^2)}{b_3^3} \right]. \end{aligned} \quad (4.58)$$

Under the condition that  $|c| > |c_0|$  (notice that  $c_0^2 = b_1b_2$ ) and

$$4c^6 + 12c_0^3c^3 + 9c_0^4c^2 - 160c_0^6 < 0, \quad (4.59)$$

the model has solitary wave solutions, as  $f(V)$  has three real roots with same sign depending on the traveling direction, corresponding to the sign of  $c$  and the sign of elevation/depression wave criterion  $\rho_2 h_1^2 - \rho_1 h_2^2$ , which in turn corresponds to the sign of  $b_3$ . When  $b_3c > 0$ ,  $f(V)$  has three positive roots. When  $b_3c < 0$ ,  $f(V)$  has three negative roots. Consider the case when  $b_3 < 0$  and  $c > 0$  for right going depression traveling waves:

$$f(V) = -\frac{b_1b_3^3}{5b_2^2b_4c} V^2 (V + V_1)(V + V_2)(V + V_3). \quad (4.60)$$

Write

$$\Delta_0 = \frac{10c_0^2}{b_3^2}, \quad \Delta_1 = -\frac{5(2c^3 + 3cc_0^2)}{b_3^3}, \quad \text{and} \quad C = \left( \frac{\Delta_1 + \sqrt{\Delta_1^2 - 4\Delta_0^3}}{2} \right)^{\frac{1}{3}},$$

and the three roots have the form

$$\begin{aligned} V_1 &= \frac{1}{3} \left( -\frac{5c}{b_3} + e^{-\frac{2}{3}\pi i} C + e^{\frac{2}{3}\pi i} \frac{\Delta_0}{C} \right), \\ V_2 &= \frac{1}{3} \left( -\frac{5c}{b_3} + C + \frac{\Delta_0}{C} \right), \\ V_3 &= \frac{1}{3} \left( -\frac{5c}{b_3} + e^{\frac{2}{3}\pi i} C + e^{-\frac{2}{3}\pi i} \frac{\Delta_0}{C} \right). \end{aligned}$$

The imaginary parts are always canceled by complex conjugates. The differential equation (4.57) is now

$$V' = \kappa \frac{V \sqrt{(V + V_1)(V + V_2)(V + V_3)}}{c - b_3 V}. \quad (4.61)$$

Using integration by parts yields

$$\kappa dX = \frac{c}{V \sqrt{(V + V_1)(V + V_2)(V + V_3)}} dV - \frac{b_3}{\sqrt{(V + V_1)(V + V_2)(V + V_3)}} dV. \quad (4.62)$$

A solution can be expressed implicitly by elliptical integrals, with the assumption that  $V_1 > V_2 > V_3 > V \geq 0$ ,

$$\kappa X = -\frac{2(c + b_3 V_2)}{V_2 \sqrt{V_3 - V_1}} F(\phi, m) - \frac{2c(V_2 - V_1)}{V_1 V_2 \sqrt{V_3 - V_1}} \Pi(n; \phi, m), \quad (4.63)$$

where

$$\sin \phi \equiv \left( \frac{V + V_1}{V + V_2} \right)^{\frac{1}{2}}, \quad m^2 \equiv \frac{V_3 - V_2}{V_3 - V_1}, \quad n \equiv \frac{V_2}{V_1}, \quad (4.64)$$

and the coefficient  $\kappa$  is

$$\kappa = \left| \frac{b_1 b_3^3}{5b_4 c} \right|^{\frac{1}{2}}. \quad (4.65)$$

Here  $F(\cdot, \cdot)$  and  $\Pi(\cdot; \cdot, \cdot)$  stand for the first and third elliptic integrals (Byrd [7]).

### 4.5.3 The two-layer Boussinesq equations

The two-layer Boussinesq equation is another weakly nonlinear model for the bi-directional wave propagation, written in terms of the interface displacement  $\zeta$  and the mean upper layer horizontal velocity  $\bar{u}_1$ :

$$\zeta_t - [(h_1 - \zeta)\bar{u}_1]_x = 0, \quad (4.66)$$

$$\bar{u}_{1t} + d_1 \bar{u}_1 \bar{u}_{1x} + (d_2 + d_3 \zeta) \zeta_x = d_4 \bar{u}_{1xxt} + O(\alpha \epsilon^4, \alpha^2 \epsilon^2), \quad (4.67)$$

where

$$\begin{aligned} d_1 &= \frac{\rho_1 h_2^2 - \rho_2 h_1 (h_1 + h_2) - \rho_2 h_1^2}{\rho_1 h_2^2 + \rho_2 h_1 h_2}, & d_2 &= \frac{g(\rho_1 - \rho_2) h_2}{\rho_1 h_2 + \rho_2 h_1}, \\ d_3 &= \frac{g \rho_2 (\rho_1 - \rho_2) (h_1 + h_2)}{(\rho_1 h_2 + \rho_2 h_1)^2}, & d_4 &= \frac{1}{3} \frac{\rho_1 h_1^2 h_2 + \rho_2 h_1 h_2^2}{\rho_1 h_2 + \rho_2 h_1}. \end{aligned}$$

We first show that the Boussinesq and Kaup equations are asymptotically equivalent under the zero flux assumption:

$$Q(t) = \int_{-h_2}^{h_1} u(x, z, t) dz = 0, \quad (4.68)$$

which holds for a variety of conditions: waves in an infinite domain, symmetric waves, rigid walls at boundary, etc. In the shallow-water configuration, there is an approximate relation between layer-averaged velocities  $\bar{u}_1$  and  $\bar{u}_2$  and local velocities  $u_1(x, z, t)$  and  $u_2(x, z, t)$  (Camassa *et al.* [10]):

$$u_2(x, z, t) = \bar{u}_2(x, t) + \left( \frac{(\eta_2(x, t))^2}{6} - \frac{(z + h_2)^2}{2} \right) \partial_x^2 \bar{u}_2(x, t) + O(\epsilon^4 \alpha^2), \quad (4.69)$$



with  $-h_2 < z < \zeta$  for the lower layer, and

$$u_1(x, z, t) = \bar{u}_1(x, t) + \left( \frac{(\eta_1(x, t))^2}{6} - \frac{(z - h_1)^2}{2} \right) \partial_x^2 \bar{u}_1(x, t) + O(\epsilon^4 \alpha^2) \quad (4.70)$$

with  $\zeta < z < h_1$  for the upper layer. Neglecting higher order terms, at the interface we have

$$\check{u}_2 = \bar{u}_2 - \frac{\eta_2^2}{3} \bar{u}_{2xx}, \quad \text{and} \quad \check{u}_1 = \bar{u}_1 - \frac{\eta_1^2}{3} \bar{u}_{1xx}. \quad (4.71)$$

With mean horizontal velocities  $\bar{u}_i$ s, the zero-flux constraint (4.68) can be written as

$$\bar{u}_1 \eta_1 + \bar{u}_2 \eta_2 = 0. \quad (4.72)$$

We now have

$$\bar{u}_2 = -\frac{h_1 - \zeta}{h_2 + \zeta} \bar{u}_1 = \left[ -\frac{h_1}{h_2} + \frac{h_1 + h_2}{h_2^2} \zeta + O(\alpha^2) \right] \bar{u}_1 \quad (4.73)$$

and

$$\begin{aligned} v &= \rho_2 \check{u}_2 - \rho_1 \check{u}_1, \\ &= \rho_2 \bar{u}_2 - \frac{\rho_2 \eta_2^2}{3} \bar{u}_{2xx} - \rho_1 \bar{u}_1 + \frac{\rho_1 \eta_1^2}{3} \bar{u}_{1xx} + O(\epsilon^4 \alpha^2), \\ &= -\frac{\rho_1 h_2 + \rho_2 h_1}{h_2} \bar{u}_1 + \frac{\rho_2 (h_1 + h_2)}{h_2^2} \zeta \bar{u}_1 + \frac{\rho_1 h_1^2 + \rho_2 h_1 h_2}{3} \bar{u}_{1xx} + O(\epsilon \alpha^2). \end{aligned} \quad (4.74)$$

Substituting (4.74) into (4.25) yields

$$\begin{aligned} \zeta_t - b_1 \frac{\rho_1 h_2 + \rho_2 h_1}{h_2} \bar{u}_{1x} + b_1 \frac{\rho_2 (h_1 + h_2)}{h_2^2} (\zeta \bar{u}_1)_x + \frac{b_1 (\rho_1 h_1^2 + \rho_2 h_1 h_2)}{3} \bar{u}_{1xxx}, \\ -b_3 \frac{\rho_1 h_2 + \rho_2 h_1}{h_2} (\zeta \bar{u}_1)_x - b_4 \frac{\rho_1 h_2 + \rho_2 h_1}{h_2} \bar{u}_{1xxx} = 0, \end{aligned} \quad (4.75)$$

which is identical to the  $\zeta$  equation of the Boussinesq system (4.77). With (4.74), equation (4.26) becomes

$$\begin{aligned} & \frac{\rho_2(h_1 + h_2)\zeta - (\rho_1 h_2^2 + \rho_2 h_1 h_2)}{h_2^2} \bar{u}_{1t} + \frac{\rho_2(h_1 + h_2)}{h_2^2} (\zeta \bar{u}_{1t} + \zeta_t \bar{u}_1) \\ & - \frac{\rho_1 h_1^2 + \rho_2 h_1 h_2}{3} \bar{u}_{1xxt} + b_2 \zeta_x + b_3 \frac{(\rho_1 h_2 + \rho_2 h_1)^2}{h_2^2} \bar{u}_1 \bar{u}_{1x} = 0. \end{aligned} \quad (4.76)$$

Because of

$$\zeta_t = [(h_1 - \zeta) \bar{u}_1]_x = (h_1 \bar{u}_1)_x + O(\epsilon \alpha^2), \quad (4.77)$$

and the inversion of the parameter of  $\bar{u}_{1t}$  term in (4.76), this can be written as

$$\begin{aligned} & \frac{h_2^2}{\rho_2(h_1 + h_2)\zeta - (\rho_1 h_2^2 + \rho_2 h_1 h_2)} \\ = & -\frac{h_2}{\rho_1 h_2 + \rho_2 h_1} - \frac{\rho_2(h_1 + h_2)}{(\rho_1 h_2 + \rho_2 h_1)^2} \zeta + O(\alpha^2) \end{aligned} \quad (4.78)$$

Thus, equation (4.76) is asymptotically equivalent to

$$\begin{aligned} & \bar{u}_{1t} - \frac{b_2 h_2}{\rho_1 h_2 + \rho_2 h_1} \zeta_x - \frac{b_2 \rho_2 (h_1 + h_2)}{(\rho_1 h_2 + \rho_2 h_1)^2} \zeta \zeta_x - \frac{(\rho_1 h_1 + \rho_2 h_2) h_1 h_2}{3(\rho_1 h_2 + \rho_2 h_1)} \bar{u}_{1xxt} \\ & - \frac{b_3 (\rho_1 h_2 + \rho_2 h_1)^2 + \rho_2 h_1 (h_1 + h_2)}{h_2 (\rho_1 h_2 + \rho_2 h_1)} \bar{u}_1 \bar{u}_{1x} = 0, \end{aligned} \quad (4.79)$$

which is exactly the evolution equation for  $\bar{u}_1$  of the Boussinesq equations (4.79).

We remark that the two-layer Boussinesq equations have the linear dispersion relation

$$\omega^2(k) = \frac{d_1^2 d_2}{d_4} - \frac{d_1^3 d_2}{d_1 d_4 + d_4^2 k^2}, \quad (4.80)$$

which is identical as the regularized Kaup equations (4.25)-(4.26). We notice that  $|\omega(k)| \leq d_1 \sqrt{\frac{d_2}{d_4}}$ , so that the high wavenumbers modes travel slowly.

We seek traveling wave solutions for the Boussinesq equation by writing

$$U(X) = \bar{u}_1(x, t), \quad \text{and} \quad H(X) = \zeta(x, t), \quad (4.81)$$

where  $X = x - ct$  with  $c$  the traveling wave speed in equations (4.77) and (4.79), the differential equation for  $U(X)$  can be written as

$$\begin{aligned} f(U) &= U_X^2 \\ &= \frac{2}{d_4 c} \left[ \frac{c}{2} U^2 - \frac{d_1}{6} U^3 - \left( d_2 h_1 + \frac{d_3 h_1^2}{2} \right) U - (d_2 h_1 c + d_3 h_1^2 c) \log \left| \frac{c - U}{c} \right| \right] \\ &\quad + \frac{d_3 h_1^2 c}{d_4} \left( \frac{1}{U - c} + \frac{1}{c} \right). \end{aligned} \quad (4.82)$$

Here the presence of the logarithm prevents further progress, thus we expand (4.82) at  $U = 0$ ,

$$f(U) = p_2 U^2 + p_3 U^3 + p_4 U^4 + p_5 U^5 + O(U^6), \quad (4.83)$$

where

$$\begin{aligned} p_2 &= \frac{c^2 + d_2 h_1}{d_4 c^2} = \frac{c_0^2}{d_4 c^2} \left( \frac{c^2}{c_0^2} - 1 \right), \\ p_3 &= -\frac{d_1 c^2 - 2d_2 h_1 + d_3 h_1^2}{3d_4 c^3} = \frac{c_0^2}{3d_4 c^3 h_2} \left[ \left( 1 - 2\frac{c^2}{c_0^2} \right) \frac{\rho_2 h_1^2 - \rho_1 h_2^2}{\rho_2 h_1 + \rho_1 h_2} + \left( \frac{c^2}{c_0^2} - 1 \right) h_2 \right], \\ p_4 &= \frac{h_1(d_2 - d_3 h_1)}{2d_4 c^4} = \frac{c_0^2}{2d_4 c^4 h_1 h_2} (\rho_1 h_2^2 - \rho_2 h_1^2) \\ p_5 &= \frac{h_1(2d_2 - 3d_3 h_1)}{5d_4 c^5} \end{aligned}$$

From the approximate function (4.83), we are able to understand some of the features of the Boussinesq traveling wave solutions. Existence of solutions requires  $p_2 > 0$ , which leads to

$$c^2 > c_0^2 \quad (4.84)$$

i.e., the same criterion as for the Kaup equations and its regularized sibling. The polarities of the ordinary differential equation (4.82), however, need an analysis for the combination of  $f(U)$  and its derivative  $f'(U)$ . Here we consider the case when  $c > 0$ . As  $U \rightarrow -\infty$ ,  $f(U) \sim d_1 U^3$ , and therefore there is always one real root with the negative sign. When  $U \rightarrow c^-$ ,  $f(U) \rightarrow \infty$ . These asymptotic behavior of  $f(U)$  help determine the other roots. By taking the derivative of  $f(U)$ :

$$f'(U) = \frac{U}{(U - c)^2} g(U), \quad (4.85)$$

where

$$g(U) = -\frac{1}{d_1} U^3 + (1 + d_1) c U^2 - (2c^2 + \frac{d_1 c^2}{2} + b_2 h_1 + \frac{d_3 h_1^2}{2}) U + (c^3 + d_2 c h_1). \quad (4.86)$$

The criterion for  $g(U)$  to have three distinct real roots is

$$\begin{aligned} \Delta^{\text{Bsq}}(c) &= \left[ (d_1 - 2)^2 c^2 - 3d_1 h_1 (2d_2 + d_3 h_1) \right]^3 \\ &+ c^2 \left[ (-2 + d_3)^3 c^2 + 9d_1 h_1 ((1 + b_1) b_3 h_1 + (2 - b_1) b_2) \right]^2 > 0. \end{aligned} \quad (4.87)$$

From this the qualitative behavior of solitary wave solutions can be understood, and a rough estimates provided. We can only work with the local extrema from equation (4.86), which is not sufficient to make any conclusion on the polarities of  $f(U)$ . We assume that as the traveling wave speed  $c$  gets larger, it is less likely to have multiple real roots. Therefore we let  $c = c_0$  in (4.87). If  $\Delta^{\text{Bsq}}(c_0) > 0$ , it is possible to have three different real roots for  $f(U)$  on  $(-\infty, c)$  corresponding to small amplitude traveling wave solutions. By setting  $\rho_2 h_1^2 = \rho_1 h_2^2$ , this is the case when  $d_1 = -1$ , where we find that  $\Delta^{\text{Bsq}}(c_0) = 0$ . When  $d_1 < -1$ ,  $\Delta^{\text{Bsq}}(c_0) < 0$ ; and when  $d_1 > -1$ ,  $\Delta^{\text{Bsq}}(c_0) > 0$ . By looking at (4.86) we conclude that there is at least one negative

root when  $d_1 < 0$ , and all three roots are positive when  $d_1 > 0$ , with the largest one greater than  $c$ . When  $d_1 = 0$ , equation (4.86) reduces to a quadratic equation, and has two roots with positive values. Figure 4.2 is a sketch summarizing all the possibilities. Note that when  $-1 < d_1 < 0$ , two solitary waves can emerge. Both have been tested as stable in numerical computations.

We now choose a set of parameters away from  $b_3 = 0$  (see further results in § 4.7), so that the Boussinesq equation does not have dual polarity waves. We remark that all the models (regularized-Kaup, Boussinesq equations and strongly nonlinear) have maximum traveling wave speed  $c$ . For the Kaup equations, however, the traveling wave speed  $c$  goes to infinity as the differential equation associated with the Kaup model's traveling wave solution (4.88)

$$V'^2 = f(V) = \frac{1}{b_4} V^2 \left[ \frac{b_3^2}{8b_2} V^2 - \frac{b_3 c}{b_2} V - \left( b_1 - \frac{c^2}{b_2} \right) \right], \quad (4.88)$$

always has two roots with the same sign when  $c^2 > c_0^2$ , with amplitude being linearly dependent on  $c$ .

#### 4.5.4 The derivation of KdV equation from the Kaup equation

Based on the scalings in (4.8) and (4.12), we non-dimensionalize all physical variables as

$$x = L\tilde{x}, \quad t = \frac{L}{U_0}\tilde{t}, \quad \zeta = a\tilde{\zeta}, \quad v = (\rho_2 - \rho_1)U_0\tilde{v}, \quad (4.89)$$

and assumes that all variables adorned with tildes are  $O(1)$  in  $\epsilon$ . Then the Kaup equations in dimensionless form is

$$\tilde{\zeta}_{\tilde{t}} + b_1\tilde{v}_{\tilde{x}} + \epsilon b_3(\tilde{\zeta}\tilde{v})_{\tilde{x}} + \alpha b_4\tilde{v}_{\tilde{x}\tilde{x}\tilde{x}} = 0 \quad (4.90)$$

$$\tilde{v}_{\tilde{t}} + b_2\tilde{\zeta}_{\tilde{x}} + \epsilon b_3\tilde{v}\tilde{v}_{\tilde{x}} = 0 \quad (4.91)$$

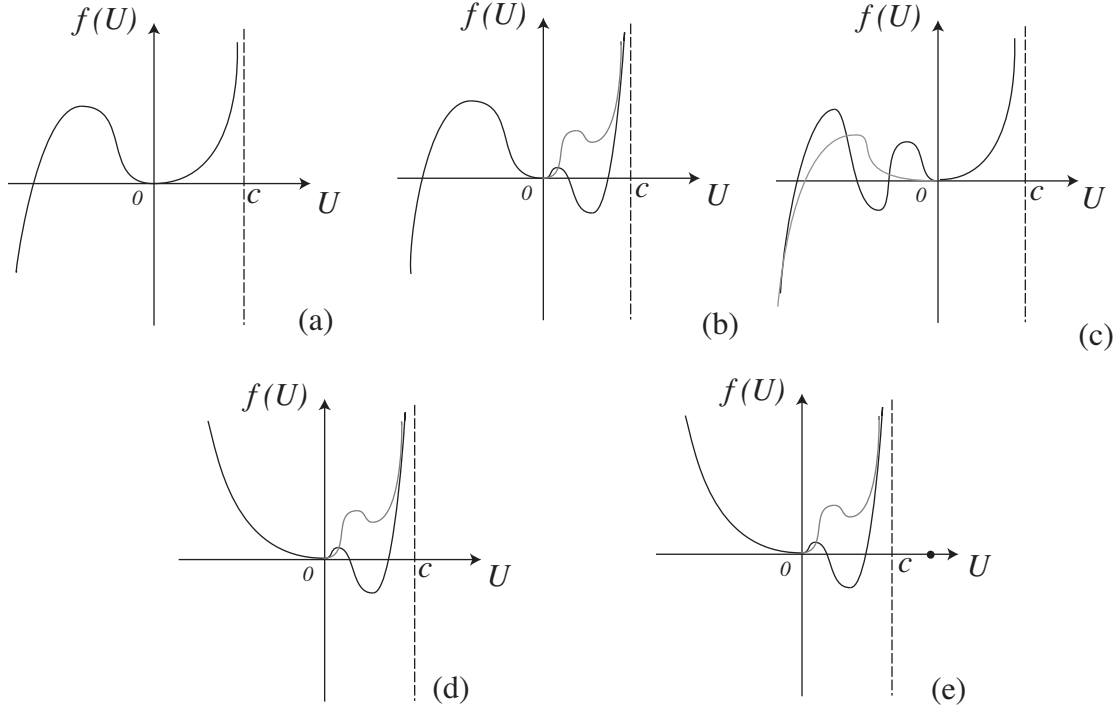


Figure 4.2: Sketch of  $f(U)$  in equation (4.82) with all possibilities for different values of  $d_1$ . Note that the gray curves do not lead to solitary wave solutions.

(a):  $d_1 \leq -1$ , one negative root for  $f(U)$ .

(b):  $-1 < d_1 < 0$ , three real roots for  $g(U)$ , with one negative and two positive. The black and gray curves represent possible situations for  $f(U)$ , with different choices of  $\rho_i$ ,  $h_i$  and  $c$ .

(c):  $-1 < d_1 < 0$ , three real roots for  $g(U)$ , all negative. The black and gray curves represent possible situations for  $f(U)$ , with different choices of  $\rho_i$ ,  $h_i$  and  $c$ .

(d):  $d_1 = 0$ , two positive roots for  $g(U)$ . The black and gray curves represent possible situations for  $f(U)$ , with different choices of  $\rho_i$ ,  $h_i$  and  $c$ .

(e):  $d_1 > 0$ , three positive roots for  $g(U)$ . The black and gray curves represent possible situations for  $f(U)$ , with different choices of  $\rho_i$ ,  $h_i$  and  $c$ .

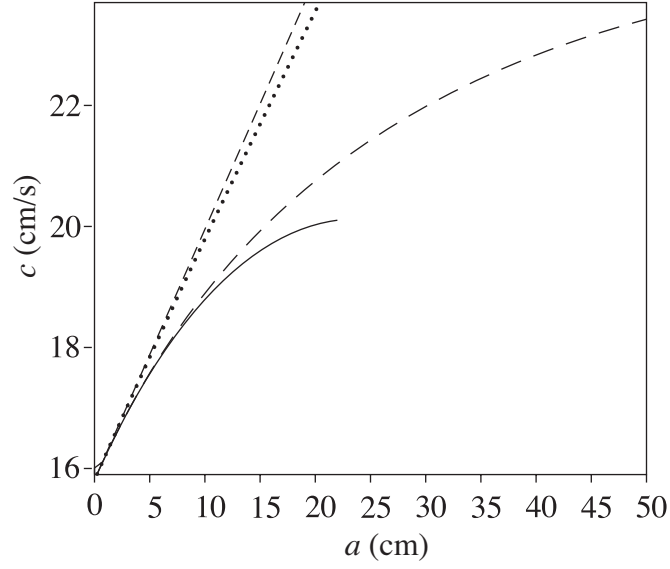


Figure 4.3: The relationship between traveling wave speed and amplitude with parameters in the laboratory experiments introduced in Chapter 3. Solid: strongly nonlinear; long dashed: Boussinesq; dotted: regularized Kaup; short dashed: Kaup model

Applying the strategy introduced in Whitham [37], we seek the unidirectional model corrected to first order in  $\epsilon$  and  $\alpha$ , in the form of

$$\tilde{v} = \sqrt{\frac{b_2}{b_1}} \tilde{\zeta} + \epsilon A + \alpha B + O(\epsilon^2 + \alpha^2) \quad (4.92)$$

where  $A$  and  $B$  are functions of  $\tilde{\zeta}$  and its  $\tilde{x}$  derivatives. Equations (4.90)-(4.91) become

$$\begin{aligned} \tilde{\zeta}_{\tilde{t}} + \sqrt{b_1 b_2} \tilde{\zeta}_{\tilde{x}} + \epsilon \left( \sqrt{b_1 b_2} A_{\tilde{x}} + 2b_3 \sqrt{\frac{b_2}{b_1}} \tilde{\zeta} \tilde{\zeta}_{\tilde{x}} \right) + \alpha \left( \sqrt{b_1 b_2} B_{\tilde{x}} + b_4 \sqrt{\frac{b_2}{b_1}} \tilde{\zeta}_{\tilde{x} \tilde{x} \tilde{x}} \right) \\ + O(\epsilon^2 + \alpha^2) = 0 \end{aligned} \quad (4.93)$$

$$\tilde{\zeta}_{\tilde{t}} + \sqrt{b_1 b_2} \tilde{\zeta}_{\tilde{x}} + \epsilon \left( \sqrt{\frac{b_1}{b_2}} A_{\tilde{t}} + b_3 \sqrt{\frac{b_2}{b_1}} \tilde{\zeta} \tilde{\zeta}_{\tilde{x}} \right) + \alpha \sqrt{\frac{b_1}{b_2}} B_{\tilde{t}} + O(\epsilon^2 + \alpha^2) = 0 \quad (4.94)$$

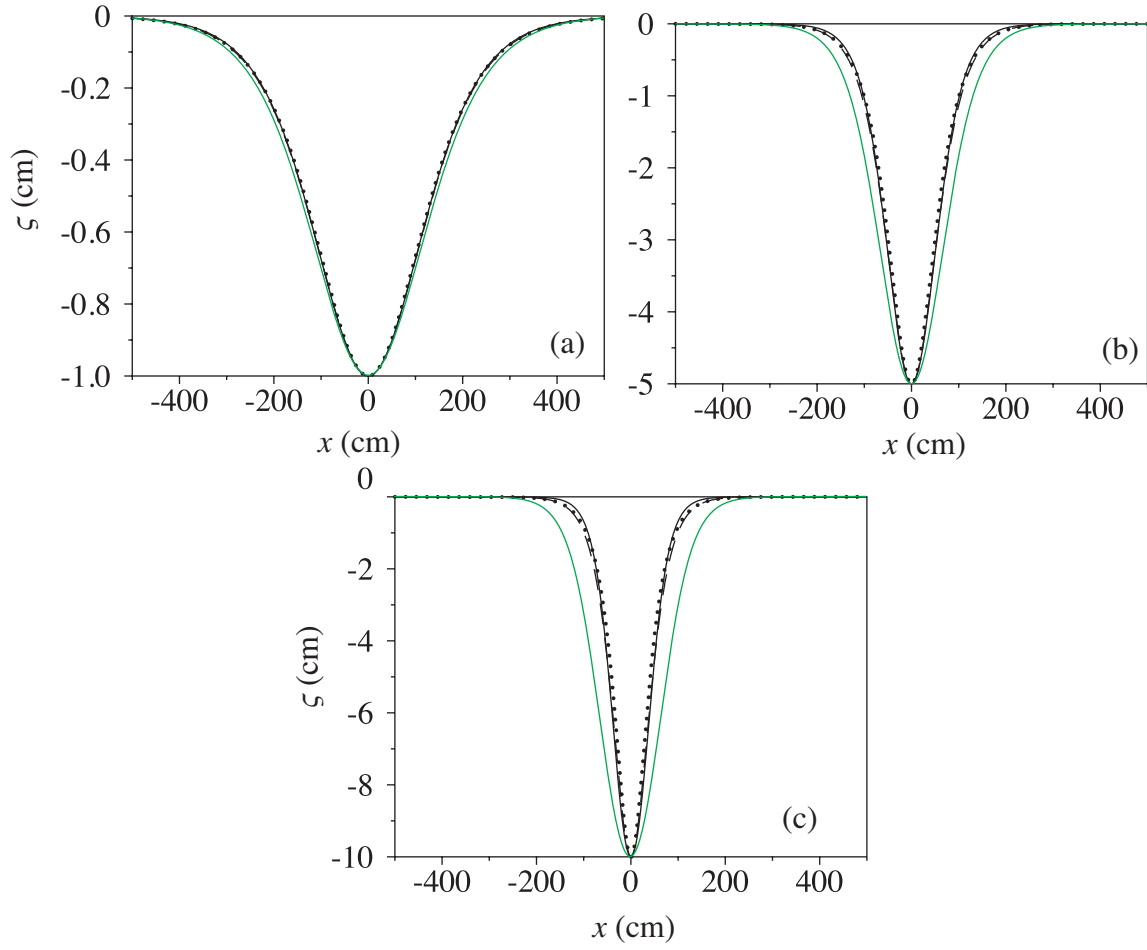


Figure 4.4: Traveling wave solutions from the strongly nonlinear model (solid green), the Kaup equations (solid), the regularized Kaup equations (dashed) and the Boussinesq equations (dotted) matching amplitude  $a$  with physical parameters introduced in § 4.7. (a):  $a = -1$  cm, (b):  $a = -5$  cm and (c):  $a = -10$  cm.



Since  $\tilde{\zeta}_t = -\sqrt{b_1 b_2} \tilde{\zeta}_{\tilde{x}} + O(\epsilon, \alpha)$ , all  $\tilde{t}$  derivatives in the first order terms may be replaced by  $x$  derivatives. Then the two equations are consistent if

$$A = -\frac{b_3}{4b_1} \sqrt{\frac{b_2}{b_1}} \tilde{\zeta}^2, \quad B = -\frac{b_4}{2b_1} \sqrt{\frac{b_2}{b_1}} \tilde{\zeta}_{\tilde{x}\tilde{x}} \quad (4.95)$$

Hence we have

$$\tilde{v} = \sqrt{\frac{b_2}{b_1}} \tilde{\zeta} - \epsilon \frac{b_3}{4b_1} \sqrt{\frac{b_2}{b_1}} \tilde{\zeta}^2 - \alpha \frac{b_4}{b_1} \sqrt{\frac{b_2}{b_1}} \tilde{\zeta}_{\tilde{x}\tilde{x}} \quad (4.96)$$

and

$$\tilde{\zeta}_{\tilde{t}} + \sqrt{b_1 b_2} \tilde{\zeta}_{\tilde{x}} + \epsilon \frac{3b_3}{2} \sqrt{\frac{b_2}{b_1}} \tilde{\zeta} \tilde{\zeta}_{\tilde{x}} + \alpha \frac{b_4}{2} \sqrt{\frac{b_2}{b_1}} \tilde{\zeta}_{\tilde{x}\tilde{x}\tilde{x}} = 0. \quad (4.97)$$

Writing in dimensional quantities, we get the two-layer KdV equation (4.13).

## 4.6 Higher-order uni-directional models

We carry out a comparison between the strongly nonlinear system and its unidirectional approximations, which stand in closer relation with the classical weakly nonlinear theories in the KdV family. By expanding the strongly nonlinear system in the two small parameters  $(\epsilon, \alpha)$ , with the amplitude scale parameter  $\alpha$  chosen to satisfy the relative ordering

$$\epsilon^2 < \alpha < \epsilon \quad (4.98)$$

with respect to the long wave parameter  $\epsilon$ , the following equation for the interface displacement  $\zeta(x, t)$  can be derived (in dimensional form)

$$\zeta_t + c_0 \zeta_x + c_1 \zeta \zeta_x + c_2 \zeta_{xxx} + c_3 (\zeta^3)_x + (c_4 \zeta_x^2 + c_5 \zeta \zeta_{xx})_x = 0. \quad (4.99)$$

Here the right-hand side would be of order  $O(\epsilon^4)$  or higher, and we truncate the expansion by setting it to zero. The coefficients  $c_i$ ,  $i = 1, \dots, 5$  depend on the depth and

density parameters (Choi & Camassa [15]):

$$\begin{aligned} c_3 &= \frac{7c_1^2}{18c_0} - \frac{c_0(\rho_1 h_2^3 + \rho_2 h_1^3)}{h_1^2 h_2^2 (\rho_1 h_2 + \rho_2 h_1)}, & c_4 &= \frac{17c_1 c_2}{12c_0} + \frac{c_0 h_1 h_2 (\rho_1 - \rho_2)}{12(\rho_1 h_2 + \rho_2 h_1)}, \\ c_5 &= \frac{7c_1 c_2}{3c_0} + \frac{c_0 h_1 h_2 (\rho_1 - \rho_2)}{6(\rho_1 h_2 + \rho_2 h_1)}. \end{aligned}$$

The terms multiplying the coefficients  $c_2$  through  $c_5$  are formally of higher order,  $O(\epsilon^2)$ ,  $O(\alpha^2)$  and  $O(\epsilon^2 \alpha)$ , than the first three of order  $O(1)$ ,  $O(1)$  and  $O(\alpha)$ , respectively. This leaves some asymptotic freedom in that one can add to (4.99) the second derivative of the lower order terms

$$\mu(\zeta_t + c_0 \zeta_x + c_1 \zeta \zeta_x)_{xx},$$

for any constant  $\mu$ , without altering the asymptotic accuracy of the equation. Hence

$$\zeta_t + c_0 \zeta_x + c_1 \zeta \zeta_x + \mu \zeta_{xxt} + (c_2 + \mu c_0) \zeta_{xxx} + c_3 (\zeta^3)_x + ((c_4 + \mu c_1) \zeta_x^2 + (c_5 + \mu c_1) \zeta \zeta_{xx})_x = 0, \quad (4.100)$$

can be taken as the most general asymptotically consistent form of the class of unidirectional equations expressing the ordering  $(\epsilon, \alpha)$  above.

#### 4.6.1 Choice of $\mu$ for conserved quantity

Various realizations by fixing  $\mu$  are now possible, depending on which property one chooses to focus on. For instance, requiring that during the evolution an intensity-like integral, i.e., one that involves the squares of the wave elevation  $\zeta^2$ , is conserved, leads to the choice

$$\mu \equiv \tilde{\mu} = \frac{c_5 - 2c_4}{c_1} = -\frac{h_1 h_2 (h_1 \rho_1 + h_2 \rho_2)}{12(h_2 \rho_1 + h_1 \rho_2)} = -\frac{c_2}{2c_0}. \quad (4.101)$$

With this  $\mu$ , it is easy to see that the positive definite quantity

$$\mathcal{E} = \frac{1}{2} \int_{-\infty}^{+\infty} \left[ \zeta^2 + \left( \frac{2c_4 - c_5}{c_1} \right) \zeta_x^2 \right] dx = \frac{1}{2} \int_{-\infty}^{+\infty} \left[ \zeta^2 + \frac{c_2}{2c_0} \zeta_x^2 \right] dx, \quad (4.102)$$

is conserved by equation (4.100), which reads explicitly

$$\zeta_t + c_0 \zeta_x + c_1 \zeta \zeta_x - \frac{c_2}{2c_0} \zeta_{xxt} + \frac{c_2}{2} \zeta_{xxx} + c_3 (\zeta^3)_x + (c_5 - c_4) (\zeta_x^2 + 2\zeta \zeta_{xx})_x = 0. \quad (4.103)$$

Traveling wave solutions of (4.103) with  $X = x - ct$  can be computed by quadratures thanks to the existence of this conservation law. For solitary waves, equation (4.103) reduces to

$$\zeta_x = c_u \frac{\zeta^2 (\zeta - a_+) (\zeta - a_-)}{\zeta - a_*}, \quad (4.104)$$

where the coefficient  $C_u$  is

$$c_u = \frac{c_3}{4(c_4 - c_5)},$$

the denominator's root  $a_*$  is

$$a_* = \frac{c_2(c_0 + c)}{4c_0(c_4 - c_5)} \quad (4.105)$$

and  $a_{\pm}$  are the roots of the quadratic equation

$$\zeta + \frac{2c_1}{3c_3} \zeta + 2 \frac{c_0 - c}{c_3} = 0, \quad (4.106)$$

respectively. Whether the traveling wave solution is of elevation or depression still depends on the sign of  $\rho_1 h^2 - \rho_2 h_1^2$ . The negative sign gives a wave of depression, and can be expressed in terms of elliptic integrals:

$$X = -\frac{2(a_* - a_+)}{a_+ n \sqrt{(-c_u(a_* - a_-))}} [F(\phi, m) + (n - 1)\Pi(n, \phi, m)], \quad (4.107)$$

where

$$\sin \phi = \left[ \frac{(a_* - a_-)(\zeta - a_+)}{(a_* - a_-)(\zeta - a_-)} \right]^2, \quad m = \frac{a_* - a_+}{a_* - a_-}, \quad n = \frac{a_-(a_* - a_+)}{a_+(a_* - a_-)}. \quad (4.108)$$

The structure of the solution is very similar to that of the strongly nonlinear wave model. We compare the traveling solution of the strongly nonlinear model, KdV equation and the higher order uni-directional model with the choice  $\mu = \tilde{\mu}$  in figure 4.5. As the amplitude gets larger, the higher order uni-directional model provides a traveling wave solution which is closer to the strongly nonlinear model than the KdV equation, which agrees with its higher order asymptotic equivalence.

#### 4.7 The solitary waves produced by an arbitrary initial disturbance

The problem we are looking at is motivated by the laboratory experiment of Grue (see Chapter 3). We have shown in Chapter 3 that certain gate smoothing does not affect the wave profile substantially, especially for the primary solitary wave. We analyze the solitary wave solution by the inverse scattering transform with the step function initial condition, while setting  $\lambda = 0.1$  in numerical computations. With the goal of comparing numerical solutions with the analytical predictions from the inverse scattering transform technique, we set the domain and the final time to be long enough for the solitary waves to fully develop. Typically, we choose the tank length to be  $L = 128 \times 77 = 9856$  cm, so that the the total length of the extended domain is  $2L = 19712$  cm and the code runs up to  $T = 500$  s. Because of the long domain, for convenience, we only show waves in the subsection at the right end, from 4000 cm to 9856 cm.

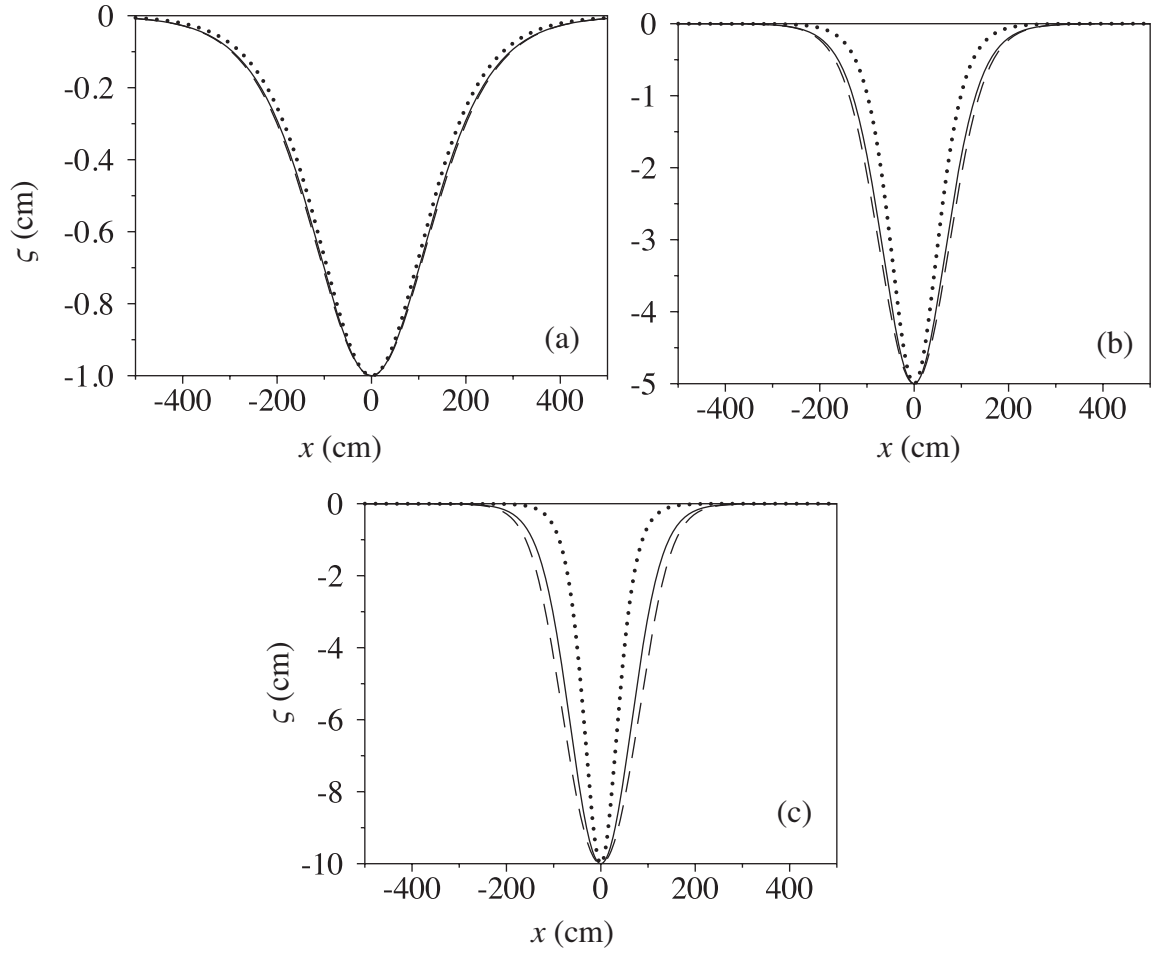


Figure 4.5: Traveling wave solutions from the strongly nonlinear model (solid), the higher-order unidirectional model with  $\mu = \tilde{\mu}$  (dashed) and the KdV equation (dotted) matching amplitude  $a$  with physical parameters introduced in § 4.7. (a):  $a = -1$  cm, (b):  $a = -5$  cm and (c):  $a = -10$  cm.

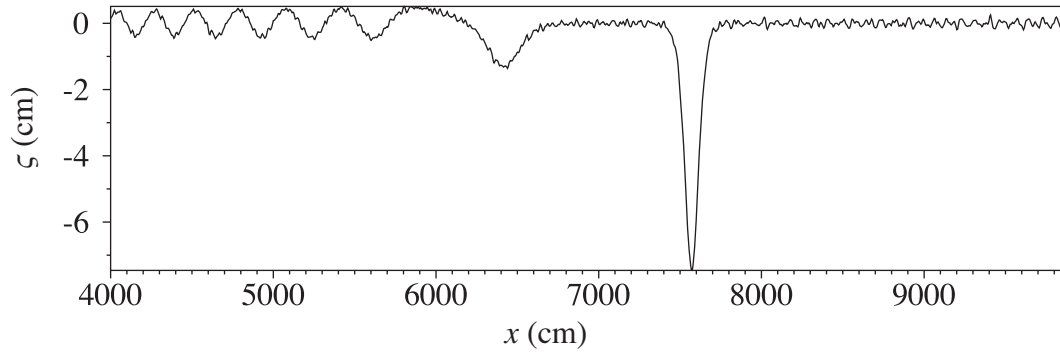


Figure 4.6: Snapshot of time evolution at  $T = 500$  s from the KdV equation.

#### 4.7.1 Solutions for the two-layer KdV equation

The initial conditions for our simulations are zero velocities and interface displacement given by

$$\zeta(x, 0) = \begin{cases} -h_{\text{gate}}, & |x| \leq L_{\text{gate}} \\ 0, & |x| > L_{\text{gate}} \end{cases} \quad (4.109)$$

where  $h_{\text{gate}} > 0$  and  $L_{\text{gate}} > 0$ . Waves generated by this initial condition propagate would physically propagate in both direction of the extended domain. A corresponding initial condition for uni-directional models needs to be defined. With zero initial velocity, the emerging waves can be viewed as superposition of the left and right going waves from the uni-directional model, to leading order (Wu [39])

$$\zeta_+(x, t) = \zeta_-(x, t) = \frac{1}{2}\zeta(x, t), \quad (4.110)$$

for  $t \geq 0$ . Applying the leading order formula for the uni-directional model, we obtain the initial conditions for  $\zeta_{\pm}$  as approximately

$$\zeta_{\pm}(x, 0) = \begin{cases} -\frac{1}{2}h_{\text{gate}}, & |x| \leq L_{\text{gate}} \\ 0, & |x| > L_{\text{gate}} \end{cases} \quad (4.111)$$

With the rescaling (4.15), the initial condition for equation (4.16) becomes

$$\zeta'_{\pm}(x, 0) = \begin{cases} \frac{1}{12}c_1c_2^{-\frac{1}{3}}h_{\text{gate}}, & |x| \leq c_2^{-\frac{1}{3}}L_{\text{gate}} \\ 0, & |x| > c_2^{-\frac{1}{3}}L_{\text{gate}} \end{cases} \quad (4.112)$$

This is a rectangular well of width  $l_{\text{well}} = 2c_2^{-\frac{1}{3}}L_{\text{gate}} > 0$  and depth  $d_{\text{well}} = \frac{1}{12}c_1c_2^{-\frac{1}{3}}h_{\text{gate}} >$

0. It gives rise to the eigenvalues (Landau & Lifshitz [30])

$$\sin\left(\frac{l_{\text{well}}\sqrt{d_{\text{well}} - k_n^2}}{2}\right) = \frac{k_n}{d_{\text{well}}}, \quad (4.113)$$

Depending on the values of  $l_{\text{well}}$  and  $d_{\text{well}}$ , there is always at least one eigenvalue. This might seem surprising, since even when  $l_{\text{well}}$  and  $d_{\text{well}}$  are very small, this result predicts that there will always be a solitary wave emerging from this potential well problem.

With the physical parameter  $h_{\text{gate}} = 10$  cm and  $L_{\text{gate}} = 100$  cm, following the inverse scattering transform technique in § 4.4, we find that there are two solitary waves emerging from this initial condition with amplitudes  $a_i^{\text{KdV}}$  and traveling speeds  $c_i^{\text{KdV}}$

$$a_1^{\text{KdV}} = -7.456 \text{ cm}, \quad c_1^{\text{KdV}} = 18.78 \text{ cm} \cdot \text{s}^{-1}; \quad a_2^{\text{KdV}} = -1.253 \text{ cm}, \quad c_2^{\text{KdV}} = 16.33 \text{ cm} \cdot \text{s}^{-1}, \quad (4.114)$$

A Crank-Nicolson scheme with pseudo-spectral method is applied to the two-layer KdV equation. As described in § 4.4, the time-step of the KdV equation is determined by the asymptotic behavior of the linear dispersion relation (4.22), so that

$$\Delta t < \frac{(\Delta x)^3}{\pi^2 c_2}. \quad (4.115)$$

We typically use  $\Delta t = 10^{-5}$  s for the choice of  $\Delta x = \frac{77}{32}$  cm grid size. This choice of time step allows the solution to achieve the second order convergence in time and the relative error is within 5e-3 in the infinite norm measurement at  $T = 500$  s. Because of the large speed for the high modes traveling to the opposite direction of the front wave in the periodic domain, the oscillation can cross the boundary quickly and affect the solitary wave (figure 4.6 ), resulting in the Talbot fractal effect (Chen & Olver [13]). We record the amplitude and phase of the front wave in table 4.1 at  $T = 100N$  s ,

Table 4.1: Tracking front wave amplitude  $a^{\text{KdV}}$  and phase  $X^{\text{KdV}}$  from two-layer KdV model for the two-layer dam-break problem with  $L_{\text{gate}} = 100$  cm and  $h_{\text{gate}} = 10$  cm at different snapshots.

$T$ (s)	100	200	300	400	500
$a^{\text{KdV}}$ (cm)	-7.45	-7.34	-7.41	-7.46	-7.40
$X^{\text{KdV}}$ (cm)	1917	3798	5689	7591	9462

where  $(N = 1, 2, 3, 4, 5)$ . The phase speed of the front wave seems to have settled to an asymptotic value already, whereas the amplitude of the front wave keeps oscillating due to Talbot-like effects.

#### 4.7.2 Solutions for the two-layer weakly nonlinear models for bi-directional waves

For the Kaup equations, with the initial condition (4.109) and rescaling (4.29), the potentials in the eigenvalue problem (4.32) are

$$q = 0, \quad \text{and} \quad r = \begin{cases} -\frac{b_3}{4b_1} h_{\text{gate}}, & \text{for } |x| \leq \sqrt{\frac{b_1}{b_4}} L_{\text{gate}} \\ 0, & \text{for } |x| > \sqrt{\frac{b_1}{b_4}} L_{\text{gate}} \end{cases} \quad (4.116)$$

Because of  $q = 0$ , the eigenvalue problem (4.32) is similar to the Schrödinger eigenvalue problem related to the KdV equation (4.17) by assigning

$$-\sigma_1^2 = \gamma^2 + \frac{1}{4}. \quad (4.117)$$

The solitary wave solutions are given by the inverse scattering transform (4.33), (4.37)-(4.39). For  $h_{\text{gate}} = 10$  cm and  $L_{\text{gate}} = 100$  cm, there are two solitary waves, with amplitudes and phase speeds in the same scaling as that from the the inverse scattering



prediction of the KdV equation:

$$a_1^{\text{Kaup}} = -6.843 \text{ cm}, c_1^{\text{Kaup}} = 18.645 \text{ cm}\cdot\text{s}^{-1}; a_2^{\text{Kaup}} = -1.233 \text{ cm}, c_2^{\text{Kaup}} = 16.320 \text{ cm}\cdot\text{s}^{-1}. \quad (4.118)$$

Because of the ill-posedness of the Kaup equations, we are unable to compare the numerical results with the inverse scattering predictions. Nonetheless, thanks to their asymptotic equivalences, the regularized Kaup equations (4.53)-(4.54) and the Boussinesq equations (4.77)-(4.79) can all be used to test the analytical predictions, since they are well-posed models and are numerically feasible.

The numerical scheme is a Runge-Kutta time integration with pseudo-spectral method. The linear dispersion relations of both models are the same as (4.80), and the asymptotic behavior for high modes allows  $\Delta t < \pi\sqrt{b_4/(b_1^2 b_2)}$ , regardless of the choice of  $\Delta x$ . We typically choose  $\Delta t = 5 \times 10^{-3}$  s and  $\Delta x = 77/128$  cm. By halving and doubling time-steps and grid sizes, we conclude that the relative error at  $T = 500$  s is 1e-6 in the infinite norm measurement. Table 4.2 are the amplitudes and phases of the front waves from two models. From  $T = 200$  s the front waves have settled to the speed of a solitary wave with no significant change in phases  $X$  and amplitudes  $a$ . From the figure, it is remarkable that the strongly nonlinear model agrees with the Euler simulations not only in well-capturing the front wave, but, also, in reproducing a large portion of the dispersive tail. The amplitude of the front wave from the regularized Kaup equations is closer to the inverse scattering prediction (4.118), with 1% difference, while that from the Boussinesq equations is within 11%.

The secondary waves from the two models, though not fully developed at  $T = 500$  s are also reported here for reference:  $a_2 = -1.293$  cm and  $-1.094$  cm for the regularized Kaup equations and the Boussinesq equations, respectively. For the secondary wave, the Boussinesq equations is slightly better, with 4.8% difference, than the regularized

Table 4.2: Tracking front wave amplitudes  $a$  and phases  $X$  from the two-layer regularized Kaup equations and the Boussinesq equations for the two-layer dam-break problem with  $L_{\text{gate}} = 100$  cm and  $h_{\text{gate}} = 10$  cm at different snapshots.

$T(\text{s})$	100	200	300	400	500
$a^{\text{reg}} (\text{cm})$	-6.763	-6.774	-6.774	-6.774	-6.774
$X^{\text{reg}} (\text{cm})$	1862	3715	5570	7423	9277
$a^{\text{Bs q}} (\text{cm})$	-7.549	-7.571	-7.572	-7.572	-7.571
$X^{\text{Bs q}} (\text{cm})$	1837	3667	5497	7327	9157
$a^{\text{Strongly}} (\text{cm})$	-5.995	-5.954	-5.950	-5.950	-5.950
$X^{\text{Strongly}} (\text{cm})$	1774	3557	5340	7124	8907

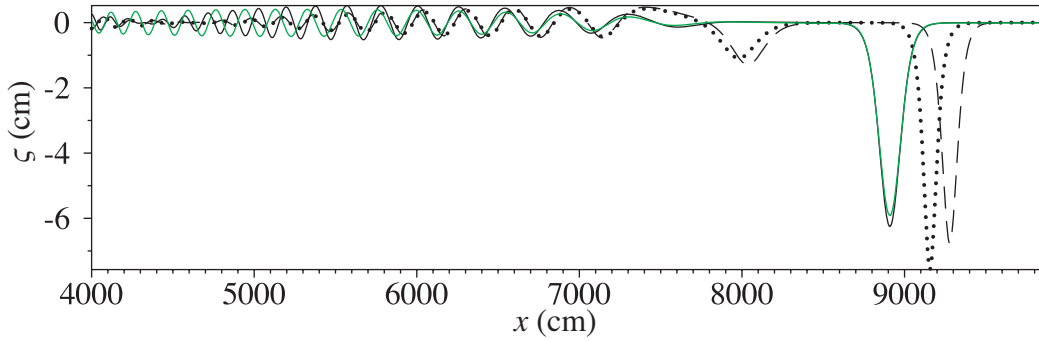


Figure 4.7: Snapshot of the time evolution from the regularized Kaup equations (dashed), the Boussinesq equations (dotted), the strongly nonlinear model (solid green) and the Euler simulation (solid) with the initial condition  $h_{\text{gate}} = 10$  cm and  $L_{\text{gate}} = 100$  cm, at  $T = 500$  s.

Kaup equations, with 11% difference. Overall, the regularized Kaup equations get result closer to the predictions from the Kaup equations in terms of amplitudes of solitary waves. Figure 4.7 is the snapshot at  $T = 500$  s with the regularized Kaup equations, the Boussinesq equations and the mean density isopycnocline from Euler simulations. Both models have big discrepancies on the phase comparing with the Euler simulations, while the regularized Kaup equations has a much better fit in amplitude of the front wave.

With the goal of predicting secondary solitary waves, we choose a wider gate with  $L_{\text{gate}} = 200$  cm and keep  $h_{\text{gate}} = 10$  cm. From the inverse scattering transform, there are three solitary waves with amplitudes (table 4.2). The amplitudes of front waves of

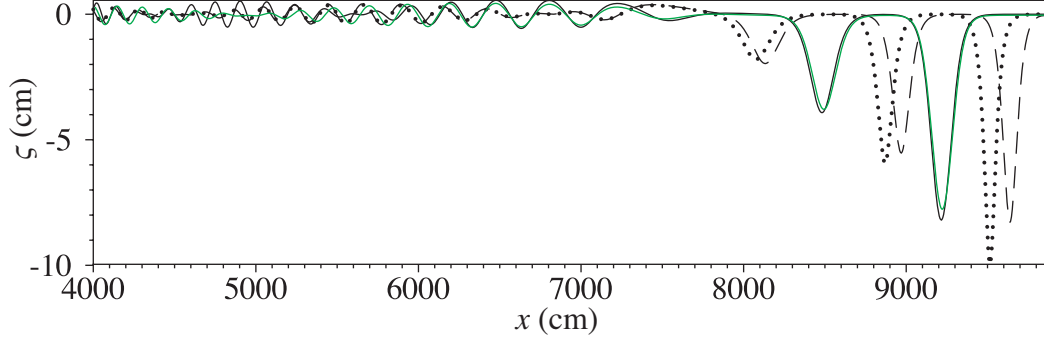


Figure 4.8: Snapshot of the time evolution from the regularized Kaup equations (dashed), the Boussinesq equations (dotted), the strongly nonlinear model (solid green) and the Euler simulation (solid) with the initial condition  $h_{\text{gate}} = 10$  cm and  $L_{\text{gate}} = 200$  cm, at  $T = 500$  s.

the numerical solutions from the two models are also reported in table 4.2. We find that the agreement between the regularized Kaup equations and the analytical predictions is significantly better for the first solitary wave. The Boussinesq equations have a slight better agreement for the secondary wave. For the third waves, although these have not formed at  $T = 500$  s, the regularized Kaup equations are better considering that the amplitudes will decrease after the solitary wave forms completely. Figure 4.8 is the snapshot at  $T = 500$  s from the regularized Kaup equations, the Boussinesq equations and the mean density isopycnocline from Euler simulations. The weakly nonlinear models from the analytical predictions and the numerical solutions from weakly nonlinear models all show that three solitary waves will emerge (table 4.3), with the regularized Kaup equations a better match for the front wave. Comparing to the Euler simulations, disregarding the phase shift, the regularized Kaup equations seems to predict the amplitude of the front wave from the Euler simulations quite accurately.

The wave amplitudes in this study, being around 7 cm as opposed to top layer thickness of 15 cm depth, may violate the assumption underlying the weakly nonlinear models, which could contribute to the discrepancies between the weakly nonlinear models and the Euler simulations. A smaller amplitude case, when  $h_{\text{gate}} = 1$  cm, can

Table 4.3: Values of amplitudes from inverse scattering predictions from Kaup equations and time evolutions from regularized Kaup equations, the Boussinesq equations and the Euler simulations at  $T = 500$  s for  $L_{\text{gate}} = 200$  cm and  $h_{\text{gate}} = 10$  cm.

$a^{\text{Kaup}}$ (cm)	-8.190	-5.902	-2.194
$a^{\text{reg}}$ (cm)	-8.281	-5.529	-1.965
$a^{\text{Bsqr}}$ (cm)	-8.960	-5.936	-1.790
$a^{\text{Strongly}}$ (cm)	-7.812	-3.789	N/A
$a^{\text{Euler}}$ (cm)	-8.198	-3.921	N/A

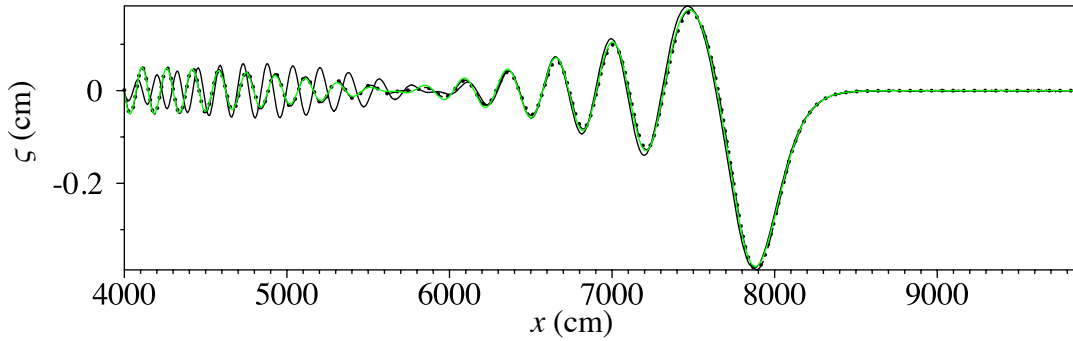


Figure 4.9: Snapshot of the time evolution from the regularized Kaup equations (dashed), the Boussinesq equations (dotted), the strongly nonlinear model (solid green) and the Euler simulation (solid) with the initial condition  $h_{\text{gate}} = 1$  cm and  $L_{\text{gate}} = 100$  cm, at  $T = 500$  s.

be used to test the importance of the small amplitude assumption. In figure 4.9, the strongly nonlinear models and the weakly nonlinear models provide similar wave structure, capturing front waves, but missing the dispersive tails at a distance. Note that in this case the solitary wave has not formed yet.

Initial conditions such as the step which violate the long wave assumption could also contribute to the occurrence of the ever forming dispersive tails. Next, we choose a long-wave initial condition with the interface located at

$$\zeta = -h_{\text{gate}} \operatorname{sech}^2 \left( \frac{x}{200} \right). \quad (4.119)$$

This is a very smooth profile comparing to the smoothed gate initial condition as

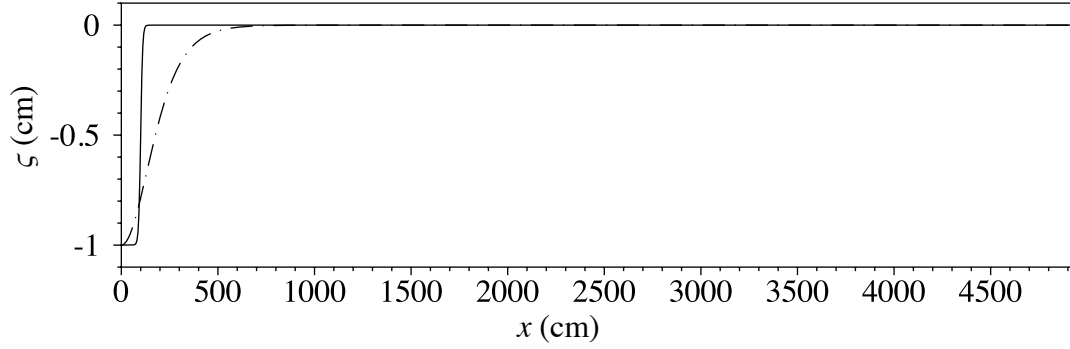


Figure 4.10: Initial conditions of  $\zeta$  with the set-up from the dam-break experiment (solid) and a long wave in the expression of equation (4.119) with the same amplitude ( $h_{\text{gate}} = 1$  cm) (dotted dash)

shown in figure 4.10. We can also apply IST to this configuration (Landau & Lifshitz [30]), where the eigenvalue problem, under appropriate transformations, turns into the equation of the associated Legendre polynomials. After rescaling variables, the initial condition becomes

$$\zeta' = \frac{b_3}{b_1} h_{\text{gate}} \operatorname{sech}^2 \left( \sqrt{\frac{b_4}{b_1}} \frac{x'}{200} \right). \quad (4.120)$$

Then  $r = -\frac{b_3}{4b_1} \zeta'$  and  $q = 0$  in the eigenvalue problem. Let  $H_0 = -\frac{b_3}{4b_1} h_{\text{gate}}$  and  $\beta = \sqrt{\frac{b_4}{b_1}}/200$ , the eigenvalue  $\gamma^2 = -(\sigma_1^2 - \frac{1}{4})$  is given by

$$\sigma_1 = \frac{\beta}{2} \left[ -(1 + 2n) + \sqrt{1 + \frac{4H_0}{\beta^2}} \right], \quad (4.121)$$

where the index  $n$  labels the possible eigenvalues,  $n = 0, 1, 2, \dots$ . For the choice  $h_{\text{gate}} = 1$  cm, we find from IST that the Kaup equations will give one solitary wave with the amplitude of  $-0.471$  cm.

Figure 4.11 shows that in this case, with  $h_{\text{gate}} = 1$  cm, the dispersive tail is much less active, being barely visible with respect to the primary wave. All three models have good agreement with the Euler simulation. Table 4.4 records amplitudes and phases at  $T = 500$  s. The discrepancy between the IST from the Kaup equations and

Table 4.4: Amplitudes and phases of front waves from models and the Euler simulations when the initial interface displacement is  $\zeta = \text{sech}^2(\frac{x}{200})$  at  $T = 500$  s.

	Kaup	reg. Kaup	Boussinesq	Strongly.	Euler
$a(\text{cm})$	-0.471	-0.487	-0.488	-0.482	-0.491
$X(\text{cm})$		7992	7991	7986	7973

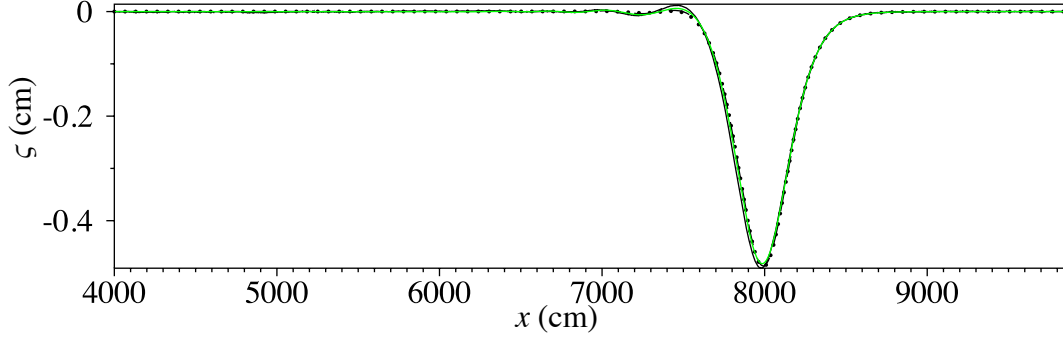


Figure 4.11: Snapshot of the time evolution from the regularized Kaup equations (dashed), the Boussinesq equations (dotted), the strongly nonlinear model (solid green) and the Euler simulation (solid) with the initial condition  $h_{\text{gate}} = 1$  cm, at  $T = 500$  s.

numerical results of weakly nonlinear models could be a consequence that the solitary waves having not completely separated from the dispersive tails.

#### 4.7.3 Higher order uni-directional model

For the high order uni-directional models, we do not have an analytical prediction for emerging solitary waves. Therefore we run numerical simulations, this time in a shorter tank with  $L = 2464$  cm and up to  $T = 80$  s. Because of its uni-directional wave propagation nature, the initial condition we choose is the same as for the KdV equation.

The linear dispersion relation for the higher order unidirectional model is

$$\omega(k) = \frac{c_0 k - (c_2 + \mu c_0) k^3}{1 - \mu k^2}, \sim (c_0 + \frac{c_2}{\mu}) k \text{ as } |k| \rightarrow \infty, \quad (4.122)$$

possibly leading to high oscillatory behavior for short waves. Note that the dispersion

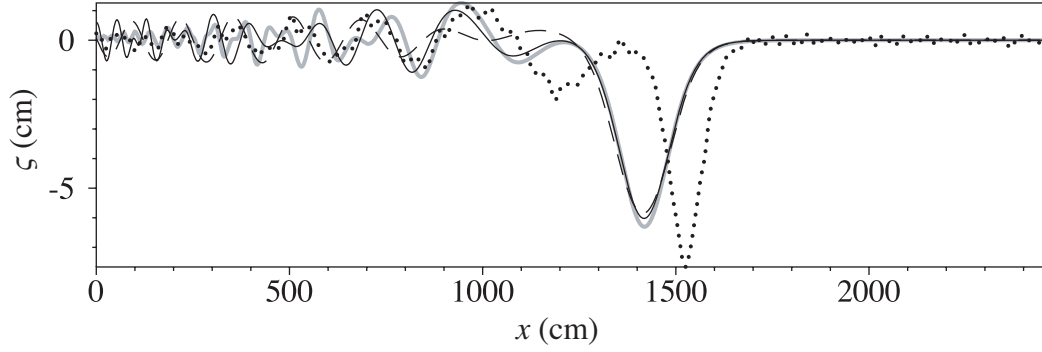


Figure 4.12: Snapshots for higher-order uni-directional model with  $\mu = \tilde{\mu}$  at  $T = 80$  s with domain  $L = 2464$  cm. Thick gray: Euler; solid: the strongly nonlinear model; dashed: higher-order uni-directional model with  $\mu = \tilde{\mu}$ ; dotted: the KdV equation

relation increases linearly with wave numbers, unlike the KdV model which has a cubic asymptotic behavior when  $k \rightarrow \infty$ . Its time step constraint is  $\Delta t < \frac{\mu \Delta x}{c_2 + c_0 \mu}$ , and the numerical schemes is Crank-Nicolson in time and pseudo-spectral in space. We typically use  $\Delta t = 10^{-3}$  s for  $\Delta x = 77/256$  cm grid sizes. At  $T = 80$  s, the higher order model with  $\mu = \tilde{\mu}$  shows an improvement from the KdV equation, in agreement with the front wave from the Euler simulation (figure 4.12). For the dispersive tails, the strongly nonlinear model again performs remarkably well. We also notice that the dispersive tail traveling to the opposite direction of the solitary wave begins to cross back into the periodic box, therefore at longer times it is expected that the dispersive tail will affect the front waves in a similar fashion as for the KdV solution.

## 4.8 Discussion

For small aspect ratios of the thickness of the fluid layers to typical wavelength, and small wave amplitude with respect to the fluid layer thicknesses, we have derived a bi-directional weakly nonlinear model by regularizing the ill-posed Kaup equations in a two-layer fluid system for the shallow water configuration. We have provided the exact traveling wave solution for the new model. Both the regularized Kaup equations and the

Boussinesq equations are put to use in the computation of the dam-break problem for internal wave generation experiments. The numerical results show excellent agreement with inverse scattering transform associated with completely integrable ill-posed Kaup equations.

For uni-directional models, we compare the two-layer KdV equation and the higher-order model suitable for moderate amplitude waves. The generic link between bi-directional and uni-directional models are yet to be found beyond the leading order, thus to choose appropriate initial condition is still an open question. For unidirectional models, the dispersion relations show high frequency oscillation in time for short waves propagating to the whole periodic domain and interacting with solitary waves. As a consequence, small time-step have to chosen to ensure numerical convergence. This phenomenon is believed to be a consequence of the asymptotic behavior of linear dispersion relations for short waves (Chen & Olver [13]). The higher-order uni-directional model is capable to handle moderate amplitude waves emerging from the potential well problem and compares well to the strongly nonlinear model. Its benign dispersion relation, in that high wavenumbers oscillations are limited to certain regimes to not overly restrict the time-step in numerical computations.

We have found intrinsic connections among different models. The combinations of inverse scattering transform theory has shown good agreement with numerical computations as far as the models' asymptotic equivalence. To the particular potential well problem in this work, it remains unclear whether there is a secondary wave emerging or not from the strongly nonlinear model and uni-directional model. Our investigation shows that the problem of seeking an appropriate model in the nonlinear regime with solvability both analytically and numerically remains open.



## Appendix A

### TRANSLATIONAL INVARIANCE AND SYMMETRIES

In this appendix we discuss the translational invariance of the system. Indeed, regardless of the kind of constraint represented by the lids, translation along the horizontal axis is a symmetry of the system, so that a conservation law should ensue, as already clearly pointed out by Benjamin [5]. However, this conserved quantity for motion between two rigid lids does *not* correspond to the horizontal component of momentum, as is usually the case in unconstrained dynamics; instead it includes a contribution from boundary terms, as we briefly summarize below. To tackle these issues, we review the Lagrangian and Hamiltonian formulation of the governing equation (2.1) for a heterogeneous fluid. It is fair to say that the results of this appendix can be derived from those in the referenced literature. However, it is useful to collect them here for self-consistency and ease of reference.

As it is well known, the Euler system (2.1) admits a variational formulation. We focus first on the Lagrangian approach, following Zakharov *et al.* [42], Zakharov & Kuznetsov [41]. The basic idea is to use a subset of the Euler equations as constraints in the Lagrangian. Thus, the action is written with the usual difference between kinetic and potential energy, plus terms with Lagrange multiplier for constraints,

$$\begin{aligned}
 A &\equiv \int_{t_0}^{t_1} L dt \\
 &= \int_{t_0}^{t_1} \left( \frac{1}{2} \int_{\mathcal{D}} \rho |\mathbf{v}|^2 dV - \int_{\mathcal{D}} \rho g z dV \right) dt \\
 &\quad + \int_{t_0}^{t_1} \left( \int_{\mathcal{D}} \Phi \nabla \cdot \mathbf{v} dV - \int_{\mathcal{D}} \lambda (\rho_t + (\mathbf{v} \cdot \nabla) \rho) dV \right) dt,
 \end{aligned} \tag{A.1}$$

where  $\mathcal{D}$  is the fluid domain and  $dV$  its (two-dimensional) volume measure. By varying the action  $A$  with respect to all the fields entering  $L$ , we get the following equations

$$\begin{aligned}\frac{\delta A}{\delta \Phi} = 0 &\Rightarrow \nabla \cdot \mathbf{v} = 0, & \frac{\delta A}{\delta \lambda} = 0 &\Rightarrow \rho_t + (\mathbf{v} \cdot \nabla) \rho = 0, \\ \frac{\delta A}{\delta \rho} = 0 &\Rightarrow \lambda_t + \nabla \cdot (\lambda \mathbf{v}) + \frac{1}{2} |\mathbf{v}|^2 - g z,\end{aligned}\tag{A.2}$$

and, in particular, the defining relation

$$\frac{\delta A}{\delta \mathbf{v}} = 0 \Rightarrow \rho \mathbf{v} - \nabla \Phi - \lambda \nabla \rho = 0.\tag{A.3}$$

This set of equations (Zakharov & Kuznetsov [41]) can be considered to be equivalent to the Euler equations (2.1).

When the domain, as in our case, is the infinite strip  $\mathcal{S} = \mathbb{R} \times [0, h]$ , translation along the  $x$ -axis is a symmetry of the system, and Noether's (first) theorem yields a conservation law for the Euler equations. As well known, for a Lagrangian system in 2 spatial dimensions with  $N$  fields  $(\varphi_1, \varphi_2, \dots, \varphi_N)$ , the expression for such a conservation law is

$$\sum_{\alpha=1}^N \left( \frac{\partial}{\partial t} \left( \frac{\partial L}{\partial \varphi_{\alpha,t}} \delta \varphi_{\alpha} \right) + \nabla \cdot \left( \frac{\partial L}{\partial \nabla \varphi_{\alpha}} \delta \varphi_{\alpha} \right) \right) = 0,\tag{A.4}$$

$\delta \varphi_{\alpha}$  being the infinitesimal variations of the field  $\varphi_{\alpha}$ . Taking into account that for  $x$ -translations  $\delta \varphi_{\alpha} = \varphi_{\alpha x}$ , the corresponding conservation law for the Lagrangian (A.1) is given by

$$\frac{\partial}{\partial t} (\lambda \rho_x) = \nabla \cdot \mathbf{J}, \quad \mathbf{J} = (\Phi u_x - \lambda u \rho_x, \Phi w_x - \lambda w \rho_x).\tag{A.5}$$

In order to properly identify the conserved quantity

$$\mathcal{I} = \int_{\mathcal{S}} \lambda \rho_x dV\tag{A.6}$$

it is useful to cast the problem in the Hamiltonian formalism.

The Hamiltonian  $H = T + U$  associated with the Lagrangian in (A.1) makes use of a pair of Clebsch variables  $(\lambda, \Phi)$  (the Lagrange multipliers of the Lagrangian), and reads

$$H = \int_S \left( \frac{1}{2} \rho |\mathbf{v}|^2 + g \rho z \right) dV \quad \text{with } \mathbf{v} = (\lambda \nabla \rho + \nabla \Phi) / \rho.$$

It turns out that the equations of motion imply

$$\rho_t = \frac{\delta H}{\delta \lambda}, \quad \lambda_t = -\frac{\delta H}{\delta \rho},$$

that is, the density  $\rho$  and the Clebsch variable  $\lambda$  are canonically conjugated to each other. We thus recover the conserved quantity (A.6), since, with respect to the canonical brackets, the functional generating translations along  $x$  is indeed

$$\mathcal{I} = \int_S \lambda \rho_x dV.$$

To proceed further, we connect this formalism with the set-up of Benjamin [5], which does not make use of the (implicitly defined) Clebsch variables. The basic variables here are the density  $\rho$  together with a kind of “density-weighted vorticity”  $\sigma$  defined by

$$\sigma = (\rho w)_x - (\rho u)_z. \tag{A.7}$$

The equations of motion for these two fields are

$$\begin{aligned} \rho_t + u \rho_x + w \rho_z &= 0 \\ \sigma_t + u \sigma_x + w \sigma_z + \rho_x \left( g z - \frac{1}{2} (u^2 + w^2) \right)_z + \frac{1}{2} \rho_z (u^2 + w^2)_x &= 0 \end{aligned} \tag{A.8}$$

They can be written in the form

$$\rho_t = - \left[ \rho, \frac{\delta H}{\delta \sigma} \right], \quad \sigma_t = - \left[ \rho, \frac{\delta H}{\delta \rho} \right] - \left[ \sigma, \frac{\delta H}{\delta \sigma} \right], \tag{A.9}$$

where, by definition,  $[A, B] := A_x B_z - A_z B_x$ , and

$$H = \int_S \frac{1}{2} \rho (|\mathbf{v}|^2 + gz) \, dV. \quad (\text{A.10})$$

In turn, the Hamiltonian  $H$  is to be written in terms of the stream function  $\psi$ , which is related to Benjamin's variables  $(\rho, \sigma)$  via

$$\sigma = (\rho w)_x - (\rho u)_z = -(\rho \psi_x)_x - (\rho \psi_z)_z = -\rho \nabla^2 \psi - \nabla \rho \cdot \nabla \psi. \quad (\text{A.11})$$

As shown by Benjamin, equations (A.9) are actually a Hamiltonian system with respect to a non-canonical (actually, Lie algebraic) Hamiltonian structure, i.e., (A.8) can be written as

$$\rho_t = \{\rho, H\}_B, \quad \sigma_t = \{\sigma, H\}_B$$

for the Poisson bracket that can be easily spelled out by (A.9).

A straightforward computation shows that the canonical (Zakharov *et al.* [42]) and modified (Benjamin [5]) Hamiltonian structures are equivalent under the “coordinate transformation”

$$(\rho, \lambda) \rightarrow (\rho, \sigma) = (\rho, \lambda_x \rho_z - \lambda_z \rho_x), \quad (\text{A.12})$$

where the equality  $\sigma = \lambda_x \rho_z - \lambda_z \rho_x$  is a consequence of (A.3).

Benjamin's formalism [5] is explicitly tailored for symmetries. The generator of translations along the horizontal directions (the “impulse”) is, as it is easily verified,

$$\mathcal{I} = \int_{\mathcal{D}} z \sigma(x, z) \, dV.$$

In particular, for two-dimensional motion between two rigid horizontal lids we have a

bulk and boundary components,

$$\mathcal{I} = \int_{\mathcal{S}} \rho u \, dV - \int_{\mathbb{R}} z \rho u|_{z=0}^{z=h} \, dx,$$

where the first term in this sum is the ordinary total horizontal momentum, while the second term is a boundary term — called  $B_6$  in [5]. Indeed we have, in the infinite strip  $\mathcal{S} = \mathbb{R} \times [0, h]$ ,

$$\begin{aligned} \int_{\mathcal{S}} z \sigma \, dV &= \int_{\mathcal{S}} z(\rho w)_x \, dV - \int_{\mathcal{S}} z(\rho u)_z \, dV \\ &= \int_0^h \left( \int_{\mathbb{R}} (z \rho w)_x \, dx \right) dz - \int_{\mathbb{R}} \left( \int_0^h z(\rho u)_z \, dz \right) dx \\ &= \int_0^h z \rho w|_{x=-\infty}^{x=+\infty} \, dz - \int_{\mathbb{R}} z \rho u|_{z=0}^{z=h} \, dx + \int_{\mathcal{S}} \rho u \, dV \\ &= - \int_{\mathbb{R}} z \rho u|_{z=0}^{z=h} \, dx + \int_{\mathcal{S}} \rho u \, dV, \end{aligned} \tag{A.13}$$

thanks to the boundary conditions. This yields

$$\mathcal{I} + \int_{\mathbb{R}} z \rho u|_{z=0}^{z=h} \, dx = \int_{\mathbb{R} \times [0, h]} \rho u \, dV.$$

Using the Euler equation for the horizontal momentum (see (2.4))

$$(\rho u)_t = -\frac{1}{2} \rho_x (u^2 + w^2) - \left[ \frac{1}{2} \rho (u^2 + w^2) + p \right]_x + w \sigma \tag{A.14}$$

at  $z = h$  (where  $w$  vanishes) yields

$$(\rho u)_t = -\frac{1}{2} \rho_x (u^2) - \left[ \frac{1}{2} \rho u^2 + p \right]_x,$$

and so

$$\frac{dB_6}{dt} = -h \left( \int_{\mathbb{R}} \frac{1}{2} \rho_x (u^2)|_{z=h} \, dx + p(+\infty, h) - p(-\infty, h) \right). \tag{A.15}$$

In the case of constant density at the top lid, and with an equilibrium distribution  $\rho_0 = \rho_0(z)$  (the case of Benjamin [5]), this reduces to

$$\frac{dB_6}{dt} = -h(p(+\infty, h) - p(-\infty, h)).$$

Quoting Benjamin [5]:

*“Here  $p(+\infty, h)$  and  $p(-\infty, h)$  are the pressure levels as  $x = +\infty$  and  $x = -\infty$  relative to hydrostatic pressure in the quiescent state of the whole system; and while only their difference can have any dynamic significance there is no reason in general for it to be zero or take any other constant value.”*

In the bulk of the paper we have constructed solutions for which this pressure difference can be computed analytically. Here we have consistently recovered that the system admits a conservation law corresponding to the  $x$ -translational invariance, but this quantity might not coincide (in general) with the  $x$ -component of the total momentum. Rather, the invariant is the sum of such a bulk term and of the boundary term  $B_6$ , whose time variation is given by the pressure imbalance of the system for  $x \rightarrow \pm\infty$ .

## Appendix B

### BOUNDARY EFFECTS IN AIR WATER SYSTEMS

For those configurations in which the interface of a two-layer fluid coincides somewhere with one of the channel upper or lower boundaries, the formulae previously computed may, in general, be incorrect and have to be appropriately modified. This is best appreciated by looking at specific examples, which we consider next. A deeper and more systematic analysis of this kind of phenomena would be outside of the aims of the present paper and will be reported separately. Here we limit ourselves to a brief discussion, by using the long-wave model, of how the combination of “air-water”-like stratification and boundary effects influence the pressure imbalance.

As previously remarked, in the long-wave (dispersionless) approximation, the pressure difference  $P_\Delta$  is given by

$$P_\Delta = h \int_{-\infty}^{\infty} \frac{(\overline{u_1} \overline{u_2})_x}{\eta_2/\rho_2 + \eta_1/\rho_1} dx. \quad (\text{B.1})$$

If the interface is (sufficiently) far from the upper boundary (that is, if  $\eta_2(x) = \eta(x) \neq h$  for all  $x$ ), then  $P_\Delta$ , for fixed  $\rho_2$ , goes to zero when  $\rho_1$  goes to zero. However, the same conclusion cannot be drawn when the region occupied by the lighter fluid is disconnected.

In order to study this problem for  $\rho_1 \rightarrow 0$ , let us rewrite (B.1) as

$$P_\Delta = h \int_{\mathbb{R}/\mathcal{C}} \frac{(\overline{u_1} \overline{u_2})_x}{\eta_2/\rho_2 + \eta_1/\rho_1} dx + h \int_{\mathcal{C}} \frac{(\overline{u_1} \overline{u_2})_x}{\eta_2/\rho_2 + \eta_1/\rho_1} dx, \quad (\text{B.2})$$

where  $\mathcal{C}$  is the subset of  $\mathbb{R}$  (which we can assume, for the sake of definiteness, to be the

segment  $\mathcal{C} = [x^L, x^R]$  ) where  $\eta_1$  is sufficiently small in such a way that

$$\frac{\rho_1}{\eta_1} \simeq \frac{\rho_2}{\eta_2} \quad (\text{B.3})$$

holds even if  $\rho_1 \ll \rho_2$ . In this case only the second integral contributes to the pressure imbalance  $P_\Delta$ . If we consider the double scaling limit  $\rho_1/\eta_1 \simeq \rho_2/\eta_2$  for  $\rho_1 \rightarrow 0$  and  $\eta_1 \rightarrow 0$  (and therefore  $\mathcal{C} = \{x \in \mathbb{R} \mid \eta_1(x) \leq h\rho_1/\rho_2\}$ ), then relation (B.2) becomes

$$P_\Delta = \rho_2 h \int_{\mathcal{C}} \frac{(\overline{u_1} \overline{u_2})_x}{2\eta_2} dx \simeq \frac{\rho_2}{2} \overline{u_1} \overline{u_2} \Big|_{x^L}^{x^R}. \quad (\text{B.4})$$

Hence, in this particular limit, there is no reason for  $P_\Delta$  to vanish when  $\rho_1$  goes to zero.

We finally mention that a similar qualitative result can be obtained in the case of zero initial velocities, provided that the dispersive terms of (2.45) be included in the calculation of  $P_\Delta$ . In the same approximations of the dispersionless case we obtain the estimate

$$P_\Delta \sim -\frac{g\rho_2 h^2}{12} \eta_{2xx} \Big|_{x^L}^{x^R}. \quad (\text{B.5})$$



## Appendix C

### INDEPENDENT DIRECT NUMERICAL SIMULATIONS

#### C.1 Solitary wave collisions

Chapter 2 reveals that the pressure imbalance at infinite ends for an incompressible stratified Euler fluid with initial interface displacement localized in the center. Chapter 3 presents that a two-layer dam break problem can generate solitary waves. Now we consider to place dams at both ends of the long wave channel with rigid wall boundary conditions. There should be pressure difference when the two dams are not symmetrically built from the very beginning. We carry out numerical studies for both symmetric and asymmetric case.

The physical parameters are same as introduced in Chapter 3, where  $\rho_1 = 0.999 \text{ g}\cdot\text{cm}^{-3}$ ,  $\rho_2 = 1.022 \text{ g}\cdot\text{cm}^{-3}$ ,  $h_1 = 15 \text{ cm}$ ,  $h_2 = 62 \text{ cm}$  and  $g = 981 \text{ cm}\cdot\text{s}^{-2}$ . The transition layer is approximately 4 cm. For the symmetric case, we choose  $h_{\text{gate}} = 10 \text{ cm}$  and  $L_{\text{gate}} = 100 \text{ cm}$  for both left and right side. For the asymmetric case, we alter the height of the gate at the right end to be 15 cm. The gate are smoothed by a hyperbolic tangent function as in Chapter 3 where  $\lambda = 0.1$ .

The snapshots for both cases are in figure C.1. The symmetric initial condition maintains its symmetry from the beginning to end, where the emerged solitary waves begin to collide at around 60 s. The asymmetric initial condition generate solitary waves with different amplitudes, and they begin to collide at around 60 s. The pressure difference at far ends should be zero for the symmetric case as suggested in Chapter 2, but not for the asymmetric case. Figure C.2 records the pressure difference for the two cases, we note that the pressure imbalance for the asymmetric case is largest at the

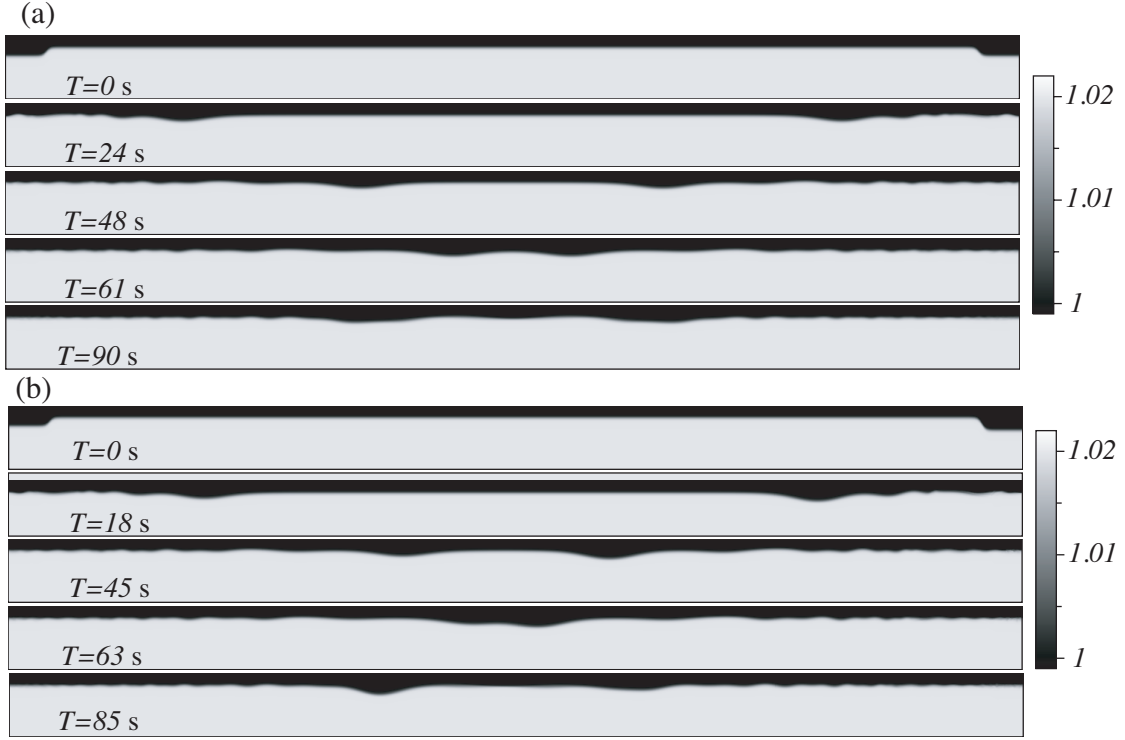


Figure C.1: Snapshots of collisions of two solitary waves generated from dam-break at two ends. (a): symmetric case; (b) asymmetric case with different gate height at two ends

initial times. It settles to zero and then slowly begins to form an oscillatory pattern around zero.

## C.2 Dam-break problem

This section is a direction numerical simulation with the physical parameter close to an experiment performed in the wave tank in the Fluids Lab at UNC, where  $\rho_1 = 0.989 \text{ g}\cdot\text{cm}^{-3}$ ,  $\rho_2 = 1.011 \text{ g}\cdot\text{cm}^{-3}$ ,  $h_1 = 12 \text{ cm}$ ,  $h_2 = 30 \text{ cm}$  and  $g = 981 \text{ cm}\cdot\text{s}^{-2}$ . The tank is 2688 cm long, and  $L_{\text{gate}} = 900 \text{ cm}$  and  $h_{\text{gate}} = 9 \text{ cm}$ . The thickness of the pycnocline is about 4 cm and the gate is represented as a strict step function, without any smoothing effect. Figure C.3 is snapshots from the numerical simulation.

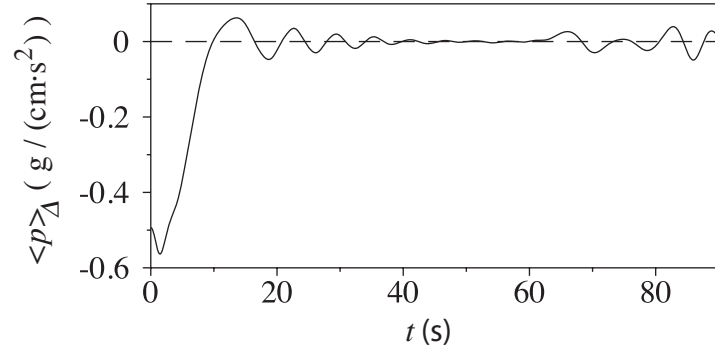


Figure C.2: Time series of  $P_{\Delta}$  for solitary wave collisions with symmetric dam set-up (dashed) and asymmetric dam set-up (solid)

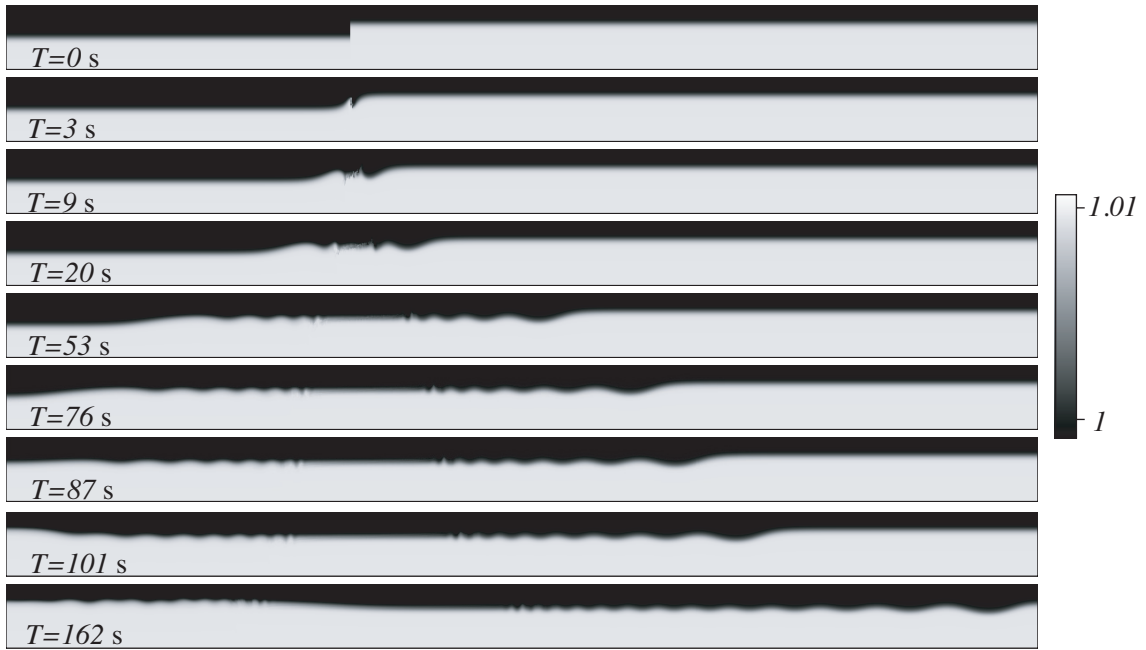


Figure C.3: Snapshots of the dam-break problem with a gate in the dimension of  $L_{\text{gate}} = 900$  cm and  $h_{\text{gate}} = 9$  cm in a 2688 cm long tank.

## Appendix D

### CODES FOR MODELS

#### D.1 The strongly nonlinear model

##### Main code

```
PROGRAM GreenNaghdi

  use parameters

  implicit none

  double precision, dimension(0:nx-1) :: x, u, eta, zeta, u1, zeta1
  double complex :: Dfft(0:nxhalf)
  double complex, parameter :: I = cmplx(0.d0, 1.d0)
  double precision:: k0, tnow, M0, E0
  double precision :: tnow1
  double precision, dimension(0:nx-1) :: uK1, uK2, uK3, uK4
  double precision, dimension(0:nx-1) :: zetaK1, zetaK2, zetaK3, zetaK4
  double precision :: xval

  integer *8 plan
  integer :: remainfilter
  integer kstep, tstep, cut1
  double precision:: dx, dt, timerecord
  integer :: nframe
  character(len = 20) :: nu, nzeta

  dt = dt_fix
  xval = 0.d0
  dx = (R-L)/nx
```

```

nframe = 0

tnow = 0.d0

timerecord = 0.d0


do kstep = 0, nxhalf
Dfft(kstep) = 2*pi*I/(R-L)*kstep
end do

!*****initial condition
do kstep = 0, nx-1
x(kstep) = L+dx*kstep
zeta(kstep) = hgate/2.d0*(dtanh(lambda*(x(kstep)-lgate)) &
-dtanh(lambda*(x(kstep)+lgate)))
end do

u = 0.d0

!*****write initial condition
write(nu,'(a,i0,a)') 'result',nframe, '.dat'
open(11, file = nu)
do kstep = 0, nx-1
write(11,505) x(kstep), zeta(kstep), u(kstep)
end do
close (11)

nframe = nframe +1


open (41, file = 'outputTS') !write time series to file
k0 = 0.d0

cut1= nxhalf-1

```

```

remainfilter = 0

!***** first time evolution, get an estimate for uK1
call TimeDerivative2(cut1, xval, u, zeta, x, Dfft, k0, uK1, zetaK1)
do while ((tnow+1d-10).le. stop_time )
tstep = tstep+1

!***** write data every mkframe second
if((timerecord+1.d-10) .ge. mkframe) then
write(nu,'(a,i0,a)') 'result',nframe, '.dat'
open(11, file = nu)
do kstep = 0, nx-1
write(11,506) x(kstep), zeta(kstep), u(kstep)
end do
close (11)
nframe = nframe+1
timerecord = 0.d0
end if

!***** compute conserved quantities M and E
call conserve (u, zeta, Dfft, M0, E0)
write(41, 506) tnow, E0, cut1, M0

remainfilter = remainfilter+1
if (tnow+dt .ge. stop_time) then
dt = stop_time-(tnow)
end if
u1 = u
zeta1 = zeta

```

```

tnow1 = tnow
call TimeDerivative2(cut1, xval, u1, zeta1, x,Dfft, k0, uK1, zetaK1)
u1 = u+half*dt*uK1
zeta1 = zeta +half*dt*zetaK1
tnow1 = tnow +half*dt
uK2 = uK1
call TimeDerivative2(cut1, xval, u1, zeta1, x, Dfft, k0, uK2, zetaK2)
u1 = u+half*dt*uK2
zeta1 = zeta + half*dt*zetaK2
tnow1 = tnow + half*dt
uK3 = uK2
call TimeDerivative2(cut1, xval, u1, zeta1, x, Dfft, k0, uK3, zetaK3)
u1 = u+ dt*uK3
zeta1 = zeta + dt*zetaK3
tnow1 = tnow + dt
uK4 = uK3
call TimeDerivative2(cut1, xval, u1, zeta1, x, Dfft, k0, uK4, zetaK4)
u = u + dt * (uK1+2.d0*uK2+2.d0*uK3+uK4)*sixth
zeta = zeta + dt * (zetaK1+2.d0*zetaK2+2.d0*zetaK3+zetaK4)*sixth
!*****get initial guess for iteration for the next time step
uK1 = (uK1+2.d0*uK2+2.d0*uK3+uK4)*sixth
!***** decide whether or not to apply filter
if(remainfilter .ge. Nfilter ) then
call filter(cut1, u, zeta)
print *, 'filtering'
remainfilter = 0

```

```

end if

tnow = tnow + dt

timerecord = timerecord + dt

end do

!***** write final result

open(21, file = 'result.dat' ) ! final result

do kstep = 0,nx-1

write(21, 505)x(kstep), zeta(kstep), u(kstep)

end do

close (21)

close(41)

505 format(D30.20, 1x, D30.20,1x, D30.20, 1x)

506 format(D30.20, 1x, D30.20, 1x, D30.20, 1x, D30.20, 1x)

end program GreenNaghdi


subroutine filter( cut1, u, zeta)

use parameters

implicit none

include 'fftw3.f'

integer, intent(INOUT) :: cut1

double precision, dimension(0:nx-1), intent(INOUT) :: u, zeta

integer :: cut2, cut3, kstep

double complex, dimension (0:nxhalf) :: ucomplex, zetacomplex

integer *8 :: plan

cut3 = cut1

```



```

cut1 = floor(cut1_coef*cut3)
cut2 = max(floor (cut2_coef*db1e(cut3)), cut2_lim)

if (cut1 .le. nxhalf-1) then
call dfftw_plan_dft_r2c_1d(plan,nx,u,ucomplex,FFTW_ESTIMATE)
call dfftw_execute_dft_r2c(plan, u, ucomplex)
call dfftw_destroy_plan(plan)

call dfftw_plan_dft_r2c_1d(plan,nx, zeta, zetacomplex,FFTW_ESTIMATE)
call dfftw_execute_dft_r2c(plan, zeta, zetacomplx)
call dfftw_destroy_plan(plan)

ucomplex = ucomplex/db1e(nx)
zetacomplex = zetacomplex/db1e(nx)
do kstep = cut1, min(nxhalf, cut2)
ucomplex(kstep) = ucomplex(kstep) *dcos(2.d0*datan(1.d0)&
*(cut1-kstep)/(cut1-cut2))**2
zetacomplex(kstep) = zetacomplex(kstep) * dcos(2.d0*datan(1.d0)&
*(cut1-kstep)/(cut1-cut2))**2
end do

if (cut2 .le. nxhalf) then
do kstep = cut2, nxhalf
ucomplex(kstep) = 0.d0
zetacomplex(kstep) = 0.d0
end do

```

```

end if

call dfftw_plan_dft_c2r_1d(plan,nx, ucomplex, u,FFTW_ESTIMATE)
call dfftw_execute_dft_c2r(plan, ucomplex, u)
call dfftw_destroy_plan(plan)
call dfftw_plan_dft_c2r_1d(plan,nx, zetacomplex, zeta, FFTW_ESTIMATE)
call dfftw_execute_dft_c2r(plan, zetacomplex, zeta)
call dfftw_destroy_plan(plan)
end if

cut1 = cut3

end subroutine filter

subroutine TimeDerivative2(cut1, xval, u1, zeta, x, Dfft, k0, &
                           u1RHS, zetaRHS )

use parameters

implicit none

include 'fftw3.f'

integer, intent(INOUT) :: cut1

double precision, intent(INOUT) :: xval, k0

double precision, dimension(0:nx-1), intent(IN) :: u1, zeta, x
double precision, dimension(0:nx-1), intent(INOUT):: u1RHS, zetaRHS
double complex , dimension(0:nxhalf), intent(IN) :: Dfft

integer *8 plan

integer :: kstep, cut2, cut3

```

```

double precision :: step, maxktemp, stablecheck
double precision :: U0, k1, nx_inv, K, f_u_mean, g_u_mean, h_u_mean
double precision :: relaxation
double complex :: Dfft_now
double precision :: f1, amp
double precision, dimension(0:nx-1) :: u2, eta1_inv, eta2_inv, add
double precision, dimension(0:nx-1) :: f_u, g_u, h_u
double precision, dimension(0:nx-1) :: f_zeta, g_zeta, h_zeta
double precision, dimension(0:nx-1) :: f_u_a, g_u_a
double precision, dimension(0:nx-1) :: h_u_a, f_zeta_z
double precision, dimension(0:nx-1) :: g_zeta_z, h_zeta_a
double precision, dimension(0:nx-1) :: eta1, eta2,
double precision, dimension(0:nx-1) :: u1_a, u2_a, zeta_a
double precision, dimension(0:nx-1) :: eta1_a, eta2_a,
double precision, dimension(0:nx-1) :: eta1_inv_a, eta2_inv_a
double precision, dimension(0:nx-1) :: u1_x, u2_x, u1_xx
double precision, dimension(0:nx-1) :: u2_xx, u1_xxx
double precision, dimension(0:nx-1) :: u2_xxx, zeta_t, zeta_tx, zeta_txx
double precision, dimension(0:nx-1) :: zeta_x, zeta_xx
double precision, dimension(0:nx-1) :: u1RHS_x, u1RHS_xx
double precision, dimension(0:nx-1) :: test1, test2, test3, total_RHS
double precision, dimension(0:nx-1) :: part1, part2, u1_add, u2_add
double precision, dimension(0:nx-1) :: resi, resi1, u1RHStemp
double precision, dimension(0:nx-1) :: part1_a, part2_a
double precision, dimension(0:nx-1) :: u1_add_a, u2_add_a
double complex, dimension(0:nxhalf):: u1_cplx, u2_cplx, zeta_cplx

```

```

double complex,    dimension(0:nxhalf)::eta1_cplx, eta2_cplx
double complex,    dimension(0:nxhalf):: eta1_inv_cplx, eta2_inv_cplx
double complex,    dimension(0:nxhalf):: u1_xcplx, u2_xcplx, u1_xxcplx
double complex,    dimension(0:nxhalf):: u2_xxcplx, zeta_xcplx
double complex,    dimension(0:nxhalf):: zeta_xxcplx, zeta_txxcplx
double complex,    dimension(0:nxhalf):: zeta_tcplx, zeta_txcplx
double complex, dimension(0:nxhalf) :: u1_xxxcplx, u2_xxxcplx
double complex, dimension(0:nxhalf) :: u1RHS_cplx
double complex, dimension(0:nxhalf) :: resi_cplx, resi1_cplx, add_cplx
double complex, dimension(0:nxhalf) :: u1RHS_xcplx, u1RHS_xxcplx

nx_inv = 1.d0/dbl(nx)

eta1 = h1 - zeta
eta2 = h2 + zeta

! *****iteration criterion
relaxation = min(h1/maxval(abs(zeta)),5.d-1)

do kstep = 0, nx-1
eta1_inv(kstep) = 1.d0/eta1(kstep)
eta2_inv(kstep) = 1.d0/eta2(kstep)
end do

call dfftw_plan_dft_r2c_1d(plan,nx,u1,u1_cplx,FFTW_ESTIMATE)
call dfftw_execute_dft_r2c(plan, u1, u1_cplx)
call dfftw_destroy_plan(plan)

call dfftw_plan_dft_r2c_1d(plan,nx, eta1_inv, eta1_inv_cplx,FFTW_ESTIMATE)
call dfftw_execute_dft_r2c(plan, eta1_inv, eta1_inv_cplx)
call dfftw_destroy_plan(plan)

```

```

call dfftw_plan_dft_r2c_1d(plan,nx, eta2_inv, eta2_inv_cplx,FFTW_ESTIMATE)
call dfftw_execute_dft_r2c(plan, eta2_inv, eta2_inv_cplx)
call dfftw_destroy_plan(plan)
call dfftw_plan_dft_r2c_1d(plan,nx, eta1, eta1_cplx,FFTW_ESTIMATE)
call dfftw_execute_dft_r2c(plan, eta1, eta1_cplx)
call dfftw_destroy_plan(plan)
call dfftw_plan_dft_r2c_1d(plan,nx, eta2, eta2_cplx,FFTW_ESTIMATE)
call dfftw_execute_dft_r2c(plan, eta2, eta2_cplx)
call dfftw_destroy_plan(plan)
call dfftw_plan_dft_r2c_1d(plan,nx, zeta, zeta_cplx,FFTW_ESTIMATE)
call dfftw_execute_dft_r2c(plan, zeta, zeta_cplx)
call dfftw_destroy_plan(plan)

u1_cplx = u1_cplx* nx_inv
eta1_cplx = eta1_cplx*nx_inv
eta2_cplx = eta2_cplx*nx_inv
eta1_inv_cplx = eta1_inv_cplx*nx_inv
eta2_inv_cplx = eta2_inv_cplx*nx_inv
zeta_cplx = zeta_cplx * nx_inv

do kstep = ceiling(nxhalf/4.d0), nxhalf
u1_cplx (kstep) = 0.d0
eta1_cplx(kstep) = 0.d0
eta2_cplx(kstep) = 0.d0
eta1_inv_cplx(kstep) = 0.d0
eta2_inv_cplx(kstep) = 0.d0

```

```

zeta_cplx(kstep) = 0.d0
end do

u1_xcplx = 0.d0
zeta_xcplx = 0.d0
u1_xxcplx = 0.d0
zeta_xxcplx = 0.d0
u1_xxxcplx = 0.d0
  do kstep = 0, floor(nxhalf/4.d0)
u1_xcplx(kstep) = u1_cplx(kstep) *Dfft(kstep)
u1_xxcplx(kstep) = u1_xcplx(kstep) *Dfft(kstep)
u1_xxxcplx(kstep) = u1_xxcplx(kstep) * Dfft(kstep)
zeta_xcplx(kstep) = zeta_cplx(kstep) *Dfft(kstep)
zeta_xxcplx(kstep) = zeta_xcplx(kstep) *Dfft(kstep)
end do

call dfftw_plan_dft_c2r_1d(plan,nx,u1_cplx, u1_a,FFTW_ESTIMATE)
call dfftw_execute_dft_c2r(plan, u1_cplx, u1_a)
call dfftw_destroy_plan(plan)
call dfftw_plan_dft_c2r_1d(plan,nx,zeta_cplx, zeta_a,FFTW_ESTIMATE)
call dfftw_execute_dft_c2r(plan, zeta_cplx, zeta_a)
call dfftw_destroy_plan(plan)
call dfftw_plan_dft_c2r_1d(plan,nx, eta1_cplx, eta1_a,FFTW_ESTIMATE)
call dfftw_execute_dft_c2r(plan, eta1_cplx, eta1_a)
call dfftw_destroy_plan(plan)
call dfftw_plan_dft_c2r_1d(plan,nx, eta2_cplx, eta2_a,&

```

```

FFTW_ESTIMATE)

call dfftw_execute_dft_c2r(plan, eta2_cplx, eta2_a)
call dfftw_destroy_plan(plan)
call dfftw_plan_dft_c2r_1d(plan,nx, eta1_inv_cplx, eta1_inv_a,&
FFTW_ESTIMATE)
call dfftw_execute_dft_c2r(plan, eta1_inv_cplx, eta1_inv_a)
call dfftw_destroy_plan(plan)
call dfftw_plan_dft_c2r_1d(plan,nx, eta2_inv_cplx, eta2_inv_a, &
FFTW_ESTIMATE)
call dfftw_execute_dft_c2r(plan, eta2_inv_cplx, eta2_inv_a)
call dfftw_destroy_plan(plan)
call dfftw_plan_dft_c2r_1d(plan,nx,u1_xcplx, u1_x,FFTW_ESTIMATE)
call dfftw_execute_dft_c2r(plan, u1_xcplx, u1_x)
call dfftw_destroy_plan(plan)
call dfftw_plan_dft_c2r_1d(plan,nx,zeta_xcplx, zeta_x,FFTW_ESTIMATE)
call dfftw_execute_dft_c2r(plan, zeta_xcplx, zeta_x)
call dfftw_destroy_plan(plan)
call dfftw_plan_dft_c2r_1d(plan,nx,u1_xxcplx, u1_xx,FFTW_ESTIMATE)
call dfftw_execute_dft_c2r(plan, u1_xxcplx, u1_xx)
call dfftw_destroy_plan(plan)
call dfftw_plan_dft_c2r_1d(plan,nx,zeta_xxcplx, zeta_xx,FFTW_ESTIMATE)
call dfftw_execute_dft_c2r(plan, zeta_xxcplx, zeta_xx)
call dfftw_destroy_plan(plan)
call dfftw_plan_dft_c2r_1d(plan,nx,u1_xxxcplx, u1_xxx,FFTW_ESTIMATE)
call dfftw_execute_dft_c2r(plan, u1_xxxcplx, u1_xxx)
call dfftw_destroy_plan(plan)

```

```

do kstep = 0, nx-1
u2(kstep) = u1_a(kstep) - hh*eta2_inv_a(kstep) * u1_a(kstep)
end do

!*****compute critical wave numbers
maxktemp = k1
call maxk (maxktemp, zeta, u1, x, xval)
k0 = maxktemp
cut3 = floor(maxktemp*R/pi)

if (cut1 .ge. (nxhalf-1)) then
cut1 = nxhalf-1    ! critical wave number no bigger than nxhalf
end if

if (cut3 .le. cut1) then
cut1 = cut3        ! once the modes are cut, not more are kept
end if

!*****compute z_t
do kstep = 0, nx-1
zetaRHS(kstep) = eta1_a(kstep) *u1_x(kstep) - zeta_x(kstep) *u1_a(kstep)
end do

zeta_t = zetaRHS

!*****compute u1_t
u2_a = u2
call dfftw_plan_dft_r2c_1d(plan,nx , u2, u2_cplx,FFTW_ESTIMATE)
call dfftw_execute_dft_r2c(plan, u2, u2_cplx)

```



```

call dfftw_destroy_plan(plan)
call dfftw_plan_dft_r2c_1d(plan,nx,zeta_t,zeta_tcplx,FFTW_ESTIMATE)
call dfftw_execute_dft_r2c(plan, zeta_t, zeta_tcplx)
call dfftw_destroy_plan(plan)

zeta_tcplx = zeta_tcplx*nx_inv
u2_cplx = u2_cplx*nx_inv
zeta_txcplx = 0.d0
zeta_txxcplx = 0.d0
u2_xcplx = 0.d0
u2_xxcplx = 0.d0
u2_xxxcplx = 0.d0

do kstep = 0, floor(nxhalf/4.d0)
zeta_txcplx (kstep) = zeta_tcplx(kstep)*Dfft(kstep)
zeta_txxcplx(kstep) = zeta_txcplx(kstep)*Dfft(kstep)
u2_xcplx  (kstep) = u2_cplx(kstep) * Dfft(kstep)
u2_xxcplx (kstep) = u2_xcplx(kstep) * Dfft(kstep)
u2_xxxcplx(kstep) = u2_xxcplx(kstep) * Dfft(kstep)
end do

call dfftw_plan_dft_c2r_1d(plan,nx, zeta_txcplx, zeta_tx, FFTW_ESTIMATE)
call dfftw_execute_dft_c2r(plan, zeta_txcplx, zeta_tx)
call dfftw_destroy_plan(plan)
call dfftw_plan_dft_c2r_1d(plan,nx, zeta_txxcplx, zeta_txx, FFTW_ESTIMATE)
call dfftw_execute_dft_c2r(plan, zeta_txxcplx, zeta_txx)

```

```

call dfftw_destroy_plan(plan)
call dfftw_plan_dft_c2r_1d(plan,nx, u2_xcplx, u2_x, FFTW_ESTIMATE)
call dfftw_execute_dft_c2r(plan, u2_xcplx, u2_x)
call dfftw_destroy_plan(plan)
call dfftw_plan_dft_c2r_1d(plan,nx, u2_xxcplx, u2_xx, FFTW_ESTIMATE)
call dfftw_execute_dft_c2r(plan, u2_xxcplx, u2_xx)
call dfftw_destroy_plan(plan)
call dfftw_plan_dft_c2r_1d(plan,nx, u2_xxxcplx, u2_xxx, FFTW_ESTIMATE)
call dfftw_execute_dft_c2r(plan, u2_xxxcplx, u2_xxx)
call dfftw_destroy_plan(plan)

do kstep = 0, nx-1
part1(kstep) = rho2*u2_a(kstep)*u2_x(kstep)&
-rho1*u1_a(kstep)*u1_x(kstep) &
+ grav*(rho2-rho1)*zeta_x(kstep)
part2(kstep) = -1.d0*rho2*eta2_a(kstep)*zeta_x(kstep)&
               * (u2_a(kstep)*u2_xx(kstep)-u2_x(kstep)**2) &
               - rho1*eta1_a(kstep)*zeta_x(kstep)* &
               (u1_a(kstep)*u1_xx(kstep)-u1_x(kstep)**2)
u1_add(kstep) = rho1*alpha*eta1_a(kstep)**2&
               *(-1.d0*u1_x(kstep)*u1_xx(kstep)+u1_a(kstep)*u1_xxx(kstep))
u2_add(kstep) = -1.d0*rho2*alpha*eta2_a(kstep)**2 &
               *(-1.d0*u2_x(kstep)*u2_xx(kstep)+u2_a(kstep)*u2_xxx(kstep))
f_zeta(kstep) = rho2*hh*u1_a(kstep)*eta2_inv_a(kstep)**2 &
               +hh*rho2*alpha *(2.d0*u1_a(kstep)*zeta_xx(kstep)&
               *eta2_inv_a(kstep) +u1_x(kstep)*zeta_x(kstep) &

```

```

*eta2_inv_a(kstep)-u1_xx(kstep))
g_zeta(kstep) = hh*rho2*alpha*(u1_a(kstep) &
*zeta_x(kstep)*eta2_inv_a(kstep)-2.d0*u1_x(kstep))
h_zeta(kstep) = -1.d0*alpha*rho2*hh*u1_a(kstep)
f_u (kstep) = rho1-rho2+rho2*hh*eta2_inv_a(kstep)&
+ alpha*rho2*hh*(zeta_xx(kstep)+zeta_x(kstep)**2 &
*eta2_inv_a(kstep))
g_u(kstep) = rho1*eta1_a(kstep)*zeta_x(kstep)&
+ alpha *rho2*(3.d0*eta2_a(kstep)-hh)*zeta_x(kstep)
h_u(kstep) = -1.d0*alpha *(rho1*eta1_a(kstep)**2 &
+rho2*eta1_a(kstep)*eta2_a(kstep))
end do

call antialiase ( 7, f_u, f_u_a)
call antialiase ( 7, g_u, g_u_a)
call antialiase ( 7, h_u, h_u_a)

do kstep = 0, nx-1
test1(kstep) = f_zeta(kstep)*zeta_t(kstep)&
+ g_zeta(kstep)*zeta_tx(kstep) &
+h_zeta(kstep)*zeta_txx(kstep)
end do

test2 = part1 + part2 + u1_add + u2_add + test1
call antialiase(7, test2, total_RHS)

```

```

f_u_mean = 0.d0
g_u_mean = 0.d0
h_u_mean = 0.d0
do kstep = 0, nx-1
f_u_mean = f_u_mean + f_u_a(kstep)
g_u_mean = g_u_mean + g_u_a(kstep)
h_u_mean = h_u_mean + h_u_a(kstep)
end do

f_u_mean = f_u_mean *nx_inv
g_u_mean = g_u_mean * nx_inv
h_u_mean = h_u_mean * nx_inv
do kstep = 0, nx-1
resi1(kstep) = total_RHS(kstep)-&
(u1RHS(kstep)*f_u(kstep)+u1RHS_x(kstep)*g_u(kstep) &
+u1RHS_xx(kstep)*h_u(kstep))
end do

call antialiase( 7, resi1, resi)
add = resi
u1RHStemp = u1RHS
relaxation = abs(h_u_mean)/maxval(abs(h_u))

!*****iteration begins here
do while( (maxval(abs(add))/maxval(abs(u1RHS)))>. 1.d-14)
call dfftw_plan_dft_r2c_1d(plan,nx, resi, resi_cplx,FFTW_ESTIMATE)
call dfftw_execute_dft_r2c(plan, resi, resi_cplx)
call dfftw_destroy_plan(plan)
resi_cplx = resi_cplx*nx_inv

```

```

do kstep = 0, nxhalf
add_cplx(kstep) = resi_cplx(kstep)&
/(f_u_mean+g_u_mean*Dfft(kstep)+h_u_mean*Dfft(kstep)**2)
end do

call dfftw_plan_dft_c2r_1d(plan, nx, add_cplx, add, FFTW_ESTIMATE)
call dfftw_execute_dft_c2r(plan, add_cplx, add)
call dfftw_destroy_plan(plan)
u1RHStemp = u1RHStemp + add*relaxation
u1RHS = u1RHStemp
call dfftw_plan_dft_r2c_1d(plan, nx, u1RHS, u1RHS_cplx, FFTW_ESTIMATE)
call dfftw_execute_dft_r2c(plan, u1RHS, u1RHS_cplx)
call dfftw_destroy_plan(plan)
u1RHS_cplx = u1RHS_cplx * nx_inv
do kstep = 0, nxhalf
u1RHS_xcplx(kstep) = u1RHS_cplx(kstep) * Dfft(kstep)
u1RHS_xx_cplx(kstep) = u1RHS_xcplx(kstep) * Dfft(kstep)
end do
call dfftw_plan_dft_c2r_1d(plan, nx, u1RHS_xcplx, u1RHS_x, FFTW_ESTIMATE)
call dfftw_execute_dft_c2r(plan, u1RHS_xcplx, u1RHS_x)
call dfftw_destroy_plan(plan)
call dfftw_plan_dft_c2r_1d(plan, nx, u1RHS_xx_cplx, u1RHS_xx, FFTW_ESTIMATE)
call dfftw_execute_dft_c2r(plan, u1RHS_xx_cplx, u1RHS_xx)
call dfftw_destroy_plan(plan)
do kstep = 0, nx-1
resi1(kstep) = total_RHS(kstep)-&

```

```

(u1RHS(kstep)*f_u(kstep)+u1RHS_x(kstep)*g_u(kstep)&
+u1RHS_xx(kstep)*h_u(kstep))
end do

call antialias( 7, resi1, resi)

    end do

end subroutine TimeDerivative2


subroutine antialias(order, u, u_a)

! anti-aliasing to remove high wave numbers according to order
use parameters

implicit none

include 'fftw3.f'

integer, intent(IN) :: order

double precision, dimension(0:nx-1), intent(IN) :: u
double precision, dimension(0:nx-1), intent(OUT):: u_a

integer *8 plan

integer :: kstep

double complex, dimension(0:nxhalf):: u_cplx

double precision :: factor

factor = 2.d0/dble(order +1)

call dfftw_plan_dft_r2c_1d(plan,nx,u,u_cplx,FFTW_ESTIMATE)

call dfftw_execute_dft_r2c(plan, u, u_cplx)

call dfftw_destroy_plan(plan)

u_cplx = u_cplx/dble(nx)

do kstep = floor( nxhalf*factor), nxhalf

```

```

u_cplx(kstep) = 0.d0
end do

call dfftw_plan_dft_c2r_1d(plan, nx, u_cplx, u_a, FFTW_ESTIMATE)
call dfftw_execute_dft_c2r(plan, u_cplx, u_a)
call dfftw_destroy_plan(plan)
end subroutine antialias

subroutine maxk (kmax, zeta, u1, x, xval)
! compute critical wave numbers in non-dimensional form
use parameters
implicit none
double precision, dimension(0:nx-1), intent(IN) :: zeta, u1, x
double precision, intent(INOUT) :: kmax, xval
double precision, dimension (0:nx-1) :: k
double precision :: f1, u2, U, eta1, eta2, a, b, c, d
double precision :: ktestmax
integer :: kstep

ktestmax = nxhalf / R * pi
xval = 0.d0
do kstep = 0, nx-1
eta1 = h1 - zeta(kstep)
eta2 = h2 + zeta(kstep)
u2 = -1.d0 * eta1 / eta2 * u1 (kstep)
U = abs(u2-u1(kstep))
a = U*U*rho1*rho2*eta1*eta1*eta2*eta2/9.d0

```

```

b = 1.d0/3.d0 * (U*U*rho1*rho2*(eta1*eta1+eta2*eta2)&
  - grav * (rho2-rho1)*eta1*eta2*(rho1*eta2+rho2*eta1))
c = U*U*rho1*rho2-grav *(rho2-rho1)*(rho1 * eta2 + rho2 * eta1)
d = b*b - 4.d0*a*c
if ( f1 (ktestmax, zeta(kstep), u1(kstep)) .le. 0.d0) then
k(kstep) = nxhalf / R * pi
else
k(kstep) = dsqrt(-2.d0*c/(b + dsqrt(d)))
end if
if (k(kstep) .le. ktestmax) then
xval = x(kstep)
ktestmax = k(kstep)
endif
end do
kmax = minval(k)
end subroutine maxk

function f1(x, zeta, u1)
! stability criterion
use parameters
implicit none
double precision, intent(IN) ::x, zeta, u1
double precision :: u2, u, eta1, eta2, f1
double precision :: temp
eta1 = h1 - zeta
eta2 = h2 + zeta

```



```

u2 = -1.d0 * eta1 / eta2 * u1

u = abs(u1-u2)

temp = 1.d0/3.d0*x*x

f1 = u*u - grav*(rho2-rho1) *(eta2/rho2/(1.d0+temp*eta2*eta2)&
      + eta1/rho1/(1.d0+temp*eta1*eta1))

end function f1


subroutine conserve(u, zeta, Dfft, M0, E0)

use parameters

implicit none

include 'fftw3.f'

double precision, dimension (0:nx-1), intent (IN) :: u, zeta, Dfft
double precision, intent (INOUT) :: M0, E0

double precision, dimension (0:nx-1)      :: u1, u2, eta1, eta2
double precision, dimension (0:nx-1)      :: u1_x, u2_x
double complex, dimension (0: nxhalf) :: u1complex, u2complex
double complex, dimension (0: nxhalf) :: u1_xcomplex, u2_xcomplex
double precision :: dx

integer :: kstep

integer *8 :: plan


dx = (R-L)/dble(nx)

u1 = u

eta1 = h1 - zeta
eta2 = h2 + zeta

u2 = -1.d0*(u1*eta1)/eta2

```

```

call dfftw_plan_dft_r2c_1d(plan,nx,u1,u1complex,FFTW_ESTIMATE)
call dfftw_execute_dft_r2c(plan, u1, u1complex)
call dfftw_destroy_plan(plan)
call dfftw_plan_dft_r2c_1d(plan,nx,u2,u2complex,FFTW_ESTIMATE)
call dfftw_execute_dft_r2c(plan, u2, u2complex)
call dfftw_destroy_plan(plan)
u1complex = u1complex /dbple(nx)
u2complex = u2complex /dbple(nx)
do kstep = 0, nxhalf
u1_xcomplex = u1complex(kstep) * Dfft(kstep)
u2_xcomplex = u2complex(kstep) * Dfft(kstep)
end do

call dfftw_plan_dft_c2r_1d(plan,nx,u2_xcomplex,u2_x,FFTW_ESTIMATE)
call dfftw_execute_dft_c2r(plan, u2_xcomplex, u2_x)
call dfftw_destroy_plan(plan)
call dfftw_plan_dft_c2r_1d(plan,nx,u1_xcomplex,u1_x,FFTW_ESTIMATE)
call dfftw_execute_dft_c2r(plan, u1_xcomplex, u1_x)
call dfftw_destroy_plan(plan)

M0 = 0.d0
E0 = 0.d0
do kstep = 0, nx-1
M0 = M0+zeta(kstep)
E0 = E0 + HALF*grav*zeta(kstep)**2*(rho2-rho1) &
+ HALF*rho1*(eta1(kstep)*u1(kstep)**2 &

```

```

+ eta1(kstep)**3*u1_x(kstep)**2/3.d0)&
+ HALF*rho2*(eta2(kstep)*u2(kstep)**2 &
+ eta2(kstep)**3*u2_x(kstep)**2/3.d0)
end do
M0 = M0*dx
E0 = E0*dx
E0 = E0/2.d0 + (rho1*(h1/2.d0+h2)*h1 + rho2*h2/2.d0*h2)*grav*R
end subroutine conserve

```

## D.2 The regularized Kaup equations

### Main code

```

module parameters
integer, parameter :: nx =8192
integer, parameter :: nxhalf = ceiling(nx/2.d0)
double precision, parameter :: stop_time =8.d1
double precision, parameter :: lambda = 1.d-1, mkframe = 2.5d0
double precision, parameter :: R = 1.232d3*2.d0, L = -1.d0*R
double precision, parameter :: hgate = 1.d0, lgate =1.d2
double precision, parameter :: hh = 77.d0, grav = 981.d0
!lambda = 0.5
!double precision, parameter :: rho1 = 0.9998817144855958d0
!double precision, parameter :: rho2 = 1.0215548370691494d0
!double precision, parameter :: h1 = 14.551541169411323d0
!lambda = 1
!double precision, parameter :: rho1 = 0.9994235006405087
!double precision, parameter :: rho2 = 1.0217692795999886

```

```

!double precision, parameter :: h1 = 14.753638180803918
!lambda = 0.25
!double precision, parameter :: rho1 = 1.0009125274217063
double precision, parameter :: rho2 = 1.0211814125745406
!double precision, parameter :: h1 = 14.321902674392888
double precision, parameter :: rho1 = 9.99d-1, rho2 = 1.022d0
double precision, parameter :: h1 = 1.5d1

double precision, parameter :: h2 = hh -h1
double precision, parameter :: b1 = (h1*h2)/(rho2*h1+rho1*h2)
double precision, parameter :: b2 = grav*(rho2-rho1)
double precision, parameter :: b3 = (rho2*h1*h1-rho1*h2*h2)&
    /(rho1*h2+rho2*h1)**2
double precision, parameter :: b4 = (h1*h2)**2*(rho1*h1+rho2*h2)/3.d0 &
    /(rho1*h2+rho2*h1)**2

end module parameters

PROGRAM REGULAR_KAUP

!external

use parameters

implicit none

include 'fftw3.f'

double precision, dimension(0:nx-1) :: x, u, u2, eta
double precision, dimension(0:nx-1) :: zeta, u1, zeta1
double complex :: Dfft(0:nxhalf)
double complex, parameter :: I = cmplx(0.d0, 1.d0)

```

```

double precision:: alpha, k0, k01, tnow, dt, K, M0, E0
double precision :: ONE, HALF, SIXTH, tnow1
double precision, dimension(0:nx-1) :: uK1, uK2, uK3, uK4
double precision, dimension(0:nx-1) :: eta1, eta2
double precision, dimension(0:nx-1) :: zetaK1, zetaK2, zetaK3, zetaK4

!internal

integer kstep, tstep, cut1

double precision:: pi,dx, timerecord

integer:: nt

real, dimension(2) :: tarray1, tarray2

integer :: nframe

character(len = 20) :: nu, nzeta

print *, b1, b2,b3,b4

pi = 4.d0 *datan(1.d0)

alpha = 1.d0/3.d0

ONE = 1.d0

hALF = 0.5d0

SIXTH = 1.d0/6.d0

dx = (R-L)/nx

dt = 1.d-2

K = 2.0*pi/(R-L)

nt = ceiling(stop_time/dt)

do kstep = 0,nxhalf

Dfft(kstep) = 2*pi*I/(R-L)*kstep

end do

do kstep = 0, nx-1

```

```

x(kstep) = L+dx*kstep
zeta(kstep) = hgate/2.d0*(dtanh(lambda*(x(kstep)-lgate))&
-dtanh(lambda*(x(kstep)+lgate)))
end do
u = 0.d0
nframe = 0
tnow = 0.d0
nframe = nframe +1
timerecord = 0.d0
do while ((tnow+1d-10).le. stop_time )
print *, 'time = ', tnow
tstep = tstep+1
u1 = u
eta1 = h1 - zeta
eta2 = h2 + zeta
if (tnow+dt .ge. stop_time) then
dt = stop_time-(tnow)
end if
u1 = u
zeta1 = zeta
tnow1 = tnow
call TimeDerivative3( u1, zeta1, Dfft, uK1, zetaK1)
u1 = u+half*dt*uK1
zeta1 = zeta +half*dt*zetaK1
tnow1 = tnow +half*dt
call TimeDerivative3( u1, zeta1, Dfft, uK2, zetaK2)

```

```

u1 = u+half*dt*uK2
zeta1 = zeta + half*dt*zetaK2
tnow1 = tnow + half*dt
call TimeDerivative3( u1, zeta1, Dfft, uK3, zetaK3)
u1 = u+ dt*uK3
zeta1 = zeta + dt*zetaK3
tnow1 = tnow + dt
call TimeDerivative3( u1, zeta1, Dfft, uK4, zetaK4)
u = u + dt * (uK1+2.d0*uK2+2.d0*uK3+uK4)*sixth
zeta = zeta + dt * (zetaK1+2.d0*zetaK2+2.d0*zetaK3+zetaK4)*sixth
uK1 = (uK1+2.d0*uK2+2.d0*uK3+uK4)*sixth
tnow = tnow + dt
timerecord = timerecord + dt
end do
call ETIME(tarray2, result2)

open(31, file = 'result.dat')
do kstep = 0,nx-1
write(31, 503) x(kstep), zeta(kstep), u(kstep)
end do
close(31)

502 format(D30.20)
505 format(D30.20, 1x, D30.20,1x)
503 format(D30.20, 1x, D30.20, 1x, D30.20)

```

```

end program REGULAR_KAUP

subroutine TimeDerivative3(u, zeta, Dfft, uRhs, zetaRHS)
use parameters
implicit none
include 'fftw3.f'
integer *8 plan
double precision, dimension(0:nx-1):: u, zeta, u_x, u_xxx, zeta_x
double precision, dimension(0:nx-1):: uzeta, uzeta_x, u2, u2_x
double precision, dimension(0:nx-1):: uRHS, zetaRHS
double complex, dimension(0:nxhalf):: Dfft, u_cplx, zeta_cplx, u_x_cplx
double complex, dimension(0:nxhalf):: u_xxx_cplx, zeta_x_cplx, uzeta_cplx
double complex, dimension(0:nxhalf):: uzeta_x_cplx, u2_cplx, u2_x_cplx
double complex, dimension(0:nxhalf):: zetaRHS_cplx, RHS_cplx, uRHS_cplx
double precision :: nx_inv = 1.d0/dble(nx)
integer :: kstep, alias_k = floor(dble(nxhalf)/2.d0)

call dfftw_plan_dft_r2c_1d(plan,nx,zeta,zeta_cplx,FFTW_ESTIMATE)
call dfftw_execute_dft_r2c(plan, zeta, zeta_cplx)
call dfftw_destroy_plan(plan)
call dfftw_plan_dft_r2c_1d(plan,nx,u,u_cplx,FFTW_ESTIMATE)
call dfftw_execute_dft_r2c(plan, u, u_cplx)
call dfftw_destroy_plan(plan)

zeta_cplx = zeta_cplx *nx_inv
u_cplx = u_cplx * nx_inv

```



```

do kstep = alias_k+1, nxhalf
  zeta_cplx(kstep) = 0.d0
  u_cplx(kstep) = 0.d0
end do

u_x_cplx = 0.d0
zeta_x_cplx = 0.d0
u_xxx_cplx = 0.d0

do kstep = 0, alias_k
  u_x_cplx(kstep) = u_cplx(kstep)*Dfft(kstep)
  u_xxx_cplx(kstep) = u_x_cplx(kstep)*Dfft(kstep)**2
  zeta_x_cplx(kstep) = zeta_cplx(kstep)*Dfft(kstep)
end do

call dfftw_plan_dft_c2r_1d(plan,nx,zeta_cplx, zeta,FFTW_ESTIMATE)
call dfftw_execute_dft_c2r(plan, zeta_cplx, zeta)
call dfftw_destroy_plan(plan)
call dfftw_plan_dft_c2r_1d(plan,nx,u_cplx, u,FFTW_ESTIMATE)
call dfftw_execute_dft_c2r(plan, u_cplx, u)
call dfftw_destroy_plan(plan)

u2 = u * u
uzeta = u *zeta

call dfftw_plan_dft_r2c_1d(plan,nx,u2 ,u2_cplx,FFTW_ESTIMATE)
call dfftw_execute_dft_r2c(plan, u2, u2_cplx)

```

```

call dfftw_destroy_plan(plan)
call dfftw_plan_dft_r2c_1d(plan,nx,uzeta,uzeta_cplx,FFTW_ESTIMATE)
call dfftw_execute_dft_r2c(plan, uzeta, uzeta_cplx)
call dfftw_destroy_plan(plan)

u2_cplx= u2_cplx *nx_inv
uzeta_cplx = uzeta_cplx*nx_inv
u2_x_cplx = 0.d0
uzeta_x_cplx = 0.d0
do kstep = 0, alias_k
    u2_x_cplx(kstep) = u2_cplx(kstep) * Dfft(kstep)
    uzeta_x_cplx(kstep) = uzeta_cplx(kstep) * Dfft(kstep)
end do
uRHS_cplx = -1.d0*(b2*zeta_x_cplx + b3*5.d-1*u2_x_cplx)
zetaRHS_cplx = 0.d0
RHS_cplx = b1*u_x_cplx + b3*uzeta_x_cplx
do kstep = 0, alias_k
    zetaRHS_cplx(kstep) = -1.d0/(1.d0-b4/b1*Dfft(kstep)**2)*RHS_cplx(kstep)
end do

call dfftw_plan_dft_c2r_1d(plan,nx,uRHS_cplx, uRHS,FFTW_ESTIMATE)
call dfftw_execute_dft_c2r(plan, uRHS_cplx, uRHS)
call dfftw_destroy_plan(plan)
call dfftw_plan_dft_c2r_1d(plan,nx,zetaRHS_cplx, zetaRHS,FFTW_ESTIMATE)
call dfftw_execute_dft_c2r(plan, zetaRHS_cplx, zetaRHS)
call dfftw_destroy_plan(plan)

```

```
end subroutine TimeDerivative3
```

### D.3 The Boussinesq equations

#### Main code

```
module parameters
integer, parameter:: nx =4096*4
integer, parameter :: nxhalf = ceiling(nx/2.d0)
double precision, parameter :: amp = 1.d-1/16.d0
double precision, parameter:: stop_time = 5.d2 , dt = 1.d-1/2.d0
double precision, parameter :: lambda = 0.1d0, mkframe = 1.d2
double precision, parameter:: R = 2.464d3*4.d0, L = -1.d0*R
double precision, parameter :: hgate = 10.d0, lgate = 1.d2
!lambda = 0.5
double precision, parameter :: rho1 = 0.9998817144855958d0
double precision, parameter :: rho2 = 1.0215548370691494d0
double precision, parameter :: h1 = 14.551541169411323d0
!lambda = 1
!double precision, parameter :: rho1 = 0.9994235006405087
!double precision, parameter :: rho2 = 1.0217692795999886
!double precision, parameter :: h1 = 14.753638180803918
!lambda = 0.25
!double precision, parameter :: rho1 = 1.0009125274217063
!double precision, parameter :: rho2 = 1.0211814125745406
!double precision, parameter :: h1 = 14.321902674392888
!double precision, parameter:: rho1 = 9.99d-1, rho2 = 1.022d0
```

```

!double precision, parameter :: h1 = 1.5d1
double precision, parameter:: h2 = 7.7d1-h1, grav = 9.81d2
double precision, parameter:: b1=(rho1*h2*h2-rho2*h1*h2&
-2.d0*rho2*h1*h1)/(rho1*h2*h2+rho2*h1*h2)
double precision, parameter:: b2 = grav*h2*(rho1-rho2)&
/(rho1*h2+rho2*h1)
double precision, parameter:: b3 = grav*rho2*(rho1-rho2)*(h1+h2)&
/(rho1*h2+rho2*h1)**2
double precision, parameter:: b4 = 1.d0/3.d0&
*(rho1*h1*h1*h2+rho2*h1*h2*h2)/(rho1*h2+rho2*h1)
double precision, parameter:: dx = (R-L)/dble(nx)
double precision, parameter :: pi = 4.d0*datan(1.d0)
end module parameters

```

```

program BOUSSINESQ
use parameters
!external
implicit none
include 'fftw3.f'
double precision, dimension(0:nx-1) :: u, eta, zeta, u1, eta1
double complex :: Dfft(0:nxhalf)
double complex, parameter :: I = cmplx(0.d0, 1.d0)
double precision:: x(0:nx-1),tnow, dt1
double precision :: ONE, HALF, SIXTH, tnow1,
double precision, dimension(0:nx-1) :: uK1, uK2, uK3, uK4
double precision, dimension(0:nx-1) :: etaK1, etaK2, etaK3, etaK4

```

```

double precision :: initial_value

integer *8 plan

integer :: nframe

double precision :: timerecord

character(len = 20) :: nu, nzeta

!internal

integer kstep, tstep

integer nt

real, dimension(2) :: tarray1, tarray2

real :: result1, result2


print *, b1, b2, b3, b4

ONE = 1.d0

HALF = 0.5d0

SIXTH = 1.d0/6.d0

nt = ceiling(stop_time/dt)


open(33, file = 'gridset')

write(33, 1100) mkframe, dx, L, nx

close(33)


do kstep = 0, nxhalf
  Dfft(kstep) = 2*pi*I/(R-L)*kstep
end do

do kstep = 0, nx-1
  x(kstep) = L+dx*kstep

```

```

u(kstep) = 0.d0
zeta(kstep) = initial_value(x(kstep))
end do
eta = h1-zeta
tnow = 0.d0
tstep = 0

call ETIME(tarray1, result1)
uK1 = 0.d0
etaK1 = 0.d0
uK2 = 0.d0
etaK2 = 0.d0
uK3 = 0.d0
etaK3 = 0.d0
uK4 = 0.d0
etaK4 = 0.d0

nframe = 0
write(nu,'(a,i0,a)') 'bsq_result',nframe, '.dat'
open(11, file=nu)
do kstep = 0, nx-1
write(11,502) x(kstep), zeta(kstep), u(kstep)
end do
close (11)
timerecord = 0.d0
dt1 = dt

```

```

nframe = nframe +1
op_shift1 = 0.d0
do while ((tnow+dt).le.(stop_time+1d-10) .and. (tstep) .le. nt )
tstep = tstep+1
if (tnow+dt .ge. stop_time) then
dt1 = stop_time-(tnow)
end if

u1 = u
eta1 = eta
tnow1 = tnow
call TimeDerivative( u1, eta1, Dfft, uK1, etaK1)
u1 = u+half*dt1*uK1
eta1 = eta +half*dt1*etaK1
tnow1 = tnow +half*dt1
call TimeDerivative(u1, eta1, Dfft, uK2, etaK2)
u1 = u+half*dt1*uK2
eta1 = eta + half*dt1*etaK2
tnow1 = tnow + half*dt1
call TimeDerivative(u1, eta1, Dfft, uK3, etaK3)
u1 = u + dt1*uK3
eta1 = eta + dt1*etaK3
tnow1 = tnow+dt1
call TimeDerivative(u1, eta1, Dfft, uK4, etaK4)
u = u + dt1 * (uK1+2.d0*uK2+2.d0*uK3+uK4)*sixth
eta = eta + dt1 * (etaK1+2.d0*etaK2+2.d0*etaK3+etaK4)*sixth

```

```

timerecord = timerecord + dt1

tnow = tnow + dt1

if((timerecord+1.d-10) .ge. mkframe) then
zeta = h1-eta

write(nu,'(a,i0,a)') 'bsq_result',nframe, '.dat'

open(11, file = nu)

do kstep = 0, nx-1
write(11,502) x(kstep), zeta(kstep), u(kstep)
end do

close (11)

nframe = nframe + 1

timerecord = 0.d0

end if

end do


zeta = h1 - eta

open(21, file = 'bsq_result')

do kstep = 0, nx-1
write(21, 502)x(kstep),zeta(kstep), u(kstep)
end do

close (21)


502 format(D30.20, 1x, D30.20, 1x, D30.20)
503 format(D30.20, 1x, D30.20, 1x, D30.20, 1x, D30.20, 1x)

end program BOUSSINESQ

```



```

subroutine TimeDerivative( u, eta, Dfft, uRHS, etaRHS )

use parameters

implicit none

include 'fftw3.f'

integer :: kstep

double precision :: half, nx_inv, mx_inv, tnow

double complex, dimension(0:nxhalf) :: Dfft

double precision, dimension(0:nx-1) :: u, eta, zeta, ueta, ueta_x

double precision, dimension(0:nx-1) :: zetazeta_x, uzeta_xtest

double precision, dimension(0:mx-1) :: u1, zeta1, u_x1, zeta_x1

double precision, dimension(0:mx-1) :: uzeta1, uu_x1

double precision, dimension (0:mx-1) :: uzeta_x1, zetazeta_x1

double precision, dimension(0:nx-1) :: u_x, uu_x, zeta_x, uRHS, etaRHS,

double precision, dimension (0:nx-1) :: etaRHS1, uSource

double complex, dimension(0:nxhalf) :: zetacomplex, ucomplex

double complex, dimension(0:nxhalf) :: zeta_xcomplex

double precision, dimension (0:nxhalf) :: zetazeta_xcomplex

double complex, dimension(0:nxhalf) :: zeta_xcomplexsave

double complex, dimension(0:nxhalf) :: u_xcomplexsave

double complex, dimension(0:nxhalf) :: uSourcecomplex

double complex, dimension(0:nxhalf) :: u_xcomplex, uu_xcomplex

double complex, dimension(0:nxhalf) :: uetacomplex, ueta_xcomplex

double complex, dimension(0:nxhalf) :: uRHScomplex, etaRHScomplex

double complex, dimension(0:mxhalf) :: u1complex, zeta1complex

double complex, dimension(0:mxhalf) :: u_x1complex, zeta_x1complex

```

```

double complex, dimension(0:mxhalf) :: uzeta_x1complex
double complex, dimension(0:nxhalf) :: zetazeta_x1complex
double complex, dimension(0:mxhalf) :: uu_x1complex, uzeta1complex
double complex, dimension(0:nxhalf) :: uu_xcomplextest
double complex, dimension(0:nxhalf) :: zetazeta_xcomplextest
double complex, dimension(0:mxhalf) :: uzeta_xcomplextest
double precision :: RHS1, RHS2

integer *8 plan

half = 5.d-1
nx_inv = 1.d0/dble(nx)
mx_inv = 1.d0/dble(mx)
zeta = h1-eta
do kstep = 0, nx-1
  ueta(kstep) = u(kstep) *eta(kstep)
end do

call dfftw_plan_dft_r2c_1d(plan,nx,u,ucomplex,FFTW_ESTIMATE)
call dfftw_execute_dft_r2c(plan, u, ucomplex)
call dfftw_destroy_plan(plan)
call dfftw_plan_dft_r2c_1d(plan,nx,zeta,zetacomplex,FFTW_ESTIMATE)
call dfftw_execute_dft_r2c(plan, zeta,zetacomplex)
call dfftw_destroy_plan(plan)
call dfftw_plan_dft_r2c_1d(plan,nx,ueta,uetacomplex,FFTW_ESTIMATE)
call dfftw_execute_dft_r2c(plan, ueta,uetacomplex)
call dfftw_destroy_plan(plan)

```

```

ucomplex = ucomplex*nx_inv
zetacomplex = zetacomplex*nx_inv
uetacomplex = uetacomplex*nx_inv
do kstep = 0, nxhalf
u_xcomplex(kstep) = ucomplex(kstep)*Dfft(kstep)
zeta_xcomplex(kstep) = zetacomplex(kstep) *Dfft(kstep)
ueta_xcomplex(kstep) = uetacomplex(kstep)*Dfft(kstep)
end do
u_xcomplexsave = u_xcomplex
zeta_xcomplexsave = zeta_xcomplex

call dfftw_plan_dft_c2r_1d(plan, nx, u_xcomplex, u_x, FFTW_ESTIMATE)
call dfftw_execute_dft_c2r(plan, u_xcomplex, u_x)
call dfftw_destroy_plan(plan)
call dfftw_plan_dft_c2r_1d(plan, nx, zeta_xcomplex, zeta_x, &
FFTW_ESTIMATE)
call dfftw_execute_dft_c2r(plan, zeta_xcomplex, zeta_x)
call dfftw_destroy_plan(plan)
call dfftw_plan_dft_c2r_1d(plan, nx, ueta_xcomplex, ueta_x, &
FFTW_ESTIMATE)
call dfftw_execute_dft_c2r(plan, ueta_xcomplex, ueta_x)
call dfftw_destroy_plan(plan)
u_xcomplex = u_xcomplexsave
zeta_xcomplex = zeta_xcomplexsave

!!!!!!!!!!!!!!!!!!!!!!!!!!!!!!

```

```

!!!!dealiasing!!!!!!!!!!!!

u1complex = 0.d0
zeta1complex = 0.d0
u_x1complex = 0.d0
zeta_x1complex = 0.d0
do kstep = 0, nxhalf
  u1complex(kstep) = ucomplex(kstep)
  zeta1complex(kstep) = zetacomplex(kstep)
  u_x1complex(kstep) = u_xcomplex(kstep)
  zeta_x1complex(kstep) = zeta_xcomplex(kstep)
end do

call dfftw_plan_dft_c2r_1d(plan, mx, u1complex, u1, FFTW_ESTIMATE)
call dfftw_execute_dft_c2r(plan, u1complex, u1)
call dfftw_destroy_plan(plan)
call dfftw_plan_dft_c2r_1d(plan, mx, u_x1complex, u_x1, FFTW_ESTIMATE)
call dfftw_execute_dft_c2r(plan, u_x1complex, u_x1)
call dfftw_destroy_plan(plan)
call dfftw_plan_dft_c2r_1d(plan, mx, zeta1complex, zeta1, FFTW_ESTIMATE)
call dfftw_execute_dft_c2r(plan, zeta1complex, zeta1)
call dfftw_destroy_plan(plan)
call dfftw_plan_dft_c2r_1d(plan, mx, zeta_x1complex, zeta_x1, FFTW_ESTIMATE)
call dfftw_execute_dft_c2r(plan, zeta_x1complex, zeta_x1)
call dfftw_destroy_plan(plan)

do kstep = 0, mx-1

```

```

uu_x1(kstep) = u1(kstep)*u_x1(kstep)
zetazeta_x1(kstep) = zeta1(kstep)*zeta_x1(kstep)
uzeta1(kstep) = u1(kstep)*zeta1(kstep)
end do

call dfftw_plan_dft_r2c_1d(plan,mx,uu_x1,uu_x1complex,FFTW_ESTIMATE)
call dfftw_execute_dft_r2c(plan, uu_x1, uu_x1complex)
call dfftw_destroy_plan(plan)
call dfftw_plan_dft_r2c_1d(plan,mx,zetazeta_x1,zetazeta_x1complex,&
FFTW_ESTIMATE)
call dfftw_execute_dft_r2c(plan, zetazeta_x1, zetazeta_x1complex)
call dfftw_destroy_plan(plan)
call dfftw_plan_dft_r2c_1d(plan,mx, uzeta1,uzeta1complex,FFTW_ESTIMATE)
call dfftw_execute_dft_r2c(plan, uzeta1, uzeta1complex)
call dfftw_destroy_plan(plan)

uu_x1complex = uu_x1complex*mx_inv
zetazeta_x1complex = zetazeta_x1complex*mx_inv
uzeta1complex = uzeta1complex*mx_inv
do kstep = 0, nxhalf
uu_xcomplextest(kstep) = uu_x1complex(kstep)
zetazeta_xcomplextest(kstep) = zetazeta_x1complex(kstep)
uzeta_xcomplextest(kstep) = uzeta1complex(kstep)*Dfft(kstep)
end do

!!!!!!!!!!!!!!!!!!!!!!!!dealiasing!!!!!!!!!!!!!!!!!!!!
!!!!!!!!!!!!!!!!!!!!!!!!!!!!!!!!!!!!!!!!!!!!!!!!!!!!

```

```

call dfftw_plan_dft_c2r_1d(plan, nx, uzeta_xcomplextest, uzeta_xtest,&
FFTW_ESTIMATE)

call dfftw_execute_dft_c2r(plan, uzeta_xcomplextest, uzeta_xtest)

call dfftw_destroy_plan(plan)

do kstep = 0, nx-1
etaRHS(kstep) = uzeta_xtest(kstep) - h1*u_x(kstep)
end do

do kstep = 0, nx-1
uu_x(kstep) = u(kstep)*u_x(kstep)
zetazeta_x(kstep) = zeta(kstep)*zeta_x(kstep)
end do


call dfftw_plan_dft_r2c_1d(plan,nx,uu_x,uu_xcomplex,FFTW_ESTIMATE)
call dfftw_execute_dft_r2c(plan, uu_x, uu_xcomplex)
call dfftw_destroy_plan(plan)

call dfftw_plan_dft_r2c_1d(plan,nx,zetazeta_x,zetazeta_xcomplex,&
FFTW_ESTIMATE)

call dfftw_execute_dft_r2c(plan, zetazeta_x, zetazeta_xcomplex)
call dfftw_destroy_plan(plan)


zetazeta_xcomplex = zetazeta_xcomplex*nx_inv
uu_xcomplex = uu_xcomplex*nx_inv

do kstep = 0, nxhalf
uRHScomplex(kstep) &
& = (-1.d0*b1*uu_xcomplextest(kstep)-b2*zeta_xcomplex(kstep)&
&-b3*zetazeta_xcomplextest(kstep))&

```

```

&/(1-b4*Dfft(kstep)*Dfft(kstep))
end do

call dfftw_plan_dft_c2r_1d(plan, nx, uRHScomplex, uRHS, FFTW_ESTIMATE)
call dfftw_execute_dft_c2r(plan, uRHScomplex, uRHS)
call dfftw_destroy_plan(plan)
end subroutine TimeDerivative


function initial_value(x)
use parameters
implicit none
double precision :: x, initial_value
initial_value = hgate *(dtanh(lambda*(x-lgate)) &
- dtanh(lambda *(x+lgate)))/2.d0
return
end function initial_value

```

## D.4 The KdV equation

### Main code

```

PROGRAM KDV
!external
implicit none
include 'fftw3.f'
integer, parameter :: nx = 1024
integer, parameter :: nxhalf = ceiling(nx/2.d0)
integer:: mx, mxhalf
double precision, dimension(0:nx-1) :: zeta, zetabi, zeta1

```

```

double complex :: Dfft(0:nxhalf)
double complex, parameter :: I = cmplx(0.d0, 1.d0)
double complex :: slope
double precision:: x(0:nx-1),c0,c1,c2,c3, c4,rho1,rho2,h1, h2,&
& L, R, stop_time, grav, tnow, K
double precision :: ONE, HALF, SIXTH, tnow1
double precision, dimension(0:nx-1) :: zetaK1, zetaK2, zetaK3, zetaK4
double precision :: RHS1, RHS2
double precision :: hgate = 1.d1, lgate =1.d2, lambda = 2.d-1
integer :: nframe
character(len = 20) :: nu, nzeta
double precision :: mkframe, timerecord
!internal
integer kstep, tstep
double precision:: pi,dx, dt
integer nt
real, dimension(2) :: tarray1, tarray2
real :: result1, result2

mx = ceiling(nx*2.d0)
mxhalf = ceiling(mx/2.d0)
pi = 4.d0 *datan(1.d0)
L = -2.464d3
R = 2.464d3
!lambda = 0.5
h1 = 14.551541169411323d0

```



```

rho1 =0.9998817144855958d0
rho2 = 1.0215548370691494d0

!lambda = 1.0

!h1      = 14.753638180803918d0
!rho1 = 0.9994235006405087d0
!rho2 = 1.0217692795999886d0

!lambda = 0.25

!h1      = 14.321902674392888d0
!rho1 = 1.0009125274217063d0
!rho2 = 1.0211814125745406d0

!rho1 = 0.999d0
!rho2 = 1.022d0

!h1 = 1.5d1
h2 = 7.7d1-h1
grav = 9.81d2
c0 = dsqrt(grav*h1*h2*(rho2-rho1)/(rho1*h2+rho2*h1))
c1 = -1.5d0*c0*(rho1*h2**2-rho2*h1**2)/(rho1*h1*h2**2+rho2*h1**2*h2)
c2 = c0/6.d0*(rho1*h1**2*h2+rho2*h1*h2**2)/(rho1*h2+rho2*h1)
write(*,*) c0, c1, c2

stop_time = 8.d1

ONE = 1.d0
HALF = 0.5d0
SIXTH = 1.d0/6.d0

dx = (R-L)/nx
dt = 4.d-5
K = 2.0*pi/(R-L)

```

```

nt = ceiling(stop_time/dt)

do kstep = 0, nx-1
x(kstep) = L + kstep*dx
zeta(kstep)=hgate/4.d0*(dtanh(lambda*(x(kstep)-lgate))&
-dtanh(lambda*(x(kstep)+lgate)))
end do

do kstep = 0,nxhalf
Dfft(kstep) = 2*pi*I/(R-L)*kstep
end do

do kstep = 0, nx-1
x(kstep) = L+dx*kstep
end do

tnow = 0.d0

tstep = 0

mkframe = 2.5d0

timerecord = 0.d0

nframe = 0

write(nzeta,'(a, i0,a)') 'zeta',nframe, '.dat'
open(21, file = nzeta)
write(21,501)(zetabi(kstep), kstep = 0, nx-1)
close (21)

nframe = nframe +1

call ETIME(tarray1, result1)

```

```

do while ((tnow+dt).le.(stop_time+1d-10) )
tstep = tstep+1
if((timerecord+1d-10) .ge. mkframe) then
nframe = nframe+1
timerecord = 0.d0
end if
if (tnow+dt > stop_time) then
dt = stop_time-(tnow)
end if
call TimeDerivative(nx,nxhalf,c0, c1, c2, c3, dt,  zeta, Dfft,  zeta1)
zeta = zeta1
timerecord = timerecord + dt
tnow  = tnow + dt
end do
call ETIME(tarray2, result2)

open(21, file = 'zeta_raw.dat')
do kstep = 0, nx-1
write(21,505) x(kstep), zeta(kstep)
end do
close(21)

print * , 'execution time = ', tarray2(1)-tarray1(1)
501 format(2048(D30.20,1x),1x)
502 format(D30.20)
503 format(D30.20, 1x, D30.20, 1x, D30.20)
505 format(D30.20, 1x, D30.20,1x)

```

```
end program KDV
```

```
subroutine TimeDerivative(nx,nxhalf, c0, c1, c2, c3, &
dt, zeta, Dfft, zetanew )
implicit none
include 'fftw3.f'
integer :: nx,nxhalf, mx, mxhalf, kstep
double precision :: c0, c1, c2, c3, half
double precision :: nx_inv, mx_inv, dt
double complex, dimension(0:nxhalf) :: Dfft
double precision, dimension(0:nx-1) :: zeta, zetaleft
double precision, dimension(0:nx-1) :: zeta2, zeta2x, zeta3
double precision, dimension(0:nx-1) :: zetanew, zetap, zetap2
double precision, dimension(0:nx-1) :: zetapleft, zetap2x, zetap3
double precision, dimension(0:nx-1) :: zetaRHS
double complex, dimension(0:nxhalf) :: zetacomplex, zeta2complex
double complex, dimension(0:nxhalf) :: zeta2xcomplex
double complex, dimension(0:nxhalf) :: zeta3complex, zetap2complex
double complex, dimension(0:nxhalf) :: Rt, St1, St2
double complex, dimension(0:nxhalf) :: zetapcomplex, zetap2xcomplex
double complex, dimension(0:nxhalf) :: zetap3complex
integer *8 plan

half = 5.d-1
nx_inv = 1.d0/dble(nx)
```

```

do kstep = 0, nxhalf
  Rt(kstep) = (1.d0- dt*5.d-1*c0*Dfft(kstep)&
    -dt*5.d-1*c2*Dfft(kstep)**3) &
    /(1.d0+dt*5.d-1*c0*Dfft(kstep)+ dt*5.d-1*c2*Dfft(kstep)**3)
  St1(kstep) = -2.5d-1*c1*dt*Dfft(kstep)&
    /(1.d0+dt*5.d-1*c0*Dfft(kstep)+ dt*5.d-1*c2*Dfft(kstep)**3)
  St2(kstep) = -2.5d-1*c3*dt &
    /(1.d0+dt*5.d-1*c0*Dfft(kstep)+ dt*5.d-1*c2*Dfft(kstep)**3)
end do

zetaleft (0) = zeta(0)

do kstep = 1, nx-1
  zetaleft(kstep) = zeta(nx-kstep)
end do

call dot21(nx, nxhalf, zeta, zeta, zeta2)
call dfftw_plan_dft_r2c_1d(plan,nx,zeta,zetacomplex,FFTW_ESTIMATE)
call dfftw_execute_dft_r2c(plan, zeta, zetacomplex)
call dfftw_destroy_plan(plan)
call dfftw_plan_dft_r2c_1d(plan,nx,zeta2,zeta2complex,FFTW_ESTIMATE)
call dfftw_execute_dft_r2c(plan, zeta2, zeta2complex)
call dfftw_destroy_plan(plan)

zetacomplex = zetacomplex*nx_inv
zeta2complex = zeta2complex*nx_inv

zetap = zeta

zetanew = 1.d0

do kstep = 0, nxhalf
  zeta2xcomplex(kstep) = Dfft(kstep) * zeta2complex(kstep)

```

```

end do

call dfftw_plan_dft_c2r_1d(plan,nx, zeta2xcomplex, zeta2x, FFTW_ESTIMATE)
call dfftw_execute_dft_c2r(plan, zeta2xcomplex, zeta2x)
call dfftw_destroy_plan(plan)

call dot21(nx, nxhalf, zeta2x, zetaleft, zeta3)

call dfftw_plan_dft_r2c_1d(plan,nx,zeta3,zeta3complex,FFTW_ESTIMATE)
call dfftw_execute_dft_r2c(plan, zeta3, zeta3complex)
call dfftw_destroy_plan(plan)

zeta3complex = zeta3complex * nx_inv

do while (maxval(abs(zetap-zetanew))> 1.d-13)

zetanew = zetap

zetapleft (0) = zetap(0)

  do kstep = 1, nx-1

zetapleft(kstep) = zetap(nx-kstep)

end do

call dot21(nx, nxhalf, zetap, zetap, zetap2)

call dfftw_plan_dft_r2c_1d(plan,nx,zetap,zetapcomplex,FFTW_ESTIMATE)
call dfftw_execute_dft_r2c(plan, zetap, zetapcomplex)
call dfftw_destroy_plan(plan)

call dfftw_plan_dft_r2c_1d(plan,nx,zetap2,zetap2complex,FFTW_ESTIMATE)
call dfftw_execute_dft_r2c(plan, zetap2, zetap2complex)
call dfftw_destroy_plan(plan)

zetap2complex = zetap2complex*nx_inv

zetapcomplex = zetapcomplex * nx_inv

do kstep = 0, nxhalf

zetap2xcomplex(kstep) = Dfft(kstep) * zetap2complex(kstep)

```

```

end do

call dfftw_plan_dft_c2r_1d(plan,nx,zetap2xcomplex,zetap2x,FFTW_ESTIMATE)
call dfftw_execute_dft_c2r(plan, zetap2xcomplex, zetap2x)
call dfftw_destroy_plan(plan)

call dot21(nx, nxhalf, zetap2x, zetapleft, zetap3)

call dfftw_plan_dft_r2c_1d(plan,nx,zetap3,zetap3complex,FFTW_ESTIMATE)
call dfftw_execute_dft_r2c(plan, zetap3, zetap3complex)
call dfftw_destroy_plan(plan)

zetap3complex = zetap3complex * nx_inv

do kstep = 0, nxhalf

zetapcomplex (kstep) = Rt(kstep)*zetacomplex(kstep) &
+ St1(kstep) *(zeta2complex(kstep)+zetap2complex(kstep))&
+ St2(kstep) * (zeta3complex(kstep)+ zetap3complex(kstep))

end do

call dfftw_plan_dft_c2r_1d(plan,nx,zetapcomplex,zetap,FFTW_ESTIMATE)
call dfftw_execute_dft_c2r(plan, zetapcomplex, zetap)
call dfftw_destroy_plan(plan)

end do

zetanew = zetap

end subroutine TimeDerivative


subroutine dot21(nx, nxhalf, a, b, result)

implicit none

include 'fftw3.f'

integer :: nx, nxhalf, kstep

double precision , dimension(0: nx-1) :: a, b, a1, b1,result

```

```

double complex, dimension(0: nxhalf) :: acomplex, bcomplex
double complex, dimension(0: nxhalf) :: a1complex, b1complex
integer *8 plan

call dfftw_plan_dft_r2c_1d(plan, nx, a, acomplex, FFTW_ESTIMATE)
call dfftw_execute_dft_r2c(plan, a, acomplex)
call dfftw_destroy_plan(plan)
call dfftw_plan_dft_r2c_1d(plan, nx, b, bcomplex, FFTW_ESTIMATE)
call dfftw_execute_dft_r2c(plan, b, bcomplex)
call dfftw_destroy_plan(plan)
acomplex = acomplex /dble(nx)
bcomplex = bcomplex/dble(nx)
a1complex = acomplex
b1complex = bcomplex
do kstep = floor(nxhalf/2.d0)-1, nxhalf
a1complex(kstep) = 0.d0
b1complex(kstep) = 0.d0
end do

call dfftw_plan_dft_c2r_1d(plan, nx, acomplex, a1, FFTW_ESTIMATE)
call dfftw_execute_dft_c2r(plan, acomplex, a1)
call dfftw_destroy_plan(plan)
call dfftw_plan_dft_c2r_1d(plan, nx, bcomplex, b1, FFTW_ESTIMATE)
call dfftw_execute_dft_c2r(plan, bcomplex, b1)
call dfftw_destroy_plan(plan)

```



```

do kstep = 0, nx-1
result(kstep) = a1(kstep) * b1(kstep)
end do
end subroutine dot21

```

## D.5 Higher order uni-directional model

### Main code

```

PROGRAM HIGHER
!external
implicit none
include 'fftw3.f'
integer, parameter :: nx = 1024
integer, parameter :: nxhalf = ceiling(nx/2.d0)
integer:: mx, mxhalf
double precision, dimension(0:nx-1) :: zeta, zetabi, zeta1
double complex :: Dfft(0:nxhalf)
double complex, parameter :: I = cmplx(0.d0, 1.d0)
double complex :: slope
double precision:: x(0:nx-1),c0,c1,c2,c3, c4, c5, c7, c8, c9
double precision :: rho1,rho2,h1, h2,&
& L, R, stop_time, grav, tnow, K, temp
double precision :: ONE, HALF, SIXTH, tnow1
double precision, dimension(0:nx-1) :: zetaK1, zetaK2, zetaK3, zetaK4
double precision :: RHS1, RHS2
double precision :: hgate = 1.d1, lgate =1.d2, lambda = 1.d-1
integer :: nframe

```

```

character(len = 20) :: nu, nzeta
double precision :: mkframe, timerecord
!internal
integer kstep, tstep
double precision:: pi,dx, dt
integer nt
real, dimension(2) :: tarray1, tarray2
real :: result1, result2

mx = ceiling(nx*2.d0)
mxhalf = ceiling(mx/2.d0)
pi = 4.d0 *datan(1.d0)
L = -2.464d3
R = 2.464d3
!lambda = 0.5
h1      = 14.551541169411323d0
rho1 =0.9998817144855958d0
rho2 = 1.0215548370691494d0
!lambda = 1.0
!h1      = 14.753638180803918d0
!rho1 = 0.9994235006405087d0
!rho2 = 1.0217692795999886d0
!lambda = 0.25
!h1      = 14.321902674392888d0
!rho1 = 1.0009125274217063d0
!rho2 = 1.0211814125745406d0

```

```

!rho1 = 0.999d0

! rho2 = 1.022d0

! h1 = 1.5d1

h2 = 7.7d1-h1

grav = 9.81d2

c0 = dsqrt(grav*h1*h2*(rho2-rho1)/(rho1*h2+rho2*h1))

c1 = -1.5d0*c0*(rho1*h2**2-rho2*h1**2)/(rho1*h1*h2**2+rho2*h1**2*h2)

c2 = c0/6.d0*(rho1*h1**2*h2+rho2*h1*h2**2)/(rho1*h2+rho2*h1)

c3 = 7.d0*c1*c1/(18.d0*c0)-c0*(rho1*h2**3+rho2*h1**3)&
/(h1*h1*h2*h2)*(rho1*h2+rho2*h1))

c4 = (17.d0*c1*c2)/(12.d0*c0)+c0*h1*h2*(rho1-rho2)&
/(12.d0*(rho1*h2+rho2*h1))

c5 = 7.d0*c1*c2/(3.d0*c0) + c0*h1*h2*(rho1-rho2)&
/(6.d0*(rho1*h2+rho2*h1))

c7 = (2.d0*c4-c5)/c1

c8 = c2 + c0*(2.d0*c4-c5)/c1

c9 = c5-c4

stop_time = 8.d1

ONE = 1.d0

HALF = 0.5d0

SIXTH = 1.d0/6.d0

dx = (R-L)/nx

dt = 5.d-5

K = 2.0*pi/(R-L)

nt = ceiling(stop_time/dt)

do kstep = 0, nx-1

```

```

x(kstep) = L + kstep*dx
temp = c2**(1.d0/3.d0)
zeta(kstep)=hgate/4.d0*(dtanh(lambda*(x(kstep)-lgate))&
-dtanh(lambda*(x(kstep)+lgate)))
end do

do kstep = 0,nxhalf
Dfft(kstep) = 2*pi*I/(R-L)*kstep
end do

do kstep = 0, nx-1
x(kstep) = L+dx*kstep
end do

tnow = 0.d0
tstep = 0
mkframe = 2.5d0
timerecord = 0.d0
nframe = 0
nframe = nframe +1
call ETIME(tarray1, result1)
do while ((tnow+dt).le.(stop_time+1d-10) )
tstep = tstep+1
if (tnow+dt > stop_time) then
dt = stop_time-(tnow)
end if

call TimeDerivative(nx,nxhalf,c0, c1, c2, c3, c7,c8,c9,&
dt, zeta, Dfft, zeta1)

zeta = zeta1

```

```

timerecord = timerecord + dt

tnow  = tnow + dt

end do

open(21, file = 'zeta_raw.dat')

do kstep = 0, nx-1

write(21,505) x(kstep), zeta(kstep)

end do

close(21)

call ETIME(tarray2, result2)

print * , 'execution time = ', tarray2(1)-tarray1(1)

501 format(2048(D30.20,1x),1x)

502 format(D30.20)

503 format(D30.20, 1x, D30.20, 1x, D30.20)

505 format(D30.20, 1x, D30.20,1x)

end program HIGHER


subroutine TimeDerivative(nx,nxhalf, c0, c1, c2, &
c3, c7,c8, c9, dt, zeta, Dfft, zeta_new )

implicit none

include 'fftw3.f'

integer :: nx,nxhalf,  kstep

double precision :: c0, c1, c2, c3, c7,c8,c9, half, nx_inv, dt

double complex, dimension(0:nxhalf) :: Dfft

double precision, dimension(0:nx-1) :: zeta_test,  zeta, zeta2, zeta3

double precision, dimension(0:nx-1) ::  zeta_new, zetax, zetax2

double precision, dimension(0:nx-1) ::  zetaxx, zetazetaxx, f1

```

```

double complex, dimension(0:nxhalf) :: zetacplx, zetaxcplx, zetaxxcplx
double complex, dimension(0:nxhalf) :: f1cplx, zeta_newcplx
double precision, dimension(0:nx-1) :: zetap, zeta2p, zeta3p
double precision, dimension(0:nx-1) :: zetaxp, zetax2p, zetaxxp
double precision, dimension(0:nx-1) :: zetazetaxxp, f1p
double complex, dimension(0:nxhalf) :: zetapcplx, zetaxpcplx
double complex, dimension(0:nxhalf) :: zetaxxcplx, f1pcplx
double complex, dimension(0:nxhalf) :: St, Rt, zeta_testcplx
double complex :: dfft_now

integer *8 plan

half = 5.d-1

nx_inv = 1.d0/dble(nx)

do kstep = 0, nxhalf
dfft_now = Dfft(kstep)

St(kstep) = 1.d0+ c7* dfft_now**2&
+ c8 * dt* half * dfft_now **3&
+ c0 *dt* half * dfft_now

Rt(kstep) = 1.d0+ c7* dfft_now**2&
- c8 * dt* half * dfft_now **3&
- c0 *dt* half * dfft_now
end do

call dot21(nx, nxhalf, zeta, zeta, zeta2)
call dot21(nx, nxhalf, zeta, zeta2, zeta3)
call dfftw_plan_dft_r2c_1d(plan,nx,zeta,zetacplx,FFTW_ESTIMATE)
call dfftw_execute_dft_r2c(plan, zeta, zetacplx)
call dfftw_destroy_plan(plan)

```

```

zetacplx = zetacplx*nx_inv
zetaxcplx = 0.d0
zetaxxcplx = 0.d0
do kstep = 0, nxhalf
zetaxcplx(kstep) = Dfft(kstep) * zetacplx(kstep)
zetaxxcplx(kstep) = Dfft(kstep) * zetaxcplx(kstep)
end do

call dfftw_plan_dft_c2r_1d(plan,nx, zetaxcplx, zetax, FFTW_ESTIMATE)
call dfftw_execute_dft_c2r(plan, zetaxcplx, zetax)
call dfftw_destroy_plan(plan)

call dfftw_plan_dft_c2r_1d(plan,nx, zetaxxcplx, zetaxx, FFTW_ESTIMATE)
call dfftw_execute_dft_c2r(plan, zetaxxcplx, zetaxx)
call dfftw_destroy_plan(plan)

call dot21(nx, nxhalf, zetax, zetax, zetax2)
call dot21(nx, nxhalf, zeta, zetaxx, zetazetaxx)

f1 = c1*half *zeta2 + c3 * zeta3 + c9*(zetax2+ 2.d0*zetazetaxx)
call dfftw_plan_dft_r2c_1d(plan,nx, f1 , f1cplx ,FFTW_ESTIMATE)
call dfftw_execute_dft_r2c(plan, f1, f1cplx)
call dfftw_destroy_plan(plan)

f1cplx = f1cplx * nx_inv
zetap = 0.d0

zeta_test = zeta

do while (maxval(abs(zeta_test-zetap))/maxval(abs(zeta_test))) > 1.d-13)

zetap = zeta_test

call dot21(nx, nxhalf, zetap, zetap, zeta2p)
call dot21(nx, nxhalf, zetap, zeta2p, zeta3p)

```

```

call dfftw_plan_dft_r2c_1d(plan,nx,zetap,zetapcplx,FFTW_ESTIMATE)
call dfftw_execute_dft_r2c(plan, zetap, zetapcplx)
call dfftw_destroy_plan(plan)
zetapcplx = zetapcplx*nx_inv
zetaxpcplx = 0.d0
zetaxxpcplx = 0.d0
do kstep = 0, nxhalf
zetaxpcplx(kstep) = Dfft(kstep) * zetapcplx(kstep)
zetaxxpcplx(kstep) = Dfft(kstep) * zetaxpcplx(kstep)
end do
call dfftw_plan_dft_c2r_1d(plan,nx, zetaxpcplx, zetaxp, FFTW_ESTIMATE)
call dfftw_execute_dft_c2r(plan, zetaxpcplx, zetaxp)
call dfftw_destroy_plan(plan)
call dfftw_plan_dft_c2r_1d(plan,nx, zetaxxpcplx, zetaxxp, FFTW_ESTIMATE)
call dfftw_execute_dft_c2r(plan, zetaxxpcplx, zetaxxp)
call dfftw_destroy_plan(plan)
call dot21(nx, nxhalf, zetaxp, zetaxp, zetax2p)
call dot21(nx, nxhalf, zetap, zetaxxp, zetazetaxxp)
f1p = c1*half *zeta2p + c3 * zeta3p + c9*(zetax2p+ 2.d0*zetazetaxxp)
call dfftw_plan_dft_r2c_1d(plan,nx, f1p , f1pcplx ,FFTW_ESTIMATE)
call dfftw_execute_dft_r2c(plan, f1p, f1pcplx)
call dfftw_destroy_plan(plan)
f1pcplx = f1pcplx * nx_inv
do kstep = 0, nxhalf
zeta_testcplx(kstep) = Rt(kstep)/St(kstep) * zetacplx(kstep) &
&- half*Dfft(kstep)/St(kstep) * dt* (f1cplx(kstep)+ f1pcplx(kstep))

```



```

end do

call dfftw_plan_dft_c2r_1d(plan,nx,zeta_testcplx,zeta_test,FFTW_ESTIMATE)

call dfftw_execute_dft_c2r(plan, zeta_testcplx,  zeta_test)

call dfftw_destroy_plan(plan)

zeta_test = half * (zeta_test + zetap)

end do

zeta_new = zeta_test

end subroutine TimeDerivative


subroutine dot21(nx, nxhalf, a, b, result)

implicit none

include 'fftw3.f'

integer :: nx, nxhalf, kstep

double precision , dimension(0: nx-1) :: a, b, a1, b1,result
double complex, dimension(0: nxhalf) :: acomplex, bcomplex
double complex, dimension(0: nxhalf) :: a1complex, b1complex
integer *8 plan

call dfftw_plan_dft_r2c_1d(plan, nx, a, acomplex, FFTW_ESTIMATE)
call dfftw_execute_dft_r2c(plan, a, acomplex)
call dfftw_destroy_plan(plan)
call dfftw_plan_dft_r2c_1d(plan, nx, b, bcomplex, FFTW_ESTIMATE)
call dfftw_execute_dft_r2c(plan, b, bcomplex)
call dfftw_destroy_plan(plan)
acomplex = acomplex /dble(nx)
bcomplex = bcomplex/dble(nx)

```

```

a1complex = acomplex
b1complex = bcomplex
do kstep = floor(nxhalf/2.d0)-1, nxhalf
a1complex(kstep) = 0.d0
b1complex(kstep) = 0.d0
end do

call dfftw_plan_dft_c2r_1d(plan, nx, acomplex, a1, FFTW_ESTIMATE)
call dfftw_execute_dft_c2r(plan, acomplex, a1)
call dfftw_destroy_plan(plan)

call dfftw_plan_dft_c2r_1d(plan, nx, bcomplex, b1, FFTW_ESTIMATE)
call dfftw_execute_dft_c2r(plan, bcomplex, b1)
call dfftw_destroy_plan(plan)

do kstep = 0, nx-1
result(kstep) = a1(kstep) * b1(kstep)
end do

end subroutine dot21

```

## Bibliography

- [1] ALMGREN, A.S., BELL, J.B., COLELLA, P., HOWELL, L.H., WELCOME M.L. 1998 A conservative adaptive projection method for the variable density incompressible Navier-Stokes equations. *Journal of Computational Physics*, **142**, 1–46.
- [2] APEL, J.R., HOLBROOK, J.R., LIU, A.K., TSAI, J.J. 1985 The Sulu Sea internal soliton experiment. *Journal of Physical Oceanography*, **15**, 1625–1531
- [3] BAINES, P.G. *Topographic Effects in Stratified Flows*. Cambridge University Press, Cambridge, 1995.
- [4] BENJAMIN, T. B. 1966 Internal waves of finite amplitude and permanent form. *Journal of Fluid Mechanics*, **25**, 241–270.
- [5] BENJAMIN, T. B. 1986 On the Boussinesq model for two-dimensional wave motions in heterogeneous fluids. *Journal of Fluid Mechanics*, **165**, 445–474.
- [6] BOONKASAME, A. & MILEWSKI, P. 2011 The stability of large-amplitude shallow interfacial non-Boussinesq flows. *Studies in Applied Mathematics*, DOI: 10.1111/j.1467-9590.2011.00528.x.
- [7] BYRD, P.F. & FRIEDMAN, M. D. *Handbook of elliptic integrals for engineers and physicists*. Springer, New York, 1954.
- [8] CAMASSA, R., CHEN, S., FALQUI, G., ORTENZI, G. & PEDRONI, M. 2012 An inertia ‘paradox’ for incompressible stratified Euler fluids. *Journal of Fluid Mechanics*, **695**, 330–240.
- [9] CAMASSA, R., CHEN, S., FALQUI, G., ORTENZI, G. & PEDRONI, M. 2013 Effects of inertia and stratification in incompressible ideal fluids: pressure imbalances by rigid confinement. *Journal of Fluid Mechanics*, **726**, 404–438.

- [10] CAMASSA, R., CHOI, W., MICHALLET, H., RUSÅS, P.-O. & SVEEN, J.K. 2006 On the realm of validity of strongly nonlinear asymptotic approximations for internal waves. *Journal of Fluid Mechanics*, **549**, 1–23.
- [11] CAMASSA, R. & LEVERMORE, C.D. 1997 Layer-mean quantities, local conservation laws, and vorticity. *Physics Review Letters*, **78**, 650–653.
- [12] CAMASSA, R. & TIRON, R. 2011 Optimal two-layer approximation for continuous density stratification. *Journal of Fluid Mechanics*, **669**, 32–54.
- [13] CHEN, G. & OLVER, P.J. 2013 Dispersion of discontinuous periodic waves. *Proceedings of Royal Society A*, **469**, doi:10.1098/rspa.2012.0407
- [14] CHOI, W., BARROS, R., JO, T. 2009 A regularized model for strongly nonlinear internal solitary waves. *Journal of Fluid Mechanics*, **629**, 73–85.
- [15] CHOI, W. & CAMASSA, R. 1999 Fully nonlinear internal waves in a two-fluid system. *Journal of Fluid Mechanics*, **396**, 1–36.
- [16] CHOI, W., GOULLET, A., JO, T. 2011 An iterative method to solve a regularized model for strongly nonlinear long internal waves. *Journal of Computational Physics*, **230**, 2021–2030.
- [17] CRAIG, W., GUYENE, P., KALISCH, H. 2005 Hamiltonian long-wave expansions for free surfaces and interfaces. *Communications in Pure and Applied Mathematics*, **58**, 1587–1641
- [18] ESLER J. G. & PEARCE J. D. 2011 Dispersive dam-break and lock-exchange flows in a two-layer fluid. *Journal of Fluid Mechanics*, **667**, 555–585.
- [19] GEL’FAND, I.M. & LEVITAN, B.M. 1955 On the determination of a differential equation from its spectral function *American Mathematical Society Translations*, **(2)1**, 253–304
- [20] GELFAND, I.M & SHILOV, G.E. *Generalized Functions* Academic Press, New York, 1964.

- [21] GRADSHTEYN, I.S., RYZHIK, I.M., JEFFREY, A. & ZWILLINGER, D. *Tables of integrals, Series, and Products*. Academic Press, New York, 2000.
- [22] GREEN, A.E. & NAGHDI, P.M. 1976 A derivation of equations for wave propagation in water of variable depth. *Journal of Fluid Mechanics*, **78**, 237–246.
- [23] GRUE, J., JENSEN, A., RUSÅS, P.-O. & SVEEN, J.K. 1999 Properties of large-amplitude internal waves. *Journal of Fluid Mechanics*, **380**, 257–278.
- [24] HELFRICH, K. & MELVILLE, K. 2006 Long nonlinear internal waves. *Annual Review of Fluid Mechanics*, **38**, 395–425.
- [25] JO, T. & CHOI, W. 2002 Dynamics of strongly nonlinear internal solitary waves in shallow water *Studies in Applied Mathematics*, **109**, 205–227.
- [26] JO, T. & CHOI, W. 2008 On stabilizing the strong nonlinear internal wave model. *Studies in Applied Mathematics*, **120**, 65–85.
- [27] KAUP, D. J. 1975 Finding eigenvalue problems for solving nonlinear evolution equations. *Progress in Theoretical Physics*, **54**, 72–78.
- [28] KAUP, D. J. 1975 A higher-order water-wave equation and the method for solving it. *Progress in Theoretical Physics*, **54**, 396–408.
- [29] LAMB, H. 1932 *Hydrodynamics*, 6th edn. Cambridge, England, Cambridge University Press.
- [30] LANDAU, L. D. & LIFSHITZ, E. M. 1958 *Quantum mechanics-nonrelativistic theory*, Pergamon Pressen Addison-Wesley Publishing Co., Reading, Mass.
- [31] MARCHENKO, V.A. 1986 *Sturm-Liouville Operators and Applications*. Birkhäuser, Basel
- [32] LISKA, R., MARGOLIN, L. & WENDROFF, B. 1995 Nonhydrostatic two-layer models of incompressible flow. *Computers Math. Applic.* **29**, 25–37.

- [33] MILEWSKI, P., TABAK, E., TURNER, C., ROSALES, R.R., & MEZANQUE, F. 2004 Nonlinear stability of two-layer flows. *Communications in Mathematical Sciences*, **2**, 427–442.
- [34] MIYATA, M. 1985 An internal solitary wave of large amplitude. *La Mer*, **23**, 43–48.
- [35] MIYATA, M. 1988 Long internal waves of large amplitude. *Nonlinear Water Waves, IUTAM Symp.*, Tokyo 1987, ed. K Horikawa, H Maruo. pp. 399–406. Berlin, Germany, Springer-Verlag.
- [36] VLASENKO, V. STASHCHUK, N. HUTTER, K. 2005 *Baroclinic Tides: Theoretical Modeling and Observational Evidence.*, 1st edn. Cambridge, England, Cambridge University Press.
- [37] WHITHAM, G. B. *Linear and Nonlinear Waves*, John Wiley & Sons, New York, 1974
- [38] WU, T.Y. 1981 Long waves in ocean and coastal waters, *Journal of Engineering Mechanics*, **107** 501–522.
- [39] WU, T.Y. 2000 A bidirectional long-wave model, *Methods and Applications of Analysis*, **9340** 108–117.
- [40] YIH, C. *Stratified Flows*, Academic Press, New York, 1980.
- [41] ZAKHAROV, V.E. & KUZNETSOV, E.A. 1997 Hamiltonian formalism for nonlinear waves. *Physics Uspekhi*, **40**, 1087–1116.
- [42] ZAKHAROV, V.E., MUSHER, S.L. & RUBENCHIK, A.M. 2005 Hamiltonian approach to the description of non-linear plasma phenomena. *Physics Reports C*, 285–366.